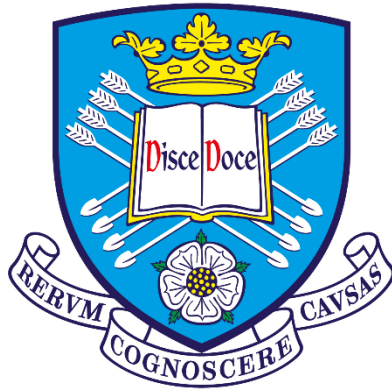


High Entropy Materials as Brazing Filler Metals for Thermoelectric Devices

Matthew John Way



The
University
Of
Sheffield.

Department of Materials Science and Engineering
University Of Sheffield

This thesis is submitted as a requirement for the degree of
Doctor of Philosophy

Submitted March 2020

Abstract

Brazing is a 5000 year-old joining process. Components are joined by heating them above the liquidus of a filler metal placed between them which forms a metallurgical bond as it solidifies. Brazed joints are relatively high strength and are often electrically conductive. As materials applications evolve, ever more is demanded of filler metals and hence applications arise in which current filler metals cannot perform sufficiently. In these cases, development of new custom-designed filler metals becomes the means of progress. The aim of this work is to design filler metals to replace ISO17672:Ag-155 when joining skutterudite thermoelectrics to copper within automotive heat-recovery devices. To do this, the class of High Entropy Alloys is explored as a source of new filler metal compositions.

Initial work here reported concludes that $R_a=0.09\mu\text{m}$ is the optimum surface roughness for wetting of Ag-155 on copper. EDX data demonstrates that excessive silver diffusion is the principal inadequacy of filler metal Ag-155; leading to the conclusion that the replacement filler metal should not contain silver.

Replacement filler metals are designed and explored. They can form low void percentage (<15%) metallurgical bonds between copper and nickel, contain 4 phases and melt between 528-681°C, with a characteristic constituent diffusion distance through nickel <70% that of filler metal Ag-155. Brazed joints formed with these fillers have lower bond strength than joints formed with Ag-155, but showed no clear decline in strength after thermal cycling; although the joint failure rate reached 40% within 20-30 cycles. Contact resistance of joints between skutterudite thermoelectrics brazed with these alloys was measured as $2.02 \times 10^{-5}\Omega\text{cm}^{-2}$, approximately half that of joints formed with Ag-155 and below the target maximum contact resistance of $5.0 \times 10^{-5}\Omega\text{cm}^{-2}$

Overall this work demonstrates the potential of some HEAs as filler metals and provides insights into designing HEA systems to fill niche filler metal applications.

Acknowledgements

Firstly, and most importantly I would like to thank Dr Russell Goodall for his constant and unwavering help, advice and support throughout the course of my Ph.D. I consider myself most fortunate to have had such a highly regarded academic as my supervisor and one who was prepared to give so much of his valuable time to ensure I succeeded not only academically but also on a personal level. I would also like to pass thanks to my industrial supervisors at Johnson Matthey; to Jack Willingham who first introduced me to brazing during my undergraduate degree and helped to grow my enthusiasm for the art; to Robert Potter who guided me through the majority of this Ph.D. and was always there to assist when I required it; and to Chris Nuttall who graciously took on the role of my industrial supervisor at a very late stage and assisted me in rounding out my Ph.D. I would like to thank Professor Eduardo Saiz and Qiaosong Cai of Imperial College London for kindly allowing me to use their furnace facilities in the Royal School of Mines and for assisting me with my wetting experiments. Finally, I would like to thank Rob Snell for assisting me as I transitioned into my Ph.D.; your help was most kind.

I would like to thank the various staff members and technicians who were not directly attached to this project but whose contributions are vital and often underappreciated. My thanks go to Lisa Hollands and Neil Hind in the foundry who were a constant source of help and support in all manner of technical aspects, with particular thanks to Neil for his invaluable brazing expertise and for providing the 'skilled industrial brazer' samples used in Chapter 4. I would like to thank Dr Nik Reeves McLaren for his assistance with conducting XRD and XRF analysis and to Dr Cheryl Shaw and Dr Le Ma of the Sorby Centre for Electron Microscopy who not only trained me to use SEMs but who were also always available for advice on imaging and technical assistance. Special thanks also go to Claire Utton for her help with conducting DSC experiments and for teaching me to use Thermo-Calc; your patience was most appreciated. Lastly I would like to thank all other staff in the department of Materials Science and Engineering at the University of Sheffield who have made this such as a special place for me to work and study over the last 7 years.

On a personal note I would like to pass on my sincerest thanks to the people in my life who have supported me throughout this journey. Firstly, to my parents who have always been there to love and support me in everything I do, thank you for always believing in me, even when I didn't believe in myself. I am truly blessed to have been raised in such a loving home and given such a platform to succeed from. I would like to thank all my friends in the nutta crew who have provided so many good memories over the last 7 years of my undergraduate and Ph.D; especially James Way, whose daily support powered me through many tough moments. Finally, and most importantly I would like to thank Stefani Ellis who has been beside me throughout this journey and helped me to be the best version of myself. I am blessed to have met you and without you this wouldn't have been possible.

Table of Contents

Chapter 1: Introduction	1
1.1. Challenges for Brazing Functional Materials	1
1.2. Technical Background.....	2
1.3. Aims and Objectives	5
1.4. Thesis Outline	5
1.5. Publications	6
1.6. References.....	6
Chapter 2: Literature Review	10
2.1. Brazing	10
2.1.1. Brazing Development and History.....	10
2.1.2. The Brazing Process	11
2.1.3. Factors Affecting Brazed Joints.....	14
2.1.4. Diffusion	17
2.1.5. Wetting, Flow, Adhesion and Bonding	18
2.1.6. Interface Types in Brazed Joints	22
2.1.7. Brazing Filler Metals	23
2.2. High Entropy Alloys	32
2.2.1. High Entropy Alloys: Discovery and Background	32
2.2.2. Empirical Parameters for Solid Solution Formation in HEAs.....	36
2.3. Thermoelectrics	43
2.3.1. Thermoelectric Devices	43
2.3.2. The Seebeck Effect	43
2.3.3. Layout of the Thermoelectric Generator	45
2.3.4. Applications of Thermoelectric Generators	46
2.3.5. Drawbacks to Using Heat Recovery Devices / TEGs.....	47
2.4. Summary	51
2.5. References.....	52
Chapter 3: Experimental Methodology	61
3.1. Alloy Manufacture.....	61
3.2. Brazed Joint Manufacture	61
3.2.1. T-joint Manufacture	61
3.2.2. Lap Joint Manufacture	64
3.3. Analytical Methodology.....	64

3.3.1.	Cutting, Grinding and Polishing.....	64
3.3.2.	Compositional Verification.....	66
3.3.3.	X-Ray Diffraction.....	67
3.4.	Microscopy	68
3.4.1.	Optical Microscopy	68
3.4.2.	Scanning Electron Microscopy (SEM).....	68
3.4.3.	Electron Dispersive X-Ray Spectroscopy (EDX)	68
3.5.	Differential Scanning Calorimetry	71
3.6.	Wetting Experiments	72
3.6.1.	Surface Roughness Characterisation.....	72
3.6.2.	Modified Sessile-Drop Experiments.....	73
3.7.	Mechanical Testing	74
3.8.	Thermal Cycling.....	75
3.9.	Contact Resistance Assessment.....	75
3.9.1.	Sample Assembly	75
3.9.2.	Contact Resistance Assessment.....	77
3.10.	References	77
Chapter 4:	Fundamental Investigations of Brazed Joints.....	78
4.1.	Introduction.....	78
4.2.	Effect of Surface Roughness on Brazed Joint Formation.....	78
4.3.	Diffusion - Zone Studies	89
4.3.1.	Influence of Torch Type and Brazing Technique on Joints Manufactured by Hand Torch Brazing.....	89
4.3.2.	Diffusion Length of Silver in Different Base Metals	98
4.4.	Summary	103
4.5.	References.....	104
Chapter 5:	Design of New Filler Metals for Thermoelectric Devices.....	106
5.1.	Introduction.....	106
5.2.	Composition Modelling.....	110
5.2.1.	Element Selection.....	110
5.2.2.	Modelling Results.....	117
5.3.	Brazing Testing	120
5.3.1.	Cu-Cu Joining.....	120
5.3.2.	Ni-Ni Joining.....	121
5.3.3.	Cu-Ni Joining	121
5.4.	Compositional Verification.....	123
5.5.	Phase Characterisation	125

5.5.1. Phase Modelling	125
5.5.2. Phase Identification	130
5.6. Melting Point Determination	144
5.7. Diffusion distance in nickel.....	145
5.8. Summary	149
5.9. References.....	150
Chapter 6: Suitability of Developed Filler metals for Joining Thermoelectric Components.....	154
6.1. Introduction.....	154
6.2. Wetting Assessment of Designed Alloys	155
6.3. Mechanical Properties of Designed Alloys.....	163
6.3.1. Room Temperature Tensile Strength	163
6.3.2. Thermal Cycling	168
6.4. Electrical Contact Resistance	174
6.5. Summary	180
6.6. References.....	181
Chapter 7: Conclusion	183
7.1. Summary	183
7.2. Future work.....	186
7.3. References.....	187
Appendices	188

Chapter 1: Introduction

1.1. Challenges for Brazing Functional Materials

Brazing as a joining process has existed for over 5000 years. A brazed joint creates a permanent metallic bond between materials by means of melting a ‘filler metal’ between two (or more) components (referred to as parent materials) and then allowing the filler to cool to form a bond. The versatility of this technique is such that not only dissimilar metals can be joined this way but entirely dissimilar classes of materials may be joined (e.g. metals to ceramics). The filler metal used in this technique will vary with the parent materials it is being used to join but must have the capability to wet the materials it joins and possess a melting temperature below the solidus of the materials it joins (in addition, to be referred to as a brazing filler metal as opposed to a solder, the fillers’ liquidus must be above the arbitrarily assigned boundary value of 450°C).

It is the versatility of brazing and its ability to form strong joints between widely different parent materials whilst eliciting minimal modification of these parent materials which makes brazing an indispensable technique in modern manufacturing. Recent examples of brazing being used as a joining technique in advanced engineering industries include sapphire-sapphire joining in aircraft windows [1], the joining of graphite to steel in petrochemical and nuclear industries [2], joining of corrosion resistant steel in rocket nozzles [3] and brazes for use with tungsten components in fusion reactor diverters [4]. Of particular interest to this project is the use of brazing to join functional materials, particularly those which operate at elevated temperatures; for which brazing is the primary joining technique. Examples include vacuum brazing of carbon nanotubes [5], and the use of Reactive Air Brazing (RAB) within Solid Oxide Fuel Cells (SOFCs) as the joining technique of choice owing to its ability to create strong electrically conductive joints which are stable at the elevated temperatures that SOFCs operate at [6][7][8]. Other elevated temperature electronics are required in down-hole oil and geothermal applications and have led to the development of new ‘high temperature solders’ such as a Ag-Au-Ge alloy whose liquidus (431°C) borders on the arbitrary temperature designation between solders and brazes [9]. The increasing use of electronic components in harsher environments will continue to drive the development of novel brazing filler metals to join electronic components where traditional solders can no longer function.

The constant evolution of materials used in modern engineering necessitates the constant development of new filler metals to join them. Many more complex materials are being developed (for both structural and electrical applications) for which current filler metals cannot bond adequately. The focus of this thesis is on the development of new filler metals for an elevated temperature electronics application (specifically the joining of components within thermoelectric devices) and aims to investigate the use of High Entropy Alloy systems (HEAs) as potential filler metal compositions suitable for this application. Whilst research into the use of HEA compositions as filler metals is currently sparse, HEAs have been shown to offer several desirable properties of brazing filler metals including good corrosion and oxidation resistance and good high temperature stability – all properties which are useful in the elevated temperature environments that brazed joints can be exposed to in service. In addition, the nature of HEA compositions forming single phases allows for the inclusion of larger quantities of elements to control and suppress melting points or improve alloy flow than in traditional brazing filler metals. If these elements were included in such high quantities in traditional brazing filler metal compositions,

they would segregate and form brittle intermetallic compounds which are known to lead to weak joints and premature failure in service (see Section 1.2. and Section 2.1.7.4 for further information). Finally, the multicomponent nature of HEAs could mediate the transition in a joint between dissimilar materials potentially minimising the effect of thermal coefficient of expansion mismatch.

1.2. Technical Background

In 2018 the annual global average carbon dioxide (CO₂) concentration reached 407.4±0.1ppm; the highest ever recorded level seen using modern instruments or in ice core records which date back 800,000 years [10]. The increasing level of greenhouse gases such as CO₂ produced by humans has led to an estimated 1.0°C average global temperature rise above pre-industrial levels [11]. This increase in global temperatures has led to an average decrease of summer sea ice in the arctic of 130,000km² per year and has helped contribute to sea levels rising over 7cm in the last 25 years [12]. Statements on the progress towards limiting global temperatures rise in the 2018 IPCC special report offered bleak conclusions towards our current likelihood of meeting targets set in the Paris Agreement.

“Estimates of the global emissions outcome of current nationally stated mitigation ambitions as submitted under the Paris Agreement would lead to global greenhouse gas emissions in 2030 of 52–58 GtCO₂ eq yr⁻¹ (medium confidence). Pathways reflecting these ambitions would not limit global warming to 1.5°C, even if supplemented by very challenging increases in the scale and ambition of emissions reductions after 2030 (high confidence).” [11]

To meet climate change targets, drastic reductions in CO₂ emissions are required. With automobiles contributing 16.4% of global CO₂ emissions annually, the transport sector is being targeted as a source of greenhouse gas emissions which needs to be reduced [13]. Whilst the gradual introduction of electric vehicles with higher efficiency engines and improved urban planning leading to greater use of public transport are both important factors in reducing the emissions of the transport sector, flaws with both these strategies (necessary innovation in battery technology to improve vehicle range and the difficulty in implementing urban planning in developing middle and low income countries) prevent them from being sufficient on their own to significantly reduce the transport sector’s CO₂ emissions [14]. Thus, technologies targeting improvements in efficiency in current automobiles are necessary to assist with emissions reductions. Currently, automobiles are very inefficient, with only 25% of the energy they release from fuel being used to propel the vehicle and a massive 40% of energy released being lost as waste heat in exhaust gases [15][16]. Thus, the recovery of some of this waste heat from engine exhaust gas is seen as a viable option to reduce vehicle CO₂ emissions by increasing fuel efficiency. A promising route to recover some of the heat lost in exhaust gases is via the use of thermoelectric generators placed in exhaust systems to convert waste heat into electricity to be fed back into the vehicle powertrain; some estimates conclude that if 6% of the waste heat lost in exhaust gases can be recovered then a 10% reduction in fuel consumption could be achieved [17].

Thermoelectric generators (TEGs) are a type of thermoelectric device which use the Seebeck effect to directly convert heat into electricity which can be then be used to do useful work. Whilst being an attractive solution to reducing CO₂ emissions, there are several challenges currently preventing the widespread commercial introduction of thermoelectric generators into automobiles. The primary bottlenecks arise from the

inefficiency of TEGs (with the efficiency of commercially available modules only reaching approximately 4-7% [18]) coupled with their high material and manufacturing costs leading to the energy they recover being too expensive to be financially viable. A reduction in cost by at least a factor of 2 is required for TEGs to be competitive with alternative heat recovery solutions such as Rankine or organic Rankine cycles which operate at an approximate cost of \$4-5/W ([19]). Some automotive manufacturers assess that electricity generation costs for TEGs need to be as low as \$0.5/W for conventional private cars [20]. Secondary issues in the commercial introduction of these devices include increasing the operating temperature range of TEG materials and issues with bonding materials used within thermoelectric devices [20]. It is this final issue which is the primary focus of the work in this thesis.

Joining of components within thermoelectric devices is primarily achieved using brazing. Brazing is a versatile metal joining process in which two (or more) components are joined with a *filler metal* (an alloy with a lower liquidus temperature than either component it is used to join). This assembly of components and filler metals (known as a *brazing assembly*) is heated to above the liquidus temperature of the filler metal (for brazing this requires a minimum liquidus of 450°C in order to differentiate the process from soldering – which uses fillers with a liquidus below 450°C) at which point the filler becomes molten. The filler metal then flows between the components and a metallurgical bond is formed between the filler metal and the components. The assembly is then cooled to allow the filler metal to solidify and form a joint. The thermoelectric materials of interest to the industrial sponsor of this work (Johnson Matthey) are skutterudite type thermoelectrics coated with a nickel diffusion barrier and brazed with a filler metal conforming to the specification of ISO 17672:2016 Ag-155 [21]. As part of the brief provided during the initial liaison meetings with Johnson Matthey it was noted that the skutterudite materials being used were suffering from performance issues due to the presence of silver-antimony compounds within the skutterudite, likely the hexagonal close packed P6₃/mmc zeta (ζ) phase and/or the tetragonal P4/mmm epsilon (ε) phase. It was the belief of Johnson Matthey technical staff attached to the project that silver from the Ag-155 filler metal used had diffused through the nickel diffusion barrier (which is applied to the thermoelectric) during the brazing cycle and reacted with the antimony present in the skutterudite thermoelectric materials to form these compounds which are detrimental to the skutterudites performance. An alternative filler metal was hence required which could be used to assemble TEGs containing these skutterudite thermoelectric materials without negatively impacting their performance.

The brazing filler metal used for joining the components within the aforementioned thermoelectric devices have several requirements which can be summarised as follows:

- The filler metal chosen must be capable of wetting the components to be joined and of forming a metallurgical bond with these materials which is capable of withstanding the thermal stresses which will be induced from a lifetime of service inside an automotive exhaust.
- The filler must melt over a suitable melting temperature range. If the melting temperature of the filler is too low (<500°C) then it will melt when exposed to the hot in-service environment inside an automotive exhaust and the TEG will be damaged. If the melting temperature is too high, then the process of joining the thermoelectric components together will damage the thermoelectric materials selected and reduce their efficiency.
- The filler metal used must not diffuse into the thermoelectric materials it joins. Thermoelectric materials are very specifically composed in order to achieve their electrical and thermal properties and the diffusion of elements from the filler metal

into the thermoelectric compound will likely alter the composition and substantially hinder its ability to function as a thermoelectric. Due to this, diffusion barriers are often applied to thermoelectric materials, in this instance the diffusion of filler metal elements must be limited to the diffusion barrier itself and not enter the thermoelectric material.

The combination of these requirements eliminates standard industrial filler metals from use and requires the design of a new filler metal which can satisfy these criteria. Developing new filler metals requires large scale investigations into potentially suitable classes of materials. The recently discovered class of materials known as high entropy alloys (HEAs) has been identified as one such class of materials warranting further investigation for this purpose.

High entropy alloys are a class of alloy system which possess multiple principal components. Unlike conventional alloys, (which are predominately a single element with others added in small amounts as ‘alloying additions’ to improve properties) high entropy alloys do not have a dominant principal element and are instead composed of many different elements in roughly equal atomic proportions. This class of alloys was first investigated in two papers published in 2004 by separate research groups. Professor Yeh in Taiwan coined the term ‘high entropy alloys’ and postulated that the increased configurational entropy associated with multiple component, near-equiatomic, alloy compositions would lead to the stabilization of random solid solution phases and a lower number of phases being present in these alloys than would traditionally be expected from phase prediction rules [22]. Simultaneously Professor Cantor and his colleagues in the UK had combined up to 20 elements in equiatomic proportions and found examples of alloys with less phases than predicted by the Gibbs phase rule. In particular, the single phase FCC, 5 component, $\text{Fe}_{20}\text{Cr}_{20}\text{Mn}_{20}\text{Ni}_{20}\text{Co}_{20}$ alloy produced in Cantor’s study (now often designated as “the Cantor alloy”) has been the subject of much investigation within the HEA field [23].

HEAs have been identified as a potentially suitable candidate class of materials for this application due to some of the interesting and impressive properties that they exhibit. Several of these properties are also sought after in brazing filler metals including their superior mechanical properties [24][25][26] (and stability [27][28][29]) at elevated temperatures, as well as a noted resistance to oxidation and corrosion [30][31][32]. Additionally, brazing filler metals require the ability to wet and interact with the base materials they are to bond to as well as being stable enough to not release low melting point elements from the filler metal whilst brazing or being subject to elevated service temperatures. Whilst not directly a property of HEAs, the compositional boundaries for HEAs allow the use of elements which are normally limited to a few atomic percent in brazing filler metals due to intermetallic formation to be incorporated in much higher percentages within designed alloy systems. The use of larger quantities of elements such as zinc (which is low cost and can lower filler melting point), gold (which offers excellent corrosion resistance and improves wetting) and tin (lowers melting point and can increase filler fluidity) offers an opportunity to develop new filler metal systems which are both innovative and could potentially be superior to current filler metals. Finally, the impressive ductility demonstrated by some HEAs [33] could be a beneficial property; as brazing filler metals are supplied in various forms including foil, rod and paste high ductility materials are more suited to the manufacturing processes required to make these forms.

1.3. Aims and Objectives

The principle aim of this thesis is to investigate high entropy alloys for their suitability as brazing filler metals for joining components in skutterudite thermoelectric devices. This primary aim can be split down into several aims which are covered throughout this thesis.

1. To investigate the influence of surface morphology on the ability of filler metals to wet a surface.
2. To discern whether the problems associated with silver-antimony compound formation in the skutterudite thermoelectric materials used by this projects sponsor are due to excessive diffusion of silver.
3. To develop alternative filler metals displaying the characteristics of high entropy alloy compositions, which can be used to braze copper to nickel. Should silver be found to be a detrimental component of filler metals in this application (aim 2) then silver must not be a component of the developed filler metals.
4. To characterise any promising filler metals developed through this project. This includes identifying their phase structure, assessing their melting ranges to see if they are appropriate for the intended application and assessing their diffusion in nickel to evaluate if they suffer from the same diffusion issue that the currently used filler metals do.
5. To investigate any promising filler metals developed in this project for their ability to perform as a filler metal in the intended application. This will include evaluating their strength, resistance to thermal cycling and their ability to wet surfaces. Due to the nature of these tests the data collected should be largely comparative to the currently used industrial filler metals (e.g. those conforming to ISO17672 Ag-155); in essence, to assess whether the developed alloys are an improvement to those currently used.

1.4. Thesis Outline

This thesis is formed of 7 chapters including this introduction; an outline of each of the subsequent 6 chapters is given below:

Chapter 2 introduces the appropriate theory concerned with the 3 primary fields in which this thesis of work is situated; brazing, high entropy alloys (HEAs) and thermoelectric devices. A comprehensive review on relevant literature pertaining to this project from these 3 fields is provided and concludes with a description of where this work places within its encompassing fields.

Chapter 3 provides a detailed account of the experimental methodology used throughout this thesis including alloy manufacture, brazing technique, sample preparation and analysis, as well as mechanical and electrical testing.

Chapter 4 covers the underpinning work of the project evaluating brazed joints using currently available filler metals. Investigations into the influence of key parameters affecting brazed joints such as surface roughness are contained in this chapter as well as research into diffusion zone sizes aimed at investigating the diffusivity of silver within nickel and other base materials

Chapter 5 encompasses the main body of work in this thesis; the development of new multi-component brazing filler metals for joining in thermoelectric devices. New alloy compositions are modelled and selected using rapid screening computer scripts, manufactured and tested as filler metals. The successful newly developed filler metals are then analysed to determine their phase structure and thermal properties before their diffusion through nickel is assessed and compared to industrially available filler metals

Chapter 6 completes the experimental work within the thesis by covering application based testing of the most successful filler metal compositions produced from the work in Chapter 5. The wetting capability of these filler metals is tested using a variation of the sessile drop technique and mechanical testing of joints brazed with the developed filler metals is conducted to compare to industrially available filler metals. Further mechanical testing examines the durability of joints using these filler metals after being subject to thermal cycling. Finally, electrical contact resistance of the copper–braze–thermoelectric interface is examined and reported on.

Chapter 7 concludes the thesis by summarising findings and offering suggestions for future work building on results collected in this thesis.

1.5. Publications

The papers published by the author which relate to the work contained within this thesis are listed below:

- Way M, Willingham J, Goodall R, Brazing filler metals. *Int. Mater. Rev.*2019;0:1–29.

1.6. References

- [1] Guo W, Wang T, Lin T, et al. Bismuth borate zinc glass braze for bonding sapphire in air. *Mater. Charact.* [Internet]. 2018;137:67–76. Available from: <https://doi.org/10.1016/j.matchar.2018.01.002>.
- [2] Jin W, He Y, Yang J, et al. Novel joining of dissimilar materials in the graphite/Hastelloy N alloy system using pure Au doped with Si particles. *Mater. Charact.* [Internet]. 2017;131:388–398. Available from: <http://dx.doi.org/10.1016/j.matchar.2017.07.034>.
- [3] Ivannikov AA, Kalin BA, Sevryukov ON, et al. Study of the Ni–Si–Be system as a base to create boron-free brazing filler metals. *Sci. Technol. Weld. Join.* 2018;23:187–197.
- [4] de Prado J, Sánchez M, Utrilla M V., et al. Study of a novel brazing process for W-W joints in fusion applications. *Mater. Des.* [Internet]. 2016;112:117–123. Available from: <http://dx.doi.org/10.1016/j.matdes.2016.09.067>.
- [5] Wu W, Hu A, Li X, et al. Vacuum brazing of carbon nanotube bundles. *Mater. Lett.* 2008;62:4486–4488.

- [6] Zhou Q, Bieler TR, Nicholas JD. Transient porous nickel interlayers for improved silver-based Solid Oxide Fuel Cell brazes. *Acta Mater.* [Internet]. 2018;148:156–162. Available from: <https://doi.org/10.1016/j.actamat.2018.01.061>.
- [7] Kim JY, Hardy JS, Weil KS. Novel Metal-Ceramic Joining for Planar SOFCs. *J. Electrochem. Soc.* [Internet]. 2005;152:J52. Available from: <http://jes.ecsdl.org/cgi/doi/10.1149/1.1896530>.
- [8] Chao CL, Chu CL, Fuh YK, et al. Interfacial characterization of nickel-yttria-stabilized zirconia cermet anode/interconnect joints with Ag-Pd-Ga active filler for use in solid-oxide fuel cells. *Int. J. Hydrogen Energy* [Internet]. 2015;40:1523–1533. Available from: <http://dx.doi.org/10.1016/j.ijhydene.2014.11.028>.
- [9] Vianco PT, Grant R, Rejent JA, et al. Ag-Au-Ge Alloys for High Temperature Geothermal and Oil Well Electronics Applications. *J. SMT Artic.* [Internet]. 2013;26. Available from: https://www.smta.org/knowledge/journal_detail.cfm?ARTICLE_ID=211.
- [10] Blunden J, Arndt DS. State of the climate in 2018. *Bull. Am. Meteorological Soc.* 2019;100.
- [11] Masson-Delmotte, V., P. Zhai, H.-O. Pörtner, D. Roberts, J. Skea PRS, A. Pirani, W. Moufouma-Okia, C. Péan, R. Pidcock, S. Connors, J.B.R. Matthews, Y. Chen, X. Zhou, M.I. Gomis, E. Lonnoy TM, M. Tignor and TW. IPCC 2018: Global Warming of 1.5°C. An IPCC Special Report on the impacts of global warming of 1.5°C above pre-industrial levels and related global greenhouse gas emission pathways, in the context of strengthening the global response to the threat of clim. 2019;1–630.
- [12] Nerem RS, Beckley BD, Fasullo JT, et al. Climate-change-driven accelerated sea-level rise detected in the altimeter era. *Proc. Natl. Acad. Sci. U. S. A.* 2018;115:2022–2025.
- [13] Shen ZG, Tian LL, Liu X. Automotive exhaust thermoelectric generators: Current status, challenges and future prospects. *Energy Convers. Manag.* [Internet]. 2019;195:1138–1173. Available from: <https://doi.org/10.1016/j.enconman.2019.05.087>.
- [14] Sivaprahasam D, Harish S, Gopalan R, et al. Automotive Waste Heat Recovery by Thermoelectric Generator Technology. *Bringing Thermoelectr. into Real.* [Internet]. InTech; 2018. p. 13. Available from: <http://www.intechopen.com/books/bringing-thermoelectricity-into-reality/automotive-waste-heat-recovery-by-thermoelectric-generator-technology>.
- [15] Kim S, Park S, Kim S, et al. A thermoelectric generator using engine coolant for light-duty internal combustion Engine-Powered Vehicles. *J. Electron. Mater.* 2011;40:812–816.
- [16] Avaritsioti E. Environmental and Economic Benefits of Car Exhaust Heat Recovery. *Transp. Res. Procedia* [Internet]. 2016;14:1003–1012. Available from: <http://dx.doi.org/10.1016/j.trpro.2016.05.080>.
- [17] Vazquez J, Sanz-Bobi M a, Palacios R, et al. State of the art of thermoelectric generators based on heat recovered from the exhaust gases of automobiles. *7th Eur. Work. Thermoelectr.* 2002;17.
- [18] MusiaŁ M, Borcuch M, Wojciechowski K. The Influence of a Dispersion Cone on the Temperature Distribution in the Heat Exchanger of a Thermoelectric Generator. *J.*

- Electron. Mater. 2016;45:1517–1522.
- [19] Leblanc S, Yee SK, Scullin ML, et al. Material and manufacturing cost considerations for thermoelectrics. *Renew. Sustain. Energy Rev.* [Internet]. 2014;32:313–327. Available from: <http://dx.doi.org/10.1016/j.rser.2013.12.030>.
- [20] Champier D. Thermoelectric generators: A review of applications. *Energy Convers. Manag.* [Internet]. 2017;140:167–181. Available from: <http://dx.doi.org/10.1016/j.enconman.2017.02.070>.
- [21] ISO/TC 44. Brazing — Filler metals (ISO 17672:2016) [Internet]. 3rd ed. British Standards Institution; 2016. Available from: <https://www.iso.org/obp/ui/#iso:std:iso:3677:ed-3:v1:en>.
- [22] Yeh JW, Chen SK, Lin SJ, et al. Nanostructured high-entropy alloys with multiple principal elements: Novel alloy design concepts and outcomes. *Adv. Eng. Mater.* 2004;6:299-303+274.
- [23] Cantor B, Chang ITH, Knight P, et al. Microstructural development in equiatomic multicomponent alloys. *Mater. Sci. Eng. A* [Internet]. 2004;375–377:213–218. Available from: <http://dx.doi.org/10.1016/j.msea.2003.10.257>.
- [24] Manzoni AM, Singh S, Daoud HM, et al. On the path to optimizing the Al-Co-Cr-Cu-Fe-Ni-Ti high entropy alloy family for high temperature applications. *Entropy.* 2016;18.
- [25] Xian X, Zhong Z, Zhang B, et al. A high-entropy V₃₅Ti₃₅Fe₁₅Cr₁₀Zr₅ alloy with excellent high-temperature strength. *Mater. Des.* [Internet]. 2017;121:229–236. Available from: <http://dx.doi.org/10.1016/j.matdes.2017.02.029>.
- [26] Senkov ON, Wilks GB, Scott JM, et al. Mechanical properties of Nb₂₅Mo₂₅Ta₂₅W₂₅ and V₂₀Nb₂₀Mo₂₀Ta₂₀W₂₀ refractory high entropy alloys. *Intermetallics* [Internet]. 2011;19:698–706. Available from: <http://dx.doi.org/10.1016/j.intermet.2011.01.004>.
- [27] Schuh B, Mendez-Martin F, Völker B, et al. Mechanical properties, microstructure and thermal stability of a nanocrystalline CoCrFeMnNi high-entropy alloy after severe plastic deformation. *Acta Mater.* [Internet]. 2015;96:258–268. Available from: <http://dx.doi.org/10.1016/j.actamat.2015.06.025>.
- [28] Dolique V, Thomann AL, Brault P, et al. Thermal stability of AlCoCrCuFeNi high entropy alloy thin films studied by in-situ XRD analysis. *Surf. Coatings Technol.* [Internet]. 2010;204:1989–1992. Available from: <http://dx.doi.org/10.1016/j.surfcoat.2009.12.006>.
- [29] Sathiyamoorthi P, Basu J, Kashyap S, et al. Thermal stability and grain boundary strengthening in ultrafine-grained CoCrFeNi high entropy alloy composite. *Mater. Des.* [Internet]. 2017;134:426–433. Available from: <https://doi.org/10.1016/j.matdes.2017.08.053>.
- [30] Holcomb GR, Tylczak J, Carney C. Oxidation of CoCrFeMnNi High Entropy Alloys. *Jom.* 2015;67:2326–2339.
- [31] Tsao TK, Yeh AC, Kuo CM, et al. High temperature oxidation and corrosion properties of high entropy superalloys. *Entropy.* 2016;18:1–13.
- [32] Tillmann W, Ulitzka T, Wojarski L, et al. Brazing of high temperature materials using melting range optimized filler metals based on the high-entropy alloy

CoCrCuFeNi. 2019.

- [33] Tsau CH, Lee PY. Microstructures of Al_{7.5}Cr_{22.5}Fe₃₅Mn₂₀Ni₁₅ high-entropy alloy and its polarization behaviors in sulfuric acid, nitric acid and hydrochloric acid solutions. *Entropy*. 2016;18.

Chapter 2: Literature Review

2.1. Brazing

Brazing is a 5000-year-old joining technique which creates a strong metallic bond between 2 or more materials (known as parent materials) by the process of melting a filler metal between them. Once the filler is molten and has flowed across the entire joint area the assembly is cooled and the filler metal solidifies forming a strong metallic bond between the materials to be joined; a schematic of these steps can be seen in Figure 2.1.

The principal characteristic of brazing which separates it from other joining techniques is its use of a filler metal to form the joint. This filler metal must be able to wet the parent materials [1] and have a liquidus temperature below that of the parent materials [2]. If the liquidus of the filler is not lower than that of the parent materials, the parent materials will melt during the joining process and as such the process would then be considered a form of welding. A (scientifically arbitrary) lower limit is imposed on the filler metals liquidus of 450°C, but this is purely to separate brazes from solders. In fact, this line is so blurred industrially that many jewellery makers refer to their craft as soldering whilst using filler metals based on gold and platinum which melt substantially above this arbitrarily assigned 450°C lower limit.

The principle reason to select brazing ahead of other joining techniques is due to its capability to join not only dissimilar materials (such as copper to nickel), but to join materials from entirely separate material classes (such as a metal to a ceramic). Additionally, the joints formed by brazing often elicit minimal evolution in the composition and microstructure of the parent materials. Whilst welding often provides a stronger joint and allows a higher operating temperature, it usually requires similar parent materials and the intense local heating can cause thermal distortion and develop a heat affected zone leading to a weakness in the finished product. Although weaker than welds in many instances, if a brazed joint is designed correctly the assembly will typically fail in the parent material as opposed to in the braze itself [2]. Finally, brazed joints are often suitably thermally and electrically conductive, making them superior to mechanical fastening and adhesive alternatives in applications which require electrical or thermal conductivity.

2.1.1. Brazing Development and History

Brazing is an ancient joining process which can trace its origins back 5000 years to Sumeria and ancient Egypt. The earliest physical evidence of the technique exists in the form of wall paintings in Egyptian tombs dating from 1475BC which depict slaves using reed blow pipes and charcoal fires to braze gold [2]. Throughout the centuries since, the development of filler metals has paralleled materials development itself; as new industrially important materials were discovered, filler metals were produced to join them. Examples of this can be seen since the 1930s in which the Handy and Harman research lab in the United States developed a series of general purpose filler metals based on silver using the AgCuZnCd and AgCuP systems. As the world emerged from the Second World War in the late 1940s filler metals based on nickel were developed to join superalloys in the nascent aerospace industry. Advancing further through the decades the increasing use of aluminium and its alloys (particularly in the automotive sector) required the development of the aluminium based filler metal systems which principally rely on

silicon as a melting point suppressant. Moving through the 21st century the joining of different classes of materials (e.g. metal to ceramic joining) became a focus area for development of innovative new filler metal compositions and brazing process. Moving beyond this and looking to the future it is the new fields of technology where brazing is likely to have its research targeted in future: joining in solid oxide fuel cells, in materials for nuclear fusion reactors and for Nano-electronic joins.

2.1.2. The Brazing Process

The brazing process describes the steps that must be taken to form a joint using brazing as the joining technique. There are many different brazing processes which have advantages and disadvantages and are thus suitable to different brazing requirements. Some of the most commonly used are listed in Table 2.1.

Table 2.1: Different brazing techniques, their advantages and disadvantages and their common applications.

Technique	Description	Advantages	Disadvantages	Applications
Flame Brazing	Heat provided by a gas flame (often hand-held) and directed at the appropriate area of the assembly. A 'jig' may be used to hold pieces in position.	Quick and cheap (no large setup costs or expensive machinery) Only the area of the parent materials local to the joint needs to be heated which can limit microstructural evolution in the bulk of the parent material.	Strength and quality of joint are dependent on the operator's skill.	Low volume production Relatively low heating temperatures.
Induction brazing	A specifically shaped inductor coil carrying high frequency current surrounds the area of the component to be brazed, causing localised heating via induced current flow.	Efficient for multiple simply-shaped components. Rapid, localised heating minimises grain growth in the parent materials.	Designing correctly shaped inductor coils can be complex Many component shapes are not suited to this process, e.g. sharp corners and screw threads are problematic.	Most effective with higher electrical resistance conductors e.g. steel.
Furnace brazing / vacuum brazing	A self-supporting assembly (parent and filler metals) is passed through a furnace at the brazing temperature. Furnace may be filled with air, inert gas or a vacuum. Components must allow filler metal to be pre-placed on or in the joint (often in paste form) as application once the batch process has commenced isn't possible	Large scale automated process. Thermal profile and atmosphere are easily controlled. Forms reproducible joints, with extremely limited void formation under vacuum.	High capital investment, high maintenance and heating costs. Batch process. Vacuum brazing requires very clean parts.	Mass production where identical conditions are needed (geometries of parts joined can vary). Vacuum brazing is most appropriate for materials with stable oxides (e.g. Ti and Al).

The most important type of brazing for use in this thesis is a variant of flame brazing which uses hand held gas burning torches to provide the heat input for the formation of the joint. A schematic of the stages of the process can be seen in Figure 2.1.

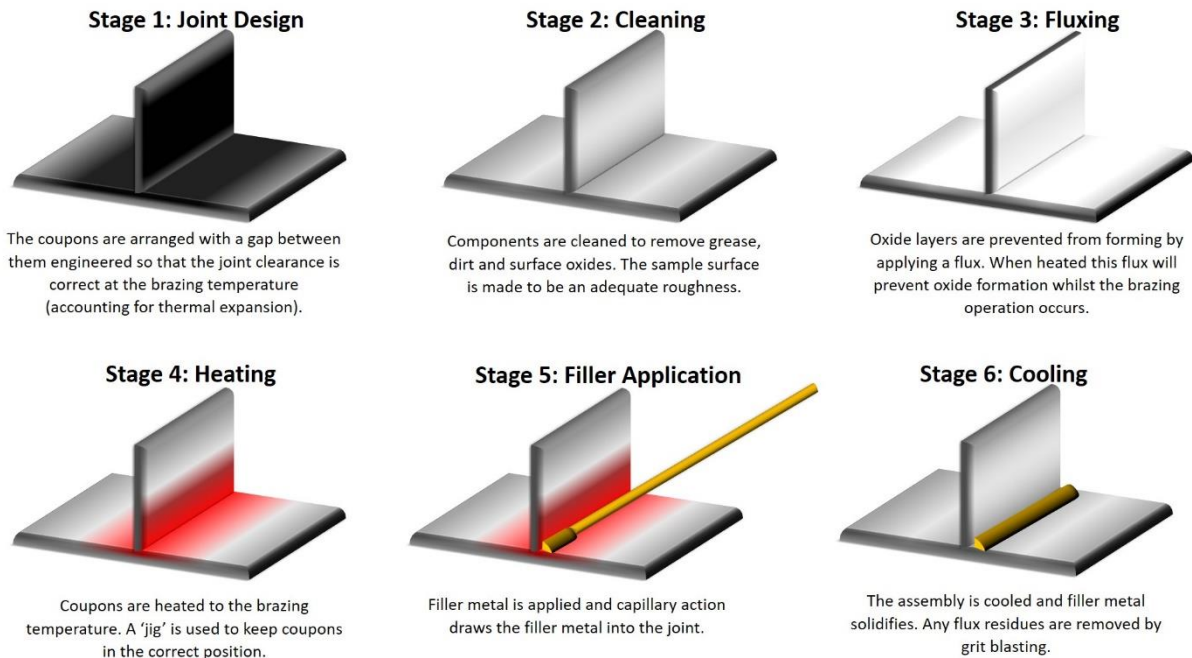


Figure 2.1: A diagram demonstrating the 6 stages involved in the hand torch brazing operation used predominately throughout this thesis. Stages will vary if alternative brazing techniques are employed.

2.1.2.1 Oxide removal

Oxide removal (and the subsequent prevention of the reformation of an oxide layer on the cleared surface) is an important stage in the brazing process, which will vary depending on the brazing process used and the materials being joined. This oxide prevention is often accomplished with the use of a flux applied to the joint. A flux is a complex mixture of chemical compounds which are applied to the joint prior to the heating of the joint. As the brazing assembly (consisting of the components to be joined and the flux applied to them) is heated the flux becomes molten and is described as 'active'. The flux forms a barrier layer across the joint, reacting with any oxides present there and removing them from the bonding surfaces. Flux is required when brazing with nearly all filler metals when used in air but is often not required when brazing in an inert or reducing atmosphere or brazing under vacuum. One well known example of brazing in air which does not require the use of flux is the brazing of high purity copper using copper-phosphorus based filler metals due to these filler metals being self-fluxing. The phosphorus within the filler metal reacts with atmospheric oxygen to form phosphorus pentoxide. This compound reacts with the copper oxide on the surface of the copper components being joined and forms a fusible slag [2].

Brazing of some classes of material (such as aluminium) can be performed under vacuum in a manner which is described as 'fluxless' but they do require the presence of an "oxygen-getter" such as magnesium (usually present as elemental magnesium placed in a crucible

in the furnace, but may also be contained as a constituent of the filler metal) instead. The magnesium disrupts the aluminium oxide layer and thus allows filler metal to contact the exposed metal surface,

Fluxes are not impermeable to oxygen and thus do not prevent surface oxidation of metals whilst the brazing operation is being undertaken, however they do continue to react with any oxides formed during the brazing process. In this way whilst it is 'active' the flux can be thought of as continually reacting with oxygen present in the joint. If the brazing operation takes a long time or too little flux is applied the flux can be used up and thus unable to prevent additional oxide formation. For this reason, an excess of flux is often applied to the joint to ensure that oxide removal occurs for the entire brazing process.

Fluxes have a wide array of properties and are designed to become active at different temperature ranges for use on different base materials and in conjunction with different filler metals; as such it is important to choose an appropriate flux to the brazing operation in question. Flux residues must often be removed after the brazing process is complete; not only are they aesthetically displeasing but are often corrosive if left on the material. As such cleaning is also an important part of joint formation which must not be neglected. Often removal is as simple as washing residues away with warm water after the joint has cooled; however, in some instances this isn't sufficient and various methods including quenching to crack off glassy flux residues, abrasive removal with wire brushes and shot blasting or chemical dissolution of flux residues with an array of chemical compounds may be required. What is important to note is that in each case the cleaning of the final joint must not weaken the joint in any way (e.g. soft base metals may be damaged by highly abrasive cleaning such as shot blasting) [1].

2.1.3. Factors Affecting Brazed Joints

The properties of a brazed joint in service are not only determined by the properties of the parent materials and the filler metal used but are also influenced by many other factors including:

- The cleanliness of the parent materials
- The surface roughness of the parent materials
- The joint clearance

2.1.3.1 *Joint Cleanliness*

Widely considered in the industrial setting to be the principle factor affecting the quality of brazed joint formed, cleanliness of the surfaces to be joined is pivotal in forming a strong brazed joint. The presence of any surface contaminants (such as oil, lubricant, dirt, grease, metals, waxes, biological contaminants or oxides) can prevent flux from acting correctly on a surface and thus prevent the strong interaction between filler metal and parent material required for a strong bond to form. Whilst known industrially to be of huge importance, little scientific investigation of the impacts of surface cleanliness has been conducted. Bobzin et al. investigated stainless steel and Inconel braze pieces and found that plasma cleaning of samples increased their surface energy; in turn giving a better wetting of the surface by the chosen filler metal and hence better joints [3].

2.1.3.2 Surface roughness

Surface roughness is one of three characteristics used to describe surface finish (the other two being the lay of the surface – which describes the overall dominant surface pattern and has been shown to influence filler metal flow [4], and the waviness which describes surface irregularities on a larger scale than the roughness). Surface roughness is a measure of the small scale deviations a surface exhibits from an ideal flat surface and is often characterised in brazed joint manufacture. It is widely considered to have a significant impact on joint formation and on the wettability of the filler metal on the surface and as such has been investigated in a variety of studies looking at different combinations of base metals and fillers.

A majority of the studies found within literature appear to conclude (at least to some extent) that a smoother surface (i.e. one with a lower surface roughness) will give better wetting and consequently stronger joint shear strengths. A study on a copper-phosphorus based filler metal (Cu-9.7Sn-5.7Ni-7P, designated MBF-2005) on copper surfaces found that lower surface roughness lead to lower void volume within the joint formed [5]. Additional studies found that an increased surface energy and an increased shear strength in subsequent joints formed on smoother surfaces down to a roughness (R_a) of $0.1\mu\text{m}$ on copper [6]. Other studies examining ceramic interfaces (such as silica, alumina and hafnium carbide) being wet by liquid element metals (copper, gallium and tin) found that increased surface roughness led to poorer wettability by the liquid metal [7] and that contact angles of an aluminium droplet on a TiN surface decreased with R_a down to at least $R_a=0.3\mu\text{m}$ [8]. Similar results have also been observed on metallised ceramic surfaces with tin-bismuth solders exhibiting reduced wettability on alumina surfaces metallised with copper [9].

Whilst a majority of papers establish a link between reduced surface roughness and increased wetting/improved joint strength there are studies which provide evidence to the contrary. Hong & Koo found improved wetting as surface roughness was increased (up to a point) leading to greater shear strengths in C103/Ti-15Cu-15Ni/Ti-6Al-4V joints brazed at 960°C for 15 minutes, with an optimum surface roughness of $0.71\text{-}0.79\mu\text{m}$ [10]. Taking these findings on board Zaharinie et al.[5] concluded that an intermediate roughness value was likely optimum and selected $R_a=0.2\mu\text{m}$ for the brazing of copper. Their explanation for this conclusion being that an increased roughness provides an increased surface area for joining and also provides capillary paths for improving filler metal flow across the surface up to the point where surface asperities are so large that they impede flow.

Evidence also exists that surface roughness has only a limited correlation on brazed joint formation. A study on filler metals on an aluminium nitride surface [11] and a study where wetting was dominated by chemical reactions indicate little impact of the roughness of the surface on the properties of the joint formed although the range of surface roughness examined in both cases was small [12].

Overall the relatively sparse range of studies on the impact of surface roughness (over a large variety of different surface and filler metal combinations) on brazed joint formation make it difficult to draw an accurate conclusion on the general influence of surface roughness on the properties of brazed joints. It is unlikely that a single value for surface roughness exists which could be universally recommended for optimal brazing; instead it is probable that the optimum roughness will vary in each specific application and with

differing parent material and filler metal combinations. A common handbook estimate for suitable surface roughness for brazing is 30-80 microinches RMS [2] which can be converted to an R_a value in the range $R_a = 0.6\text{-}1.6\mu\text{m}$ (which, as can be seen in Figure 2.2, is consistent with the surface finish produced by most milling and machining processes [13]).

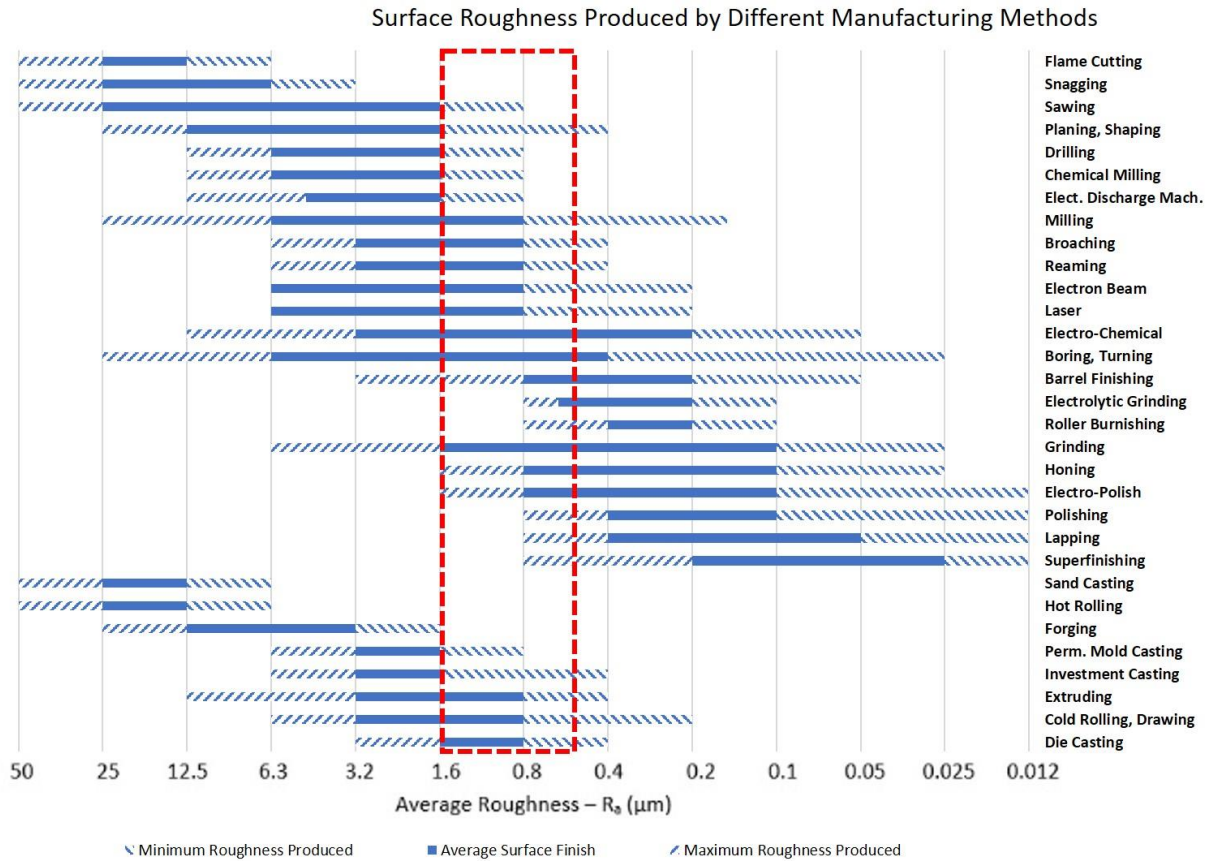


Figure 2.2: Average surface roughness typically produced by different manufacturing techniques. Image reproduced from M Way et al, Int. Mater. Rev [14] under the Creative Commons Attribution License, redrawn from [15]. The generally accepted surface roughness suitable for brazing is indicated by the red dashed box [13].

2.1.3.3 The Joint clearance

A final factor influencing the strength of a brazed joint is the joint clearance; defined as the gap between the two materials to be joined. As brazing filler metals are heated and become molten they flow into the joint gap (clearance) between the two pieces of material that are being joined. Capillary pressure drives the molten filler to flow into this gap which distributes the filler through the joint. This capillary pressure is what allows complex joint geometries to be filled by filler metal placed outside a joint and can even allow filling of areas against gravity. As all filler metals have different flow properties it is important to select a joint clearance which is optimal for the filler metal chosen to achieve the optimal capillary pressure possible. It is important to note that joint clearance should be set for the brazing temperature and not room temperature. As materials often expand when heated the joint clearance will vary as the temperature of the brazing

assembly is raised which must be accounted for when the joint clearance is set up before the brazing procedure begins.

As well as joint clearance, when joined as lap joints the overlap length of a brazed joint becomes an additional parameter of concern. Often it is desirable that brazed joints fail in the parent material rather than in the joint itself and as such the overlap length used when forming a lap joint should provide the joint with sufficient strength for the strength of the joint to exceed that of the parent material. Whilst overlap length will vary with application as well as parent materials and filler metal selected, a common rule of thumb is that to ensure failure in the parent material rather than in the joint the overlap length of a lap joint should exceed 3.5x the thickness of the thinnest joint member [2].

2.1.4. Diffusion

Diffusion is the process of material transport via atomic movement. When two different materials are in intimate contact there exists a concentration gradient at the boundary between the two materials that provides a driving force for the materials to diffuse into each other in a process known as interdiffusion. A schematic showing how concentration profiles across the interface between two different metals (copper and nickel) in intimate contact will change after exposure to heat for a time period can be seen in Figure 2.3 below [16].

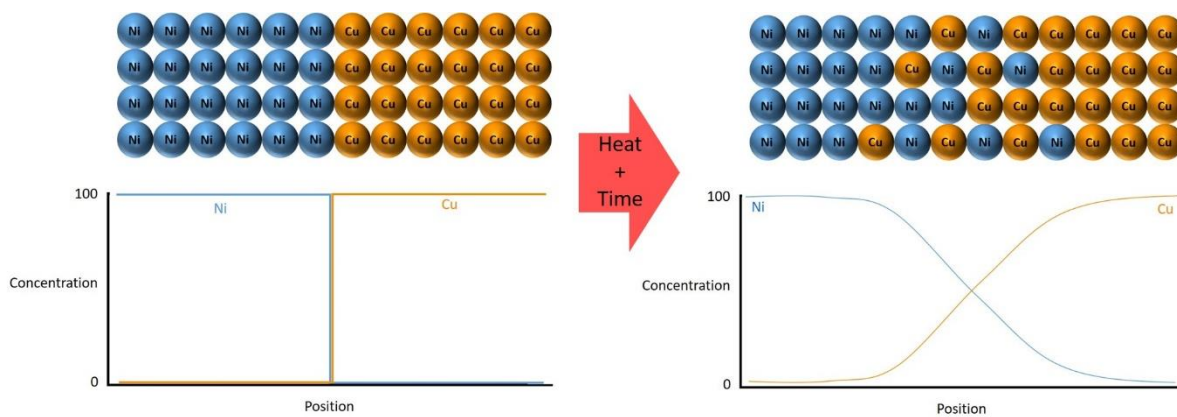


Figure 2.3: Schematic of atom position and diffusion concentration of a piece of copper in intimate contact with a piece of nickel before and after exposure to heat for a prolonged period. Redrawn from [16].

When two metals are joined in this way and allowed to diffuse, the dominant method by which diffusion occurs is via vacancy diffusion. In vacancy diffusion an atom obtains sufficient energy to overcome its bonding to its neighbour atoms and moves into an adjacent vacancy site. At any one time a certain proportion of atoms within any solid will have met the two criteria for an atom to move in this way; to have sufficient energy to break the bonds to its neighbour and to have an adjacent vacancy to move in to. The rate of diffusion will be dependent on this proportion.

As stated, the rate of diffusion is proportional to the concentration gradient with the diffusion flux, (mass of atoms diffusing through a cross sectional area of a material per unit time) given by the equation below (known as Fick's first law):

$$J = -D \frac{dC}{dx} \quad \text{Equation 2.1}$$

where J is the diffusion flux, D is the diffusion coefficient and $\frac{dc}{dx}$ is the diffusion gradient in one dimension (x). The negative sign in the equation indicates that diffusion proceeds down the concentration gradient.

The magnitude of the diffusion coefficient D is influenced by many factors.

- The diffusing species and the host material. The diffusion coefficient will vary for different materials in different hosts. Diffusion is easier for some atoms than for others in certain host materials as the energy required to break bonds with neighbouring atoms is lower and hence diffusion is more likely to occur
- Temperature. As stated above, atoms require a sufficient energy to break bonds with their neighbours and move positions. As the energy for this to occur is taken from the vibrational energy of the atom an increase in this energy will make diffusion possible for a larger proportion of atoms in the material and hence, macroscopically, diffusion will proceed faster.

The equation giving the diffusion coefficient takes these factors into account and can be stated as:

$$D = D_0 e^{\left(\frac{-Q_d}{RT}\right)} \quad \text{Equation 2.2}$$

where D_0 is a temperature independent constant (m^2s^{-1}), R is the gas constant ($8.31\text{J mol}^{-1}\text{K}^{-1}$), T is the temperature in Kelvin and Q_d is the activation energy for diffusion (Jmol^{-1}) and can be thought of as the energy required to produce the motion of one mol of atoms via diffusion. If the activation energy for diffusion is high, then for most temperatures the diffusion coefficient will be relatively small (or in other words diffusion will require more thermal energy to occur at the same rate as a system with a low activation energy). Thus we would expect systems which have a small activation energy for diffusion (Q_d) and a large temperature independent constant (D_0) to in general diffuse faster than those with a large activation energy and small independent constant.

Diffusion is a time dependent process (shown by the constant having units of m^2s^{-1}). On the macroscopic scale the amount of an element which diffuses into another is a function of time. If the time at which the materials are kept at an elevated temperature is constant or very similar, then the distance which materials diffuse into a host can be used as a relative measure of the diffusivity of the same species in different host materials. This is the case in the brazing diffusion experiments in this thesis in which a filler metal is bonded to (and hence diffuses into) different host materials. As the brazing cycle time used is the same for each system (as the heat input required to melt the filler is constant) the amount of time each system spends at elevated temperature is roughly equivalent. Therefore, the diffusion distance of filler metal constituents into the different host materials can be related to the ease of diffusion in each host material.

2.1.5. Wetting, Flow, Adhesion and Bonding

Wetting and flow are two important terms in brazing relating to how a filler metal moves once it has become molten. The flow of a filler metal is the term used to describe how well a filler metal moves when molten. A free-flowing filler metal can penetrate a smaller joint clearance than one which moves more sluggishly. For this reason, free-flowing filler metals are preferred in many applications, particularly where filler metal pre-placement within the joint is not possible. Conversely if a filler metal is too free flowing (particularly when used in conjunction with a wide joint clearance) it may fail to be retained in the joint

during the brazing process and flow through the joint rather than staying in it. This can lead to the formation of voids within the joint and hence reduce the strength of the final assembly.

The flow properties of a filler metal are primarily dictated by the relative proportions of solid and liquid which are present when it is at the brazing temperature. If the filler metal melts at a single temperature (e.g. if it is a eutectic composition or a pure metal) then it should be fully liquid at the brazing temperature and hence will flow easily. Filler metal systems containing multiple phases will likely only be partially molten at the brazing temperature and thus flow more sluggishly, this can be advantageous when joint clearances are large and filler metal retention is problematic.

Whilst all filler metals need not have good flow properties as some forms (such as paste or foils) can be pre-placed in a joint prior to assembly and thus do not need to flow into the joint; it is essential that filler metals are capable of wetting the bonding surfaces of the materials they are joining.

How well a filler metal wets a surface arises from the balances of adhesive forces (bonding between the molten filler metal and the substrate surface) and cohesive forces (bonding between the molecules and atoms within the molten filler metal). Adhesion is the physical process by which dissimilar substances 'stick together'. In order for adhesion between two surfaces to occur there must be an interaction between the two components. Whilst the mechanisms of adhesion are not fully understood [17], it is known that this phenomenon can consist of one or more of a variety of interactions; this includes mechanical interaction, but is often predominately chemical in nature.

In order for a brazing filler metal to spread across a surface (i.e. to wet it) the adhesive forces between the filler and the surface it is to join must be greater than the cohesive forces between the atoms that make up the filler itself. The overall 'adhesive force' between the filler and the substrate is dependent on the strength of the bond between the filler and the surface. Chemical and diffusive bonding dominate in many situations, although electrostatic and physical interactions are possible [17]. In chemical adhesive interactions, atoms from the filler metal form a direct bond with atoms from the substrate of either an ionic or covalent nature. The adhesion between the filler and substrate is hence formed by the network of these strong bonds across the surfaces in contact. Of course for these bonds to form the surfaces must be in intimate contact (with the gap of the order of a bond length) which is why such adhesion does not occur when the filler is not molten. The interaction of substrate and filler in this way often leads to compound formation at the interface which in many cases gives brittle joints. This type of bonding is predominantly found in metal-ceramic (active) brazing.

Where both materials are soluble in each other diffusive interactions are possible at the interface; an example of which can be seen in sintering where, under high pressure and heat, atoms can transfer from particle to particle to form a bond. In brazing this type of adhesion is more common when bonding similar metals which are mutually soluble in each other and form a metallic bond as opposed to a covalent or ionic bonds and so intermetallic compounds do not form.

Other weaker bonding interactions including hydrogen bonds are also known to cause adhesion between surfaces such as between water and glass which explains the phenomenon of water rising in a thin glass tube placed in a beaker – the adhesion of water molecules to the glass surface is stronger than the cohesion between water molecules and

so the surface of the water rises in a narrow tube. In these scenarios the adhesive force is smaller in magnitude as the hydrogen bonds formed are weaker than the covalent/ionic bonds that exist in the compound formation mentioned above and thus the driving force for adhesion is smaller than if chemical or diffusive bonding were possible. Where hydrogen bonding is not possible even weaker Van der Waals interactions can provide some adhesive driving force although this form of bonding between surfaces is substantially weaker. Evidently, these kinds of bonding do not have a significant role in brazing.

Wetting, and the wetting angle itself arise as a direct result of the balance between adhesive and cohesive forces present in the system. On a macroscopic level these forces can be described by 3 surface energy terms (Equation 2.3): γ_{SL} , the interfacial tension between solid surface and liquid, γ_{SV} , the surface free energy of the solid, and γ_{LV} , the surface tension of the liquid. A depiction of these terms can be seen in Figure 2.4.

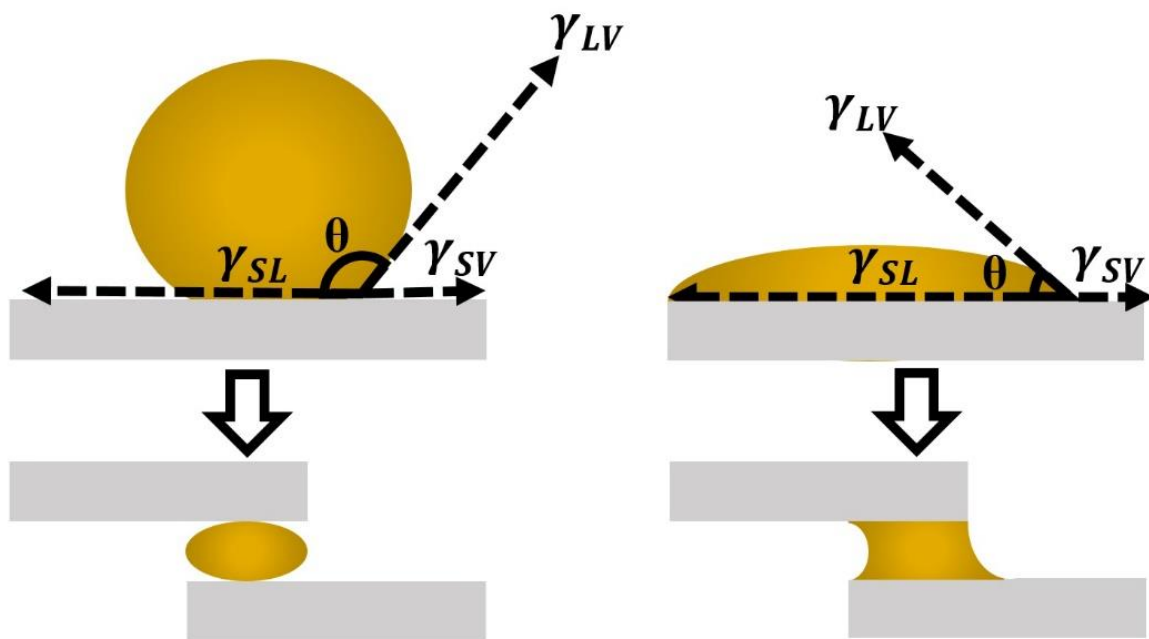


Figure 2.4: Diagram depicting a non-wetting liquid (left) on a solid substrate which has a contact angle (θ) $>90^\circ$ and a corresponding image of how this would appear in a brazed joint. A similar diagram for a wetting liquid can be seen on the right ($\theta <90^\circ$) above an image of a wetting liquid within a brazed joint. Image reproduced from M Way et al. Int. Mater. Rev. [14] under the Creative Commons Attribution License.

The driving force for wetting in this scenario is given by $\gamma_{SV} - \gamma_{SL}$ (as can be seen by the upper right diagram of Figure 2.4) [18]. As the system is in equilibrium, (the droplet is not moving – the overall force is 0) the balancing resisting force to attain equilibrium in the system must be provided by the horizontal component of the surface tension of the liquid (γ_{LV}) which is given by $\gamma_{LV} \cos \theta$. Summing these forces gives $\gamma_{SV} = \gamma_{SL} + \gamma_{LV} \cos \theta$ with θ varying to ensure that the overall force acting on the system is 0. Re-arranging these horizontal forces in equilibrium gives the Young's equation.

$$\gamma_{SL} = \gamma_{SV} - \gamma_{LV} \cos \theta \quad \text{Equation 2.3}$$

Therefore, wetting (and in particular the wetting angle) describes the balance of adhesive forces between a liquid (in this instance a molten filler metal) and a solid surface (in this case the materials being joined by brazing) and the cohesive forces within the filler metal. If the adhesive forces between molten filler and the solid surface are stronger than the fillers cohesive forces, then the molten filler will tend to spread out across the surface forming a ‘puddle’ over a large surface area until a sufficiently shallow wetting angle is attained which balances the Young’s equation. This is described as the filler metal ‘wetting’ the surface. If the cohesive forces within the filler are stronger than the adhesive forces between filler and surface, then the filler will tend to ‘ball-up’ as the fluid attempts to minimize its contact area with the surface. The angle formed between a molten filler metal and the substrate which it rests upon is called the contact angle. As contact angle will decrease as droplet contact area increases (assuming a constant droplet volume), the contact angle formed between liquid and solid surface gives an inverse measure of wettability [19]. A lower contact angle means a higher wettability (Figure 2.4). If the angle Θ required to balance these terms is $<90^\circ$ then the liquid is said to wet the surface and if the angle required to balance these terms is $>90^\circ$ then the liquid is said to be non-wetting. As such it can be inferred that stronger adhesive interactions correlate with smaller wetting angles [18]. The interactions which drive this adhesive force vary in nature depending on the brazed joint in question but the stronger the interactions between filler and solid surface the smaller the γ_{SL} term in Young’s equation and the increased driving force for wetting [18] and hence the reduced contact angle seen. That is to say that the increase in surface area of the liquid droplet (and hence increase in overall liquid surface energy) must be less than the reduction in the surface energy of the solid caused by the spreading of the filler across the surface. This minimises the energy of the system as a whole.

The surface energy terms in Young’s equation (Equation 2.3) will vary depending on various parameters which will in turn affect the contact angle that arises. Parameters influencing the surface energy terms include:

- The temperature the system is at,
- The surface roughness of the substrate,
- The presence or absence of oxide layers,
- Additions to the filler metal and/or substrate,
- The brazing time

Each of these variables will influence the surface energy terms and hence will alter the contact angle [20]. Various studies have examined the influence of one or more of these parameters on the contact angle that arises, often in an attempt to improve the wetting of the liquid in question. Kozlova et al. observed that nickel and tin additions to the copper-silver eutectic did not produce any measurable differences in the wetting curves on a 321 steel substrate but did find that Ti inclusions within the stainless steel substrate led to wetting occurring at higher temperatures than without [21]. Even small at% additions of solute elements into filler metals have been shown to drastically alter the wetting angle between filler and substrate. Voytovych et al. placed a CuAg filler metal on a sapphire surface and placed a small quantity of titanium on top of the CuAg alloy so that it did not contact the sapphire substrate. The Ti was then melted and diffused through the CuAg filler to form a CuAg-2.9at%Ti composition. The arrangement demonstrated a non-wetting contact angle ($\Theta =$ approximately 140°) until around 500 seconds had passed (a time frame suitable for the Ti to diffuse through the CuAg and

down to the CuAg-sapphire interface) at which point the wetting angle dramatically reduced to give a final steady wetting angle of approximately 10° [22].

2.1.6. Interface Types in Brazed Joints

As mentioned in 2.1.4. above, the formation of a brazed joint requires the filler metal to be capable of wetting the parent material, once this has happened an interaction between filler metal and parent material will occur as the brazing process concludes. This reaction can be one of two main types (Figure 2.5):

1. Bond formation via partial dissolution: An interaction zone may be formed from solubility of elements of the filler metal within the parent materials or of elements from the parent material within the filler. If the dissolution of the parent material by the filler metal is too extensive this is known as erosion and can lead to weaker joints.
2. A reaction between filler and parent material: More prevalent in active brazing, (particularly between fillers and ceramics), this joint type arises from a chemical reaction between the filler and parent forming a compound at the interface.

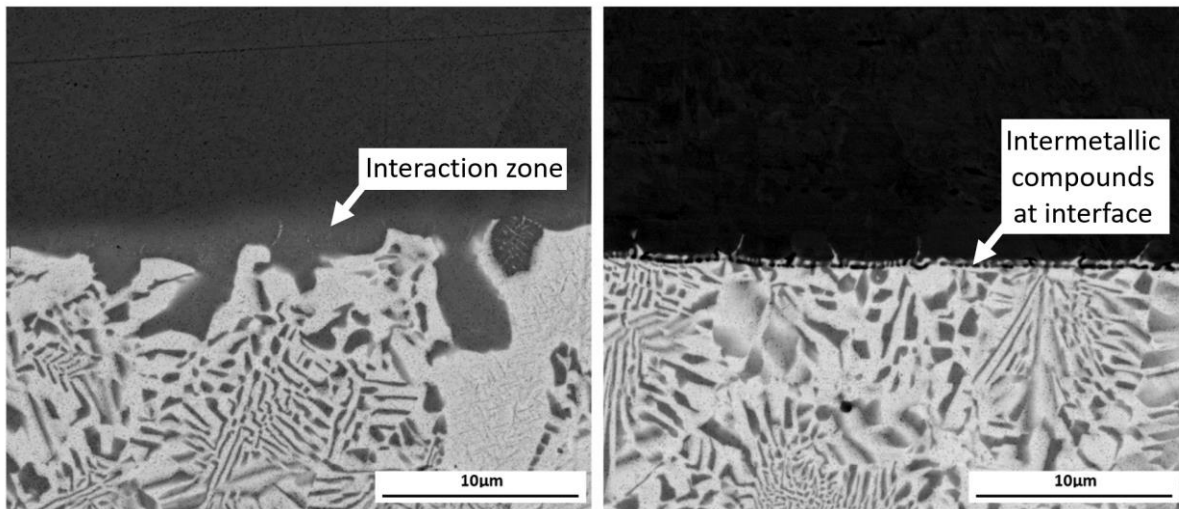


Figure 2.5: Back Scattered Electron images of a partial dissolution interface between copper plate and filler metal Ag-155 (left) and interfacial compound formation between low carbon steel and filler metal Ag-155 (right). Image reproduced from M Way et al. *Int. Mater. Rev.* [14] under the Creative Commons Attribution License.

Several recent studies have focused on the interface formed in brazed joints highlighting its importance in not only understanding the underlying reactions that occur but also attempting to alter them so as to improve the properties of joints created. One of the main systems researched is the joining of titanium alloys (predominately Ti-6Al-4V due to its prominence in the aerospace industry) to aluminium alloys of various specifications including 5A06 [23], A6061-T6 [24] and 5052 [25]. The interest in joints between these two materials is high because of their necessity in forming hybrid structures in aviation such as when joining aluminium honeycomb structures to a titanium skin to produce structures with a balance of properties; the light weight of aluminium honeycomb structures and the high strength and stiffness of titanium [26]. With the aerospace industry having such a high safety rating required on all components used, extensive knowledge of the interfaces formed between these materials and the loads they can stand is of paramount importance [27]. Takemoto and Okamoto [28] found that when brazing aluminium to titanium, inclusions of silicon in the aluminium based filler metals would

substantially reduce the size of the interfacial zone until 10at% Si was reached, at which point $Ti_7Al_5Si_{12}$ would form at the interface. Chen et al. found a similar result when an Al-12Si filler metal is used to join aluminium to titanium, that it is the silicon which diffuses to the interface but the composition and distribution of the intermetallic compounds it forms vary with the heat input to the joint [23].

The interface is often of particular interest in brazed joints on all manner of materials as interfacial compounds are often a source of weakness and hence lower joint strength. Other materials in which investigations into the properties or composition of the interface formed during brazing include SiC [29][30][31], synthetic diamond [32][33][34] and tungsten carbide [35][36]. The number of studies investigating the interface in different systems and attempting to refine it to improve properties serves to highlight the importance of interface formation in the design and selection of suitable brazing filler metals on a case by case basis.

2.1.7. Brazing Filler Metals

2.1.7.1 Commercially available filler metals

As mentioned previously the filler metal is the metal which melts and then solidifies to form the joint between the parent materials. Many hundreds of filler metals have been developed and used over time and the most common are standardised in the ISO standard ISO17672:2016 [37]. They are categorised primarily into 7 families named after the principle element of each filler metal in that family (Figure 2.6).

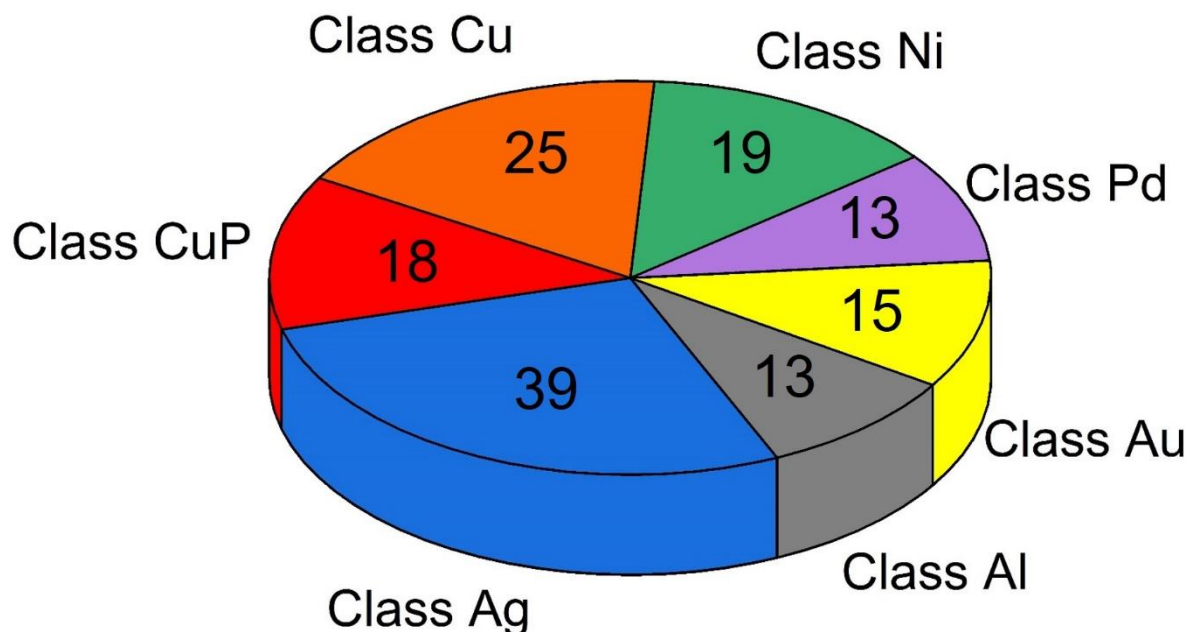


Figure 2.6: The 7 classes of brazing filler metal identified in ISO 17672:2016 and the number of alloys in each class.

The 7 classes are listed in Table 2.2 along with some of their most common applications. Class Cu is subdivided into 3 categories for the 3 different variants of copper alloys which are used for different purposes.

Table 2.2: Table of standard filler metal families found in ISO17672:2016. Adapted from [14][37].

<u>Class Designation</u>		<u>Class Applications</u>
Class Al: Aluminium and Magnesium based filler metals		Joining of aluminium and its alloys Some Al alloys are used to braze titanium. Alloy Mg001 is used for brazing high Mg alloys
Class Ag: Silver based filler metals		General purpose filler metals, used on steels (including stainless), copper, copper alloys (including brass and bronze), nickel, tungsten carbide and polycrystalline diamond.
Class CuP: Copper-phosphorus brazing filler metals		Joining of copper and copper alloys, and molybdenum. Phosphorus content enables self-fluxing when brazing copper. Poor ductility and impact resistance.
Class Cu:	High Cu alloys	Reducing atmosphere furnace brazing, e.g. of steel and tungsten carbide.
	Cu-Zn alloys	Brazing of mild steel, joining of steel to tungsten carbide, brazing of copper. Formerly the main family of filler metals used in industry, use has diminished since 1930.
	MIG brazing alloys	Developed for use with the 'MIG brazing' technique [2]. Used in the automotive industry, often to join galvanized steel.
Class Ni: Nickel (and cobalt) based filler metals		Used for stainless steels, nickel- and cobalt-based superalloys. Filler metals often brittle. Typically requires a vacuum. Excellent corrosion resistance and high services temperatures.
Class Pd: Palladium bearing filler metals		Aerospace and electronics applications, used in glass and chemical industries. Possess good strength at elevated temperatures, excellent corrosion resistance.
Class Au: Gold bearing filler metals		Aerospace and electronic applications, low volatile impurity content to be suitable for vacuum tube devices. Excellent corrosion resistance and strength at high temperatures. Jewellery solders (whilst not officially part of this category) are predominately gold (the main gold jewellery solder is based on Au-Ag-Cu-Zn).

However, these 7 families are by no means the limit of filler metals developed and with modern materials applications utilising a much wider range of materials than ever before in a range of harsh environments, more and more filler metals have been invented. It is much harder to group these more recently developed filler metal into simple 'families' as they are often designed for a specific application and not modified from previous filler metal compositions. Some examples of other filler metals can be found in Table 2.3.

Table 2.3: Additional filler metals which are not found in ISO17672:2016 and their applications.
Adapted from [14].

<u>Filler metal types</u>	<u>Applications</u>		<u>Filler metals</u>
Specialist copper based alloys	Reducing atmosphere brazing of carbon steels and stainless steels where they can offer cost benefits over silver-based filler metals		High purity copper alloys
	Elevated temperature applications and high strength joints between carbon steel and tungsten carbide.		Cu-Mn-Ni alloy systems
Platinum containing filler metals	Platinum jewellery solders Brazing molybdenum and tungsten for ultra-high temperature use.		Various Pt containing filler metal systems
Homogenous active filler metals	Used for metal-ceramic joining.		Many compositions are conventional filler metals (e.g. Silver-based) with a few percent of the active element added (Often Ti, Hf or Zr) to promote ceramic wetting.
Titanium filler metals	Joining titanium where a high specific strength to weight ratio and corrosion resistance are important (e.g. in submarine manufacture and medical devices).		Compositions are predominately titanium, often with zirconium, copper and nickel as other principal components (19-38wt% Zr, 14-21wt% Cu, 9.5-26wt% Ni). Mo, Hf and Fe may be minor additions (<1.5wt%). (AWS specification A5.8M/A5.8:2011) [38][39].
Filler metals for brazing refractory metals	Tungsten	High temperature structures	Refractory metal based compositions such as: 80Mo-20Ru 65Pd-35Co 75Pt-20Pd-5Au
	Molybdenum	Heating elements	
	Niobium	Spacecraft propulsion systems	Commercial silver, gold and platinum based alloys can be used but often produce brittle joints and have low melting points relative to likely Nb operating temperatures. Ta-V-Nb and Ta-V-Ti alloys can be used at higher brazing temperatures (1760-1925°C).
	Tantalum	capacitors	Not often brazed as it is easily welded. Specialist filler metals used include: Hf-7Mo, Hf-40Ta, Hf-19Ta-2.5Mo. [40]

With many other fields driving materials innovation there is a potent driving force for the development of even more specialised filler metals for applications where those listed in Table 2.2 and Table 2.3 are not suitable and as such, division of filler metal systems into simple classes is becoming less and less adequate.

2.1.7.2 Filler metal selection

The choice of which filler metal is best suited to a particular application involves many variables including (but not limited to):

- The parent materials being joined – A metallurgical compatibility between the filler metal and both parent materials is required so that a strong bond between the parent materials can be formed.
- Service conditions – Operating temperature for the finished assembly and the operating environment it will be expected to function in. This includes considerations on the type and degree of mechanical loading and the presence of any corrosive media which may lead to degradation of the joint over time. Due to the presence of multiple materials (with the parent materials and filler metal often being completely different classes of material) the potential for galvanic corrosion is much higher than with many other joining methods.
- Joint design – If a particular joint gap is required then a filler metal which has suitable flow properties for the clearance used must be selected. A narrow joint clearance will require a better flowing filler metal to penetrate the small joint gap. Conversely a wide gap will require a more sluggish flowing filler metal so as to avoid the filler flowing out the back of the joint and failing to be retained.
- The brazing process – The brazing process used will limit the filler metals which can be used. Often the brazing process used to form a joint will be dictated by other factors such as cost and volume of joints to be produced and as such a filler metal must be selected which is compatible with the chosen brazing process. As an example filler metals containing zinc are usually unsuitable for vacuum brazing due to the volatility of zinc.
- Brazing temperature – The brazing temperature can be limited by what temperature exposure will induce unwanted microstructural evolution in the parent materials leading to a loss of functionality. If this is the case, then only filler metals which melt below this temperature can be used.
- Filler metal form – Some filler metals are only available in certain forms, if the form of the filler metal isn't suitable for the brazing process selected then it cannot be used (e.g. many copper-phosphorus filler metals are brittle and as such are only available in directly extruded rod form. Joints which require pre-assembly with a foil therefore cannot use these fillers).
- Law and regulations – certain elements contained within some filler metals are not suitable for particular applications (e.g. cadmium-containing brazes were prohibited from use on equipment in the dairy, food and pharmaceutical industries even before the widespread European ban introduced in 2012 [41] [42]).
- Toxicity – Certain elements are not considered safe for use in certain industries such as the medical, food or dairy industries (e.g. in biomedical applications Cu^{2+} at levels above 0.5mM is considered cytotoxic to mesenchymal stem cells [43] [44]).

If no available filler metal meets all the criteria for the joint in question then a different joining process must be selected, filler metal requirements must be relaxed or a new filler metal must be designed to suit the application.

2.1.7.3 Recent filler metal developments

Brazing is a small but key area of research with several application areas currently undergoing cutting-edge research. Examples of recent areas of activity within the broad field of brazing include:

- Joining of sapphire to sapphire was achieved using a novel bismuth borate zinc glass with the composition $50\text{Bi}_2\text{O}_3-40\text{B}_2\text{O}_3-10\text{ZnO}$ (mol%). Sapphire to sapphire bonding is important as sapphire has high thermodynamic stability and excellent optical properties but is often only able to be produced in small sizes. Effective joining of sapphire components thus could expand the areas in which it can be used. Application areas include aircraft windows, micromechanical devices and scratch resistant components [45].
- The joining of bulk metallic glasses to steel. Bulk metallic glasses have attracted attention since 2000 for their good mechanical properties and their corrosion resistance [46]. Unfortunately, their impressive properties are substantially reduced when they become crystallised which is a common issue when joining them as the joining interface leads to a change in chemical composition which leads to crystallisation. This crystallisation causes embrittlement and as such progress in forming joints which do not form crystalline phases at the interface is needed; Kim and Lee managed to join a novel $\text{Cu}_{54}\text{Ni}_6\text{Zr}_{22}\text{Ti}_{18}$ bulk metallic glass without evolving detrimental phases when using a Zn-Ag-Al filler metal [47].

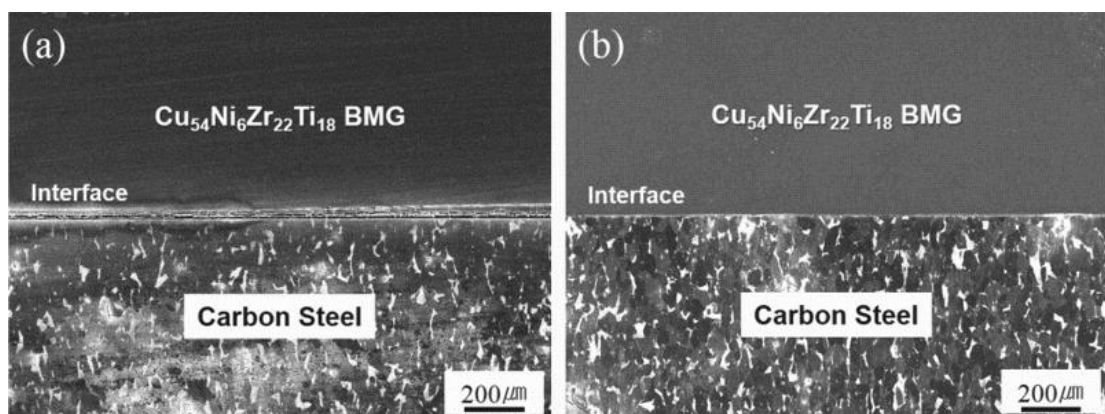


Figure 2.7: Micrographs of Bulk Metallic Glass $\text{Cu}_{54}\text{Ni}_6\text{Zr}_{22}\text{Ti}_{18}$ joined to carbon steel using pure zinc (left) and an active Zn-Ag-Al filler metal (right). The right image demonstrates a sounder interface with less discontinuities. Image from [47] with permission.

- Joining of graphite to superalloy using gold based filler metals doped with silicon particles which is promising for uses in the nuclear and petrochemical industries as structures made of carbon based materials joined to metal can utilise the high thermal shock resistance and excellent high temperature wear resistance of carbonaceous materials with the mechanical strength of metals such as Ni superalloys [48].
- The development of boron free filler metals for joining corrosion resistant steel in rocket nozzles and heat exchangers is necessary as boron containing fillers form borides in the brazing zone which have poor plastic properties and can lead to failure during operation. Recent developments of alloys in the Ni-Si-Be system eliminate boron from the filler metal and thus remove the issue of boride formation [49] (Figure 2.8).

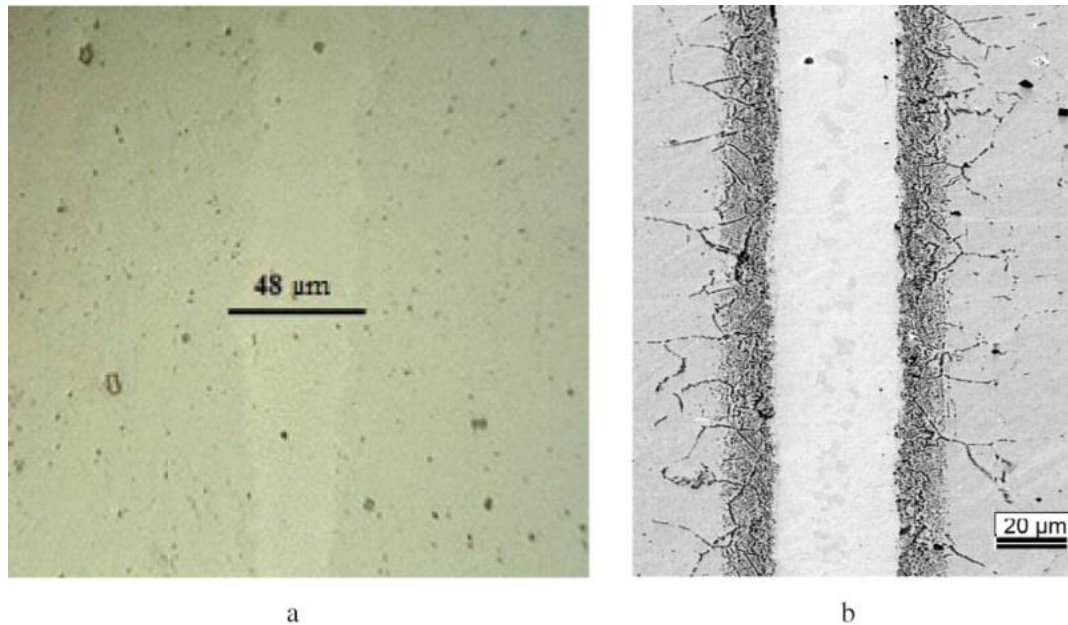


Figure 2.8: Brazed joints between pieces of 12Cr21Ni5Ti austenitic–ferritic corrosion-resistant steel using a boron free filler metal (a) and a boron-containing filler metal (b). Image from [49] with permission.

- Use of indium containing filler metals for the joining of $\text{SiO}_2/\text{SiO}_2$ composite materials for use in antenna radomes to reduce the required brazing temperature for joining is believed to reduce the residual thermal stresses in components joined with this filler and thus hopefully improve service life [50].
- Development of filler metals free from radiation sensitive elements such as Ni and Co is necessary for use in joining tungsten components in fusion reactor diverters to allow construction of plasma facing components which won't contaminate the fusion plasma. Recent articles tackle these joining issues by investigating new brazing processes utilising the mixture of pure metallic powders with organic binders [51].

This serves to demonstrate that industrially pivotal research concerning brazing and related technologies is ongoing in a wide array of different sectors of which the work contained in this thesis is small but important part serving to highlight the importance of brazing as a joining technique in modern industry.

2.1.7.4 Future areas for filler metal development

As mentioned throughout the sections above, brazing is a joining process of great significance in a wide array of cutting-edge industry joining. To date, development of brazing filler metals (and associated brazing processes) has often been driven by traditional challenges such as increased operating temperature and cost reduction however, future requirements will push these requirements beyond a traditional metallurgical focus and require input of other research specialities in order to develop increasingly complex joining procedures and filler metal compositions. The drive towards miniaturisation opens avenues for nanoscale joining and the increasingly higher operating temperatures that components are subject to is pushing the development of

composite metal-ceramic components which present a unique joining challenge. Some of the more urgent areas for development include:

Joining on the nanoscale:

Nanoscale electronics is a promising field for the next generation of miniaturised electronic components which will utilise nanoparticles, nanowires and nanotubes [52]. Currently developments in this field are being limited due to issues with joining these nanoscale components rather than by the synthesis of the components themselves. Poor or ineffective bonding between these components or between components and substrates is leading to premature mechanical and electrical failures preventing more rapid advancement of the field [53]. Some examples of recent research in this field include vacuum brazing of carbon nanotubes to each other using Ti doped AgCu active filler metal [54] and the joining of silver nanowires using a gold based solder (Au80Sn20) [55]. Joining of nanowires does not just have to be via a brazing process; direct fusion methods are also possible. For nanoparticles however direct fusion is much more difficult as controlling the melting depth is challenging and often leads to nanoparticles fully melting during the process and coalescing, defeating the point of joining them as separate entities. Brazing on the nanoscale does not require the melting of the nanoparticles themselves and as such offers a joining method which circumvents the melting depth issues associated with direct fusion methods [56]. Studies have demonstrated the feasibility of nanobrazing by using lasers of a specific wavelength to join 2 nanoparticles of different metals. The specific wavelength of the laser used is selected as to match the absorption band of one of the two nanoparticles which increases the heat distributed to this particle and causes it to melt whilst the other nanoparticle remains solid. Research has demonstrated the viability of this technique using Au and Pt [57], and Ag and Pt [56], but more studies are required for widespread use of the technique. Areas of future research relating to nanobrazing which could be explored include fundamental studies into the driving forces behind the process and into joining dissimilar materials (e.g. metal ceramic) [52], an attribute of brazing which is often considered as one of its principle advantages.

Joining in SOFC stacks:

Another field in which brazing research is currently targeted and is expected to advance in the coming years is for joining components within alternative energy production technologies such as Solid Oxide Fuel Cells (SOFCs). SOFCs oxidise a fuel directly in order to generate electricity and are the subject of much interest in the scientific community as they offer higher efficiency electricity generation with a lower environmental impact than many current technologies [58]. SOFCs are arranged in stacks of individual cells which consist of cathode-electrolyte-anode blocks (Figure 2.9).

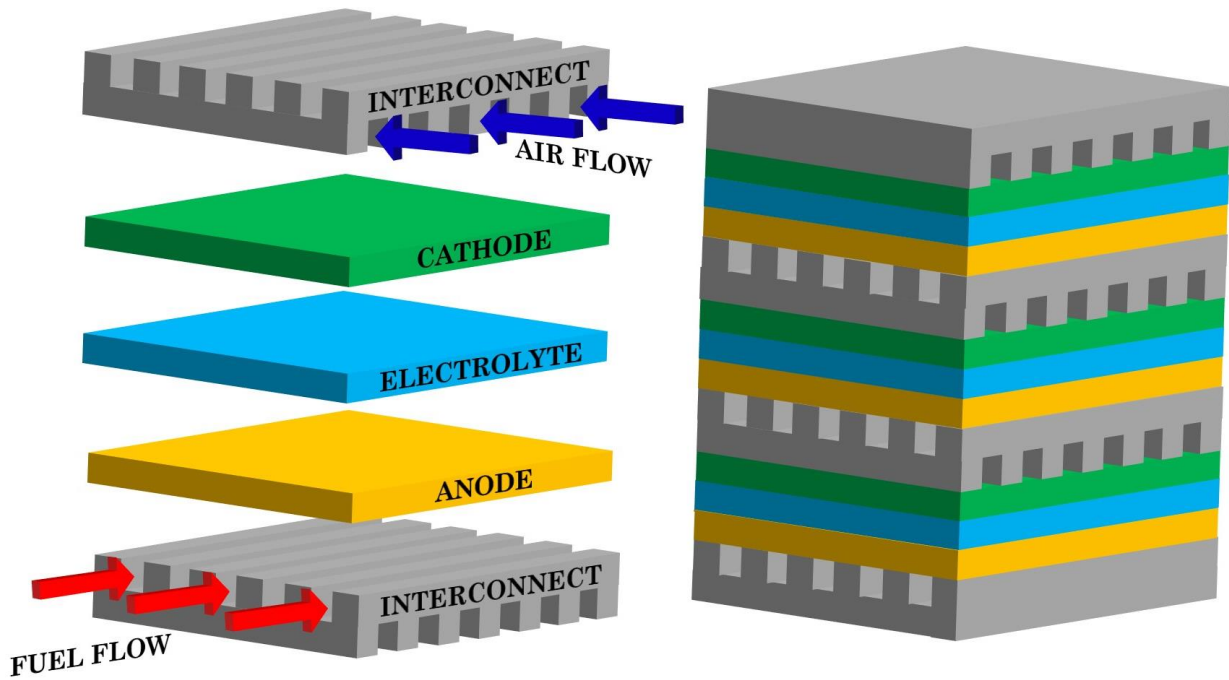


Figure 2.9: A fuel cell stack containing the interconnect-anode-electrolyte-cathode repeating unit. Brazed joints are used to join the metal interconnects to the ceramic electrodes.

These stacks of individual cells are necessary in order to produce functional electrical outputs as the voltage generated from a single cell is often small. The joining of these individual cells often requires joining of ceramic electrodes to metal interconnects which must withstand high operating temperatures (typically 500-1000°C) and as such brazing techniques are commonly used to form these joints. Active metal brazing is the most commonly used brazing technique for this application [59] but other new brazing techniques are being developed such as Reactive Air Brazing (RAB) developed by Kim, Hardy and Weil [60]. RAB has the advantage over other joining techniques that it occurs in air and as such the stability of the electrode materials in vacuum and controlled environments is not an issue [61]. The joining process also often occurs above 900°C and as such is suitable to withstand the high operating temperatures required for many SOFCs [62]. The RAB process utilises a binary component filler metal consisting of a noble metal such as silver and a reactive metal such as copper. The reactive metal (Cu) oxidises during the brazing process and helps improve the wettability of the noble metal on the ceramic. Since the promise of the technique for SOFC joining was realised, development of filler metals associated with the process has ensued and porous nickel interlayers have been investigated as a replacement for the copper as the reactive metal [58]. Additional research into the issue of joint failure due to mismatched thermal expansion coefficients between braze layer and ceramics has also led to the development of filler metals with tuneable thermal expansion coefficients by using varying levels of Al_2TiO_5 ceramic within the braze [63].

Dissimilar material joining for automotive light-weighting:

Automotive light-weighting continues to seek to replace as much steel as possible within cars with aluminium alternatives to save weight and improve fuel efficiency, however, in some areas this is not possible due to safety constraints, and as such development of joining techniques to join aluminium to steel is necessary. Joint formation between

aluminium and steel is possible but is considered industrially to be difficult [64]; primarily due to the extremely low solid solubility of iron in aluminium which often leads to the formation of intermetallics of the form Fe_xAl_y at the interface between the two materials. These precipitates have been shown to greatly reduce the mechanical properties of the joint [65]. Additions to filler metals have been investigated to attempt to reduce the size and quantity of these precipitates formed during the brazing process such as Si additions in aluminium fillers for joining 5A05 aluminium alloys to AISI 321 stainless steel [66]; Mg additions in aluminium fillers for joining 5052 Aluminium alloys to galvanised mild steel (which had little success due to Mg additions leading to high hot cracking sensitivity) [65] and Zr additions to a Zn-15Al filler metal for joining AA 6061 to 304 stainless steel [64]. Whilst some of these attempts have yielded measurable improvements (e.g. Zr additions reduced the size of the intermetallic layer leading to an increase in joint shear strength of 10%), more work is needed to produce interfaces with acceptable reliability when exposed to high operating temperatures. Further studies suggest that not just development of filler metals but also process optimization (such as an optimisation of heat input during the brazing procedure) should be investigated in future to reduce the level of intermetallic compounds produced and hence increase joint strength [67]. Finally, it is known that Si additions to Al can control the formation of the brittle Fe_xAl_y compounds by encouraging the formation of a Fe-Al-Si ternary phase instead, but the specifics of how the intermetallic layer is formed is still unknown and could benefit from systematic investigation.

High Entropy Alloys:

The primary focus of brazing filler metals developed in this work, high entropy alloys offer an exciting opportunity to expand the pool of available filler metals. Recently some investigations have begun into examining the use of HEA compositions as brazing alloys [68] [69]. Bridges et al. investigated a Ni-Mn-Fe-Co-Cu HEA and found it capable of joining Inconel® 718 with good mechanical properties until a brazing temperature 180°C above the liquidus is used, at which point excessive diffusion causes weakening of the joint [68]. Further recent conference publications including works authored by Tillman et al. focused on the doping of a CoCrCuFeNi alloy with Ge and Sn to lower its melting temperature to similar ranges as nickel based filler metal MBF 50A with joint shear strengths of the germanium doped filler reaching approximately 42.2% of the of those formed with MBF 50A [70]. Finally, Hardwick et al. developed a novel HEA in the NiCrFeGeB system which successfully joined Inconel® 718 when held at 1,100 °C for 15 minutes demonstrating further the potential that HEA compositions have to act as effective filler metals [71]. The vast number of potential novel compositions which could be investigated means that high entropy alloys offer an expansive field for development of brazing filler metals which is only just beginning to be explored.

2.2. High Entropy Alloys

As requirements for brazing filler metals become more stringent and their operating environments become harsher it has been necessary to investigate innovative new classes of materials to develop the next generation of brazing filler metals. The competitive advantage of investigating new alloy compositions from an industrial perspective is that by investigating new systems the chances of producing compositions which infringe on current patents is minimised. Research has been undertaken into the use of metal foams as brazing filler metals [72] and into the use of Bulk Metallic Glasses (BMG) as filler metals [73]. However, an area which has only recently begun to be explored is the use of high entropy alloys as filler metals [69][70].

2.2.1. High Entropy Alloys: Discovery and Background

High entropy alloys are a class of material discovered in 2004 simultaneously by two research groups. Professor Brian Cantor and co-workers in the UK published a paper titled “Microstructural Development in Equiatomic Multicomponent Alloys” describing how multicomponent systems containing more than 5 elements exhibited a reduced number of phases than predicted by the Gibbs phase rule, and in the case of a $\text{Fe}_{20}\text{Cr}_{20}\text{Mn}_{20}\text{Ni}_{20}\text{Co}_{20}$ alloy (now often referred to as “the Cantor alloy”), exhibited a single phase FCC solid solution despite the multiple principal elements it contained. At the time of this paper being published information on the central regions of high order phase diagrams (e.g. quaternary, quinary and higher order) was basically non-existent [74]. Industrially utilised alloy systems do of course feature quaternary systems, (such as 7075 aluminium alloy for aerospace which is based on a majority aluminium system with, zinc copper and magnesium additions) but most of these are still a majority one element with small additions of others and hence not located in the central regions of high order phase diagrams (Figure 2.10)

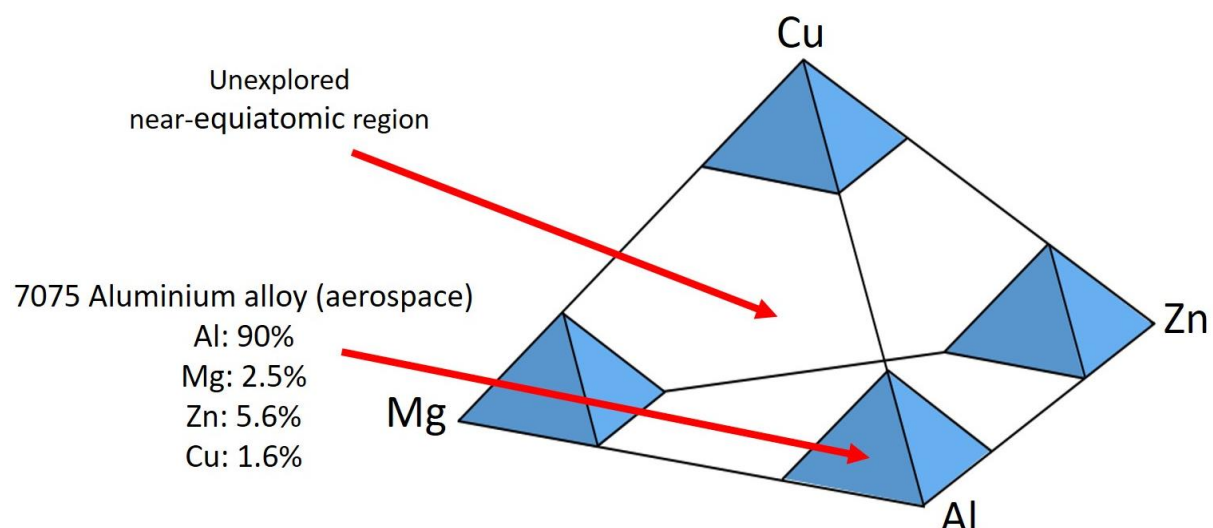


Figure 2.10: Quaternary phase diagram illustrating where industrially relevant quaternary systems are located within phase space and highlighting the unexplored central regions.

Simultaneously; Professor Yeh in Taiwan was working on producing alloy systems consisting of multiple principal components in equimolar or near-equimolar ratios and he postulated in his paper “Nanostructured high-entropy alloys with multiple principal elements: Novel alloy design concepts and outcomes” that the high configurational entropy associated with multiple principal elements in near-equimolar ratios would lead

to a stabilization of random solid solution phase and thus these alloys would exhibit a reduced number of phases in many cases (Figure 2.11). It was also Professor Yeh who first used the term ‘High Entropy Alloys’ (HEA’s) and defined them as containing between 5at% and 35at% of 5 or more constituent elements [75]. This has since spawned the field of alloy research on which the alloy systems designed in this thesis are based.

The high configurational entropy exhibited by HEA systems is used to explain the formation of single phases when the Gibbs phase rule (Equation 2.4) would predict more.

$$P = C + 1 - F \quad \text{Equation 2.4}$$

where P is the number of phases present, C is the number of components (elements) in the system and F is the degrees of freedom (this equation is only valid when pressure is constant and not a degree of freedom).

For a system with 5 components (such as the Cantor $\text{Fe}_{20}\text{Cr}_{20}\text{Mn}_{20}\text{Ni}_{20}\text{Co}_{20}$ alloy) with temperature as a degree of freedom but pressure held constant then the Gibbs phase rule would predict 5 phases ($P = (5 + 1 - 1) = 5$) which is not consistent with their observed microstructure as the system shows a simple single phase FCC structure. Another similar example is the alloy $\text{Fe}_{40}\text{Mn}_{27}\text{Ni}_{26}\text{Co}_5\text{Cr}_2$ (which while not a HEA by the original Yeh definition as one constituent is < 5at%) also exhibits a single phase [76]. It should be noted that the existence of single phases in these systems does not disprove the Gibbs phase rule which actually predicts the *maximum* number of phases which can be present within a system as pointed out by Pickering and Jones [77].

The original hypothesis from Professor Yeh [75] that the reason for multi-component systems forming far fewer phases than predicted by the Gibbs phase rule due to their increased configurational entropy these systems exhibit can be explained using the Boltzmann hypothesis (Equation 2.5).

$$\Delta S_{mix} = k \ln W \quad \text{Equation 2.5}$$

where ΔS_{mix} is the entropy of mixing, k is the Boltzmann constant and W is the total permutations of arranging the system.

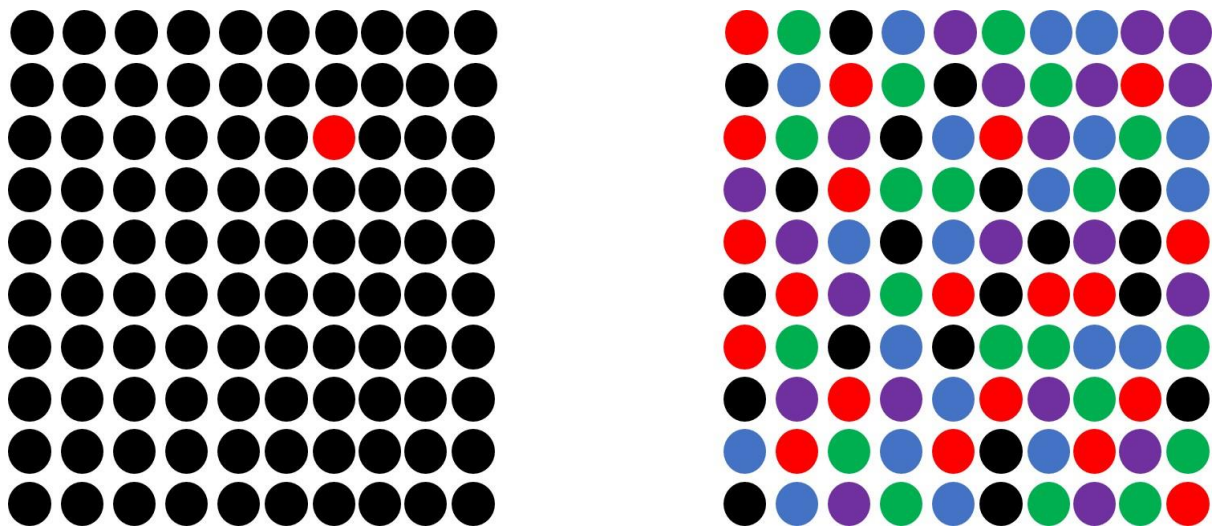


Figure 2.11: The left diagram (representing a 100 atom sample of a standard alloy of 99at% of one element and 1at% alloying additions) has 100 permutations, the configurational entropy is low.

The right diagram (representing a 100 atoms sample of a HEA with 20at% of 5 elements) has 1.09×10^{66} permutations, the configurational entropy is high. This assumes the atomic radii of all atoms are equal and that no other factors influence the arrangement of atoms.

A raise in possible permutations of atom arrangements (W) would lead to a higher entropy of mixing. The number of potential permutations of atom arrangements (W) can be increased by increasing the number of elements within the system (N) (Figure 2.11). A similar expression for the entropy of mixing can be formed using the number of elements within the system (N) [78].

$$\Delta S_{mix} = -R \sum_{i=1}^N c_i \ln c_i \quad \text{Equation 2.6}$$

where R is the gas constant ($R = 8.314 \text{ J K}^{-1} \text{ mole}^{-1}$), c_i is the atomic percentage of the i^{th} element and N is the total number of elements within the system.

The maximum possible number of permutations within a system exists when the solid solution in question is equimolar (i.e. the atomic percentage of each of the constituent elements are equal ($c_1 = c_2 = c_3 \dots = c_n$)).

In the case where the system is equimolar then the expression can be simplified to:

$$\Delta S_{mix} = R \ln N \quad \text{Equation 2.7}$$

and thus it can be shown for equimolar systems that the entropy of mixing for the system increases with the number of elements within that system (e.g. for 3, 4 and 5 elements respectively the entropy of mixing is 1.10R, 1.39R and 1.61R) [75] [78].

However, evidence exists to call into dispute the explanation of the high mixing entropy of these systems being the sole reason for the stabilisation of solid solution phases. Work by Otto et al. substituted atoms of similar atomic size and electronegativity and the same crystal structure for elements within the Cantor alloy (e.g. Ti for Co, V for Fe etc). This was to test the assumption that as long as the total number of elements present in the system is the same the mixing entropy should be the same and thus a single solid solution phase should still form if entropy is the sole driving force for the formation of solid solutions in HEAs. The substitution of one element for another led to the formation of multiple phases within all samples except the sample of Cantor alloy prepared as a reference and as such the group concluded that entropy alone was not able to override the driving forces behind phase stability. They concluded that the formation of solid solutions is consistent with the minimisation of the Gibbs energy of the system as a whole (including enthalpy) and not just due to the maximisation of configurational entropy [79].

The Gibbs free energy of a system is given by Equation 2.8:

$$\Delta G_{mix} = \Delta H_{mix} - T \Delta S_{mix} \quad \text{Equation 2.8}$$

The alloy system in question will form a solid solution if forming a solid solution is the most energetically favourable outcome for this system. This is because all systems move towards minimising the free energy within the system (ΔG_{mix}) i.e. making ΔG_{mix} as negative as possible. If the Gibbs free energy of the solid solution is lower than any other combination of phases, then it is energetically preferential for the system to move into a solid solution state. The two terms dictating this free energy term are the enthalpy term (ΔH_{mix}) and the entropy term ($T \Delta S_{mix}$), where T is the temperature of the system and ΔS_{mix} is the mixing entropy. In the vast majority of systems, the enthalpy term will be sufficiently large that even a very large entropy term will not outweigh the enthalpy term and thus a solid solution will not form. In the case where the enthalpy of mixing term (ΔH_{mix}) is small, a large entropy term ($T \Delta S_{mix}$) can outweigh this and lead to a negative

Gibbs energy overall thus making the organisation of the system in a solid solution energetically preferable. The lattice that will be formed within a solid solution of multiple principle components will differ from a base element even if the crystal structure is retained. The different atomic radii of the component elements the crystal structure of a single phase HEA (such as $V_{20}Nb_{20}Mo_{20}Ta_{20}W_{20}$ – A single phase BCC HEA reported by Senkov et al. [80]) will give a much more distorted lattice than that of a simple BCC element (such as Nb) - Figure 2.12).

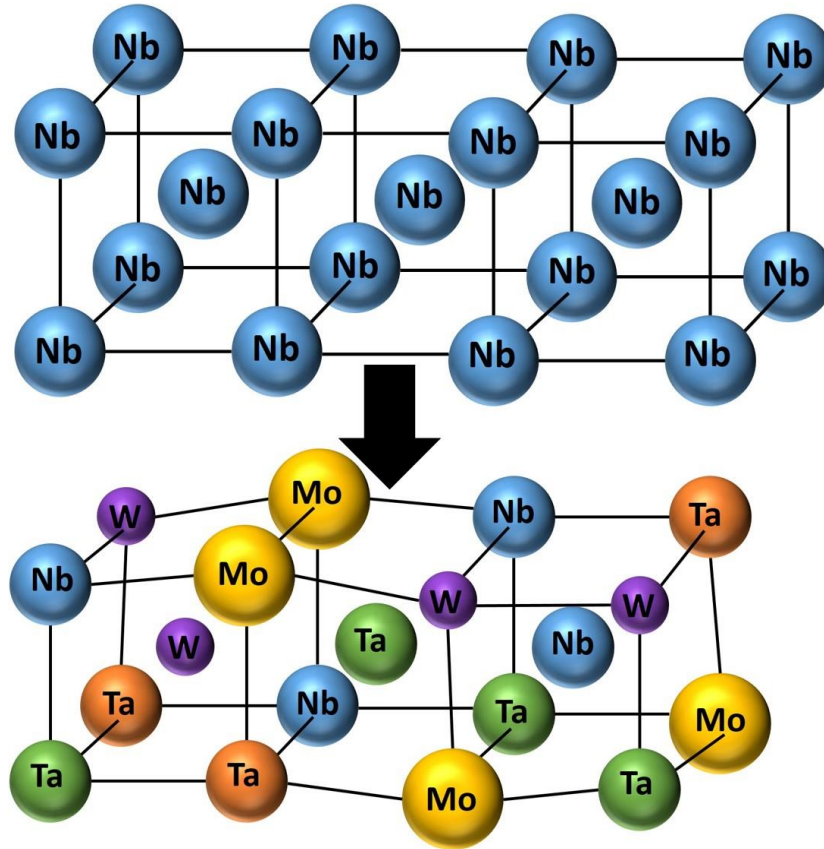


Figure 2.12: Diagram of a simple BCC element lattice (e.g. Nb) and a distorted HEA BCC lattice. Adapted and redrawn from [78].

The highly distorted lattice structure that will arise from a HEA solid solution forming can lead to interesting properties being reported for HEA systems. The large number of different sized atoms occupying the same lattice can lead to substantial solid solution strengthening which in turn can produce yield strengths of the order of gigapascals (such as the room temperature yield strength of 1246MPa for a $V_{20}Nb_{20}Mo_{20}Ta_{20}W_{20}$ alloy reported by Senkov et al. [80]). Other examples of exceptional properties reported to be exhibited by HEA compositions include a compressive yield stress of 1430MPa at room temperature for an $AlNbTiVZr_{0.5}$ alloy by Stepanov et al. [81], and a rolling extension of 4257% that has been published for a cold rolled sample of $Al_5Cr_{12}Fe_{35}Mn_{28}Ni_{20}$ [82] [83].

2.2.2. Empirical Parameters for Solid Solution Formation in HEAs

With properties as impressive as those mentioned in Section 2.2.1. above, researchers were incentivised to find rules for predicting which systems of elements would be likely to form HEAs from the almost infinite number of potential compositions (Cantor himself estimates the order of alloy compositions possible to be between 10^{78} and 10^{177} different alloys [84]). In literature many different researchers have allocated their time to attempting to quantify parameters (and associated values for these parameters) which will likely lead to the formation of single phase solid solutions.

The earliest guide to the forming of solid solutions come directly from the Hume-Rothery rules which state that elements with similar crystal structures, low atomic size differences (<15%), similar electron valences and similar electronegativity's are more likely to form solid solutions [85].

Work by Zhang et al. used 3 parameters to assess the likelihood of theoretical alloy compositions forming solid solutions: the atomic size difference, the enthalpy of mixing and the entropy of mixing [78] given by Equation 2.9 -Equation 2.11 below.

1) Atomic Size Difference

$$\delta = 100 \sqrt{\sum_{c_i}^n c_i \left(1 - \frac{r_i}{\bar{r}}\right)^2} \quad \text{Equation 2.9}$$

in which $\bar{r} = \sum_{i=1}^n c_i r_i$ where c_i is the atomic percentage of element i and r_i is the atomic radius of element i. 100 is a constant used as an amplification factor.

2) Enthalpy of Mixing

$$\Delta H_{mix} = \sum_{i=1, i \neq j}^n \Omega_{ij} c_i c_j \quad \text{Equation 2.10}$$

in which $\Omega_{ij} = 4^*(\text{mixing enthalpy of binary liquid alloys})$.

3) Entropy of Mixing

$$\Delta S_{mix} = -R \sum_{i=1}^n c_i \ln c_i \quad \text{Equation 2.11}$$

in which R is the gas constant ($8.314 \text{ Jmol}^{-1} \text{ K}^{-1}$)

Zhang et al. then plotted various graphs of combinations of these parameters to illustrate parameter boundaries within which solid solutions form; an example of which (plotting the atomic size difference against the enthalpy of mixing) can be seen in Figure 2.13. He highlighted that within the region marked by an S within his figure that only solid solutions will form. The approximate boundaries for the region marked by an S in Figure 2.13 can be given by the formulae $1 < \delta < 5$ for the atomix size difference and $-2.5455\delta - 2.4545 < \Delta H_{mix} < -\frac{15}{11}\delta + \frac{70}{11}$ for the enthalpy of mixing.

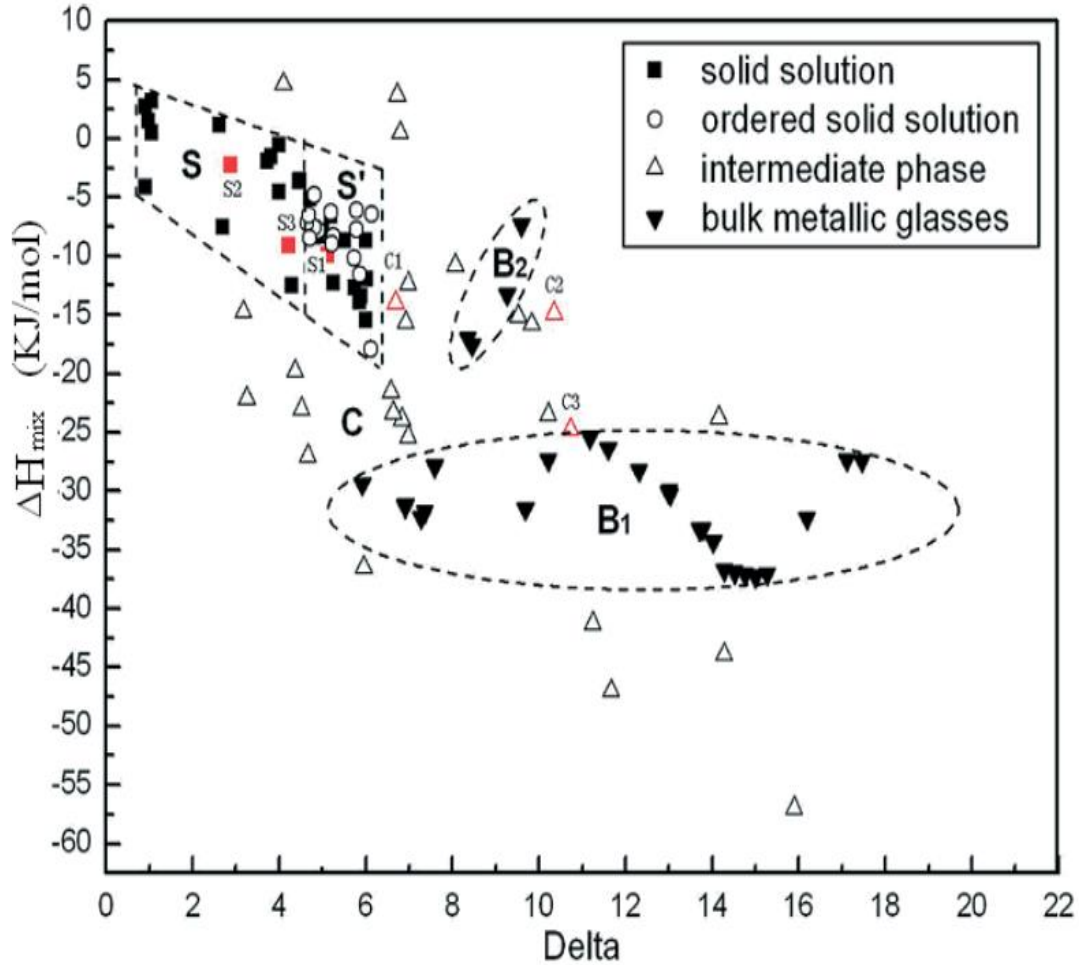


Figure 2.13: Plot of how different atomic size differences (labelled delta) and entropies of mixing (labelled ΔH_{mix}) form different alloy types. The zone in the upper left quadrant denoted by an S represents the area of the graph in which solid solutions form [78].

A similar boundary for this box proposed by Zhang et al. [86] is for the alloy to have an atomic size difference of $0 < \delta < 4.6$ and an enthalpy of mixing defined by $-2.68 \times \delta - 2.54 < \Delta H_{mix} < -1.28 \times \delta + 5.44$. This zone encompasses small atomic size differences between constituent atoms which enables substitution of elements for one another on the crystal lattice without inducing large lattice strains. Simultaneously this zone also covers enthalpies of mixing which are small and negative. This enables mixing to be possible without being low enough that the atoms are energetically favoured to form compounds. This set of boundary conditions has also been used by other researchers such as Takeuchi et al. when analysing the parameters used to form HEAs [87]. It should be noted that some opposition to the use of ΔH_{mix} as an indicator of the enthalpy of formation (ΔH_f) of the solid solution phase can be found; Pickering and Jones acknowledge that ΔH_{mix} and ΔH_f will be related as both are measures of how favourable the bonding between alloying elements is, but point out that intermetallic formation often involves a subset of the constituents of a HEA and that calculating the ΔH_{mix} for the entire multi-component system may not accurately reflect the preference of a pair of elements within the larger subset used for the HEA to form an intermetallic compound [77].

A slight increase in atomic size mismatch or a slight decrease in enthalpy tends to lead to the formation of some amount of ordered solid solution within the system which precipitates as a secondary phase [78]. This is because of the combination of a greater

atomic size mismatch necessitating a greater degree of ordering in order to accommodate lattice strains and the more negative enthalpy of mixing encouraging the precipitation of intermetallic compounds.

Other researchers have expanded upon these 3 parameters to try and improve HEA prediction parameters. Guo and Liu (2011) used the same 3 parameters as Zhang but added two others; electronegativity difference and the Valence Electron Concentration (VEC) given by Equation 2.12 and Equation 2.13 [88].

4) Electronegativity Difference

$$\Delta X = \sqrt{\sum_{i=1}^n c_i (X_i - \bar{X})^2} \quad \text{Equation 2.12}$$

where X_i is the Pauling electronegativity for element i and $\bar{X} = \sum_{i=1}^n c_i X_i$

5) Valence Electron Concentration (VEC)

$$VEC = \sum_{i=1}^n c_i (VEC)_i \quad \text{Equation 2.13}$$

where $(VEC)_i$ is the Valence Electron Concentration of element i and represents the total number of d-electrons in the valence band. Guo and Liu (2011) stated that solid solutions are formed when $\delta < 8.5\%$, $-22 \leq \Delta H_{mix} \leq 7 \text{ KJmol}^{-1}$ and $11 \leq \Delta S_{mix} \leq 19.5 \text{ KJmol}^{-1}$ [88]. Zhang (2014) looked at the solid solutions formed more specifically (i.e. excluding those with any intermetallic compounds present) and narrowed parameter ranges to $\delta < 4.0\%$, $-10 \leq \Delta H_{mix} \leq 5 \text{ KJmol}^{-1}$ and $\Delta S_{mix} > 13.38 \text{ KJmol}^{-1}$ [89]. A figure illustrating the different values of δ and ΔH_{mix} used by different researchers to predict HEA formation can be seen in Figure 2.14.

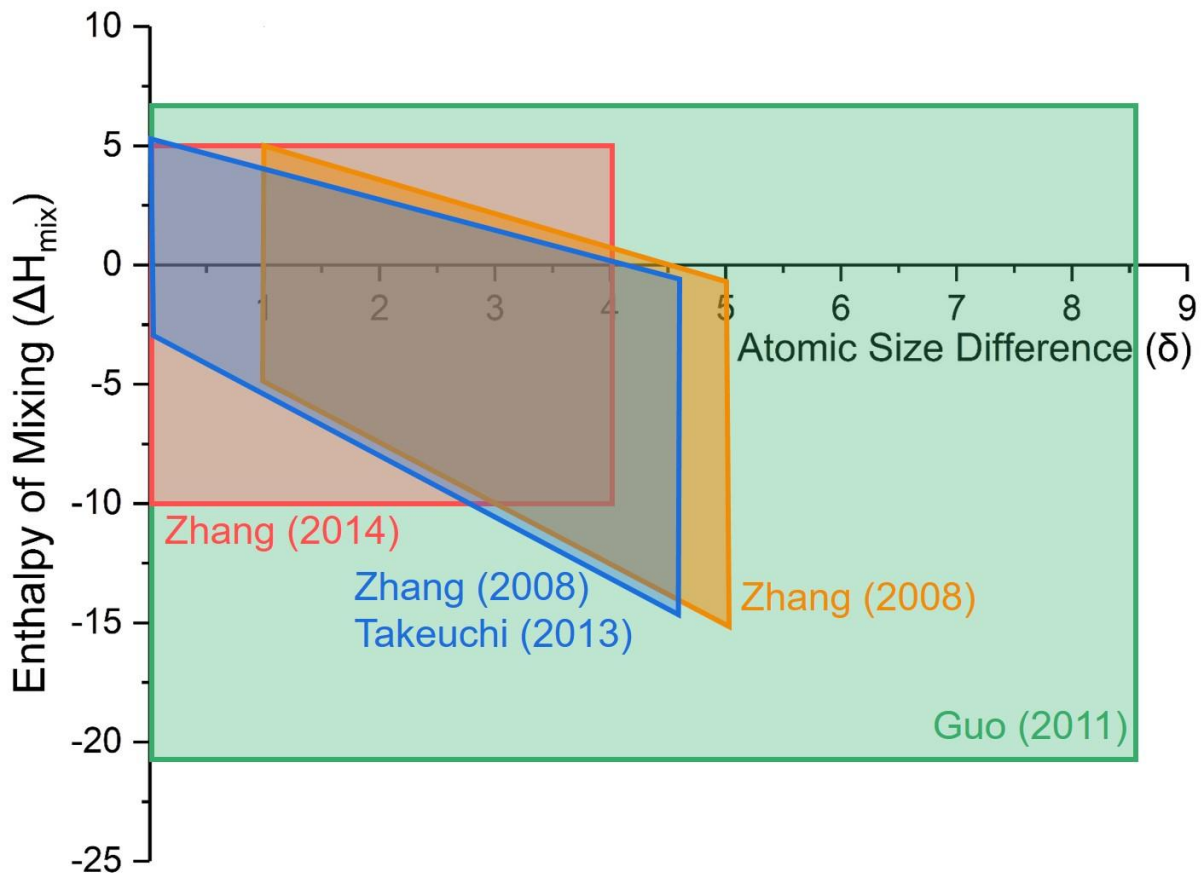


Figure 2.14: Overlay of parameter values used by different researchers to define where solid solutions form in HEAs [78] [86] [87] [88] [89].

Other solid solution formation parameters have also been proposed; Poletti and Battezzati (2014) proposed a parameter designated μ which used the ratio of the ideal melting temperature (T_m) to the spinodal point (T_{sc}); the temperature above which a given composition is a stable homogenous single phase alloy [90]. They stated that new HEA compositions should be mixed with a μ parameter value of >1.5 as well as an atomic size difference of below 6% (Figure 2.15).

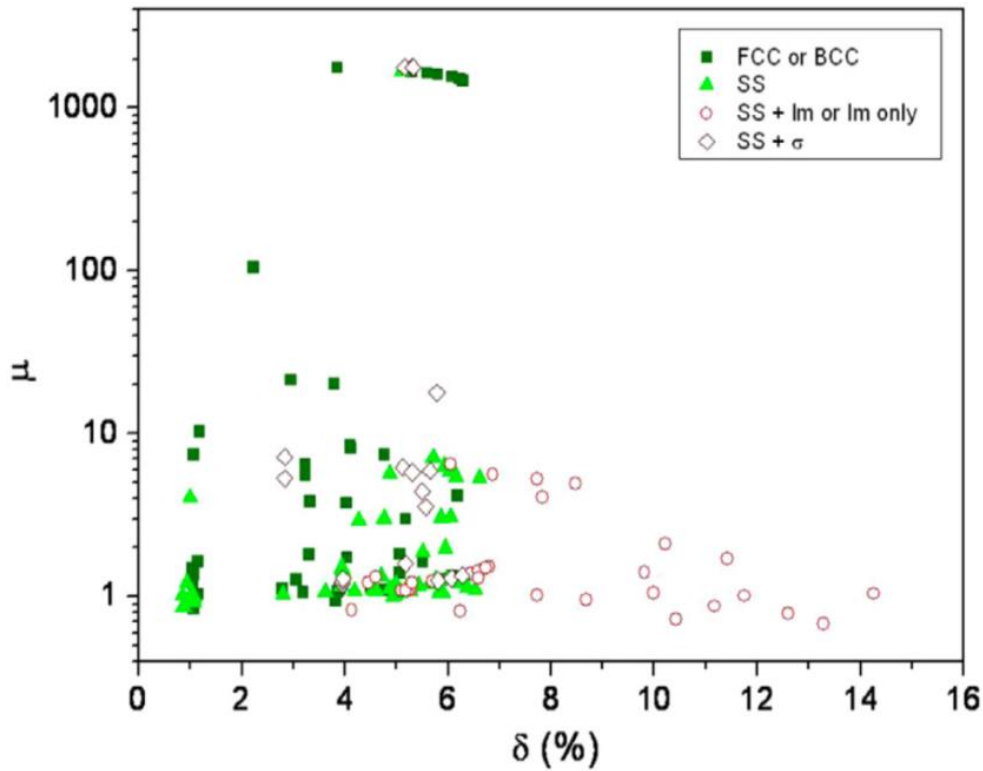


Figure 2.15: A plot depicting the positions of known HEA compositions for the μ parameter developed by Poletti and Battezzati and atomic size mismatch (δ). the symbols assigned are indicative of microstructure reported in literature.

Poletti and Battezzati also note that the values of VEC and e/a (number of itinerant electrons per atom) are indicative of whether the HEA formed will produce a BCC or an FCC composition [90]. A conclusion echoed by Guo et al. who concluded that FCC structures are found to be more stable at high VEC values ($VEC > 8$) whereas BCC phases are more stable at lower VEC values ($VEC < 6.87$). In the intermediate region ($6.87 < VEC < 8$) a mixture of BCC and FCC phases is likely (Figure 2.16) [91].

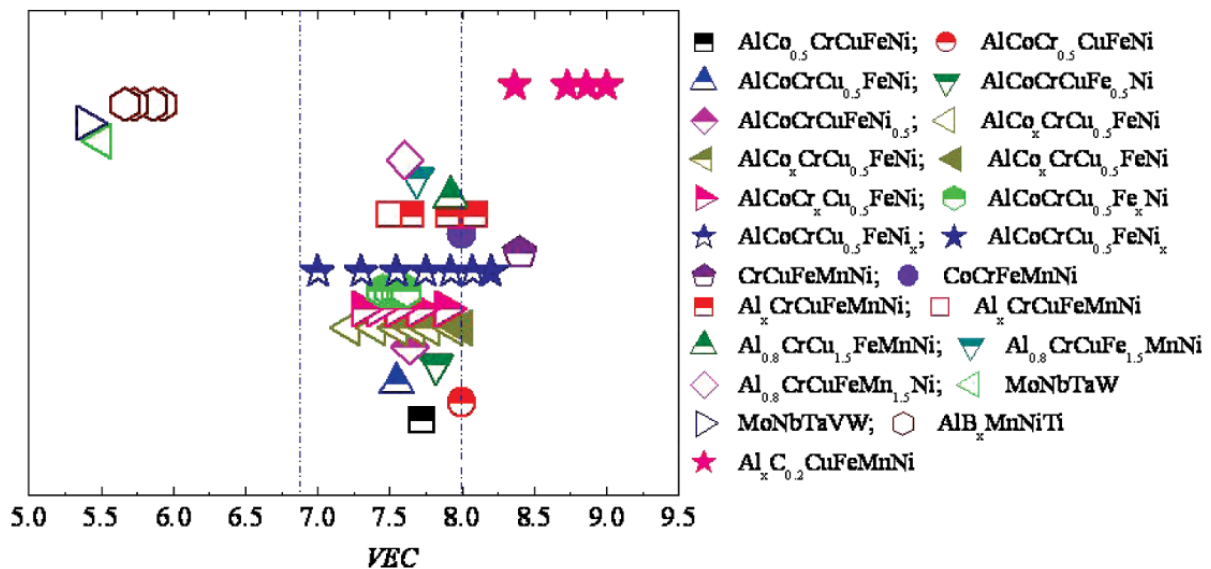


Figure 2.16: Graph depicting that FCC phases (Filled symbols) often appear at $VEC > 8$ and BCC phases (open symbols) often occur below $VEC = 6.87$. A mixture of BCC and FCC (half-filled symbols) occur in the intermediate range [91].

Review papers on the topic dispute this correlation and state that when large ranges of alloy systems are considered that no correlations are found between VEC and the crystal structure of the HEA formed [92]; however it should be noted that the Guo did acknowledge that these predictions do not hold true when certain elements (e.g. manganese) are included [91]. Further work by Tsai et al. highlights the point that the VEC predictions become less accurate when an element within the HEA separates to form its own phase as the effective VEC of the alloy may be different to its apparent HEA, particularly if the element which forms its own phase has a high VEC itself [93], the example given being for a $\text{Cr}_2\text{CuFe}_2\text{MnNi}$ which has a VEC of 8 but using the assumption that only 1/5 of Cu participates in the formation of the non-Cu-rich phase then the VEC would be lower at around 7.61 – putting the system in the mixed BCC/FCC region stipulated by Guo [91].

Further research in the field by Yang and Zhang in 2012 established a new parameter for evaluation of which compositions would likely form solid solutions in an attempt to further differentiate when HEA compositions would form solid solutions or intermetallic phases and designated it Ω given by Equation 2.14:

$$\Omega = \frac{T_m \Delta S_{mix}}{|\Delta H_{mix}|} \quad \text{Equation 2.14}$$

where T_m is the melting temperature of the alloy systems calculated via the rule of mixtures approach (Equation 2.15):

$$T_m = \sum_{i=1}^n c_i (T_m)_i \quad \text{Equation 2.15}$$

where $(T_m)_i$ is the melting temperature of the i th component of the alloy. At $\Omega > 1$ the influence of the mixing entropy is greater than the influence of the mixing enthalpy (at the melting temperature of the system) which will increase the likelihood of a solid solution forming. Yang and Zhang concluded that solid solutions would form when $\Omega > 1.1$ and the atomic size difference (Equation 2.9) was $\delta < 6.6\%$ [94] [95]. Furthermore, once $\Omega > 10$ no intermetallic phases form and only solid solutions are seen (Figure 2.17).

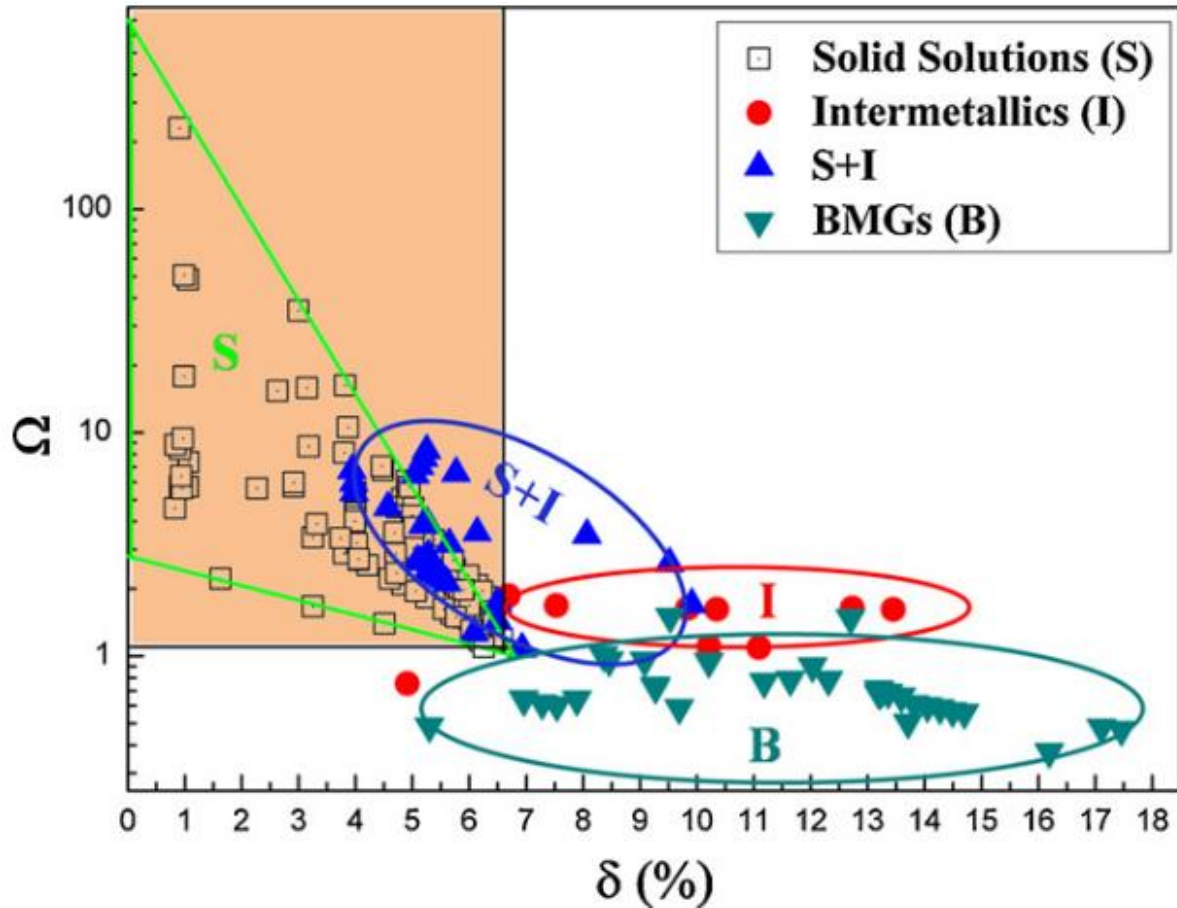


Figure 2.17: Graph depicting the formation of solid solutions at low atomic size differences and a value of the Ω parameter greater than 1.1 [94].

It must be noted that whilst these above equations have been used within multiple studies to predict solid solution formation in HEAs their accuracy is disputed. Pickering and Jones note that in many instances that the values of these parameters are chosen to fit experimental results and not derived from any theoretical basis; as such depending on the particular compositions examined in any one study differing values for the same parameter could be said to predict solid solution formation [77]. Furthermore, as pointed out by Pickering and Jones [77], the assessment of whether a composition forms a single phase often uses as-cast microstructures and as such may not accurately represent the stable microstructures of these compositions. More accurate data is likely to be found if all as-cast microstructure studied were exposed to homogenisation treatments to assess whether the solid solutions decompose into multiple phases. An example of this (using a dataset of 27 alloys) analysed by Wang et al. demonstrated that the empirical rules that produce solid solution structure in as-cast samples are wider than those that produce solid solutions in more equilibrium microstructures which have been exposed to ageing treatments in the range of $0.5 < T/T_m < 0.9$ [96]. Annealed FCC and BCC solid solution HEAs had enthalpies of mixing in the range $\Delta H_{mix} > -7.5 \text{ KJmol}^{-1}$ and an atomic size difference $\delta < 3.3\%$ whereas the as-cast structures had wider ranges ($\Delta H_{mix} > -12.5 \text{ KJmol}^{-1}$ and $\delta < 6.2\%$ [97]).

2.3. Thermoelectrics

2.3.1. Thermoelectric Devices

Thermoelectric devices (often shortened to thermoelectrics in this thesis for brevity) are devices which exhibit a thermoelectric effect. A thermoelectric effect is the conversion of heat (via a temperature gradient) into electrical voltage (or vice versa). Three specific 'thermoelectric effects' exist: the Seebeck effect (the production of a voltage between two dissimilar conductors whose junctions are held at different temperatures); the Peltier effect (the cooling or heating of a junction of two dissimilar materials subject to an electric current); and the Thomson effect (the heating or cooling of a single conductor with a maintained temperature gradient along its length).

These effects can be used for many different purposes including:

- **To measure temperature with a thermocouple.** A thermocouple utilises the Seebeck effect by placing one junction of two dissimilar metals at a known reference temperature and the second junction of these two dissimilar metals at an unknown temperature. By knowing the reference temperature and the voltage generated between the two junctions by the Seebeck effect, the temperature at the unknown junction can be calculated.
- **To convert waste heat into electrical voltage.** By keeping one junction of two dissimilar metals at a low temperature and exposing the other to a higher temperature the voltage generated between the two junctions by the Seebeck effect can be used to convert heat to electricity. This can be used to recover energy that is lost as heat. This is important as it is estimated that as much as 60% of all energy generated is lost, with most of this lost in the form of thermal energy. Recovering even a small percentage of this could have a massive effect on the efficiency of many systems [98].
- **To cool objects.** By utilising the Peltier effect to apply voltage to two dissimilar metals with two junctions we can cause cooling at one of the junctions (reversing the polarity of the applied voltage will cause heating). This can be used in refrigeration [99].

2.3.2. The Seebeck Effect

Of the three thermoelectric effects mentioned above it is the Seebeck effect which is most relevant to this project and as such the others will not be considered in any further detail. The basic principle underlying the Seebeck effect was first discovered by Thomas Seebeck in 1821 when he observed the deflection of a compass needle by two pieces of metal which were joined at two junctions held at different temperatures [100]. This deflection of the compass needle was caused not by the electrical voltage generated itself, but by the magnetic field that the flow of charged particles within the piece of metal (due to the voltage generated from the Seebeck effect) invoked [101].

The Seebeck effect is not limited merely to metals but can be observed with any material containing mobile charge carriers. When the Seebeck effect occurs to the charged particles within a semi-conductor the charges that move are dependent on the type of semiconductor material in question (n-type or p-type).

- In an n-type semiconductor the free charged particles are electrons. The electrons at the hot end of the material gain more kinetic energy from the increased heat

available at the hot end and thus move more than the electrons at the cold end. The increased movement at the hot end means that overall the electrons will move towards the cold end leaving a negative charge on the cold face of the semiconductor (Figure 2.18).

- In a p-type semi-conductor the free charged particles are holes and in a similar fashion as with the electrons in the n-type conductor, the holes will migrate towards the colder end of the semiconductor leaving a positive charge on the cold face of the semiconductor (Figure 2.18).

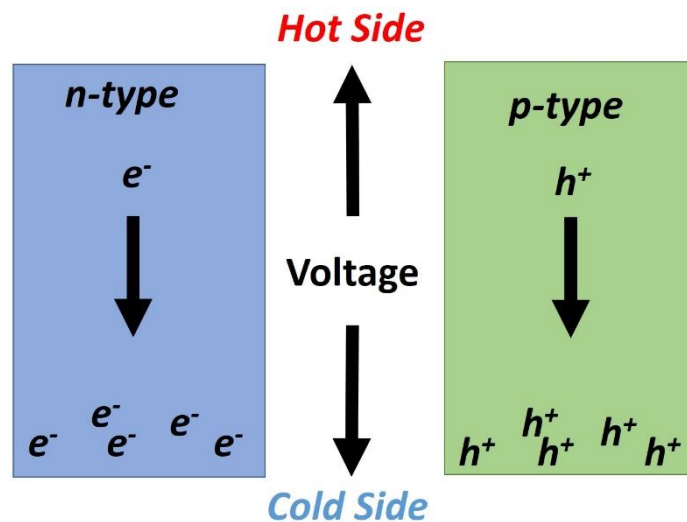


Figure 2.18: Diagram illustrating the movement of charged particles from the hot side to the cold side in a semiconductor exposed to a thermal gradient and the accumulation of these charges at the cold side.

By electrically connecting the hot ends of an n-type and a p-type semiconductor together and connecting some form of electrical load across the cold end (such as a rechargeable battery), current will flow and electrical energy can be produced from waste heat (Figure 2.19). A single piece of either n-type or p-type semiconductor used in this way is referred to as a thermoelement.

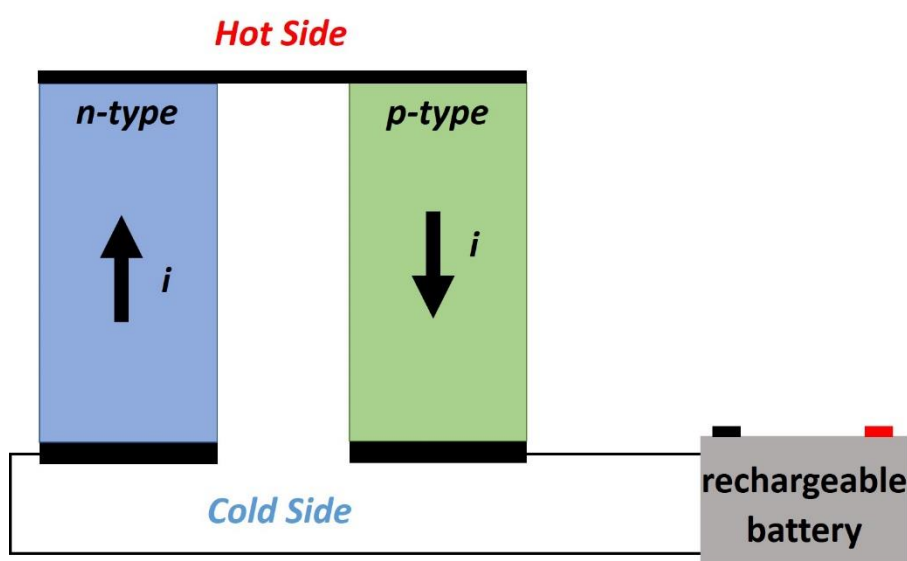


Figure 2.19: Diagram showing the flow of current that ensues once an n-type and a p-type semiconductor are connected electrically and placed across a thermal gradient.

The amount of power generated from a single thermocouple (made by the joining of an n-type thermoelement and a p-type thermoelement together - as shown in Figure 2.19) is small and as such in order to obtain a useable power output many of these individual thermocouples must be connected together to form a module known as a thermoelectric generator (TEG). The number of individual thermocouples necessary depends on the required module size and required power output; a module of approximately 1600mm² contains around 127 thermocouples and is capable of generating power outputs of between 1W (when the temperature gradient, $\Delta T=65\text{K}$) and 8W (when $\Delta T=230\text{K}$) as the magnitude of the power generated is related to the temperature difference (ΔT) by a power law [102] [103]. In a TEG the individual thermocouples (i.e. an n-type and a p-type pair) must be connected electrically in series but thermally in parallel in order for their effects to summate. To achieve this the thermocouples must be arranged in an array (Figure 2.20). The individual thermocouples are joined by conductive metal strips (silver coloured plates in Figure 2.20), which are often made of copper in a real module and arranged side by side in a grid sandwiched between thermally conductive (but electrically insulating) plates which places them thermally in parallel [103].

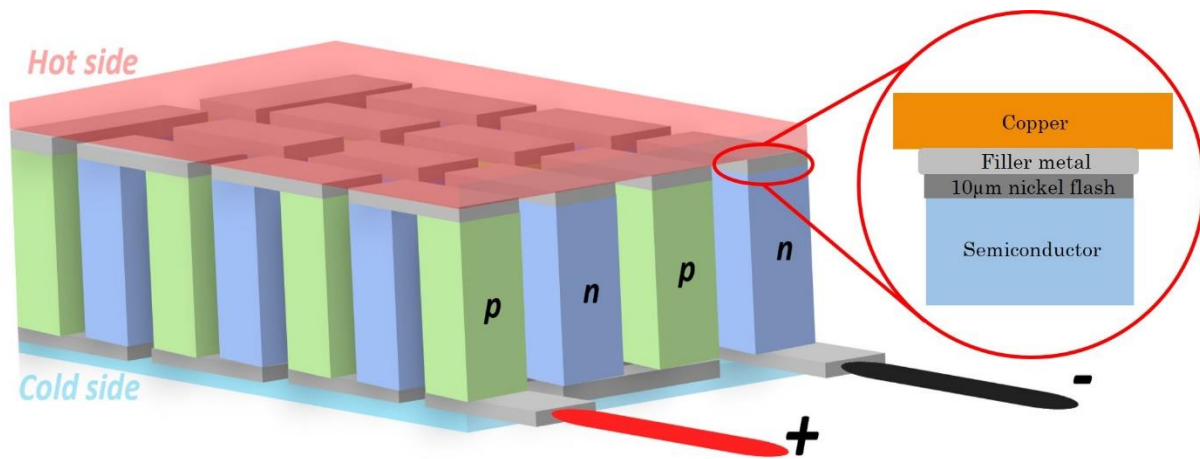


Figure 2.20: Diagram of a thermoelectric generator. Individual thermocouples are connected electrically in series (by the silver connections) but thermally in parallel. Redrawn from [104].

2.3.3. Layout of the Thermoelectric Generator

An example layout of a thermoelectric generator is shown in plan view in Figure 2.21 (left). 62 semiconductor legs (31 pairs) are arranged in an 8×8 array with the two bottom corner locations occupied by electrical contacts. The base plate is a high purity copper which is joined to semiconductor legs plated with a nickel diffusion barrier of approximately 10µm thick. The joint between copper base plate and the nickel diffusion barrier applied to the semiconductor legs is currently formed using a silver based brazing filler metal (conforming to the specification for ISO17672 Ag-155) for high temperature use or a lead based solder for low temperature use (Figure 2.21, right). The module is symmetrical across the plane of the page with the top half of the module the same as the bottom half described above but in reverse (see Figure 2.21, centre).

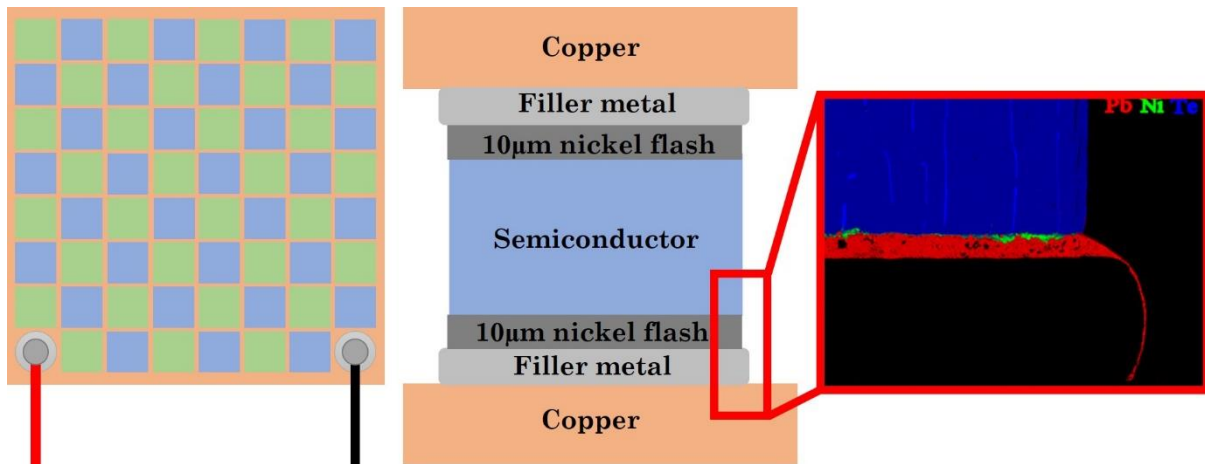


Figure 2.21: Left: A plan view diagram of the thermoelectric module showing the arrangement of semiconductor legs in a 40mm by 40mm module. Centre: A diagram showing the arrangement of materials within a single thermoelectric element within the module. Right: An EPMA map of a thermoelement joined to a copper base plate using a solder with the nickel flash layer shown.

2.3.4. Applications of Thermoelectric Generators

Thermoelectric generators (TEGs) have found only niche use to date in power generation applications despite their long list of advantages over other power generating techniques including:

- A long lifespan
- No moving parts and hence drastically reduced maintenance costs
- Direct energy conversion from heat to electricity (unlike heat engines which often convert heat to mechanical energy and then mechanical energy to electricity).
- Noiseless operation [105].

One example of a niche applications where TEGs have been utilised successfully is as a power source for unmanned space exploration vehicles. Due to the distance these craft have to travel their lifespan is very long and maintenance is not possible. The lack of moving parts and no requirement for maintenance make TEGs an ideal choice as a power source for this application. They are also very small and lightweight; factors that are important when space and weight savings are critical. The lack of heat available in space to power the TEG is solved by using the heat of decay from a radioactive isotope (usually Plutonium-238 in NASA spacecraft [106]) to heat the hot junction of the TEG. As these deep space exploration vehicles are unmanned the radiation from the plutonium decay is not a danger; particularly as many of these probes are not designed to return to earth. Both Voyager I and Voyager II used TEGs to power scientific equipment. They were launched in 1977 and are expected to have sufficient electrical power generated by the TEGs till 2020 – 43 years of continuous electricity generation [105]. Missions using Radioisotope Thermoelectric Generators (RTGs) have enabled missions to Venus, Mars, Jupiter, Uranus, Neptune and some of the main asteroid belts [107].

Other niche applications include the use of TEGs as power sources for remote lighthouses in Russia [105], and for powering sensors on industrial machinery and in factories. Current intelligent sensors are small and require only a few milliwatts of power, the cost of running electrical cables from the grid to these sensors (often installed in remote and hard to reach places on a production line) is too high and requires careful planning of

cable layouts. As such these sensors are often powered by batteries. Unfortunately, batteries will only last for a few years powering these sensors, but the life expectancy of the sensor itself can be as high as 15 years. This means the sensors must be replaced far more often than necessary. TEGs offer a method of powering these sensors for their full lifespan, they don't require costly maintenance and are suitable for use in inhospitable environments, making them ideal candidates for this niche power generation application [105].

2.3.5. Drawbacks to Using Heat Recovery Devices / TEGs

The main drawback of TEGs which prevents more widespread use of these devices is their low efficiency (<5% [108]). This drawback can be partially negated by using them as heat recovery devices rather than to directly generate power as recycling any wasted energy from a system is advantageous; whereas in direct generation a high efficiency is sought after.

The efficiency of a thermoelectric is measured using the thermoelectric figure of merit (ZT). This figure of merit is a dimensionless parameter often referred to by just the letters ZT and is defined by Equation 2.16.

$$ZT = \frac{\sigma S^2 T}{\kappa} \quad \text{Equation 2.16}$$

where σ is the electrical conductivity, S is the Seebeck coefficient and κ is the thermal conductivity of the thermoelectric material.

A higher ZT value is attained by a material with a high electrical conductivity, a high Seebeck coefficient and a low thermal conductivity. Currently, materials with a ZT value of 1-2 are not particularly economically viable with estimated paybacks within 6 years [109], Figure 2.22 shows several candidate thermoelectric materials and their ZT values as a function of operating temperature [108]. However, if ZT values of 3.0 and greater are reached then thermoelectric generators using these high ZT materials could become a prominent inclusion within modern vehicles [109]. Modelling results indicate that TEGs with a ZT of 3.0 and a unit cost half of the current average would have a payback period of less than 3 years when installed on a passenger bus [110]. Recent advances have produced materials with ZT values of 2.5 [111] by using non-equilibrium processing; highlighting the potential to reach figures of merit as high as 3.0 with continued research. Nanostructured materials with a ZT of 3.0 manufactured using Bi-doped n-type PbSeTe/PbTe quantum-dot super-lattice (QDSL) samples grown by molecular beam epitaxy (MBE) have been reported [112], but as of yet bulk materials have not been produced with a ZT this high.

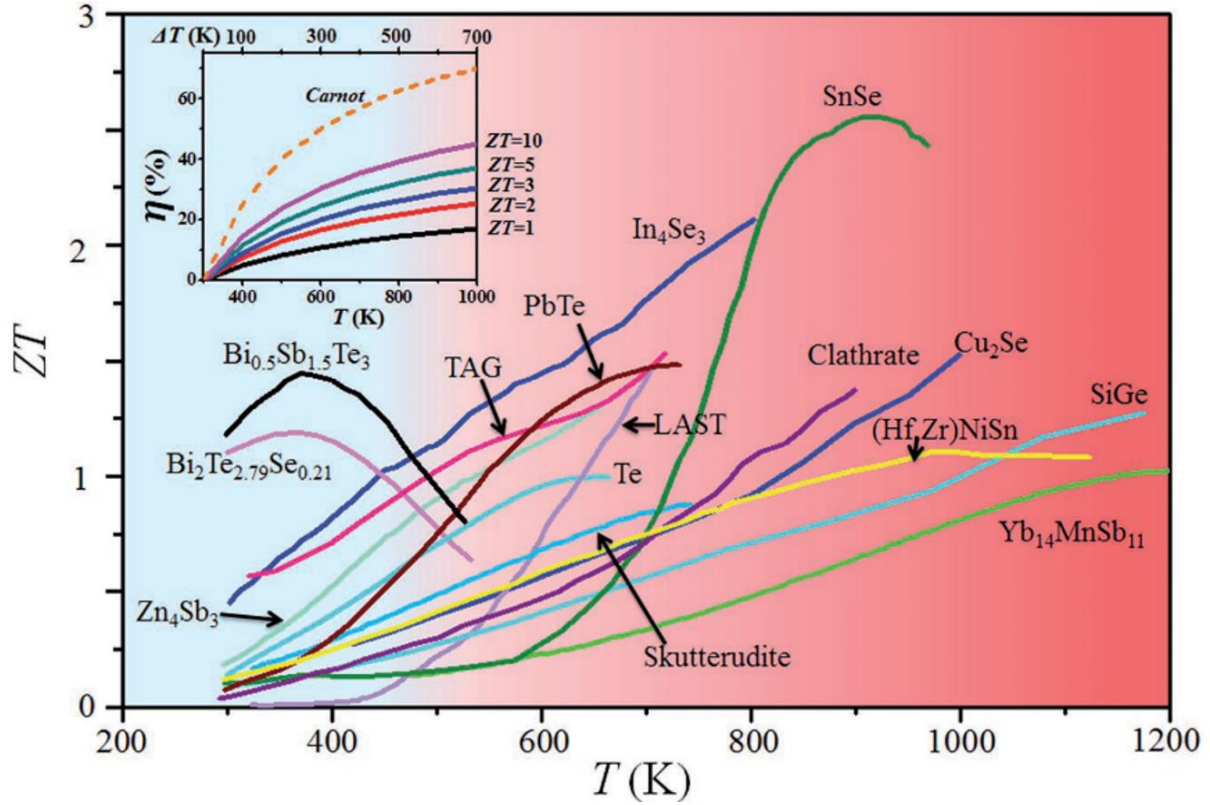


Figure 2.22: Plot of the ZT of different high performance thermoelectric as a function of operating temperatures. Image taken from [108].

Although the current efficiency of these devices is low (<5% [108]), this inefficiency is less important in heat recovery devices than in power generation as any useful power generated from a waste energy source is an improvement to overall efficiency, providing the costs of installing and transporting the device are offset. This lends the technology to areas in which wasted energy is a large concern. As vehicles are subject to taxes depending on their efficiency, the recovery of waste heat from vehicle exhausts is a promising application area where TEGs can provide a financial benefit. On the other hand, the TEGs must generate enough electricity to justify their cost and weight additions to the vehicle and as such improvements to the efficiency of thermoelectric generators is highly desirable [98]. In a car, the chemical energy stored in fuel is converted to kinetic energy via the internal combustion engine. The fuel is vaporised and compressed before being ignited by a spark. The rapidly expanding gas from the exploding fuel/air mixture moves a piston which powers the car and ejects the hot exhaust gas simultaneously. The efficiency of this process can be described using Equation 2.17 below.

$$\eta = \frac{\text{useful work done}}{\text{work done} + \text{waste heat produced}} \quad \text{Equation 2.17}$$

where η is the efficiency of the engine as a percentage. A typical internal combustion engine is approximately 25% efficient; meaning that 75% of the potential energy that could be extracted from the fuel is lost. Recovering even some of this energy via heat-recovery devices could dramatically increase the energy efficiency of the car [113] [114].

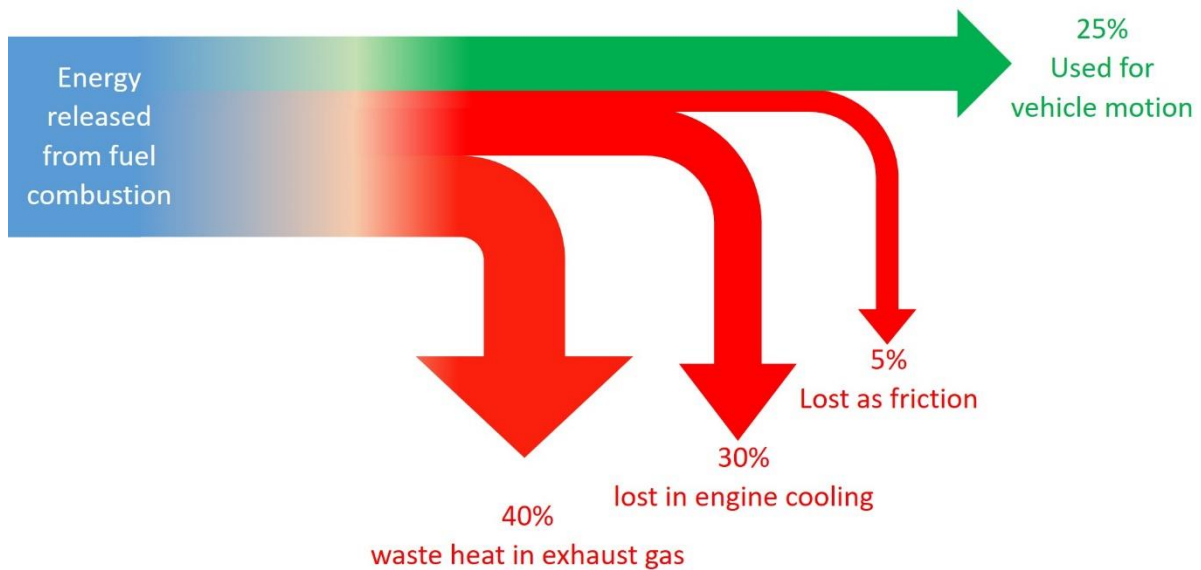


Figure 2.23: Sankey diagram showing the inefficiency of a standard internal combustion engine and the sources of wasted energy. Image redrawn from [113] [114].

A heat recovery device makes use of the wasted heat contained in the exhaust gas (approximately 40% of energy produced from burning fuel (Figure 2.23)) and converts some of this heat into electricity which can be fed back into the vehicle powertrain to do useful work propelling the car forward; thereby increasing the overall efficiency of the vehicle. The exhaust gases are used to provide the high temperature at the hot junction and the engine coolant is used at the cold junction to maintain the temperature gradient [115]. This temperature gradient is used by the TEG to form a voltage difference and can generate electricity. The main advantages to these devices are that they can be small in size and since they contain no moving parts they are very reliable and resistant to wear. They are also emission free and contain no working fluids [116]. Many of these modules can be combined in order to give appreciable power outputs which can improve the efficiency of cars and other devices which lose a lot of energy as heat. Producing no pollutants at all makes these heat recovery devices a promising area for many manufacturing companies to investigate. Many major car manufacturers have some variant of thermoelectric generator under development including BMW [117], Honda [118], Ford [119], and Renault [120] [121].

With the potential to use TEGs to recover waste energy rather than generate it directly, the primary issue of their efficiency drawbacks is offset to some extent. At this point the other problems preventing their introduction can be investigated. A secondary issue to thermoelectric devices preventing their wide scale implementation relates to bonding issues within these devices. Thermoelectric materials are often made to a very precise composition in order to achieve their electrical properties and the diffusion of other elements from a filler metal may cause a reduction in the electrical properties of the thermoelectric and hinder its capability to function as a thermoelectric material. This is a particular issue as operating temperatures for TEGs increase as the higher temperature encourages further diffusion [122]. Therefore, the extent of the reaction between filler and thermoelectric must be carefully balanced to give sufficient adhesion whilst not influencing electrical properties of the thermoelectric (e.g. the contact resistance of the interface) [123]. A particular example of this is noted in a study by Liu in which a Ni layer was hot pressed to a $\text{Bi}_2\text{Te}_{2.7}\text{Se}_{0.3}$ n-type thermoelectric [124]. Grain boundary diffusion of

nickel from the nickel layer into the thermoelectric formed a strongly bonded interface (~ 20 MPa in a tensile strength test) but led to the formation of a p-type region ($(\text{Bi}_{1-x}\text{Ni}_x)_2(\text{Te,Se})_{3-5}$) within the n-type $\text{Bi}_2\text{Te}_{2.7}\text{Se}_{0.3}$ thermoelectric as Ni is a p-type dopant for Bi_2Te_3 [123]. The formation of this p-type region in the n-type thermoelectric due to the diffusion of nickel led to a contact resistance of $R_c \sim 210 \mu\Omega \text{ cm}^2$, which was unacceptably high and required correction [124]. Further examples of excessive diffusion during bonding causing damage to thermoelectric devices include the diffusion of copper from a copper bonding layer into a $\text{Pb}_{0.6}\text{Sn}_{0.4}\text{Te}$ thermoelectric forming a Cu_2Te compound within the PbTe matrix of the thermoelectric [122] altering the composition and the diffusion of Nb from a Nb bonding foil forming a Nb_3Te_4 compound which had weak adhesion to the Nb foil giving a weak bonding interface [125]. These studies highlight the importance and challenges of finding suitable bonding materials for forming mechanically and electrically sound joints in thermoelectric assemblies, especially at hotter operating temperatures ($>300^\circ\text{C}$) which make it difficult to establish low electrical resistance contacts due to chemical reactions at the interface [122].

In recent years a dramatic increase in research in the field of thermoelectric has been seen. Increasing environmental pressures have been placed on researchers and corporations alike not only by government emissions targets but also by an increasing public movement to act on climate change. This motivation has encouraged research institutions and industry to investigate thermoelectric materials with higher and higher figures of merit in an attempt to overcome one of the main shortcomings with TEGs – the low conversion efficiency. The efficiency of a thermoelectric is most commonly measured using the “Thermoelectric Figure of Merit”. A search for papers published by year using the “Web of Science Core Collection” database using the search terms “Thermoelectric Figure of Merit” and “Brazing Filler Metals” demonstrates the rapid increase in the last 20 years for papers on the subject of the efficiency of thermoelectric devices (Figure 2.24). With comparatively few results in the area of development of brazing filler metals for joining in thermoelectric devices, a large scope for research exists and also a substantial opportunity for the development of intellectual property in relation to filler metal compositions as yet un-researched.

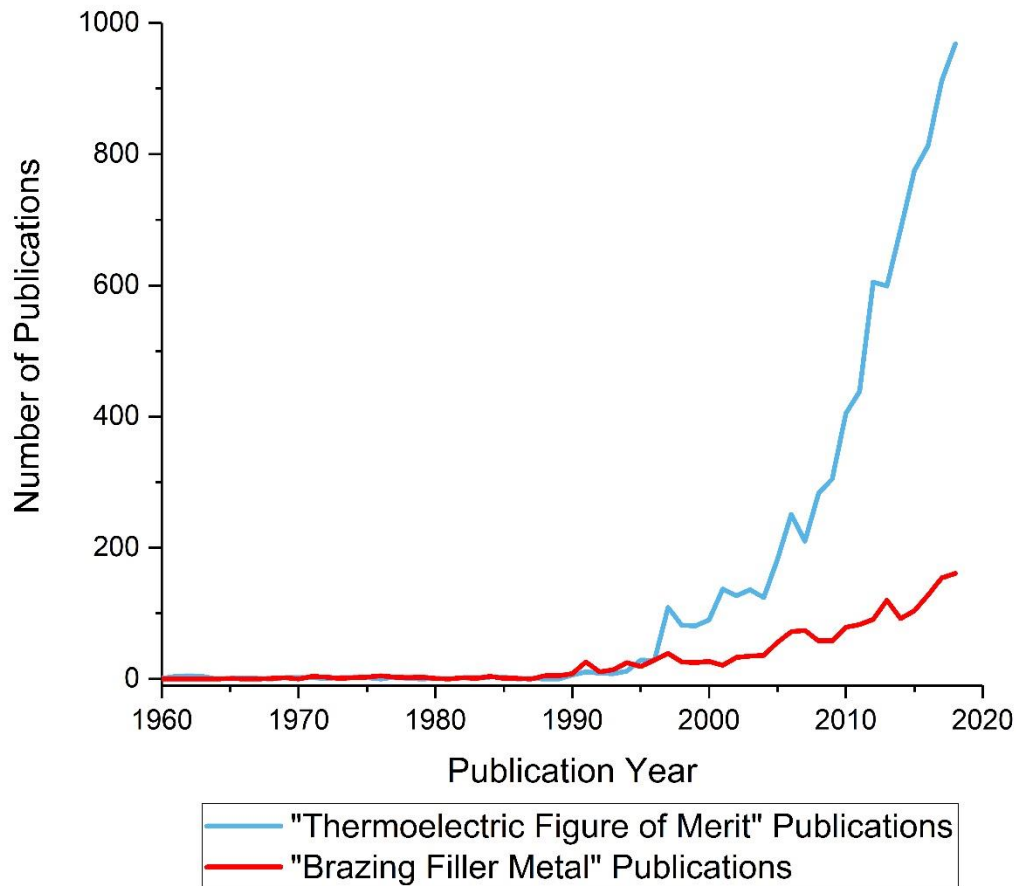


Figure 2.24: Graph displaying publication data for articles within the Clarivate Analytics "Web of Science" core collection for the period 1960-2018 using the search terms "Thermoelectric Figure Of Merit" and "Brazing Filler Metals" Data accurate as of 19/07/2019 [126].

2.4. Summary

To conclude, it is clear that brazing is a versatile joining technique pivotal in an array of modern engineering industries; and of particular importance in high temperature electronic applications including thermoelectric generators. Many issues currently prevent the wide-scale commercial introduction of thermoelectric generators including their low conversion efficiency and problems with bonding components within the devices adequately. The recently discovered class of alloy systems known as high entropy alloys offer a plethora of properties considered attractive for brazing filler metals and as such are proposed in this work as a potential source of replacement filler metals for those currently used to join components within thermoelectric devices. The following chapters aim to assess why currently used filler metals cause issues in thermoelectric devices and attempt to find innovative new filler metals to function as brazing filler metals in this application whilst comparatively assessing their performance to current filler metals.

2.5. References

- [1] American Welding Society. *Brazing Handbook*. 4th ed. Miami, Florida: American welding Society; 1991.
- [2] Roberts P. *Industrial Brazing Practice*. 2nd ed. Boca Raton, Florida: CRC press; 2013.
- [3] Bobzin K, Öte M, Wiesner S. Investigation of the effect of contaminations and cleaning processes on the surface properties of brazing surfaces. *IOP Conf. Ser. Mater. Sci. Eng.* [Internet]. 2017;181:012027. Available from: <http://stacks.iop.org/1757-899X/181/i=1/a=012027?key=crossref.05d4535700ba1c8abb1c215e3e146ce9>.
- [4] Zhao H, Elbel S, Hrnjak P. Influence of Surface Morphology on Wetting Behaviors of Liquid Metal during Aluminum Heat Exchanger Fabrication. *Int. Refrig. Air Cond. Conf.* 2014;1:1–8.
- [5] Zaharinie T, Huda Z, Izuan MF, et al. Development of optimum process parameters and a study of the effects of surface roughness on brazing of copper. *Appl. Surf. Sci.* [Internet]. 2015;331:127–131. Available from: <http://dx.doi.org/10.1016/j.apsusc.2015.01.078>.
- [6] Elsayy AH, Fahmy MF. Brazing of Si₃N₄ ceramic to copper. *J. Mater. Process. Technol.* 1998;77:266–272.
- [7] Hitchcock SJ, Carroll NT, Nicholas MG. Some effects of substrate roughness on wettability. *J. Mater. Sci.* 1981;16:714–732.
- [8] Sobczak N, Pietrzak K. Effect of Substrate Preparation on Wetting in Al-TiN System. *Trans. JWRI.* 2001. p. 173–178.
- [9] Chen YY, Duh JG, Chiou BS. Effect of substrate surface roughness on the wettability of Sn-Bi solders. *J. Mater. Sci. Mater. Electron.* 2000;11:279–283.
- [10] Hong IT, Koo CH. The study of vacuum-furnace brazing of C103 and Ti-6Al-4V using Ti-15Cu-15Ni foil. *Mater. Chem. Phys.* 2005;94:131–140.
- [11] Taranets NY, Jones H. The influence of surface roughness and pre-oxidation state on the wettability of aluminium nitride by commercial brazes. *J. Mater. Sci.* 2004;39:5727–5734.
- [12] Li Y, Liu W, Sekulic DP, et al. Reactive wetting of AgCuTi filler metal on the TiAl-based alloy substrate. *Appl. Surf. Sci.* [Internet]. 2012;259:343–348. Available from: <http://dx.doi.org/10.1016/j.apsusc.2012.07.047>.
- [13] Schwartz MM. *Brazing*. 2nd ed. ASM International; 2003.
- [14] Way M, Willingham J, Goodall R. Brazing filler metals. *Int. Mater. Rev.* [Internet]. 2019;0:1–29. Available from: <https://doi.org/10.1080/09506608.2019.1613311>.
- [15] Oberg E, Jones FD, Horton HL, et al. *Machinery's Handbook 26: A Reference Book for the Mechanical Engineer, Designer, Manufacturing Engineer, Draftsman, Toolmaker, and Machinist*. 26th ed. Industrial Press, Inc.; 2000.
- [16] Callister WD, Rethwisch DG. *Material Science and Engineering*. 8th Editio. John Wiley & Sons; 2010.
- [17] Kinloch AJ. The science of adhesion - Part 1 Surface and interfacia/ aspects. *J.*

- Mater. Sci. 1980;15:2141–2166.
- [18] Schwartz MM. Brazing [Internet]. 2nd Editio. ASM International; 2003. Available from: https://books.google.co.uk/books/about/Brazing_2nd_Edition.html?id=XSGaKuYQLjIC.
- [19] Shafrin EG, Zisman WA. Constitutive Relations in the Wetting of Low Energy Surfaces and the Theory of the Retraction Method of Preparing Monolayers. *J. Phys. Chem.* 1960;64:519–524.
- [20] Kogi S, Kajiura T, Hanada Y, et al. Wetting and spreading behavior of molten brazing filler metallic alloys on metallic substrate. *IOP Conf. Ser. Mater. Sci. Eng.* [Internet]. 2014;61:012017. Available from: <http://stacks.iop.org/1757-899X/61/i=1/a=012017?key=crossref.38a17edbe9e59c34f843e27efc47ce30>.
- [21] Kozlova O, Voytovych R, Devismes MF, et al. Wetting and brazing of stainless steels by copper-silver eutectic. *Mater. Sci. Eng. A.* 2008;495:96–101.
- [22] Voytovych R, Robaut F, Eustathopoulos N. The relation between wetting and interfacial chemistry in the CuAgTi/alumina system. *Acta Mater.* 2006;54:2205–2214.
- [23] CHEN S, LI L qun, CHEN Y bin, et al. Si diffusion behavior during laser welding-brazing of Al alloy and Ti alloy with Al-12Si filler wire. *Trans. Nonferrous Met. Soc. China (English Ed. [Internet].* 2010;20:64–70. Available from: [http://dx.doi.org/10.1016/S1003-6326\(09\)60098-4](http://dx.doi.org/10.1016/S1003-6326(09)60098-4).
- [24] Cao R, Sun JH, Chen JH. Mechanisms of joining aluminium A6061-T6 and titanium Ti-6Al-4V alloys by cold metal transfer technology. *Sci. Technol. Weld. Join.* [Internet]. 2013;18:425–433. Available from: <http://www.tandfonline.com/doi/full/10.1179/1362171813Y.0000000118>.
- [25] Chen WB. Microstructure and mechanical properties of tungsten inert gas welded-brazed Al/Ti joints. *Sci. Technol. Weld. Join.* [Internet]. 2016;21:547–554. Available from: <http://www.tandfonline.com/doi/full/10.1179/1362171814Y.0000000208>.
- [26] Zhu Z, Lee KY, Wang X. Ultrasonic welding of dissimilar metals, AA6061 and Ti6Al4V. *Int. J. Adv. Manuf. Technol.* 2012;59:569–574.
- [27] Winiowski A, Majewski D. Braze welding TIG of titanium and aluminium alloy type Al - Mg. *Arch. Metall. Mater.* 2016;61:133–142.
- [28] Takemoto T, Okamoto I. Intermetallic compounds formed during brazing of titanium with aluminium filler metals. *J. Mater. Sci.* 1988;23:1301–1308.
- [29] Zhong Z, Hou G, Zhu Z, et al. Microstructure and mechanical strength of SiC joints brazed with Cr₃C₂ particulate reinforced Ag-Cu-Ti brazing alloy. *Ceram. Int.* [Internet]. 2018;44:11862–11868. Available from: <https://doi.org/10.1016/j.ceramint.2018.04.002>.
- [30] Valenza F, Gambaro S, Muolo ML, et al. Wetting of SiC by Al-Ti alloys and joining by in-situ formation of interfacial Ti₃Si(Al)C₂. *J. Eur. Ceram. Soc.* 2018;38:3727–3734.
- [31] Tian WB, Sun ZM, Zhang P, et al. Brazing of silicon carbide ceramics with Ni-Si-Ti powder mixtures. *J. Aust. Ceram. Soc.* [Internet]. 2017;53:511–516. Available from: <http://link.springer.com/10.1007/s41779-017-0061-7>.

- [32] Chen J, Mu D, Liao X, et al. Interfacial microstructure and mechanical properties of synthetic diamond brazed by Ni-Cr-P filler alloy. *Int. J. Refract. Met. Hard Mater.* [Internet]. 2018;74:52–60. Available from: <https://doi.org/10.1016/j.ijrmhm.2018.03.005>.
- [33] Mukhopadhyay P, Raghava Simhan D, Ghosh A. Challenges in brazing large synthetic diamond grit by Ni-based filler alloy. *J. Mater. Process. Technol.* [Internet]. 2017;250:390–400. Available from: <http://dx.doi.org/10.1016/j.jmatprotec.2017.08.004>.
- [34] Mukhopadhyay P, Ghosh A. On bond wear, grit-alloy interfacial chemistry and joint strength of synthetic diamond brazed with Ni-Cr-B-Si-Fe and Ti activated Ag-Cu filler alloys. *Int. J. Refract. Met. Hard Mater.* [Internet]. 2018;72:236–243. Available from: <https://doi.org/10.1016/j.ijrmhm.2017.12.033>.
- [35] Zhang X, Liu G, Tao J, et al. Brazing of WC-8Co cemented carbide to steel using Cu-Ni-Al alloys as filler metal: Microstructures and joint mechanical behavior. *J. Mater. Sci. Technol.* [Internet]. 2018;34:1180–1188. Available from: <https://doi.org/10.1016/j.jmst.2017.11.040>.
- [36] Amirnasiri A, Parvin N, haghshenas MS. Dissimilar Diffusion Brazing of WC-Co to AISI 4145 steel using RBCuZn-D interlayer. *J. Manuf. Process.* [Internet]. 2017;28:82–93. Available from: <http://dx.doi.org/10.1016/j.jmapro.2017.06.001>.
- [37] ISO/TC 44. Brazing — Filler metals (ISO 17672:2016) [Internet]. 3rd ed. British Standards Institution; 2016. Available from: <https://www.iso.org/obp/ui/#iso:std:iso:3677:ed-3:v1:en>.
- [38] Shapiro AE. Brazing of Conventional Titanium Alloys. *ASM Handbook, New Ed.* 2016;6:36–43.
- [39] Specification for filler metals AWS A5.8M/A5.M-2011.
- [40] Batista RI. Brazing of Refractory and Reactive Metals. *ASM Handbook, Vol. 6 Welding, Brazing, Solder.* 1993;6:941–947.
- [41] Davis JR, editor. *Copper and Copper alloys.* ASM International; 2001.
- [42] European Commission. Commission regulation (EU) No 494/2011. *Off. J. Eur. Union* [Internet]. 2011;2–5. Available from: <http://www.tandfonline.com/doi/full/10.1179/1432891714Z.000000000992>.
- [43] Okulov I V., Pauly S, Kühn U, et al. Effect of microstructure on the mechanical properties of as-cast Ti-Nb-Al-Cu-Ni alloys for biomedical application. *Mater. Sci. Eng. C* [Internet]. 2013;33:4795–4801. Available from: <http://dx.doi.org/10.1016/j.msec.2013.07.042>.
- [44] Burghardt I, Lüthen F, Prinz C, et al. A dual function of copper in designing regenerative implants. *Biomaterials* [Internet]. 2015;44:36–44. Available from: <http://dx.doi.org/10.1016/j.biomaterials.2014.12.022>.
- [45] Guo W, Wang T, Lin T, et al. Bismuth borate zinc glass braze for bonding sapphire in air. *Mater. Charact.* [Internet]. 2018;137:67–76. Available from: <https://doi.org/10.1016/j.matchar.2018.01.002>.
- [46] Inoue A. Stabilization of Metallic Supercooled Liquid. *Acta Mater.* 2000;48:279–306.

- [47] Kim J, Lee T. Brazing method to join a novel Cu₅₄Ni₆Zr₂₂Ti₁₈ bulk metallic glass to carbon steel. *Sci. Technol. Weld. Join.* [Internet]. 2017;22:714–718. Available from: <https://doi.org/10.1080/13621718.2017.1306155>.
- [48] Jin W, He Y, Yang J, et al. Novel joining of dissimilar materials in the graphite/Hastelloy N alloy system using pure Au doped with Si particles. *Mater. Charact.* [Internet]. 2017;131:388–398. Available from: <http://dx.doi.org/10.1016/j.matchar.2017.07.034>.
- [49] Ivannikov AA, Kalin BA, Sevryukov ON, et al. Study of the Ni–Si–Be system as a base to create boron-free brazing filler metals. *Sci. Technol. Weld. Join.* 2018;23:187–197.
- [50] Bo C, Wen-Jiang Z, Wen-Wen L, et al. Joining of SiO₂/SiO₂ composite to Ti-6Al-4V using Ag-Cu-In-Ti brazing fillers, the joint strengths, and microstructures. *Weld. World* [Internet]. 2017;61:833–837. Available from: <http://link.springer.com/10.1007/s40194-017-0450-0>.
- [51] de Prado J, Sánchez M, Utrilla M V., et al. Study of a novel brazing process for W-W joints in fusion applications. *Mater. Des.* [Internet]. 2016;112:117–123. Available from: <http://dx.doi.org/10.1016/j.matdes.2016.09.067>.
- [52] Zhou Y, Hu A. From Microjoining to Nanojoining. *Open Surf. Sci. J.* [Internet]. 2010;3:32–41. Available from: <http://benthamopen.com/ABSTRACT/TOSURSJ-3-32>.
- [53] Cui Q, Gao F, Mukherjee S, et al. Joining and Interconnect formation of nanowires and carbon nanotubes for nanoelectronics and nanosystems. *Small.* 2009;5:1246–1257.
- [54] Wu W, Hu A, Li X, et al. Vacuum brazing of carbon nanotube bundles. *Mater. Lett.* 2008;62:4486–4488.
- [55] Li Q, Chen Z, Zhang X, et al. Au₈₀Sn₂₀-based targeted noncontact nanosoldering with low power consumption. *Opt. Lett.* 2018;43:4989–4992.
- [56] Liu L, Huang H, Hu A, et al. Nano Brazing of Pt-Ag Nanoparticles under Femtosecond Laser Irradiation. *Nano-Micro Lett.* [Internet]. 2013;5:88–92. Available from: <http://link.springer.com/10.1007/BF03353734>.
- [57] Mafuné F, Kohno J ya, Takeda Y, et al. Nanoscale soldering of metal nanoparticles for construction of higher-order structures. *J. Am. Chem. Soc.* 2003;125:1686–1687.
- [58] Zhou Q, Bieler TR, Nicholas JD. Transient porous nickel interlayers for improved silver-based Solid Oxide Fuel Cell brazes. *Acta Mater.* [Internet]. 2018;148:156–162. Available from: <https://doi.org/10.1016/j.actamat.2018.01.061>.
- [59] Chao CL, Chu CL, Fuh YK, et al. Interfacial characterization of nickel-yttria-stabilized zirconia cermet anode/interconnect joints with Ag-Pd-Ga active filler for use in solid-oxide fuel cells. *Int. J. Hydrogen Energy* [Internet]. 2015;40:1523–1533. Available from: <http://dx.doi.org/10.1016/j.ijhydene.2014.11.028>.
- [60] Kim JY, Hardy JS, Weil KS. Novel Metal-Ceramic Joining for Planar SOFCs. *J. Electrochem. Soc.* [Internet]. 2005;152:J52. Available from: <http://jes.ecsdl.org/cgi/doi/10.1149/1.1896530>.
- [61] Phongpreecha T, Nicholas JD, Bieler TR, et al. Computational design of metal

- oxides to enhance the wetting and adhesion of silver-based brazes on yttria-stabilized-zirconia. *Acta Mater.* [Internet]. 2018;152:229–238. Available from: <https://doi.org/10.1016/j.actamat.2018.04.024>.
- [62] Chen H, Li L, Kemps R, et al. Reactive air brazing for sealing mixed ionic electronic conducting hollow fibre membranes. *Acta Mater.* [Internet]. 2015;88:74–82. Available from: <http://dx.doi.org/10.1016/j.actamat.2015.01.029>.
- [63] Kiebach R, Engelbrecht K, Grahl-Madsen L, et al. An Ag based brazing system with a tunable thermal expansion for the use as sealant for solid oxide cells. *J. Power Sources* [Internet]. 2016;315:339–350. Available from: <http://dx.doi.org/10.1016/j.jpowsour.2016.03.030>.
- [64] Yang J, Xue S, Sekulic DP. An Impact of Zirconium Doping of Zn-Al Braze on the Aluminum-Stainless Steel Joint. *J. Mater. Eng. Perform.* 2017;26:358–365.
- [65] Su Y, Hua X, Wu Y. Influence of alloy elements on microstructure and mechanical property of aluminum-steel lap joint made by gas metal arc welding. *J. Mater. Process. Technol.* [Internet]. 2014;214:750–755. Available from: <http://dx.doi.org/10.1016/j.jmatprotec.2013.11.022>.
- [66] Song JL, Lin SB, Yang CL, et al. Effects of Si additions on intermetallic compound layer of aluminum-steel TIG welding-brazing joint. *J. Alloys Compd.* 2009;488:217–222.
- [67] Singh J, Arora KS, Shukla DK. Dissimilar MIG-CMT weld-brazing of aluminium to steel: A review. *J. Alloys Compd.* [Internet]. 2019;783:753–764. Available from: <https://doi.org/10.1016/j.jallcom.2018.12.336>.
- [68] Bridges D, Zhang S, Lang S, et al. Laser brazing of a nickel-based superalloy using a Ni-Mn-Fe-Co-Cu high entropy alloy filler metal. *Mater. Lett.* [Internet]. 2018;215:11–14. Available from: <https://doi.org/10.1016/j.matlet.2017.12.003>.
- [69] Snell R. The Development of Novel Silver Brazing Alloys. PhD Thesis. 2017.
- [70] Tillmann W, Ulitzka T, Wojarski L, et al. Brazing of high temperature materials using melting range optimized filler metals based on the high-entropy alloy CoCrCuFeNi. 2019.
- [71] Hardwick L, Rodgers P, Pickering EJ, et al. Development of novel nickel-based brazing alloys, utilising alternative melting point depressants and high entropy alloy concepts. *Brazing, High Temp. Brazing Diffus. Bond. LÖT* 2019. 2019. p. 7–17.
- [72] Sun R, Zhu Y, Guo W, et al. Microstructural evolution and thermal stress relaxation of Al₂O₃/1Cr18Ni9Ti brazed joints with nickel foam. *Vacuum.* 2018;148:18–26.
- [73] ZHANG J, GU J, LI L, et al. Bonding of Alumina and Metal Using Bulk Metallic Glass Forming Alloy. *Int. J. Mod. Phys. B.* 2009;23:1306–1312.
- [74] Cantor B, Chang ITH, Knight P, et al. Microstructural development in equiatomic multicomponent alloys. *Mater. Sci. Eng. A* [Internet]. 2004;375–377:213–218. Available from: <http://dx.doi.org/10.1016/j.msea.2003.10.257>.
- [75] Yeh JW, Chen SK, Lin SJ, et al. Nanostructured high-entropy alloys with multiple principal elements: Novel alloy design concepts and outcomes. *Adv. Eng. Mater.* 2004;6:299-303+274.

- [76] Yao MJ, Pradeep KG, Tasan CC, et al. A novel, single phase, non-equiatomic FeMnNiCoCr high-entropy alloy with exceptional phase stability and tensile ductility. *Scr. Mater.* [Internet]. 2014;72–73:5–8. Available from: <http://dx.doi.org/10.1016/j.scriptamat.2013.09.030>.
- [77] Pickering EJ, Jones NG. High-entropy alloys: a critical assessment of their founding principles and future prospects. *Int. Mater. Rev.* [Internet]. 2016;61:183–202. Available from: <http://www.tandfonline.com/doi/full/10.1080/09506608.2016.1180020>.
- [78] Zhang Y, Zhou YJ, Lin JP, et al. Solid-solution phase formation rules for multi-component alloys. *Adv. Eng. Mater.* 2008;10:534–538.
- [79] Otto F, Yang Y, Bei H, et al. Relative effects of enthalpy and entropy on the phase stability of equiatomic high-entropy alloys. *Acta Mater.* [Internet]. 2013;61:2628–2638. Available from: <http://dx.doi.org/10.1016/j.actamat.2013.01.042>.
- [80] Senkov ON, Wilks GB, Scott JM, et al. Mechanical properties of Nb₂₅Mo₂₅Ta₂₅W₂₅ and V₂₀Nb₂₀Mo₂₀Ta₂₀W₂₀ refractory high entropy alloys. *Intermetallics* [Internet]. 2011;19:698–706. Available from: <http://dx.doi.org/10.1016/j.intermet.2011.01.004>.
- [81] Stepanov ND, Yurchenko NY, Sokolovsky VS, et al. An AlNbTiVZr_{0.5} high-entropy alloy combining high specific strength and good ductility. *Mater. Lett.* 2015;161:136–139.
- [82] Tsau CH, Lee PY. Microstructures of Al_{7.5}Cr_{22.5}Fe₃₅Mn₂₀Ni₁₅ high-entropy alloy and its polarization behaviors in sulfuric acid, nitric acid and hydrochloric acid solutions. *Entropy.* 2016;18.
- [83] Yeh JW. Recent progress in high-entropy alloys. *Ann. Chim. Sci. des Mater.* 2006;31:633–648.
- [84] Cantor B. Multicomponent and high entropy alloys. *Entropy.* 2014;16:4749–4768.
- [85] Mizutani U. Hume-Rothery Rules for Structurally Complex Alloy Phases [Internet]. 1st Editio. Boca Raton: CRC Press; 2016. Available from: <https://books.google.co.uk/books?id=DBmO34STnZwC>.
- [86] Zhang Y, Zhou YJ. Solid Solution Formation Criteria for High Entropy Alloys. *Mater. Sci. Forum* [Internet]. 2007;561–565:1337–1339. Available from: <http://www.scientific.net/MSF.561-565.1337>.
- [87] Takeuchi A, Amiya K, Wada T, et al. Entropies in alloy design for high-entropy and bulk glassy alloys. *Entropy.* 2013;15:3810–3821.
- [88] Guo S, Liu CT. Phase stability in high entropy alloys: Formation of solid-solution phase or amorphous phase. *Prog. Nat. Sci. Mater. Int.* [Internet]. 2011;21:433–446. Available from: [http://dx.doi.org/10.1016/S1002-0071\(12\)60080-X](http://dx.doi.org/10.1016/S1002-0071(12)60080-X).
- [89] Zhang Y, Zuo TT, Tang Z, et al. Microstructures and properties of high-entropy alloys. *Prog. Mater. Sci.* [Internet]. 2014;61:1–93. Available from: <http://dx.doi.org/10.1016/j.pmatsci.2013.10.001>.
- [90] Poletti MG, Battezzati L. Electronic and thermodynamic criteria for the occurrence of high entropy alloys in metallic systems. *Acta Mater.* [Internet]. 2014;75:297–306. Available from: <http://dx.doi.org/10.1016/j.actamat.2014.04.033>.

- [91] Guo S, Ng C, Lu J, et al. Effect of valence electron concentration on stability of fcc or bcc phase in high entropy alloys. *J. Appl. Phys.* 2011;109.
- [92] Miracle DB, Senkov ON. A critical review of high entropy alloys and related concepts. *Acta Mater.* [Internet]. 2017;122:448–511. Available from: <http://dx.doi.org/10.1016/j.actamat.2016.08.081>.
- [93] Tsai MH, Tsai KY, Tsai CW, et al. Criterion for sigma phase formation in Cr- and V-Containing high-entropy alloys. *Mater. Res. Lett.* 2013;1:207–212.
- [94] Yang X, Zhang Y. Prediction of high-entropy stabilized solid-solution in multi-component alloys. *Mater. Chem. Phys.* [Internet]. 2012;132:233–238. Available from: <http://dx.doi.org/10.1016/j.matchemphys.2011.11.021>.
- [95] Zhang Y, Peng W jie. Microstructural control and properties optimization of high-entrop alloys. *Procedia Eng.* [Internet]. 2012;27:1169–1178. Available from: <http://www.sciencedirect.com/science/article/pii/S1877705811064058>.
- [96] Wang Z, Guo S, Liu CT. Phase Selection in High-Entropy Alloys: From Nonequilibrium to Equilibrium. *Jom.* 2014;66:1966–1972.
- [97] Senkov ON, Miracle DB. A new thermodynamic parameter to predict formation of solid solution or intermetallic phases in high entropy alloys. *J. Alloys Compd.* 2016;658:603–607.
- [98] Zhang X, Zhao L-D. Thermoelectric materials: Energy conversion between heat and electricity. *J. Mater.* [Internet]. 2015;1:92–105. Available from: <http://linkinghub.elsevier.com/retrieve/pii/S2352847815000258>.
- [99] Armi EL, Kirkpatrick CG. Temperature Control by Means of the Peltier Effect. *Aircr. Eng. Aerosp. Technol.* [Internet]. 1961;33:12–14. Available from: <http://www.emeraldinsight.com/doi/10.1108/eb033354>.
- [100] Seebeck Effect [Internet]. *Encycl. Br.* 1998 [cited 2017 May 31]. Available from: <https://www.britannica.com/science/Seebeck-effect>.
- [101] Northwestern University. Thermoelectrics: The Science of Thermoelectric Materials [Internet]. [cited 2016 Dec 7]. Available from: <http://thermoelectrics.matsci.northwestern.edu/thermoelectrics/#top>.
- [102] II-VI_Marlow. TG12-8-01LS POWER GENERATORS [Internet]. [cited 2017 Jun 22]. p. 1–2. Available from: <http://www.marlow.com/power-generators/standard-generators/tg12-8-01ls.html>.
- [103] Rowe DM, Min G. Evaluation of thermoelectric modules for power generation. *J. Power Sources* [Internet]. 1998;73:193–198. Available from: <http://linkinghub.elsevier.com/retrieve/pii/S0378775397028012>.
- [104] Snyder GJ, Toberer ES. Complex thermoelectric materials. *Nat. Mater.* 2008;7:105–114.
- [105] Champier D. Thermoelectric generators: A review of applications. *Energy Convers. Manag.* [Internet]. 2017;140:167–181. Available from: <http://dx.doi.org/10.1016/j.enconman.2017.02.070>.
- [106] Cotaldo R, Bennett G. U.S. Space Radioisotope Power Systems and Applications: Past, Present and Future. *Appl. Phys. Sci.* [Internet]. 2011; Available from: <http://www.intechopen.com/books/radioisotopes-applications-in-physical->

sciences/u-s-space-radioisotope-power-systems-and-applications-past-present-and-future.

- [107] NASA. NASA: A Legacy of Exploration [Internet]. [cited 2016 Dec 9]. Available from: <https://solarsystem.nasa.gov/rps/rtg.cfm>.
- [108] Yang L, Chen ZG, Dargusch MS, et al. High Performance Thermoelectric Materials: Progress and Their Applications. *Adv. Energy Mater.* 2018;8:1–28.
- [109] Liang X, Wang X, Shu G, et al. A review and selection of engine waste heat recovery technologies using analytic hierarchy process and grey relational analysis. *Int. J. Energy Res.* [Internet]. 2015 [cited 2017 May 31];39:453–471. Available from: <http://doi.wiley.com/10.1002/er.3242>.
- [110] Stobart RK, Wijewardane A, Allen C. The Potential for Thermo-Electric Devices in Passenger Vehicle Applications. *SAE Tech. Pap. Ser.* 2010;1.
- [111] Tan G, Shi F, Hao S, et al. Non-equilibrium processing leads to record high thermoelectric figure of merit in PbTe-SrTe. *Nat. Commun.* [Internet]. 2016;7. Available from: <https://www.nature.com/articles/ncomms12167>.
- [112] Harman TC, Walsh MP, Laforge BE, et al. Nanostructured Thermoelectric Materials. *J. Electron. Mater.* 2005;34:19–22.
- [113] Kim S, Park S, Kim S, et al. A thermoelectric generator using engine coolant for light-duty internal combustion Engine-Powered Vehicles. *J. Electron. Mater.* 2011;40:812–816.
- [114] Avaritsioti E. Environmental and Economic Benefits of Car Exhaust Heat Recovery. *Transp. Res. Procedia* [Internet]. 2016;14:1003–1012. Available from: <http://dx.doi.org/10.1016/j.trpro.2016.05.080>.
- [115] Stevens RJ, Weinstein SJ, Koppula KS. Theoretical limits of thermoelectric power generation from exhaust gases. *Appl. Energy* [Internet]. 2014;133:80–88. Available from: <http://dx.doi.org/10.1016/j.apenergy.2014.07.075>.
- [116] Chen WH, Wu PH, Wang XD, et al. Power output and efficiency of a thermoelectric generator under temperature control. *Energy Convers. Manag.* [Internet]. 2016;127:404–415. Available from: <http://dx.doi.org/10.1016/j.enconman.2016.09.039>.
- [117] Lagrandeur J. Automotive Waste Heat Conversion to Electric Power using Skutterudites, TAGS, PbTe and Bi₂Te₃. *Design.* 2006;1–27.
- [118] Mori M, Yamagami T, Sorazawa M, et al. Simulation of Fuel Economy Effectiveness of Exhaust Heat Recovery System Using Thermoelectric Generator in a Series Hybrid. *Soc. Automot. Eng. Int.* 2011;4:1268–1276.
- [119] Hussain QE, Brigham DR, Maranville CW. Thermoelectric Exhaust Heat Recovery for Hybrid Vehicles. *SAE Int. J. Engines* [Internet]. 2009;2:1132–1142. Available from: <http://dx.doi.org/10.4271/2009-01-1327>.
- [120] Espinosa N, Lazard M, Aixala L, et al. Modeling a thermoelectric generator applied to diesel automotive heat recovery. *J. Electron. Mater.* 2010;39:1446–1455.
- [121] Orr B, Akbarzadeh A, Mochizuki M, et al. A review of car waste heat recovery systems utilising thermoelectric generators and heat pipes. *Appl. Therm. Eng.* [Internet]. 2016;101:490–495. Available from:

<http://dx.doi.org/10.1016/j.applthermaleng.2015.10.081>.

- [122] Li CC, Drymiotis F, Liao LL, et al. Interfacial reactions between PbTe-based thermoelectric materials and Cu and Ag bonding materials. *J. Mater. Chem. C*. 2015;3:10590–10596.
- [123] He R, Schierning G, Nielsch K. Thermoelectric Devices: A Review of Devices, Architectures, and Contact Optimization. *Adv. Mater. Technol.* 2018;3.
- [124] Liu W, Wang H, Wang L, et al. Understanding of the contact of nanostructured thermoelectric n-type Bi₂Te_{2.7}Se_{0.3} legs for power generation applications. *J. Mater. Chem. A*. 2013;1:13093–13100.
- [125] Xia H, Chen CL, Drymiotis F, et al. Interfacial reaction between Nb foil and n-type PbTe thermoelectric materials during thermoelectric contact fabrication. *J. Electron. Mater.* 2014;43:4064–4069.
- [126] Clarivate Analytics. Web of Science [Internet]. [cited 2019 Jul 19]. Available from: <https://apps.webofknowledge.com>.

Chapter 3: Experimental Methodology

3.1. Alloy Manufacture

All alloys discussed in this thesis were produced via induction melting from raw elements with a purity of at least 99.99%. Alloy samples were manufactured in 20g ingots with constituents weighed out using a Precisa XB 120A balance to an accuracy of 0.01g. Alloy constituents copper, bismuth and aluminium were used in the form of shot or needles of metal with different combinations of shard sizes used to attain the desired weight. Nickel, zinc, gold and tin were cut to the appropriate weight from a length of wire or rod. Gallium ingots were raised above their melting temperature (29.76°C) by submerging the storage bottle in boiling water. The liquid metal was then transferred as droplets to weighing boats and allowed to cool before being weighed similarly to the shards and shot above. The aluminium, nickel, copper, zinc, gallium, tin and bismuth were sourced from Alfa Aesar, the germanium from Sigma Aldrich and the gold from Johnson Matthey.

Elements were then combined and their total weight checked and recorded before being transferred to a Plumbago (graphite-clay) crucible which had been pre-baked at 1000°C to remove any surface coatings and/or moisture. The crucible was then placed inside an Ambrell 2.2kW induction melter with an attached water cooler provided by Johnson Matthey. A layer of borax (sodium tetraborate anhydrous 99.5% ($B_4Na_2O_7$)) was placed over the elements within the crucible, covering them completely. The borax layer melted to form a glassy liquid layer at 743°C which was used to prevent oxidation of the alloy constituents during the melting and casting process and also prevent losses of metal from the crucible due to boiling (particularly for zinc which has a high vapour pressure). The crucible was heated at a slow, controlled rate over a period of around 15 minutes by adjusting the power level of the coils within the induction melter until all constituents were molten. At such a point the borax glass had also melted and formed a molten glassy layer above the elements and was ready for pouring. The alloy was then cast into a copper mould and left to cool in air. Once cool the newly manufactured alloy was removed from the copper mould and any borax glass present on the alloy surface was removed via mechanical abrasion.

3.2. Brazed Joint Manufacture

3.2.1. T-joint Manufacture

Brazing of samples utilised a torch brazing technique accomplished by hand. A small segment of each manufactured filler metal (approximating 5mm in diameter) was sectioned from the cast alloy using a hacksaw. This removed section was placed on the junction of two metal coupons (of dimensions 60mm × 30mm × 3mm) arranged in a T shape (see Figure 3.1 and Figure 3.2).

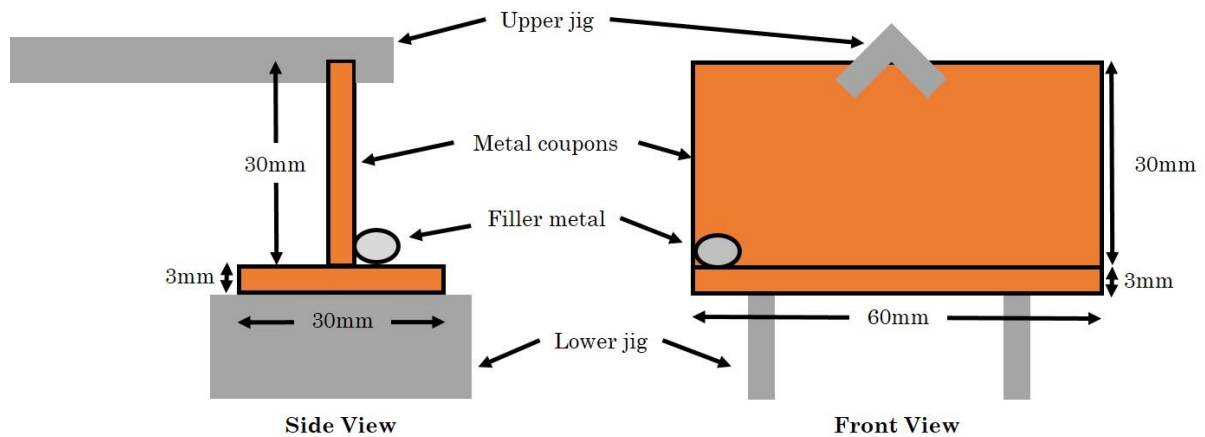


Figure 3.1: Schematic of the arrangement of metal coupons and filler metal used to trial the brazing filler metals for their brazing performance. The jigs shown were used to hold the assembly in place during brazing.

The T-shaped coupon arrangement was covered in flux paste (made by combining Johnson Matthey Tenacity™ No.14 low temperature brazing flux powder with a small quantity of water to form a paste with the approximate consistency of toothpaste) along the brazing line. The T-shaped arrangement was held in place using a custom made steel jig. The small quantity of brazing filler metal applied was also covered in flux paste.



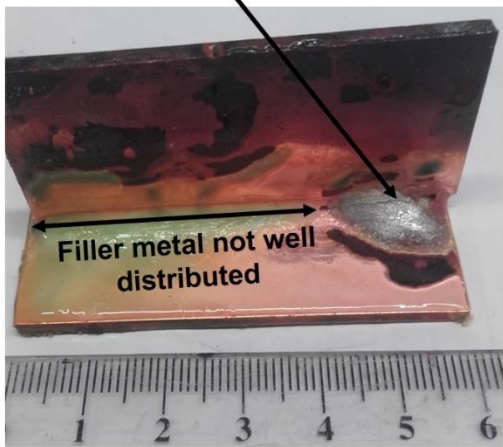
Figure 3.2: A photograph of the metal coupon arrangement held in place using jigs before the filler metal or flux paste is applied.

Once the arrangement was finalised the assembly was heated uniformly on all sides using a Bullfinch Autotorch propane torch. As the temperature rose the flux began to bubble and change colour from white to clear, forming a glassy layer on the surface of the coupons and filler metal. Conduction of heat from the heated coupons into the brazing filler metal caused it to melt as the temperature rose above the filler metal's liquidus temperature. The filler metal then began to flow along the brazing line between the two coupons. When necessary the filler metal could be encouraged along the brazing line using the heat from the torch itself as in general a filler metal will flow towards the hottest area of the joint. If the filler metal still did not flow well across the joint it could be further assisted by

angling the coupons to allow gravity to assist with flow along the brazing line or in cases of extremely poor wetting with mechanical assistance using a stainless steel rod to push the molten filler along the brazing line.

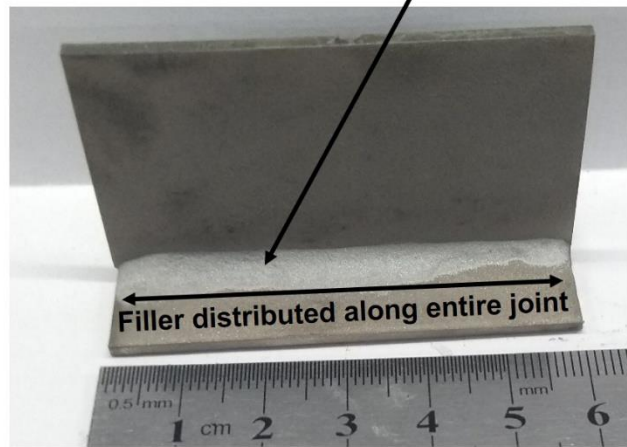
Once flow across the entire length of the brazing line was accomplished the torch was switched off and the assembly allowed to cool in air. During cooling the molten filler metal solidified and bonded the two metal coupons together. Once fully cooled the assembly was cleaned of any flux residues by grit blasting using a Guyson SF hand cabinet shot blast cabinet and the quality of the joint examined. Ideally the filler metal would be equally distributed along both sides of the joint and along the length with no obvious cracking in the filler metal present (Figure 3.3).

Visible cracking in filler metal



A poor brazed joint

No visible cracking in filler metal



A good brazed joint

Figure 3.3: Photographs illustrating the difference between a well formed brazed joint and a poor brazed joint.

3.2.2. Lap Joint Manufacture

Some brazed samples were required to be manufactured in a lap joint arrangement. Two metal coupons (of dimensions 60mm × 30mm × 3mm) were overlapped and laid on a heat resistant surface supported by a metal coupon of the same height to ensure correct alignment (Figure 3.4).

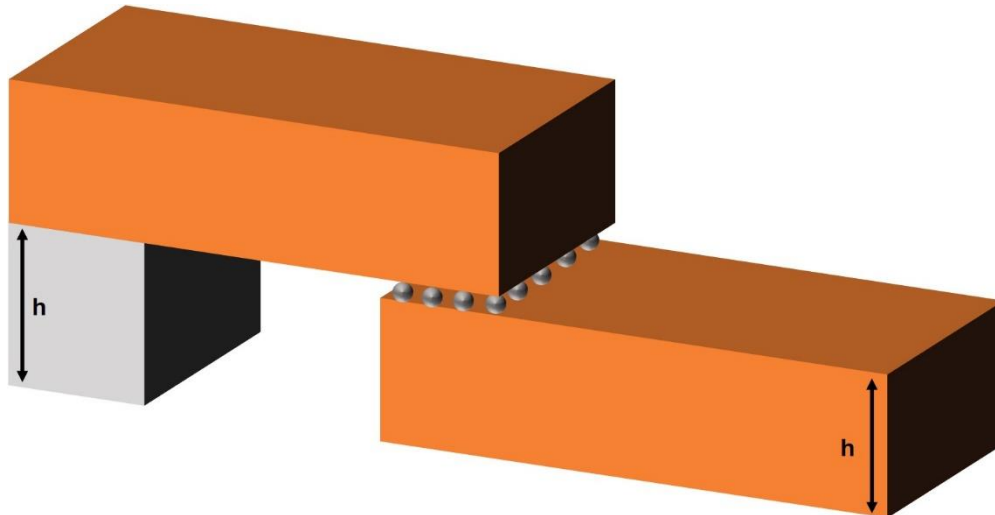


Figure 3.4: Schematic of the arrangement used to form a brazed lap joint.

Small fragments of filler metal were laid in the overlapping gap between the two coupons and flux applied both in and around the joint area. Flux paste (made by combining Johnson Matthey's Tenacity™ No.14 low temperature brazing flux powder with a small quantity of water to form a paste with the approximate consistency of toothpaste) was applied then applied to the joint area. The coupons were then uniformly heated with the same Bullfinch Autotorch propane torch as in Section 3.2.1 until the fragmented filler metal melted and flowed to fill the overlapping region and form a joint. At this point the torch was removed and the assembly left to cool. Once fully cooled the assembly was cleaned of any flux residues by grit blasting using a Guyson SF hand cabinet shot blast cabinet.

3.3. Analytical Methodology

3.3.1. Cutting, Grinding and Polishing

Metallographic preparation of samples was required in order to assess and image the structure of the filler metals prepared. Samples were sectioned to a suitable size using a Streurs Secetom-50 before being hot mounted in conductive Struers Polyfast resin using a Simplimet 1000 automatic mounting press. After mounting, samples were ground flat and polished using a Buehler Automet 250 following the grinding and polishing schedule in Table 3.1. All grinding stages were undertaken with a constant stream of water across the grinding paper to ensure removal of residue. Each polishing stage performed was completed without any water applied.

Table 3.1: Grinding and polishing schedule used to prepare samples of filler metal examined in this thesis. Schedule adapted from a standard schedule for soft alloys to suit the filler metals studied.

Stage	Surface	Load (N)	Speed (rpm)	Direction	Time (min:sec)
1	P400 grit SiC water cooled	18	201	Complimentary	Until flat
2	P600 grit SiC water cooled	18	201	Complimentary	0:30
3	P1200 grit SiC water cooled	18	201	Complimentary	0:30
4	9 μm diamond suspension	18	141	Complimentary	3:00
5	6 μm diamond suspension	18	141	Complimentary	3:00
6	3 μm diamond suspension	18	141	Complimentary	3:00
7	1 μm diamond suspension	18	141	Contra	3:00
8	Colloidal silica	18	141	Contra	2:00

After each grinding stage samples were cleaned with isopropanol and dried using hot air before being examined for scratches, after polishing was complete samples were cleaned with isopropanol again and dried with hot air before being stored in a protective plastic casing until needed for examination.

3.3.2. Compositional Verification

3.3.2.1 X-Ray Fluorescence

X-Ray Fluorescence (XRF) is a non-destructive analytical technique which was used to determine the elemental composition of filler metals produced in this work and verify that the compositions produced were as intended in the nominal compositions.

The technique works by exciting electrons in the inner shells of the elements present within the sample. The ejected electron leaves behind a hole which is rapidly filled by an outer shell electron dropping down into the lower electron shell by emitting a fluorescent X-ray (Figure 3.5).

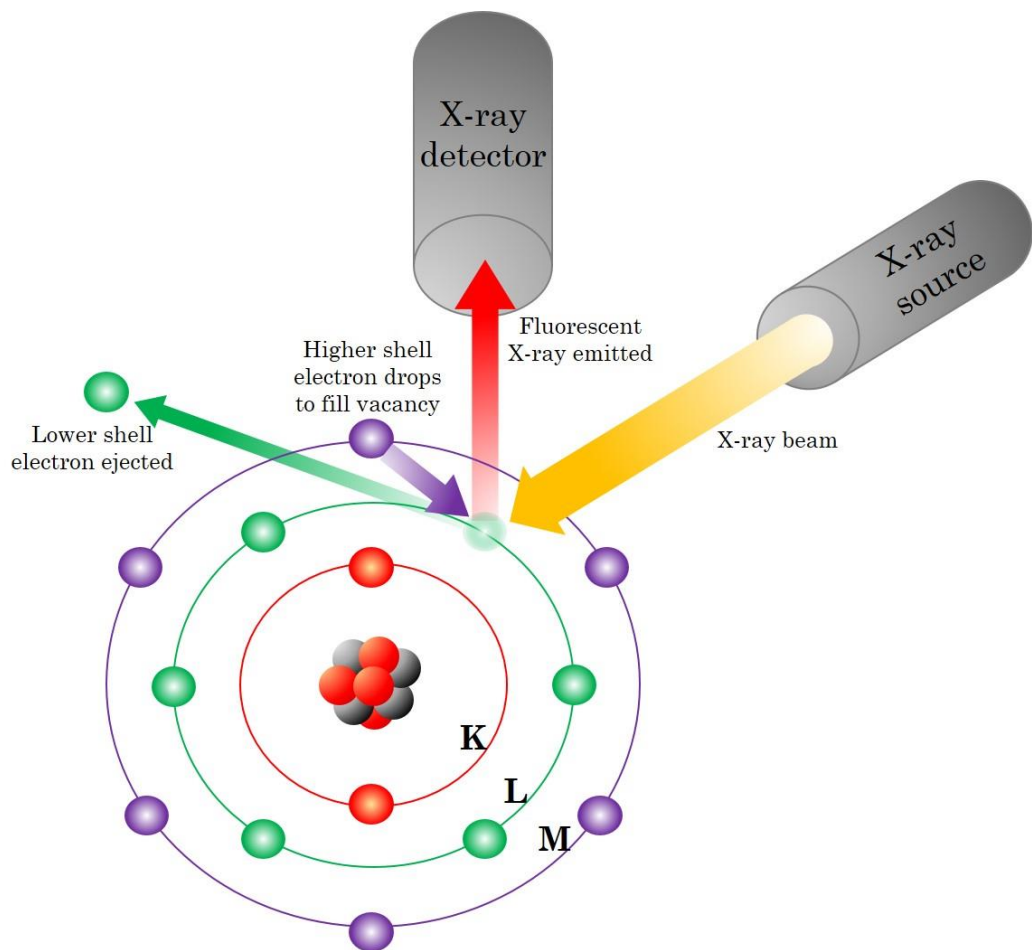


Figure 3.5: Schematic of how fluorescent X-rays are emitted by the ejection of lower shell electrons being replaced by outer shell electrons which emit an X-ray as they lower in energy.

As the energy of the fluorescent X-ray is proportional to the energy gap between the shells which the electron moved and these energy differences between shells are specific to different elements, the emitted X-rays can be identified as coming from a specific element. The intensity of the X-rays produced at each energy level may be used to quantify the amount of that element present in the sample.

XRF analysis undertaken in this work was performed on a PANalytical Zetium with a scanning time of 20 minutes. The system was run at 50kV and 30mA (I.e. 1500W).

3.3.2.2 Induction Coupled Plasma Optical Emission Spectrometry

Composition of the produced alloys was further verified by external assessment to standard ISO 17025 by a UKAS accredited laboratory. The levels of metallic elements were verified using Induction Coupled Plasma – Optical Emission Spectrometer (ICP-OES) on a Thermo ICAP instrument (6500) Additionally, impurities (nitrogen, oxygen and carbon), which could not be detected using the XRF techniques mentioned above, were analysed using LECO elemental analysers. Carbon was detected using infra-red after the sample was burnt under flux in an oxygen atmosphere. Nitrogen and oxygen were detected using inert gas fusion using a helium carrier gas. The nitrogen content was detected using thermal conductivity and the oxygen with infra-red.

3.3.3. X-Ray Diffraction

X-Ray Diffraction (XRD) is a non-destructive analytical technique used to identify the crystalline phases within a material. X-rays are a part of the electromagnetic spectrum with a wavelength (λ) of $0.01\text{\AA} < \lambda < 100\text{\AA}$; which is of the order of the inter-atomic distances in crystals. X-rays are generated by an X-ray tube which accelerates electrons at a metal target (in the analysis used in this thesis the target is copper), the collision between the accelerated electrons and the target material produces heat and X-rays of a characteristic wavelength depending on the metal target (in the case of copper this is $\lambda = 1.5419\text{\AA}$). These X-rays travel towards the sample in the diffractometer where the regular spacing between planes of atoms present in a phase act as a diffraction grating for these incident X-rays causing constructive or destructive interference depending on the angle of incidence of the x-rays on the sample. By changing the incident angle and recording the X-ray intensity at each angle a diffraction pattern of recorded X-ray intensities at different angles can be produced. The diffraction pattern produced can be used to identify phases and compounds present within the sample by matching to known diffraction patterns within a software database.

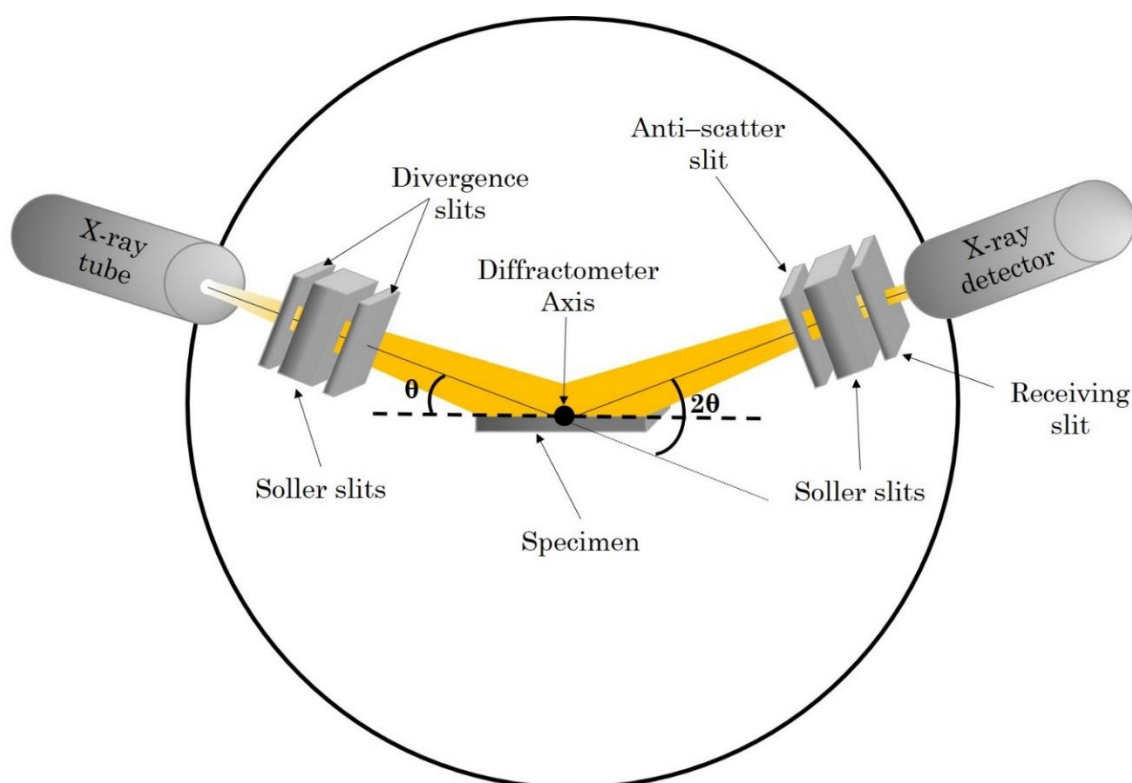


Figure 3.6: Schematic of the Bragg-Brentano geometry used inside the Bruker D2 phaser.

In this work samples were mounted in Apiezon putty in the centre of a Poly-methyl—methacrylate (PMMA) specimen dish. The samples were pressed into the Apiezon putty using a glass slide to ensure a flat surface parallel to the top of the sample holder for accurate angle measurements.

Diffraction data was collected on a Bruker D2 Phaser using 2.5° Soller slits. Copper K_{α} radiation with a wavelength of 1.5419Å (4 d.p) was used to scan the sample and a divergence slit of 0.6mm was used in focusing the beam onto the sample. Two nickel filters (2.5Ni and 0.5Ni) were used to suppress >99.99% of the K_{β} radiation (Figure 3.6). Each sample was scanned using a dwell time of 0.4 seconds per step over 3472 steps in the angular range of 10° to 80° giving a total scan time of approximately 25 minutes.

3.4. Microscopy

3.4.1. Optical Microscopy

All optical images taken in this work were taken on a Nikon Eclipse microscope in the magnification range 5× to 100×. Exposure time was 1/8th of a second with the white balance set to 2500K unless otherwise stated.

3.4.2. Scanning Electron Microscopy (SEM)

Higher resolution images of samples manufactured throughout this work are taken on an FEI Inspect F50 Scanning Electron Microscope (SEM) equipped with a Field Emission Gun (FEG) using both Secondary Electron (SE) and Back Scattered Electron (BSE) imaging. An accelerating voltage of 20kV was used for imaging with a spot size of 4.0.

SE images are highly topographically sensitive and are suitable for high resolution imaging of sample surfaces; they are predominately used for microstructural observations in this work. The FEI Inspect F50 is equipped with an Everhart-Thornley detector (ETD) for secondary electron imaging.

BSE images are formed from back scattered electrons emitted from the sample and come from a much larger interaction volume than secondary electrons. As larger atoms scatter electrons much more strongly than lighter atoms, BSE images are sensitive to the atomic number of atoms. This imaging type is hence useful for distinguishing phases and is primarily used in this work for the imaging of interfaces between filler metal and substrate as well as examining the number of phases present in each sample, in conjunction with EDX.

3.4.3. Electron Dispersive X-Ray Spectroscopy (EDX)

A final analytical technique used throughout this work is Energy Dispersive X-ray spectroscopy (EDX). EDX uses similar principles to XRF described above, with characteristic X-rays caused by electron transitions from higher shells to fill a hole created in a lower shell being detected. Again, the detected X-rays are of a specific energy which can be related to a specific transition (e.g. from the L to the K shell in a copper atom) and thus the elements present can be identified. Observation of the intensity of X-rays at each energy level can be used to quantify the amount of each element present at different points within a sample. The three principal ways in which EDX was used in this study are outlined below.

3.4.3.1 EDX point scans

EDX point scans were used to identify the composition of phases within a sample. A phase was identified by contrast in a BSE image and then targeted for EDX analysis. The EDX analysis would then produce a spectrum for the phase in question and provide a quantitative result for the elements present within that phase in order to assist with phase identification. An example EDX point scan spectrum can be seen in Figure 3.7.

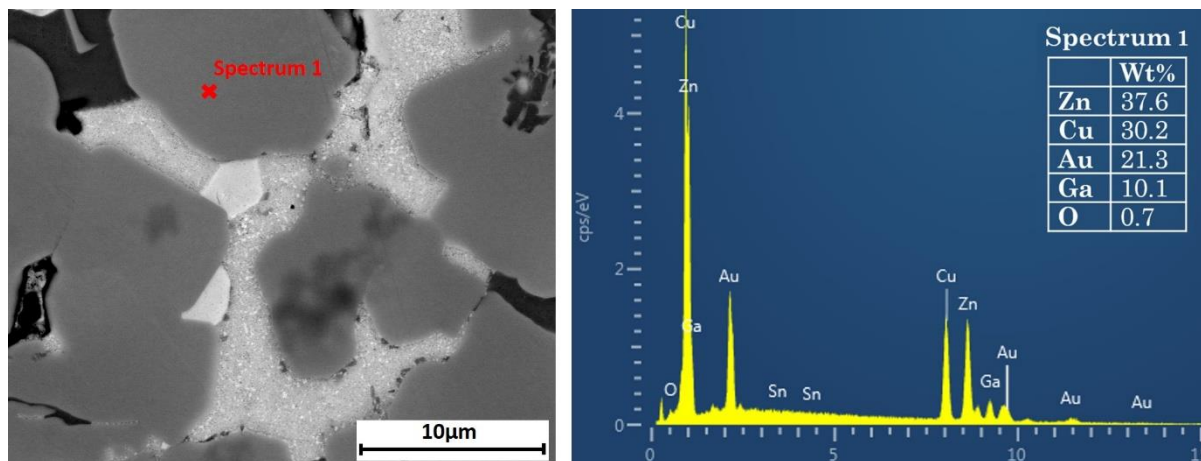


Figure 3.7: BSE image of alloy D with point scan location marked. Right: EDX point scan generated spectrum for Phase 1 of alloy D.

3.4.3.2 EDX line scans

EDX line scans are the type of EDX analysis most commonly used in this work. EDX line scans are used to measure the relative concentration of elements along an arbitrary line drawn across a sample to assess how elemental composition varies with that distance. In this work EDX line scans were predominately used to assess the diffusion profiles of elements at interfaces between filler metal and substrates; for example, to assess the depth within a substrate which a constituent element of a filler metal will diffuse after being subject to a standard brazing cycle. The end application for filler metals developed in this work requires that diffusion be limited to a certain depth (within a diffusion barrier 10 μm thick) so as not to contaminate any thermoelectric components that are being joined. EDX line scans could be used to measure the depth each constituent element within the filler metal diffused to assess whether the diffusion distance was less than the 10 μm required. An example EDX linescan taken across the interface between brazing filler metal Ag-155 [1] and a nickel plate is shown in Figure 3.8 showing how element concentration varies across the interface. The diffusion depth can be determined by recording the length along the line at which the concentration of an element begins to fall and length along the line at which the concentration of an element levels out again at a lower value.

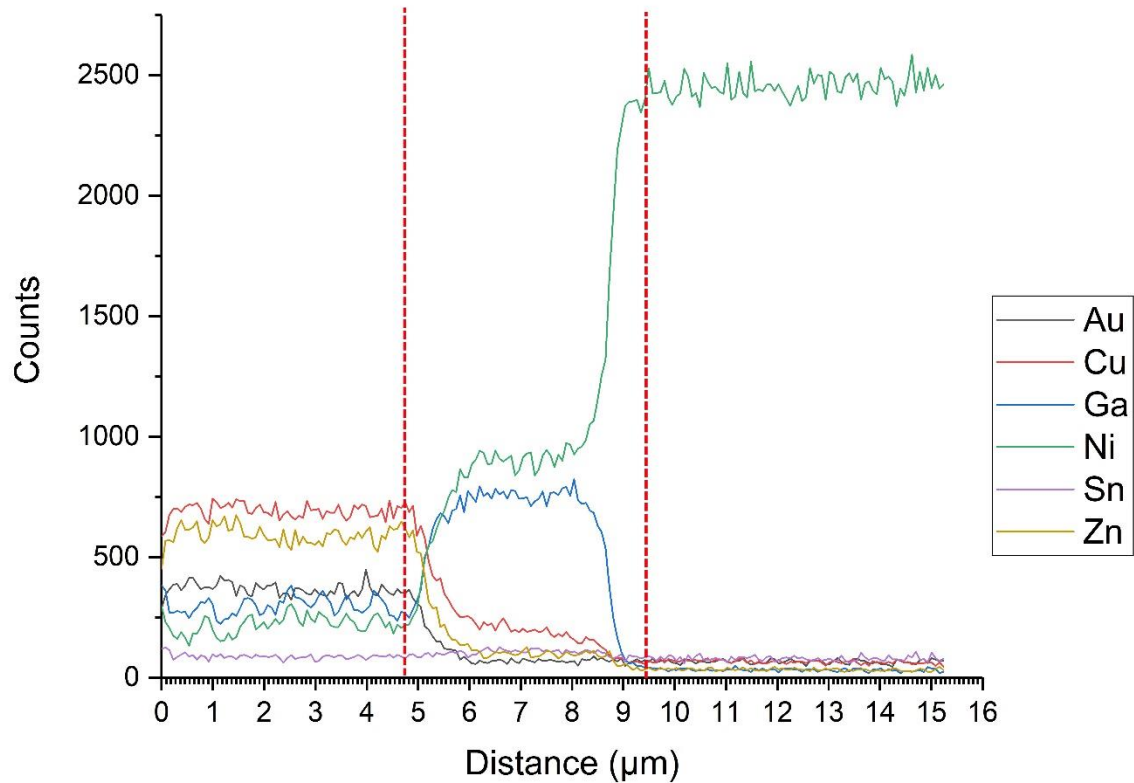


Figure 3.8: EDX line scan across an interface between brazing filler metal (alloy D) and nickel plate. The size of the diffusion zone is marked by the red dotted lines.

3.4.3.3 EDX maps

The third and final use of EDX analysis within this work is in the generation of EDX maps. EDX mapping essentially records EDX spectra at multiple points within an area and converts these into an intensity value for each element present at each point thus giving a 2D colour map representing the spatial distribution of elements within a sample. This offers advantages over simple BSE images of an area which can only provide contrast depending on the average Z-number of a phase and not say precisely which elements are present. This is demonstrated in Figure 3.9 below, where the BSE image of the area highlights different phases via the Z contrast but the EDX map is required to know element distribution within the observed phases.

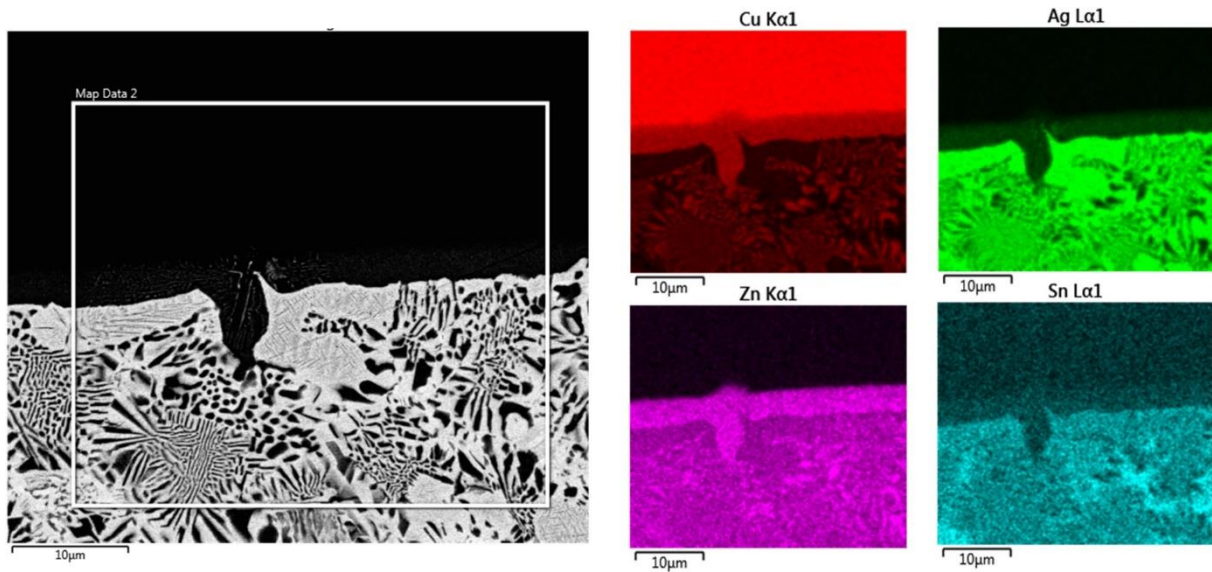


Figure 3.9: Left: BSE image of an interface between brazing filler metal Ag-155 (bottom) and copper (top). Right: EDX maps of the same interface: Top left: copper, Top right: silver, Bottom left: zinc, Bottom right: tin. The BSE image highlights the different phases but EDX maps are required to give elemental distribution.

3.5. Differential Scanning Calorimetry

One of the stated requirements for alloys developed in this project was to have a melting temperature within a specific range (550°C-620°C). To assess the melting temperature of filler metals Differential Scanning Calorimetry (DSC) was performed on all developed alloys.

Differential Scanning Calorimetry is a thermal analysis technique in which a sample and a reference material (in this case an empty alumina crucible) are heated over the temperature range of interest at the same rate and the difference in heat required to raise the temperature of both samples is recorded. Physical transformations occurring in the sample can be detected when more or less heat is needed to flow into the sample (when compared to the reference) in order to raise the temperature by the same amount. As an example, when a sample melts, more heat will be required in order to raise the temperature of the sample when compared to the reference. This latent heat is needed for the endothermic phase transition from solid to liquid requiring absorption of extra heat.

The instrument used to carry out DSC experiments throughout this work is a Netzsch STA 449 F3 'Jupiter'. Samples were tested in alumina crucibles with alumina lids over the temperature range of 25°C - 800°C. Both sample and reference were heated at a rate of 10°C min⁻¹ under a protective atmosphere of nitrogen (N₂) at a flow rate of 50ml min⁻¹.

3.6. Wetting Experiments

Wetting experiments conducted for this thesis were carried out by the author, using equipment at the Royal School of Mines in Imperial College London. Samples of filler metal were ground into $2\text{mm} \times 2\text{mm} \times 2\text{mm}$ cubes and placed on a copper substrate of known (varying) surface roughness. Wetting assessments were made using standard filler metals (conforming to Ag-155 in ISO17672:2016 [1]) on substrates of varying roughness in Chapter 4 and using various filler metals developed in this study in Chapter 6.

3.6.1. Surface Roughness Characterisation

Copper substrates were prepared by grinding as-cut copper coupons ($20\text{mm} \times 20\text{mm} \times 2\text{mm}$ in dimensions, O.F.H.C purity) using silicon carbide grinding paper in a single direction until no scratches in other directions could be observed to ensure the correct roughness had been achieved across the entire sample. Then samples were ground for 1 minute in all directions using a circular motion to remove any influence of surface lay on the flow of filler metal. Surface roughness of the samples was measured using a Veeco Dektak 150. The stylus used had a $12.5\mu\text{m}$ radius tip with an applied load of 3.00mg and was scanned across a length of $300\mu\text{m}$ for each of the 3 measurements taken per sample. The duration of each scan was 60 seconds and a total of 18,000 points were sampled along the $300\mu\text{m}$ length giving a resolution of $0.017\mu\text{m}$ per sampling point. Measurements were taken 3 times at angles 120° from each other (as shown in Figure 3.10) to ensure that the surface had a similar structure in all directions and averaged to give a single roughness value for the surface. The results of the 3 measurements were averaged and this average used as the R_a for the surface.

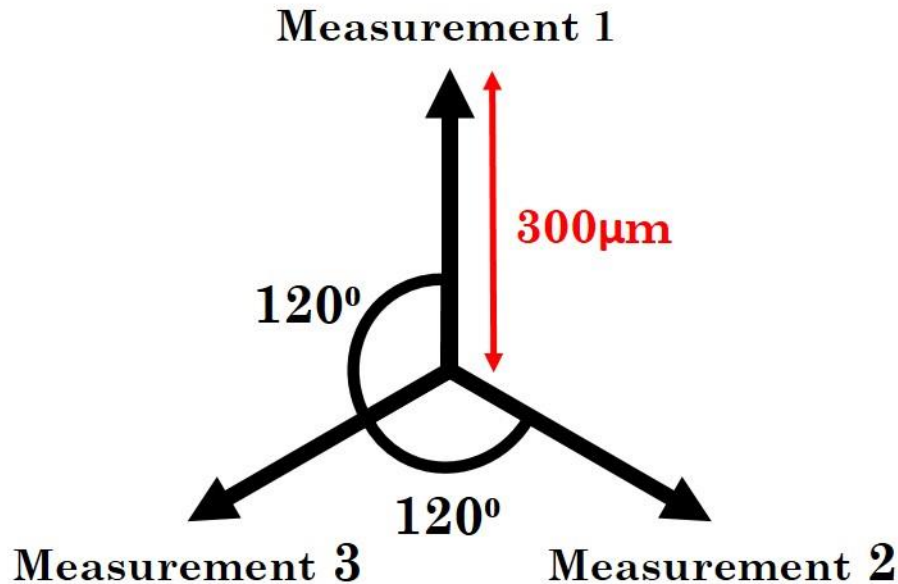


Figure 3.10: Diagram of the lines of measurement for finding the roughness of copper substrates used in wetting trials.

3.6.2. Modified Sessile-Drop Experiments

Copper substrates were placed on a specially manufactured stainless steel sample holder and a 2mm side length cube of filler metal placed in the centre of the substrate (Figure 3.11). The stainless steel holder is an 80mm elevated platform with a 20mm × 20mm square in the centre. The area around the square is milled out to catch excess filler metal should any overflow the substrates placed onto the holder.

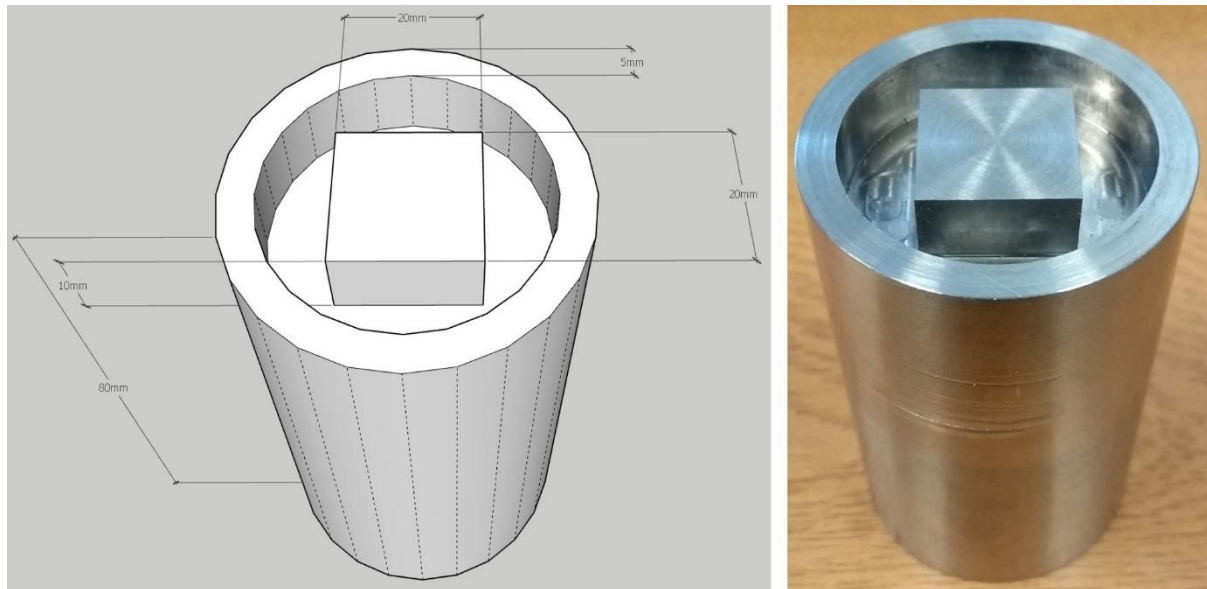


Figure 3.11: The custom stainless steel sample holder used to hold samples in the wetting trials. (Left) the CAD drawing used to manufacture the platform. (Right) The sample holder prior to use.

The samples were then loaded into a Thermal Technology LLC model 1160-2560-12 furnace which was filled with an atmosphere comprising of 90% Ar and 10% H₂. An ImagingSource DMK 23GP031 camera taking photos at 25 frames per second was set up to take images at 1 second intervals of the filler metal and substrate within the furnace. The temperature of the furnace was then raised according to the heating schedule depicted in Figure 3.12 from room temperature to 800°C at 20°C per minute from room temperature to 500°C and then 5°C per minute from 500°C until 800°C. Once 800°C was reached the sample was held at a steady temperature for 15 minutes before being furnace cooled to room temperature at a rate of approximately 20°C per minute. During the heating cycle from 500°C onwards photographs were taken by the camera of the sample at 1 second intervals and these images were analysed by the software “Drop_angle” (Developed at the Berkeley National Lab in November 2002 by Laurent Gremilard with the help of Nicole Rauch and Eduardo Saiz – version 7.5.45 [2]) to extract contact angle information.

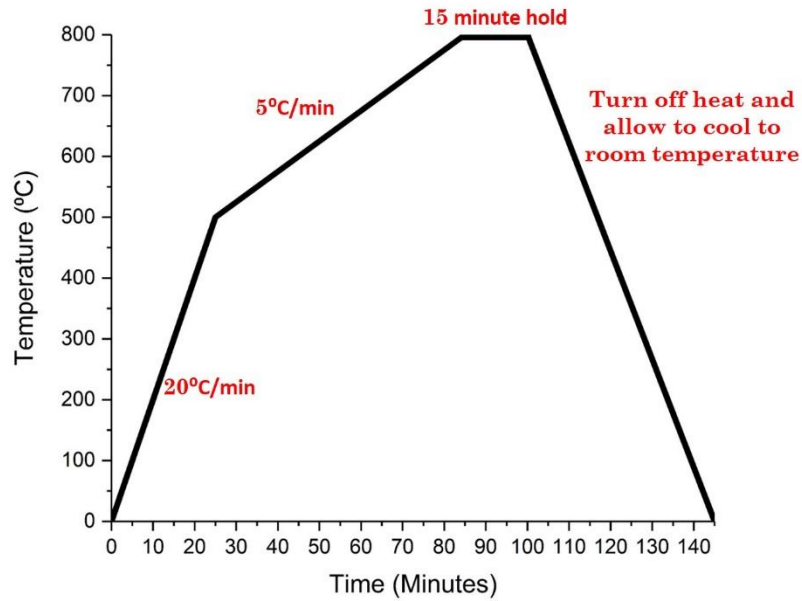


Figure 3.12: Heating schedule used to raise filler metal cubes temperature within the furnace during wetting experiments.

3.7. Mechanical Testing

Mechanical testing of brazed samples was used to assess strength of brazed joints; particularly in a comparative capacity. Samples were produced according to the dimensions in Figure 3.13 in two variants. Samples to be subject to thermal cycling before mechanical assessment were formed of copper joined to nickel whereas samples for room temperature assessment of brazed joint strength were formed from nickel joined to nickel.

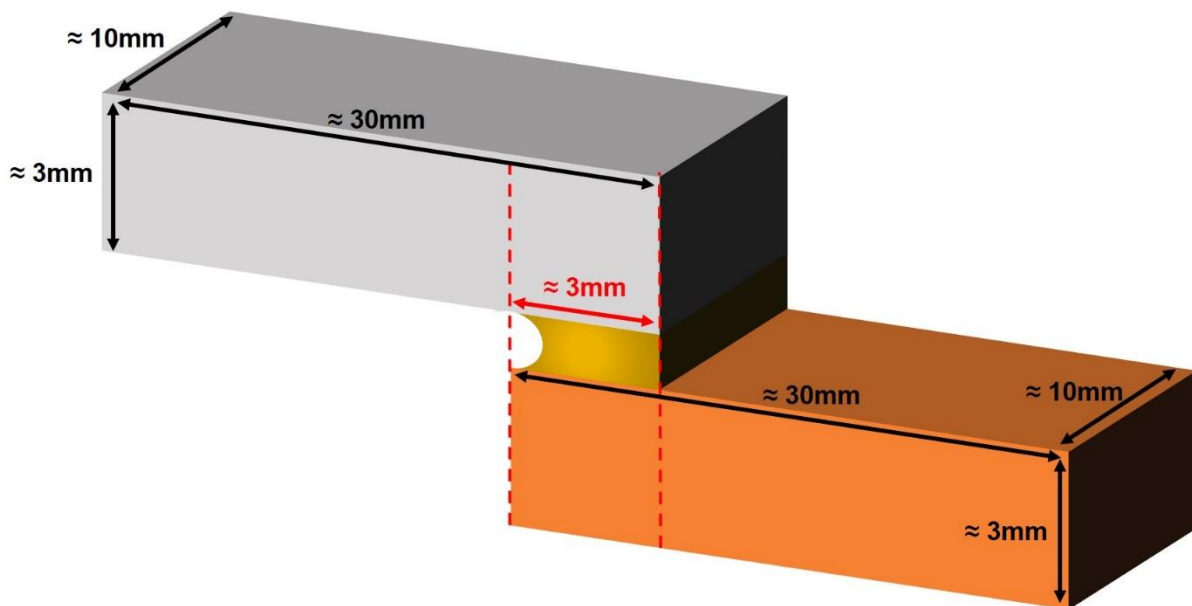


Figure 3.13: Approximate dimensions of specimens used for tensile testing. Samples formed of copper joined to nickel were subject to thermal cycling prior to testing.

Both variants were mechanically assessed identically. Samples were loaded into a Zwick/Roell Z050 tensile tester with a 50kN load cell and 20kN tensile testing grips attached. The brazed joint to be tested was held equidistant between the two grips and parallel to the axis of tension so as to load the brazed joint in shear. The sample was tested using crosshead position movement of 1mm min^{-1} until the sample failed. Load-strain data was captured at intervals of $10\mu\text{m}$ crosshead movement during the testing.

3.8. Thermal Cycling

Thermal cycling was used in this study to assess the impact that repeated heating and cooling would have on brazed joints between dissimilar materials in this study. Brazed samples were produced between pieces of copper and pieces of nickel of approximate dimensions $30\text{mm} \times 10\text{mm} \times 3\text{mm}$ using the hand torch brazing procedure described in Section 3.2.2. The overlap length on the brazed joints was made equal to the thickness of the samples ($\approx 3\text{mm}$).

30 samples were produced, 15 joined with an industrially available filler metal conforming to ISO17672:2016 Ag-155 and 15 joined with a filler metal developed in this study (alloy D). Once all samples had been produced an Elite Thermal System BCF11/18 furnace with a 2.0kVA rating was raised to 625°C under an air atmosphere. 6 samples (3 each of joints with Ag-155 and alloy D) were placed to one side and designated as samples which had received 0 cycles. The remaining 24 of the 30 samples were arranged on a ceramic plate along with a dummy sample with an attached thermocouple used to record sample temperature. The ceramic plate with all remaining samples on was placed into the furnace and the temperature of the thermocouple monitored. When the thermocouple read that sample temperature had reached 575°C the ceramic plate was removed from the furnace and all samples (including the dummy sample with mounted thermocouple) were transferred to a separate ceramic plate to cool with the thermocouple temperature monitored to assess sample temperature. Once the thermocouple read that the sample temperature had dropped to 50°C the samples were placed back on the original ceramic plate and reloaded into the furnace. This constituted a single cycle. This process was repeated 50 times. 6 samples (3 joined with Ag-155 and 3 with alloy D) were removed after 10 cycles, a further 6 were removed after 20 cycles, a further 6 after 30 cycles and the final 6 after 50 cycles. Any samples breakages during the thermal cycling were recorded along with the cycle number at which the sample broke.

3.9. Contact Resistance Assessment

3.9.1. Sample Assembly

Contact resistance measurements were taken to examine the quality of the electrical interface formed between brazing filler metal and n-type thermoelectric components (composition $\text{CoSb}_{2.75}\text{Sn}_{0.05}\text{Te}_{0.20}$). Two variants of the thermoelectric components were used; coated and uncoated. Coated thermoelectrics had a $0.7\mu\text{m}$ layer of Ni deposited on their surface by thermal deposition. Deposition was attained via a thermal deposition process using a Wordentec EVAP300 thermal evaporator with a deposition rate of 1.6\AA s^{-1} . The growth pressure in the chamber was $2.1 \times 10^{-6}\text{mbar}$ and the nickel powder used for deposition had a purity of 99.5% with a maximum particle size of $250\mu\text{m}$. Uncoated samples were used as received.

Brazed joints were formed between two pieces of thermoelectric measuring approximately $2.5\text{mm} \times 2.5\text{mm} \times 3\text{mm}$ using a similar hand torch brazing procedure described in (Section 3.2.1). Due to the small nature of components the pieces were clamped in position during the brazing procedure as shown in Figure 3.14 to prevent slipping of layers relative to each other.

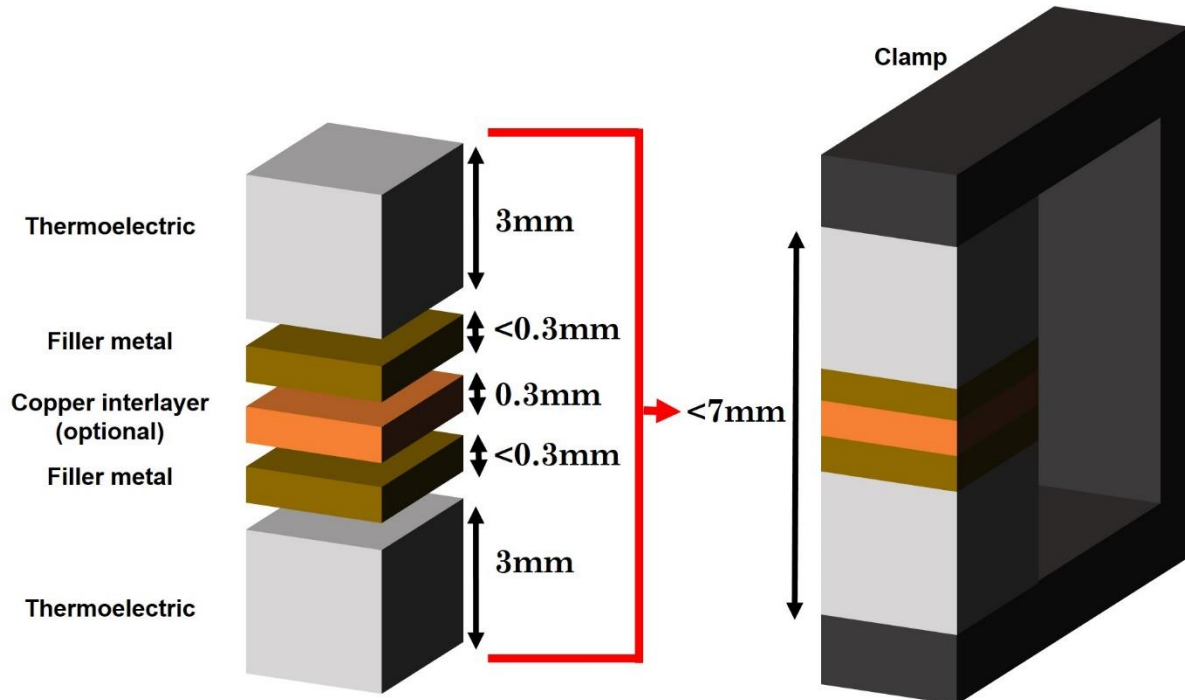


Figure 3.14: Diagram of the layers assembled to form samples for assessment of the electrical interface formed between filler metal and thermoelectric.

Samples were assembled layer by layer within the clamp including a central metal foil if required. After layers were assembled the assembly was clamped and flux paste (made by combining Johnson Matthey's Tenacity™ No.14 low temperature brazing flux powder with a small quantity of water to form a paste with the approximate consistency of toothpaste) was applied to the sides of the assembly covering all layers. The assembly was then uniformly heated with the same Bullfinch Autotorch propane torch as in Section 3.2.1 but with the flame held at a greater distance than usually used for brazing to ensure the small components did not heat too quickly and crack. Heating continued until the filler metal layer had melted and flowed to form the joint. At this point the torch was removed and the assembly left to cool. Once fully cooled the assembly was cleaned of any flux residues by hand grinding with P800 SiC grit paper due to the fragile nature of the sample.

3.9.2. Contact Resistance Assessment

Once prepared, samples are connected into a circuit with a resistance scanning probe arrangement. 3 probes are connected to the sample; 2 are fixed at either end of the sample and one is free to move laterally along the samples surface. The two fixed probes are connected to an AC voltage and an ammeter to measure current. The final moving probe is held to the sample with pressure in order to make good electrical contact and is moved perpendicular to the interfaces between filler and thermoelectric. This 3rd probe is connected via a voltmeter to the rest of the circuit. This enables collection of voltage data as a function of the probes lateral position along the sample. A circuit diagram detailing this arrangement can be seen in Figure 3.15.

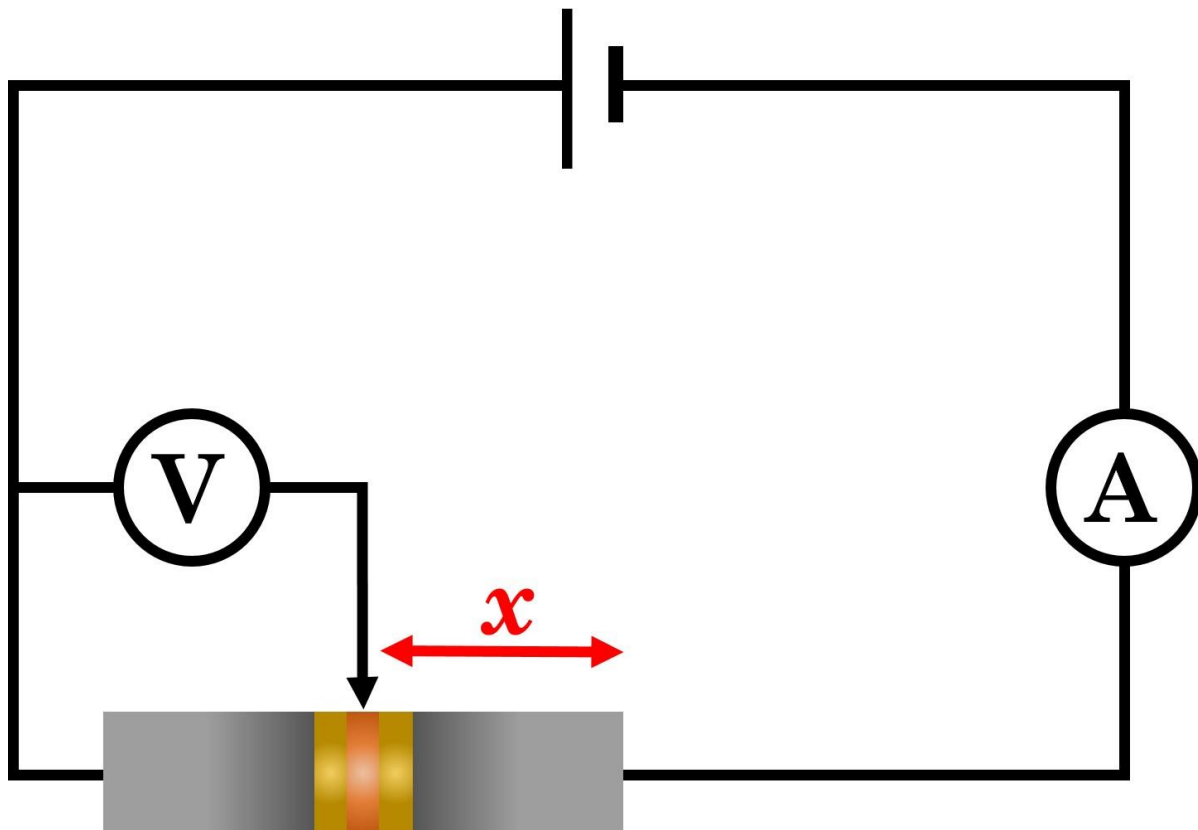


Figure 3.15: Circuit diagram of the circuit used to measure voltage as a function of position along brazed thermoelectric samples.

3.10. References

- [1] ISO/TC 44. Brazing — Filler metals (ISO 17672:2016) [Internet]. 3rd ed. British Standards Institution; 2016. Available from: <https://www.iso.org/obp/ui/#iso:std:iso:3677:ed-3:v1:en>.
- [2] Gremillard L, Rauch N, Saiz E. Drop_angle [Internet]. Berkeley: Lawrence Berkeley National Laboratory; 2002. Available from: [http://lgremillard.free.fr/Lgremillard Main En.html](http://lgremillard.free.fr/Lgremillard/Main%20En.html).

Chapter 4: Fundamental Investigations of Brazed Joints

4.1. Introduction

Brazing has been undertaken for many thousands of years, and a large portion of the knowledge base for the technique is held within an industrial setting. Many of the rules and 'best practice' for the technique are known via trial and error and practice on the most common engineering systems and often values for experimental parameters such as joint gap, surface roughness, surface cleaning and other similar design criteria, are recommended on a case by case basis depending on the joint in question, with few studies in scientific literature examining the effect of these important parameters on the joint formed.

This chapter looks to examine the influence of certain variables within the brazing process (such as surface roughness of base materials) on the formation of a brazed joint and to examine with greater scientific rigour some of the 'best practice' knowledge contained within the industrial setting in the hope of acquiring understanding which can be transferred from brazing systems involving industrially standard filler metals to systems using the filler metals developed later in this thesis.

4.2. Effect of Surface Roughness on Brazed Joint Formation

Surface roughness is one of the three components of surface texture, and is the factor most often characterised within the field of brazing (see Section 2.1.3.2). In this chapter the influence of surface roughness on the wetting angle formed between a commonly used industrial filler metal (SILVER-FLO 55™, which conforms to the compositional requirements for Ag-155 in BS EN ISO 17672-2016 [1]) and copper substrates of various roughness levels is investigated. This experiment is undertaken in order to understand if roughness could impact on the bonding between substrate and filler metals in results later in this thesis, and to recommend suitable levels of roughness to use. It is hypothesised that during this experiment it will be shown that the smoother the sample surface is the lower the final contact angle between filler metal and substrate will be. This hypothesis conflicts with the general recommendation given in many industrial handbooks for optimum surface roughness of base materials being in the range $R_a = 0.6\mu\text{m} - 1.6\mu\text{m}$ [2]. 7 copper substrates with varying surface roughness were prepared by grinding copper coupons with different grit-size silicon carbide papers before their surface roughness was measured using a Veeco Dektak 150 (as described in Section 3.6.1). The R_a value - the arithmetic average roughness of the surface - was recorded in three directions 120° apart as described in Section 3.6.1, and is displayed in Table 4.1 for each sample along with the averaged roughness of the 3 measurements. The equation used to calculate the arithmetic average can be found in Equation 4.1 where n is the number of points sampled and y_i is the profile height deviation of each point from the mean line).

$$R_a = \frac{1}{n} \sum_{i=1}^n |y_i| \quad \text{Equation 4.1}$$

Table 4.1: Table of the roughness values of copper substrates formed after grinding with different grit sized silicon carbide papers.

Grit paper size	R _a (μm)				Standard error of the mean (S _{x̄})
	Measurement 1 (0° axis)	Measurement 2 (120° axis)	Measurement 3 (240° axis)	Average	
P120	0.980	1.087	0.992	1.020	±0.034
P220	0.521	0.474	0.652	0.549	±0.053
P400	0.208	0.239	0.286	0.244	±0.023
P600	0.284	0.270	0.208	0.254	±0.023
P1200	0.142	0.153	0.171	0.155	±0.009
P2500	0.079	0.113	0.083	0.092	±0.011
P4000	0.013	0.011	0.012	0.012	±0.001

Plotting these surface roughness values against the grit size of paper used to produce them leads to the expected conclusion that as the P number of the grit paper rises (i.e. as a finer grit is used) the surface becomes smoother (Figure 4.1); but that the relationship is not linear.

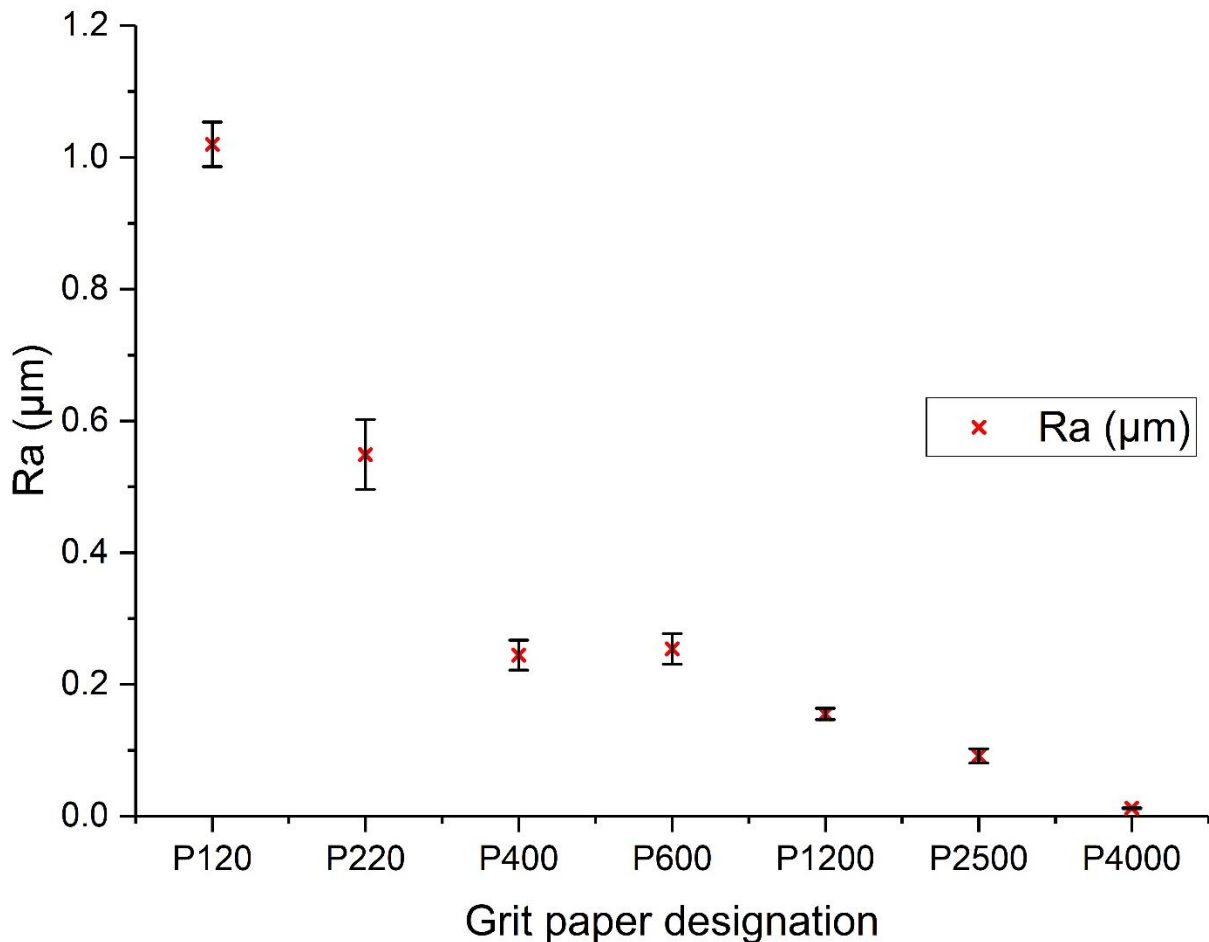


Figure 4.1: Graph depicting the arithmetic average roughness (R_a) of each copper sample compared to the grit paper designation used to produce them.

A general negative trend can be observed with a finer grit size (corresponding to a higher P number) tending to produce a smoother surface (i.e. one with a lower R_a). It should be noted that the trend would not be expected to appear linear as the P number of grit paper does not correspond directly to grit size and thus is not linear with respect to surface finish produced. Rather, it refers to the number of strands per unit length in a woven mesh the abrasive particles would pass through if sieved, and thus an inverse square relationship would be expected. It must also be noted that the average surface roughness produced by the P600 paper on the copper substrate was actually rougher than the average surface roughness produced by the P400 paper. This possibly indicates that the P400 sample was not ground with P400 paper for sufficiently long in order to adequately roughen the surface to the appropriate level. Additional evidence for the theory that the sample was not ground sufficiently comes from work by Zaharanie et al. in which a grit size 400 grinding paper gave a surface roughness value of $R_a = 0.38\mu\text{m}$ when grinding copper surfaces for wetting investigations [3], a higher value than the $R_a = 0.24\mu\text{m}$ measured for the sample ground in this study. A value of $R_a = 0.38\mu\text{m}$ would also fit better with the trend in surface roughness with respect to grit size seen in Figure 4.1.

These copper substrates with varying roughness levels were then used in wetting experiments as described in section 3.6 with the anticipation that the surface roughness would influence the contact angle between the filler metal and the substrate. A small cube of filler metal (approximately $2\text{mm} \times 2\text{mm} \times 2\text{mm}$) was placed on each surface and heated through a heating schedule up to 800°C (substantially above the melting range of the filler metal Ag-155, given as $630\text{-}660^\circ\text{C}$ [1]). Photographs of the filler metal were taken throughout the entire heating schedule however contact angles between filler and substrate could only be measured after the filler metal had become molten. Photographs were continually taken even after initial melting and contact angle formation to observe how the contact angle varied with temperature and were only stopped once no further change in filler metal contact angle could be observed whilst the experiment was taking place or the experiment heating schedule concluded. Once photographs for all substrates in question had been taken they were examined at 5 degree intervals (1 photograph per minute) using a piece of software called “Drop_angle” [4].

Each image was loaded into the “Drop_angle” software and 5 points assigned by the user to specific points on the image. The first two points were placed on the surface of the substrate, one either side of the droplet, to define the substrate surface level. This substrate level needed to be defined to allow the construction of line “CH” in Figure 4.2 which was perpendicular to the substrate surface and joined the focus of the circle to the substrate. The next 3 points were placed on the surface of the droplet of molten filler metal. As long as these 3 assigned points are not co-linear the software can calculate the circumference of a circle which passes through these 3 points. The focus of this circle is designated C and its radius designated CI (with it being axiomatic that the distance between all three points selected on the circumference designated 3, 4 and 5 in Figure 4.2 and the centre (C) being equal i.e. $C3=C4=C5=CI$). Once all 5 points had been placed the Drop_angle software can form a straight line connecting the focus of the circle it constructed between points 3, 4 and 5 (Denoted ‘C’ in Figure 4.2); and one of the two intersections between the substrate line drawn between points 1 and 2 and the circles circumference (denoted ‘T’ in Figure 4.2). Then a perpendicular bisector of the line formed between points 1 and 2 which passes through the circles focus (point C) can be constructed. Where this perpendicular bisector crosses the line formed between points 1 and 2 is

labelled as ‘H’. A right angle triangle can then be drawn between these 3 points (triangle CIH in Figure 4.2).

The wetting angle of a filler metal droplet on a surface is the angle formed between a tangent to the surface of the filler metal droplet at the point where the filler metal droplet meets the substrate it rests on. In Figure 4.2 this would be the angle between the tangent of point ‘I’ and the substrate surface.

Given that we know the length ‘CI’ (as it is the radius of the circle) and the length ‘CH’ (as this is the shortest distance between the focus of the circle and the line between points 1 and 2), the wetting angle can be calculated using trigonometry. The trigonometric expression required is given by Equation 4.2.

$$\theta = \frac{\pi}{2} \pm \arcsin \frac{CH}{CI} \quad \text{Equation 4.2}$$

If the centre of the circle (C) is higher than the intersection between the perpendicular radius and the substrate (H) then a “+” is required in Equation 4.2 to calculate the wetting angle and if the centre is below the line of the substrate, then a “-” is required in Equation 4.2. Figure 4.2 depicts the terms used in Equation 4.2 for clarity.

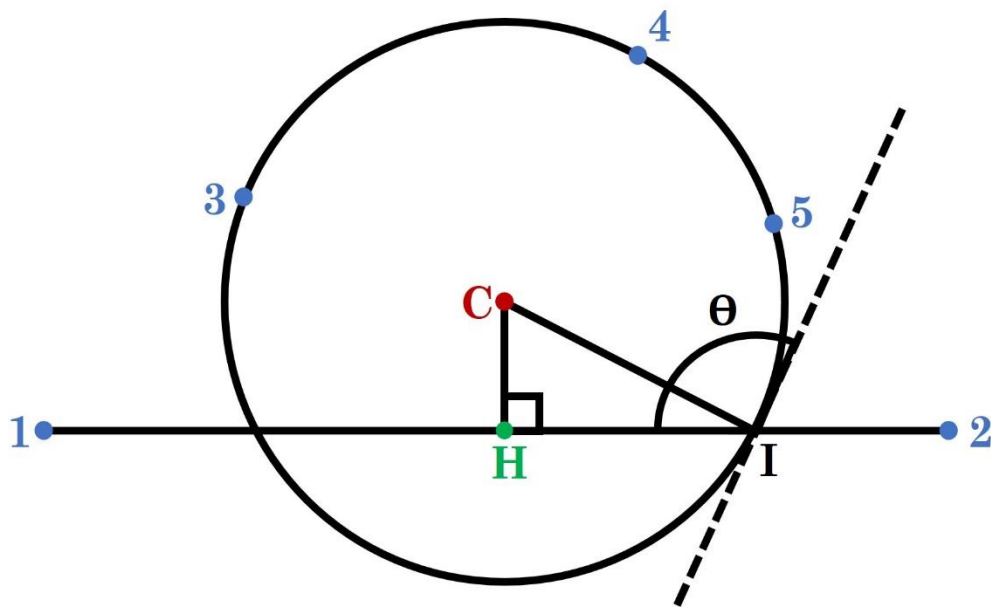


Figure 4.2: Diagram of the circle constructed by the Drop_angle software to calculate the wetting angle between droplet and substrate. The 5 points in blue are the user-designated inputs to define the substrate and the circumference of the droplet [4].

It must be stated that this approach assumes that the droplet has a circular profile and as such any droplet asymmetry caused by any of the following reasons could lead to errors in determining the true wetting angle between droplet and substrate:

- If the drop of molten filler metal is large enough then gravity may affect the sides of the drop as it is on the surface, pulling the edges down and creating a “squashed” oval shaped drop (with the long axis parallel to the substrate). This is primarily accounted for and avoided by using sufficiently small volumes of filler metal (initial size pre-melting of 2mm cubes).
- Inhomogeneity of filler metals or poor phase distribution across the filler metal sample may lead to melting of some areas of the filler metal droplet before others.

This is primarily a manufacturing issue and should be avoided by good mixing of alloys during melting and casting. As the filler metals used in this experiment were manufactured industrially by a reputable supplier and not manufactured in house it is assumed that a high standard of alloy production is followed and as such this issue is unlikely.

- Any oxide scale or compounds present on the filler metal may not melt at the same temperature as the filler metal and may leave a residue which can be seen on the camera images but are not a true reflection of the wetting properties of the filler metal. A well ground surface should be free from a majority of oxides prior to entering the furnace chamber however the accumulation of some oxide prior to insertion into the controlled atmosphere furnace is unavoidable. Where oxide presence is seen on the surface of samples after the wetting experiment caution should be taken when evaluating the wetting images to attempt to place points on the filler metal surface but not on any oxide residue.

Before using the software on unknown angles in experimental images a series of calibration images were drawn to known angles, photographed and then used in the software to assess how accurately the software measured known angles (Figure 4.3). The error between the angle recorded by the program and the known value of the constructed angles would allow a gauge of the accuracy of the program in measuring contact angle values.

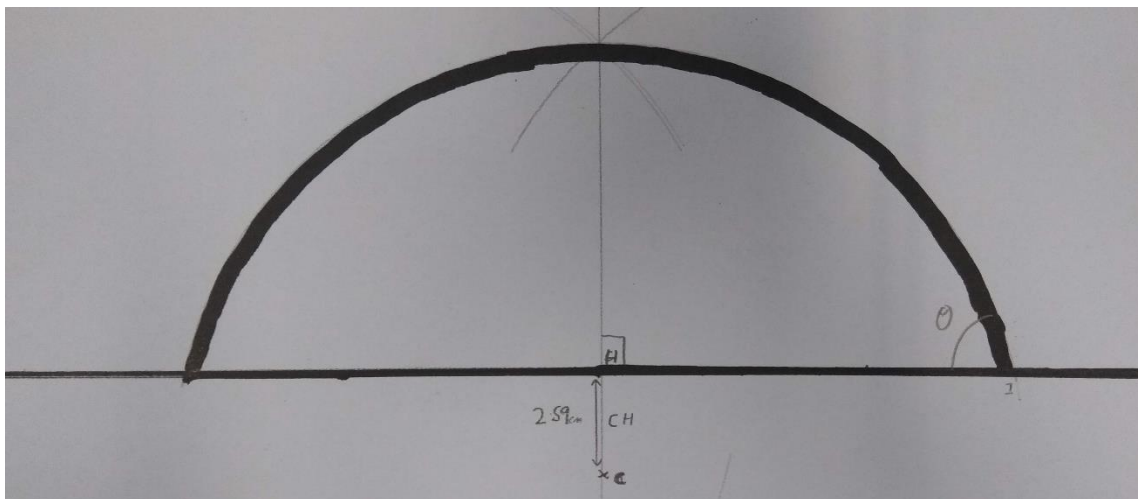


Figure 4.3: One of the calibration angles ($\theta = 75^\circ$) used to assess the accuracy of the Drop_angle software before applying it to unknown angle.

The known calibration angles and the measurements produced by the Drop_angle software are recorded in Table 4.2.

Table 4.2: Table of the Drop_angle software measurements of known angles for calibration purposes. The average angle measurement and the Root Mean Square Error assess the accuracy of the software in measuring known angles.

Angle (°)	Measurement 1 (°)	Measurement 2 (°)	Measurement 3 (°)	Average (°)	RMSE (°)
15	13.9	14.7	14.6	14.4	±0.7
30	28.3	28.4	28.4	28.4	±1.6
45	45.0	44.9	44.7	44.9	±0.2
60	58.9	58.7	59.0	58.9	±1.1
75	75.3	75.3	75.8	75.5	±0.5
90	91.5	91.0	90.8	91.1	±1.1
105	104.4	104.2	105.2	104.6	±0.6
120	119.5	118.4	118.9	118.9	±1.2
135	134.2	134.6	134.8	134.5	±0.5
150	148.3	149.2	148.8	148.8	±1.3
165	163.5	165.1	162.5	163.7	±1.7
180	178.5	180.0	176.7	178.4	±2.1

The Root Mean Squared Error of the 3 measurements taken for each known angle (given by Equation 4.3 – with the known value given by column 1 of Table 4.2 and the measured value given by columns 2,3 and 4) was calculated and is recorded in Table 4.2 showing that the software is accurate to within a maximum of ±2.1° across all angles.

$$\text{Root Mean Square Error} = \sqrt{\frac{\sum_{i=1}^n (\text{measured value} - \text{known value})^2}{n}} \quad \text{Equation 4.3}$$

The series of experimental images taken for each substrate were then examined visually to find the first one (chronologically) in which the drop was molten and could hence be analysed by the software. The time stamp associated with this image was recorded and then images were sampled at 1 minute intervals from this point. Each image was loaded into the Drop_angle software in turn and the results written to a text file which could later be extracted into an excel document. Once this had been done a temperature had to be assigned to each timestamping on the image. As the furnace used in these experiments had no method of electronically linking to the camera and laptop used to record the images to the furnace thermocouples, real time temperature data was not automatically assigned to the time stamps on the images taken. As the furnace was set to raise the temperature at a set heating rate (5°C per minute) an initial time stamp was recorded manually when the furnace temperature hit 500°C and all other temperature values were extrapolated from this. This data could then be used to compile wetting angle vs temperature data over the range of temperatures between the drop becoming observably molten (which occurred in range of 610-635°C depending on the roughness of the substrate) and either the heating cycle finishing or the drop angle remaining observably constant for several minutes. The temperature against wetting angle data for all 7 samples tested can be seen in Figure 4.4.

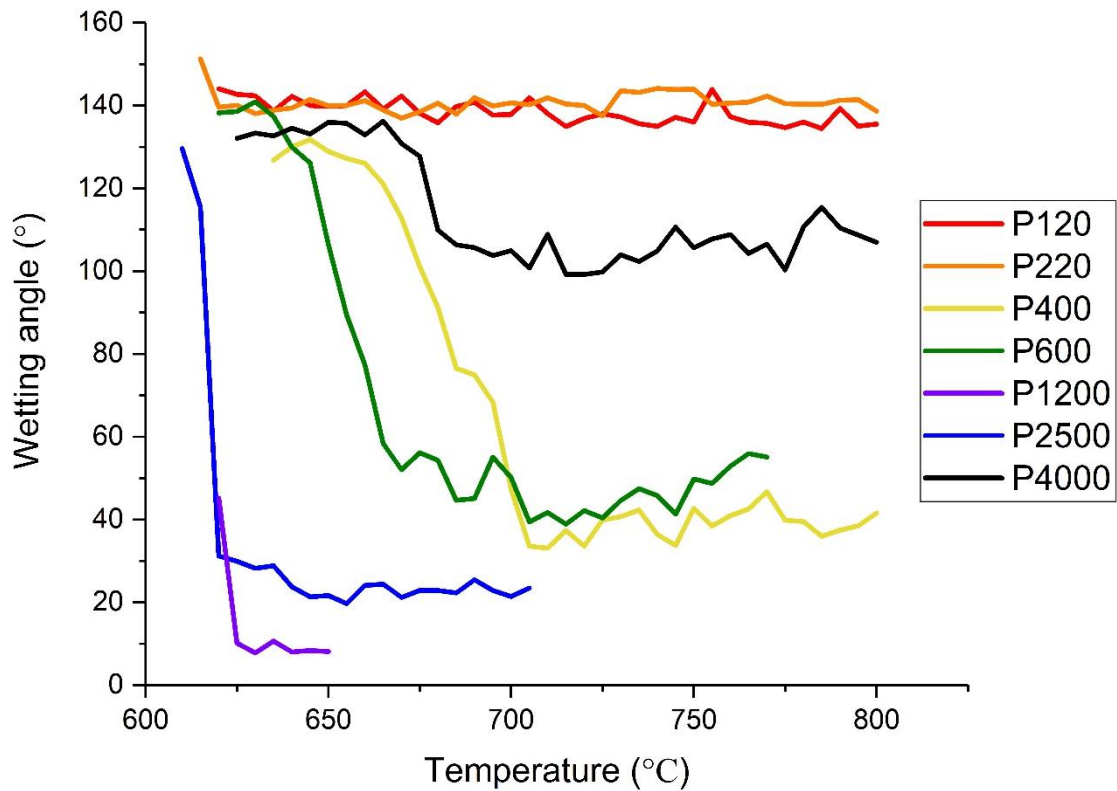


Figure 4.4: Wetting angle vs temperature plot for filler metal Ag-155 melting on substrates of different roughness.

The final average wetting angle for each sample was calculated and is recorded in Table 4.3.

Table 4.3: The average final wetting angle calculated for each copper substrate tested.

Grit paper designation	R _a (μm)	Initial contact angle (°)	Average final contact angle (°)	Standard error of the mean for averaged final contact angle (S _{x̄})
P120	1.02	144.0	138.0	±0.4
P220	0.55	151.3	140.6	±0.3
P400	0.24	126.8	39.6	±0.9
P600	0.25	138.2	47.7	±1.3
P1200	0.16	45.2	8.8	±0.5
P2500	0.09	129.6	24.2	±0.8
P4000	0.01	132.0	108.0	±0.8

As can be seen from Figure 4.4, the surface roughness of the substrate clearly has a dramatic effect on the wetting and spreading behaviour of the Ag-155 filler metal. The filler metal on the two roughest substrates (P120 and P220) showed very little variance in contact angle between its melting and the end of the temperature cycle with the filler metal samples placed on both substrates forming a ball and maintaining a high contact angle of around 140° (138.0 ± 0.4° and 140.6 ± 0.3° respectively) for the entirety of the experiment.

Samples of intermediate roughness (P400 and P600) demonstrated a much greater variance in wetting angle across the temperature range. Their initial melting produced a high contact angle similar to that of the rougher samples but they both gradually reduced their contact angle with the surface as the temperature increased. The P400 samples moved from its initial contact angle of 126.8° to its final average wetting angle of $39.6 \pm 0.9^\circ$ over a temperature range of 65°C or 14 minutes. The P600 sample moved from its initial contact angle of 138.2° to its final average contact angle of $47.7 \pm 1.3^\circ$ over a temperature range of 50°C or 11 minutes. Whilst the P400 sample required a slightly longer time to reach its average final wetting angle and its average final wetting angle was slightly lower the wetting curves formed from both samples are very similar overall. This result is expected as the actual surface roughness of the two samples was very similar (P400, $R_a = 0.24\mu\text{m}$ P600, $R_a = 0.25\mu\text{m}$).

Samples with very smooth surfaces (P1200 and P2500 with average roughness of $R_a = 0.16\mu\text{m}$ and $0.09\mu\text{m}$ respectively) both rapidly reduced their contact angle upon melting, going from 45.2° and 129.6° down to $8.8 \pm 0.5^\circ$ and $24.2 \pm 0.8^\circ$ respectively within a 15°C temperature range (3-minute time period). It would be expected the average final wetting angle for the P2500 sample would be shallower if the hypothesis proposed at the start of this investigation was correct. However, this is not shown to be true in this experiment with the smoother of these two samples having a higher average final contact angle.

The smoothest sample tested ground with a P4000 grit paper (to give a surface roughness of $R_a = 0.01\mu\text{m}$) appears to disprove the hypothesis created at the start of this experiment. Although it was the smoothest substrate utilised in these experiments it did not demonstrate the shallowest final wetting angle. The final wetting angle this sample reached was only $108.0 \pm 0.8^\circ$ which is a higher contact angle than all but the roughest two substrates tested. Several potential reasons exist as to why this (apparently outlying) result may have occurred; although further testing of substrates at roughness levels smoother than the P2500 sample would need to be done in order to provide sufficient evidence to substantiate the explanations provided below:

- The original hypothesis predicting a shallower wetting angle as the surface roughness decreased (i.e. a linear correlation) could have been wrong. Evidence exists in literature that there could be a limit at which point reducing surface roughness beyond this value actually leads to an increase in wetting angle; although to confirm this phenomenon occurring in this particular system (Ag-155 on copper substrates) further data points with R_a values lower than that of the P4000 sample would be required. Ideally intermediate roughness values between that of the P1200 sample and the P4000 sample would also be evaluated. Some authors suggest “*Successful brazing and good wetting can be achieved by the least voids by using an intermediate surface roughness*” when using copper based filler metals on copper substrates [3] (In this study $R_a=0.2\mu\text{m}$ was suggested to be optimal). Additionally, it is often recommended in an industrial setting that in general the “as-cut” surface finish (which is often in the region of $R_a = 0.6\text{--}1.6$ [2]—see Section 2.1.3.2, Figure 2.2) is most suitable and additional smoothing of the surface beyond this state is not required [5]. No further evidence from this study can be presented which favours this explanation as the reason for the observed higher contact angle on the P4000 sample and as such it is a less favoured explanation than those which follow.

- Although available literature is split on the influence of surface roughness on the reformation of passivating oxide layers on metal surfaces, some sources claim that a reduction in surface roughness (i.e. a smoother surface finish) can accelerate the formation of a passivating oxide layer. A paper by Nowak found that, contrary to expectation, a polished surface of a Ni based superalloy (IN 625) led to a faster oxidation rate (by a factor of approximately 2) when compared to a ground surface [6]. A similar result was found by Eubanks and Moore who investigated the effects of surface roughness on the oxidation rate of iron held at 800°C in air. They concluded that samples which had been grit blasted oxidised at a slower rate than those which were smooth; with the reduction in oxidation rate being a function of the degree of surface roughening [7]. Evidence to the contrary also exists; A study by Evans evaluated the influence of surface roughness on the oxidation of a nickel superalloy (ME3) and found that the rougher the surface the higher the mass gain of the sample due to oxidation for each time frame measured between 1 hour and 31 hours [8]. No information on the influence of surface roughness on the effect of oxide layer formation on copper substrates specifically could be found. It is possible that the reduced roughness of the copper surface found on the P4000 sample encouraged rapid reformation of the passivating oxide layer on the metal surface that would have been removed when they were ground before the experiment. If the passivating layer had reformed more quickly than on other samples then the P4000 sample would not truly be a Cu surface but instead a copper oxide surface over which the filler metal was spreading. If this was indeed the case, reduced wetting would be expected as oxide layers often inhibit wetting and spreading of filler metals [9].

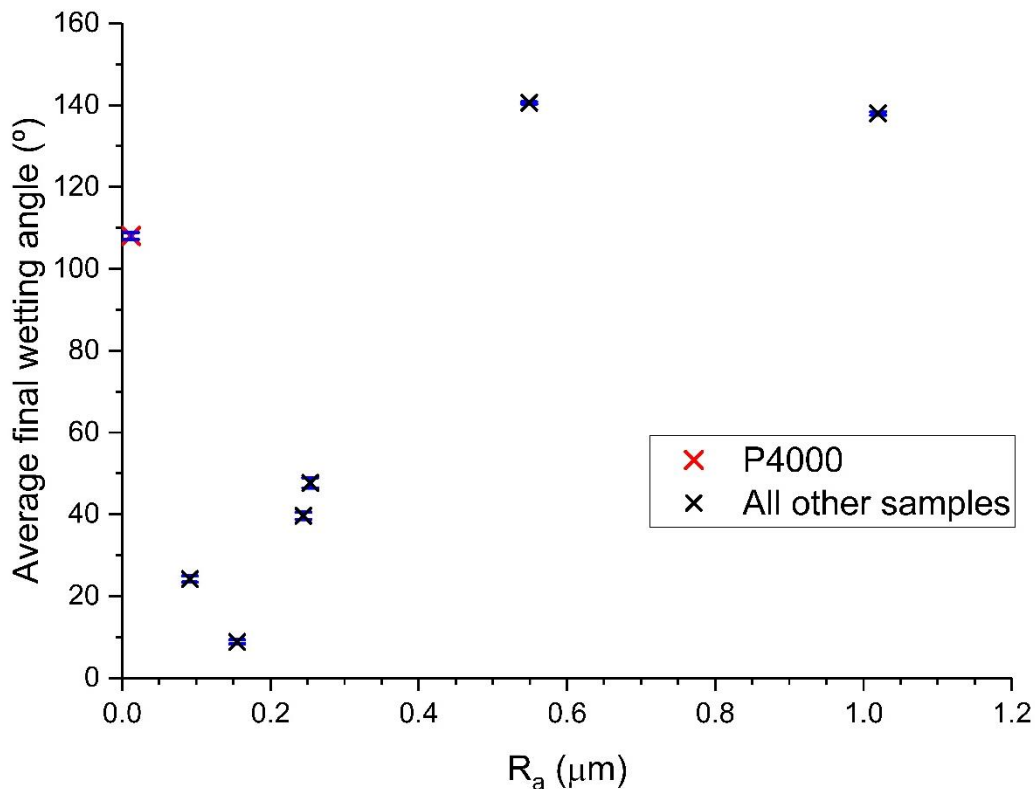


Figure 4.5: Graph displaying the final recorded wetting angle of Ag-155 on substrates of various roughness.

As can be seen from Figure 4.5, a conclusive statement on the influence of the surface roughness on wetting angle is difficult to discern. Whilst it is clear that generally rougher surfaces are a hindrance to the wetting of filler metal Ag-155 on copper surfaces the smoothest samples did not display the lowest wetting angle as expected. The two roughest surfaces - P120 and P220 - exhibited the highest average final wetting angles of $138.0 \pm 0.4^\circ$ and $140.6 \pm 0.3^\circ$ respectively but the P120 sample did not have a wetting angle higher than that of P220 as would be expected for a sample almost twice as rough. The similarity of these two results indicates a limit to the effect that roughening a substrate can have on the final wetting angle produced, although more data using even rougher surfaces (i.e. those with $R_a > 1.02\mu\text{m}$) is required before such a statement can be adequately justified.

A further observation of note is that an oxide residue on the P600 sample may have obscured the Drop_angle software from accurately measuring the wetting angle in the later stages of the experiment. An example of the apparent residue can be seen in Figure 4.6 which shows 3 pictures of the P600 sample; the first 2 are taken 3 minutes apart at 645°C and 660°C as the Ag-155 cube melts. The third image is taken at 740°C showing a residue still remaining around 90°C after the cube was seen to begin melting and spreading out. The final image shows the sample post-experiment completion with a small black residue visible in the centre of the sample. It is likely that this residue is an oxide that had contaminated the filler metal cube and was visible in all images taken after the filler metal had melt and spread, leading to difficulty in accurately measuring the wetting angle of the filler metal on this substrate. Further evidence to this is the large surface area occupied by filler metal in the final image, for such a large spreading of filler across the surface, a lower wetting angle would be expected than the final one recorded for the P600 sample of $47.7 \pm 1.3^\circ$.

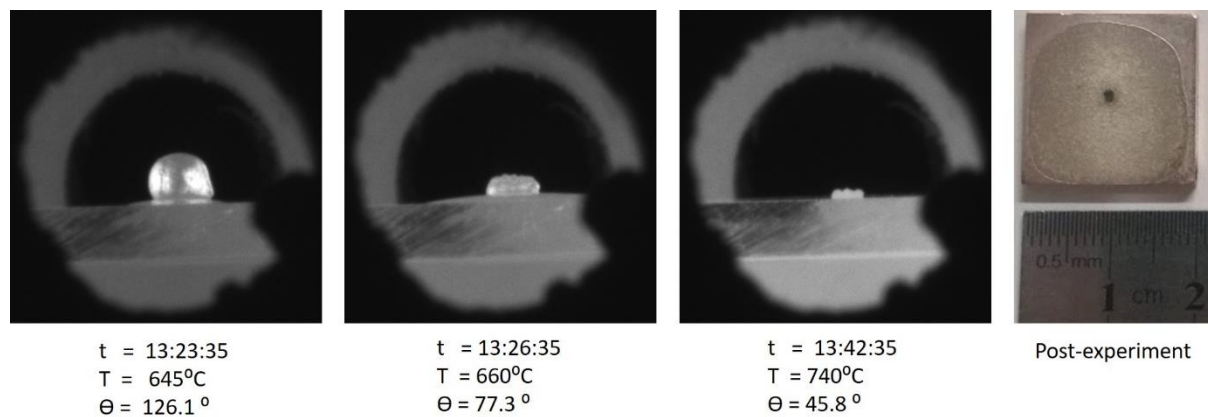


Figure 4.6: Sequence of pictures of an Ag-155 filler metal cube melting on a P600 substrate. t gives the experimental time; T, the furnace temperature at the time of the photograph and Θ , the wetting angle determined by the Drop_angle software after the experiments completion.

A similar observation of oxide residue may explain the unexpected result of the P2500 sample having a higher final wetting angle ($24.2 \pm 0.8^\circ$) than the P1200 sample ($8.8 \pm 0.5^\circ$). Figure 4.7 shows a comparison of the P1200 and P2500 samples during and post-experiment; similarly to the P600 sample above, a black residue can be seen on the P2500 sample post-experiment. A comparison of images taken at 650°C for the P1200 sample and P2500 sample show the residue being visible in the images which leads to the Drop_angle software recognising the residue as being a part of the droplet. This consequently gives a higher wetting angle even though a visual inspection of the two samples post-experiment shows that the filler metal on the P2500 sample appears to have spread out more. It is likely that if the residue seen in the P2500 sample was not present

that the Drop_angle software would read a lower wetting angle more similar to or perhaps even below that of the angle determined for the P1200 sample.

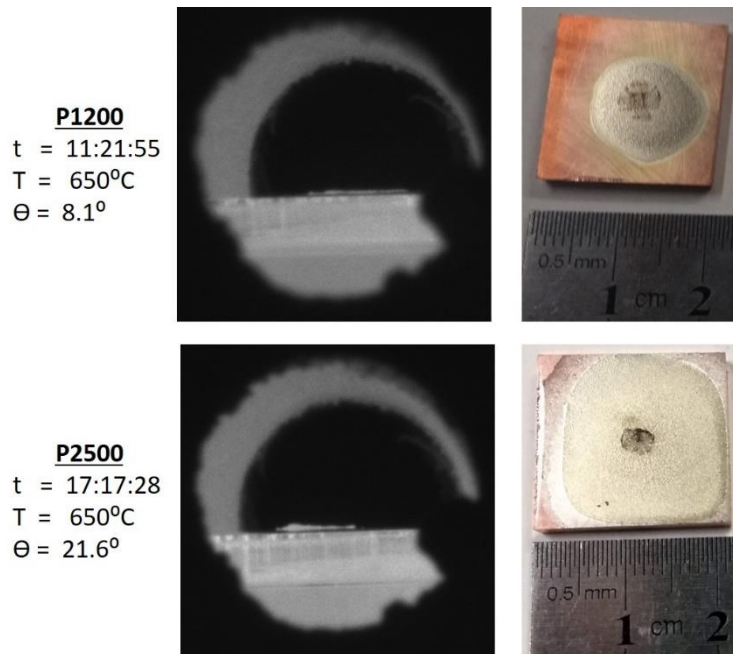


Figure 4.7: Comparison of P1200 and P2500 substrates at 650°C (Left), and post-experiment (right). A residue can be seen on the P2500 sample both during the experiment and post-experiment.

In conclusion, it appears from the data collected in this experiment that the surface roughness of the substrate clearly has an influence on the contact angle between the filler metal Ag-155 and a copper substrate. Data collected suggest that there is a positive correlation with rougher surfaces exhibiting higher final contact angles than smoother ones but further data is needed to give a conclusive trend. Explanations relating to the presence of oxide residues on some samples provide possible reasons as to why the data collected did not fit the expected trend as well as anticipated for some samples. One sample (ground with P4000 SiC paper) did not fit the stated trend and may indicate that in fact an optimum roughness level exists and that increasing the smoothness of the surface will not indefinitely improve wetting; further testing would be needed to assess the validity of this statement, specifically by repeating the above experiment using roughness values between that of the P1200 sample and the P4000 sample ($R_a = 0.01\mu\text{m} - 0.16\mu\text{m}$) and potentially samples smoother than the smoothest sample tested ($R_a < 0.01\mu\text{m}$). Additionally, to inhibit oxide formation on samples after grinding, if any future testing is to occur, the samples should be ground as close to the time of use as possible and stored in airtight containers to minimise potential oxidation in the hope of providing more accurate data.

4.3. Diffusion - Zone Studies

4.3.1. Influence of Torch Type and Brazer Technique on Joints Manufactured by Hand Torch Brazing

An assessment of the impact of torch type and brazer technique on joint formation was made by examining joints formed between filler metal Ag-155 and copper substrates whilst changing the brazer carrying out the operation (between the author and an experienced technician) and by using different torches to provide the heat input to form the joint. The aim of this study was to assess whether joint quality would be inhibited by using a less experienced brazer (as torch brazing is generally considered to be a skilful process, with many variables influenced by small details of the technique used in handling the torch) or a lower heat input torch to form joints. Investigating these effects is important as otherwise data gathered in this study may reflect unfairly on the performance filler metals produced within this thesis of work when compared to data obtained from known filler metal joints produced by experienced brazers using different brazing torches).

The bond between a brazing filler metal and the materials it joins consists of two components.

- The first and simplest part of the joint is the mechanical component. The surface that the brazing filler metal flows across will not be completely flat (even if this cannot be seen above a microscopic scale). When the liquid filler metal flows across the rough surface it will penetrate into any depressions on the surface, some of which will have overhangs. When the filler metal cools after the joining takes place it will conform to the surface and as such a mechanical adhesion will occur (as can be seen in Figure 4.8). This keying is similar to how Teflon™ primer coats adhere to the surface of a frying pan when applied (Teflon™ is a non-stick coating designed not to interact chemically with substances placed on it and hence an alternative method of affixing it to the base of the pan via the mechanical interaction is necessary).

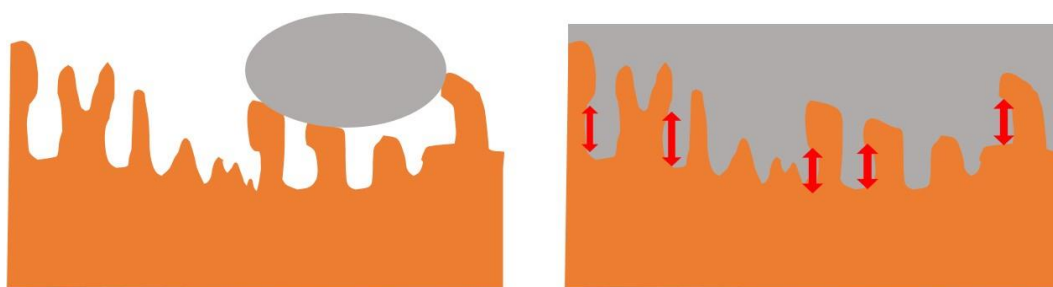


Figure 4.8: Diagram illustrating how a droplet of filler metal conforms to a surface after melting and showing the mechanical interaction that causes adhesion.

- The second (and usually stronger) adhesion between the base metal and the filler metal is a chemical interaction caused by either the solubility of one element from the brazing filler metal within the base metal; solubility of the base metal in the brazing filler metal; or a reaction between components of both filler and base material to form an interfacial compound.

By examining the diffusion zone (if present) between the filler metal and the base metal using a backscattered electron image (BSE) on a scanning electron microscope (SEM) the width of the diffusion zone can be observed and measured. After examining the width of the zone, Energy Dispersive X-Ray Spectroscopy (EDX) can be used to identify which elements predominately diffuse into the base metal to form the diffusion zone. This is useful for addressing the concerns of the industrial sponsors that silver diffuses through the Ni diffusion barrier and forms silver-antimony compounds. If the diffusion distance is revealed to be large ($>10\mu\text{m}$ – the length of the Ni diffusion barrier applied) then the probability that silver does diffuse through the diffusion barrier and form compounds with elements contained in the skutterudite thermoelectrics (e.g. antimony in $\text{CoSb}_{2.75}\text{Sn}_{0.05}\text{Te}_{0.20}$) is higher. The phase diagram for silver-antimony (Figure 4.9) does reveal that several compounds exist between silver and antimony including the hexagonal close packed $P6_3/mmc$ zeta (ζ) phase and/or the tetragonal $P4/mmm$ epsilon (ϵ) phase which supports the theory that the formation of silver-antimony compounds is possible.

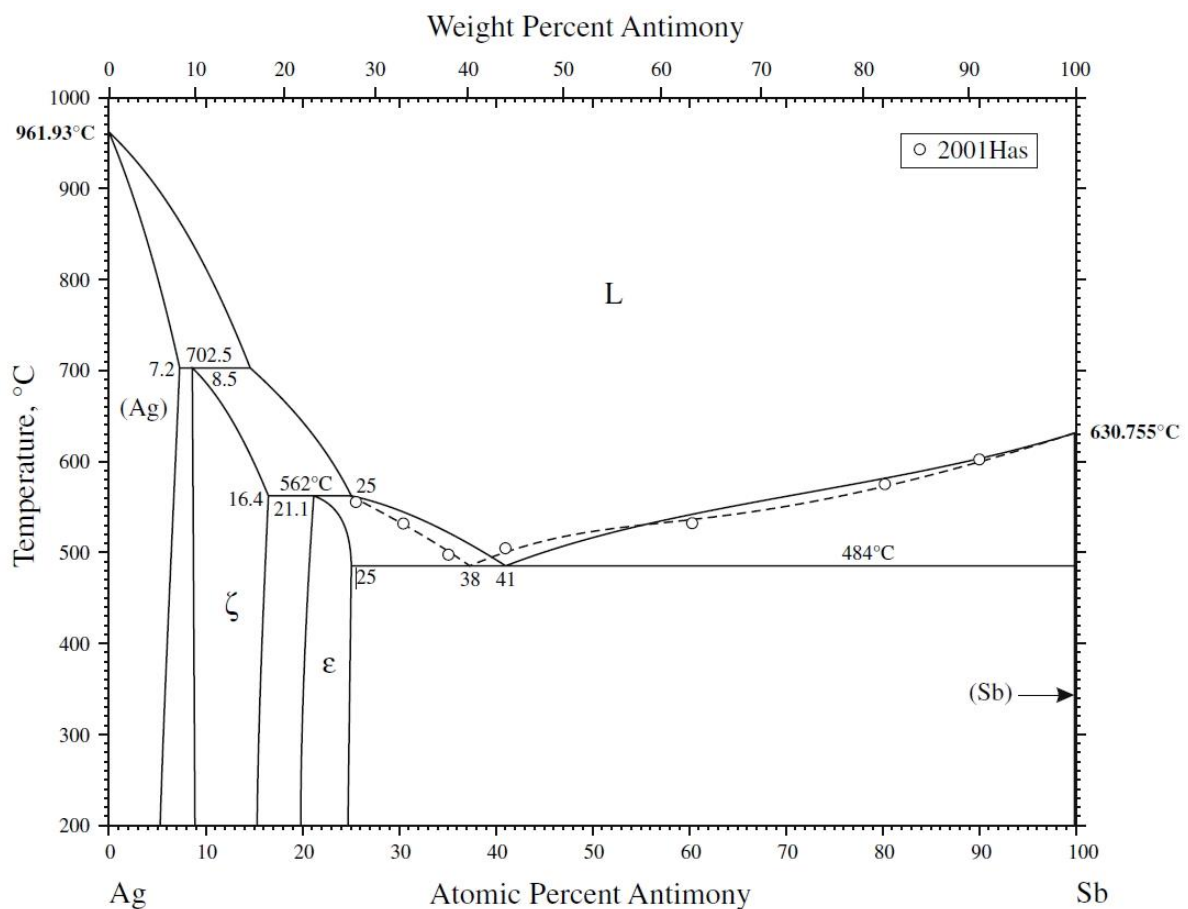


Figure 4.9: The silver-antimony phase diagram.

Additionally, by understanding which other elements are soluble in different base metals we can hope to better design new alloys which have an equally strong adhesion to base metals and thus improve the performance of brazing filler metals developed through this project.

Brazing using a hand-held torch in air is the simplest of all brazing techniques. The principle is simple; a joint is assembled (see Section 3.2.1 Figure 3.1), with surfaces cleaned and prepared as required and the joint gap set at the desired width. A flux is applied to the joint (to prevent oxidation, as the joining process takes place in air) and

then a hand-held torch is used to heat the components up to the brazing temperature (the melting temperature of the filler metal being used to form the joint). Once the brazing assembly is at the correct temperature the filler metal is applied and becomes molten. The molten filler flows across the joining surfaces. Once in the correct position, the torch is removed and the assembly allowed to cool, solidifying the filler metal and forming a joint between the components.

A variety of different torches burning different fuels can be used to deliver the heat input into the joint. These torches burn at different temperatures and thus heat the assembly at different rates. Two commonly used torch types for brazing are propane and oxy-acetylene. Propane torches burn at around 1,982°C [10] and generally have quite a wide flame, whereas oxy-acetylene fuel blends will burn much hotter – reaching temperatures of 3,480°C [11] and have a much more pointed and directional flame. The more intense heat of the oxy-acetylene torch coupled with the narrower and more targetable flame is expected to lead to a faster and more localised heating of the workpiece. A propane torch, with its lower heat input and wider flame, should heat the workpiece more slowly and evenly. It is considered possible that, due to these differences, the heat input source used is a variable which could influence the size and structure of the diffusion zone created between filler and base material during the joining process. To compare the influence of the heat input on the joint formed, copper samples were brazed together using a common industrial filler metal (conforming to ISO17672 Ag-155) using both a propane torch and an oxy-acetylene torch.

Additionally, especially with hand held torch brazing, the technique of the brazer potentially influences the joint formed. A more competent brazer will have a better understanding of exactly what heat input is required and what the optimal temperature is to form a joint correctly and will likely be more skilled at knowing when and how to apply filler metal to the brazing assembly. A less skilled brazer may struggle with the delicate control needed in the process and apply too much or too little filler metal. Furthermore, the heat input from a less skilled brazer may be poorly distributed and less efficient. In order to assess whether the user technique influences the size of the diffusion zone formed, copper samples were brazed by 2 different brazers; a skilled industrial brazer (6 years industrial brazing experience) and also by a novice brazer with less experience (2 years of laboratory research brazing experience). Both brazers used both torch types to produce 4 samples:

- Brazed by an experienced brazer using an oxyacetylene flame
- Brazed by an experienced brazer using a propane flame
- Brazed by a novice brazer using an oxyacetylene flame
- Brazed by a novice brazer using a propane flame

All 4 samples were assessed using EDX in order to assess the diffusion profiles of filler metal components into the copper. The purpose of this study was to assess whether the variance in heat input caused by torch type and brazer skill influenced the metallurgical structure of the joints produced.

The samples produced by both brazers and both torches were T-shaped butt joints as shown in Chapter 3 Figure 3.1. The T-shaped joints were sectioned to reveal a cross-section which was then mounted, ground and polished according to the schedule in Section 3.3 Table 3.1. Polished samples were then examined in an FEI Inspect F50 SEM and imaged at 6000x magnification at a high contrast to clearly show the diffusion zone formed

(Figure 4.11 - left). In order to verify that the diffusion zone which could be seen in the high contrast BSE images was really the result of diffusion and not an artefact present due to the high contrast imaging used; EDX point scans were used to verify that the composition in the diffusion zone region was different to both the copper base region and the filler metal region. A matrix of 9 EDS point scans was taken on each sample. 3 located in the copper base metal (spectra 1, 4 and 7); 3 located in the diffusion zone (spectra 2, 5 and 8) and 3 located in the filler metal (spectra 3, 6 and 9). As can be seen from Figure 4.10 the EDX spectra associated with each of the 3 regions are visibly different and the corresponding compositions determined by EDX verify that the diffusion zone does indeed exist and can be imaged and measured within these samples.

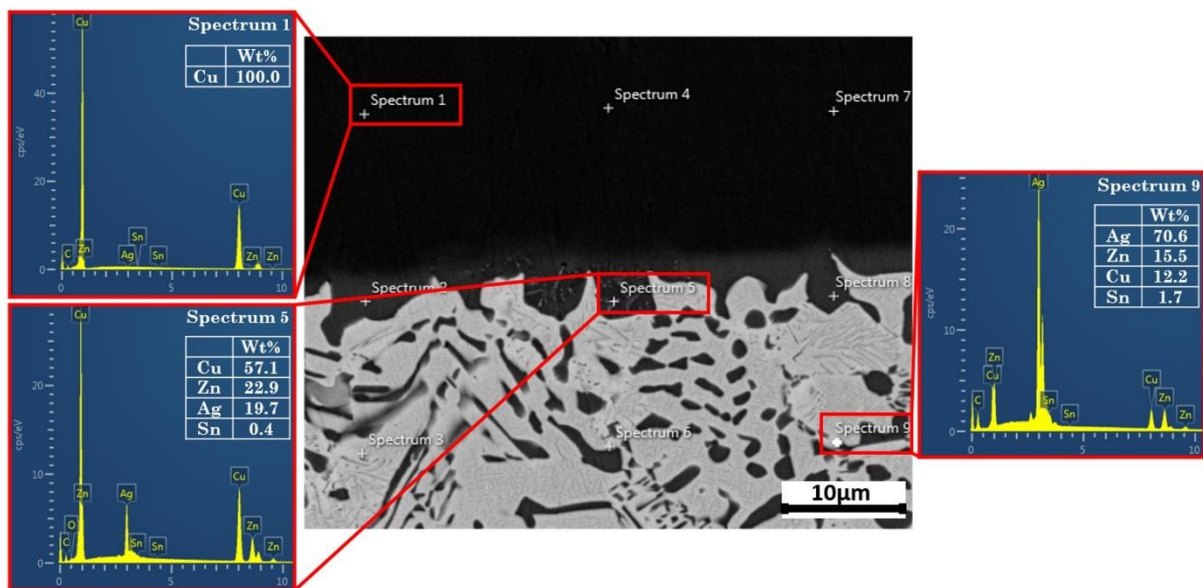


Figure 4.10: A BSE SEM image of the interface region of the joint between copper plate and an alloy conforming to ISO17672 Ag-155 with the positions of point scans marked. EDX point scans for the copper plate (top left), the diffusion zone (bottom left) and filler metal (right) are included.

Once the presence of the diffusion zone was confirmed, the size of the diffusion zone needed to be measured to assess whether the changing of brazer and brazing torch influenced the size of the diffusion zone produced. The BSE images of each sample were then edited so that the diffusion zone was highlighted in white and the filler metal and base metal in black; An example of this can be seen in Figure 4.11. This was done to assist with identification of the boundaries between diffusion zone and base/filler metal by the image analysis script ‘Analyze_stripes’ (Copyright 2013 Justin R. Bickford [12]) in the methods described below.

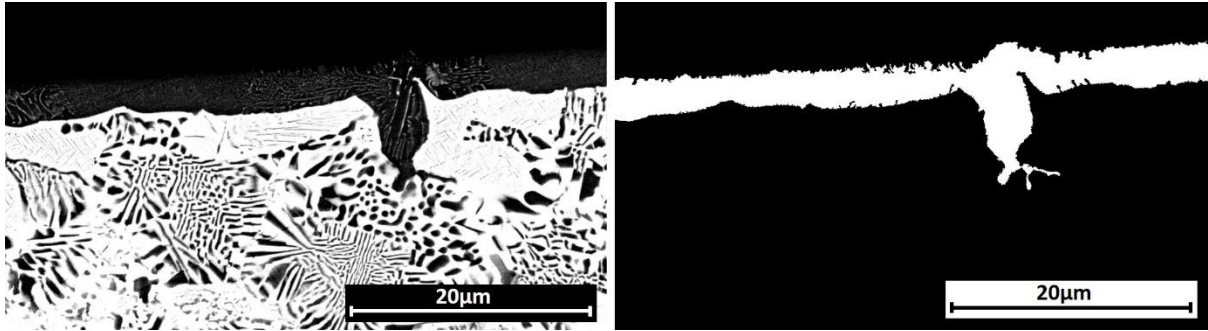


Figure 4.11: (Left) A pre-edited SEM image taken on an FEI Inspect F50 using the BSE imaging mode, A high contrast has been applied to the image to make determination of the diffusion zone boundaries clearer. (Right) The edited SEM image with the top copper surface and the bottom Ag-155 surface edited to black and the diffusion zone highlighted in white. This image processing was necessary to allow the ‘Analyze_Stripes’ script to accurately identify the interface boundaries.

The diffusion zone formed between copper and filler metal was then measured using 4 different methods and the results compared.

1. **Analyze_Stripes full image scan.** A computer script designed for measuring the stripe width of electron beam lithography stripes developed by Justin R Bickford [12] was downloaded and used on the edited high contrast images of each of the 4 samples. The computer script scans a region of interest (ROI) of the image selected by the user and wherever it detects adjacent pixels with high variance between their grayscale values (e.g. where a black pixel is next to a white pixel) the software marks the point and uses it to construct a red line, highlighting the diffusion zone as intended (Figure 4.12, bottom left); the user can refine the selected points using the threshold tool to produce continuous narrow red lines around both sides of the stripe of interest. Several parameters relating to the selected lines are then outputted by the programme, of which only the linewidth (calculated by an average of the highlighted pixels) is relevant in this study.

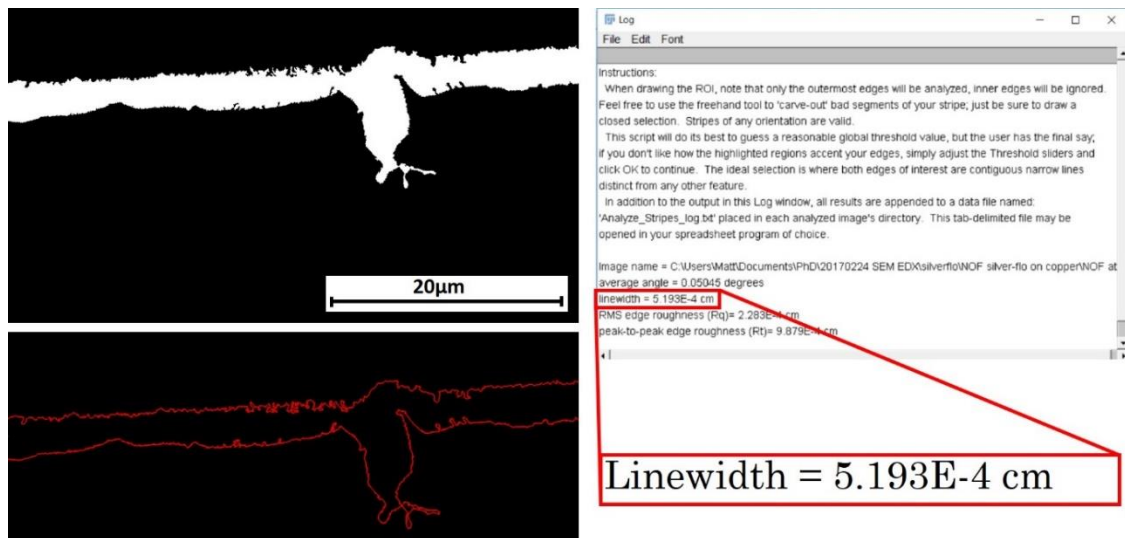


Figure 4.12: (Top left) Edited image before the running of the ‘Analyze_Stripes’ script; (Bottom left) Edge detection completed within ImageJ by the ‘Analyze_Stripes’ script. (Right) Output data produced by the script including the data of interest “Linewidth” which is the average distance between the two lines according to the programs algorithm.

- 2. Non-overhanging areas Analyze_Stripes.** Due to the roughness of the surfaces under investigation several overhanging sections could be observed. It was noted that this probably interfered with the ability of the script to determine what the width of the diffusion zone is (as the top part of the overhanging structure would be recognised by the script and not the part overshadowed by the overhang). In order to attempt to remove this error only the sections of the image which did not contain any overhanging parts were analysed and then the results averaged. It is acknowledged that this exclusion of areas which contain overhanging regions is likely to produce smaller diffusion widths than other assessments due to the largest regions being systematically excluded.

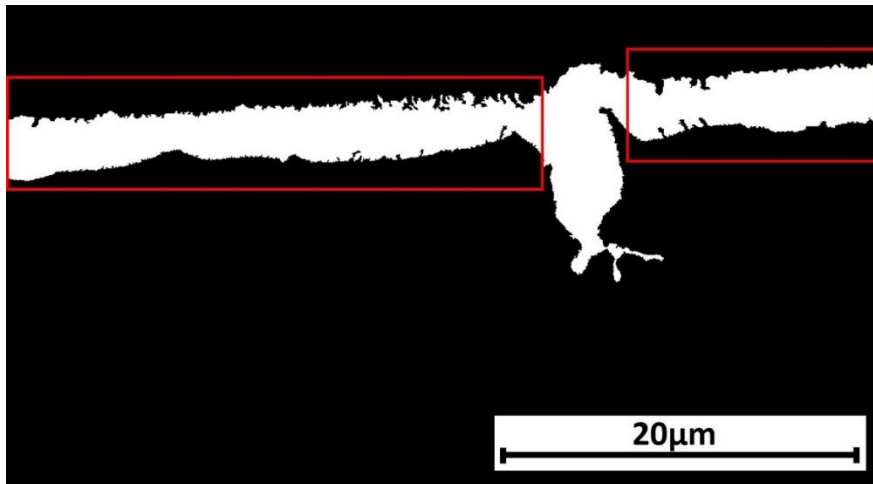


Figure 4.13: An example of the exclusion of overhanging areas used in method 2. Two separate sections of the image (within the red boxes) are scanned with the 'Analyze_Stripes' script. The results from each scan were recorded and averaged to give a value for the image as a whole.

- 3. Overhangs removed Analyze_Stripes.** In another attempt to eliminate the issues caused by the overhanging sections the image was edited further to remove all overhanging sections and then the script run over the entire edited image.

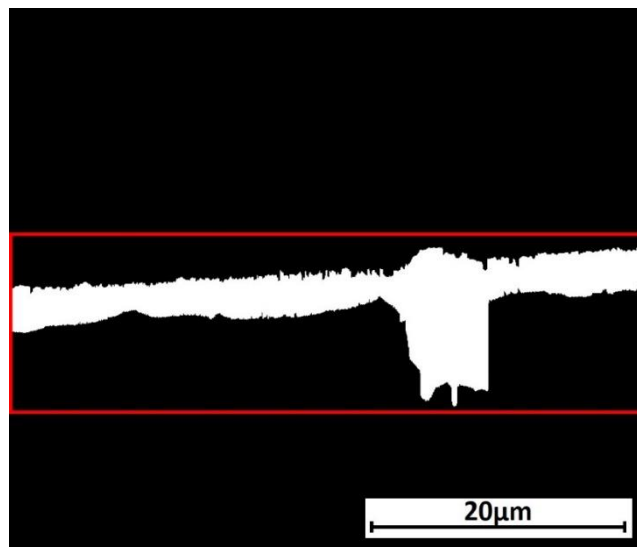


Figure 4.14: The same image used in methods 1 and 2 except with any overhanging areas edited out before subjecting the entire image to the 'Analyze_Stripes' script.

4. **Measured by hand.** Finally, the diffusion zone width was measured by hand at regular intervals across the image with the overhangs included. 20 measurements were taken at regular intervals and the average of these 20 measurements taken to give the average diffusion zone width.

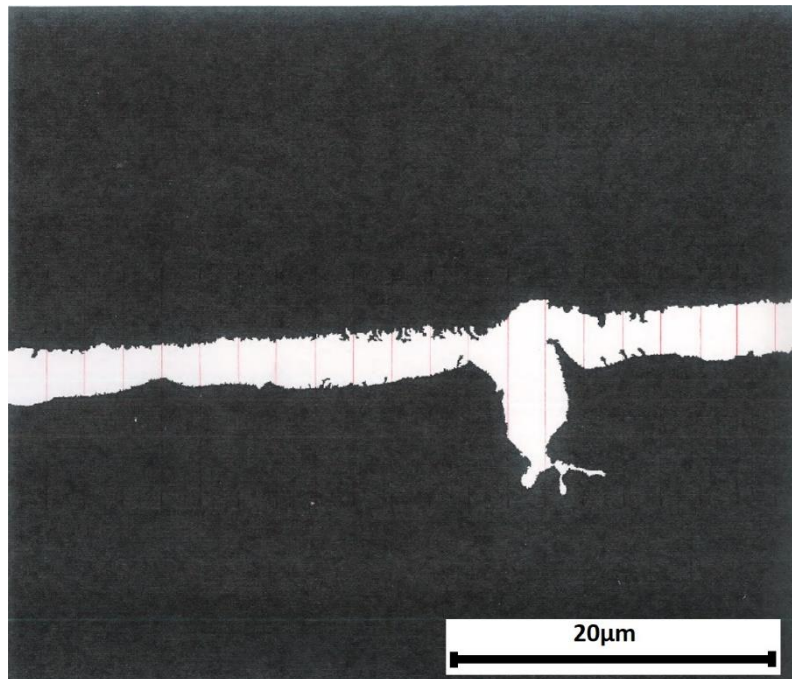


Figure 4.15: The same image used in methods 1 and 2 was printed and the diffusion zone measured by hand at 20 equally spaced intervals. These results were then averaged to give the average diffusion zone width.

Figure 4.16 shows the results of all 4 diffusion zone width measurements for each of the 4 samples.

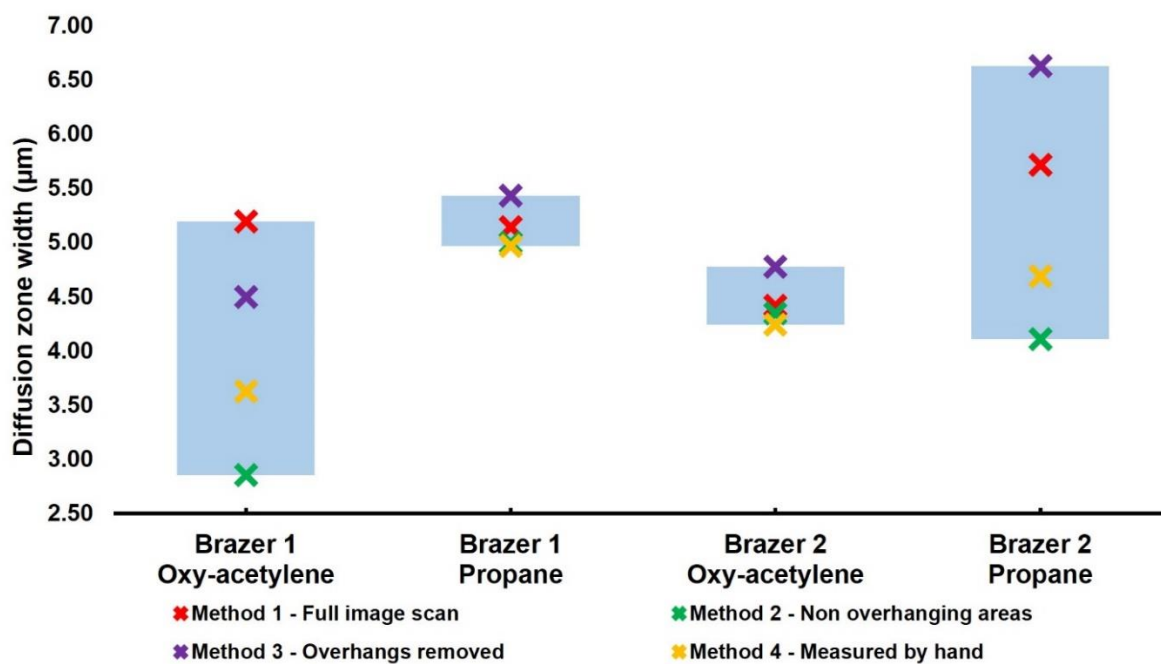


Figure 4.16: Bar chart comparing the measured diffusion zone size measured for each of the 4 samples analysed by each of the 4 methods described in Section 4.3.1. Brazer 1 is the experienced brazer, brazer 2 is the novice brazer.

The following observations on the different methods of diffusion zone width measurement should be noted:

1. Method 2 (the examination of areas which do not contain overhangs) is likely to offer an underestimate of the average diffusion zone width. The diffusion zone width tends to be larger at areas where overhangs and recesses are present (due to these areas offering an increased surface area from which brazing filler metal can diffuse from). Systematically ignoring the wider areas of the diffusion zone is therefore likely to lead to an underestimate of the zone width. Evidence for this theory can be seen by the fact that this method (method 2 in Figure 4.16) gives the lowest average diffusion zone width for 2 of the 4 measured samples and the second lowest for the other 2.
2. Method 3 (the examination of an image which has been edited to remove any overhanging sections in an attempt to improve zone width estimation) is likely to provide an overestimation of the average diffusion zone width. The removal of overhanging sections increases the size of the diffusion zone substantially in the vicinity of these surface features which will push the average width higher than it actually is. This is evidenced by Method 3 providing the largest average diffusion zone width in 3 of the 4 samples (Figure 4.16) and the second largest in the final sample. Incidentally the single sample in which this method does not provide the largest estimation is for the sample with the fewest large scale surface features.

Removal of the methods described above as likely to overestimate or underestimate yields the graph below (Figure 4.17).

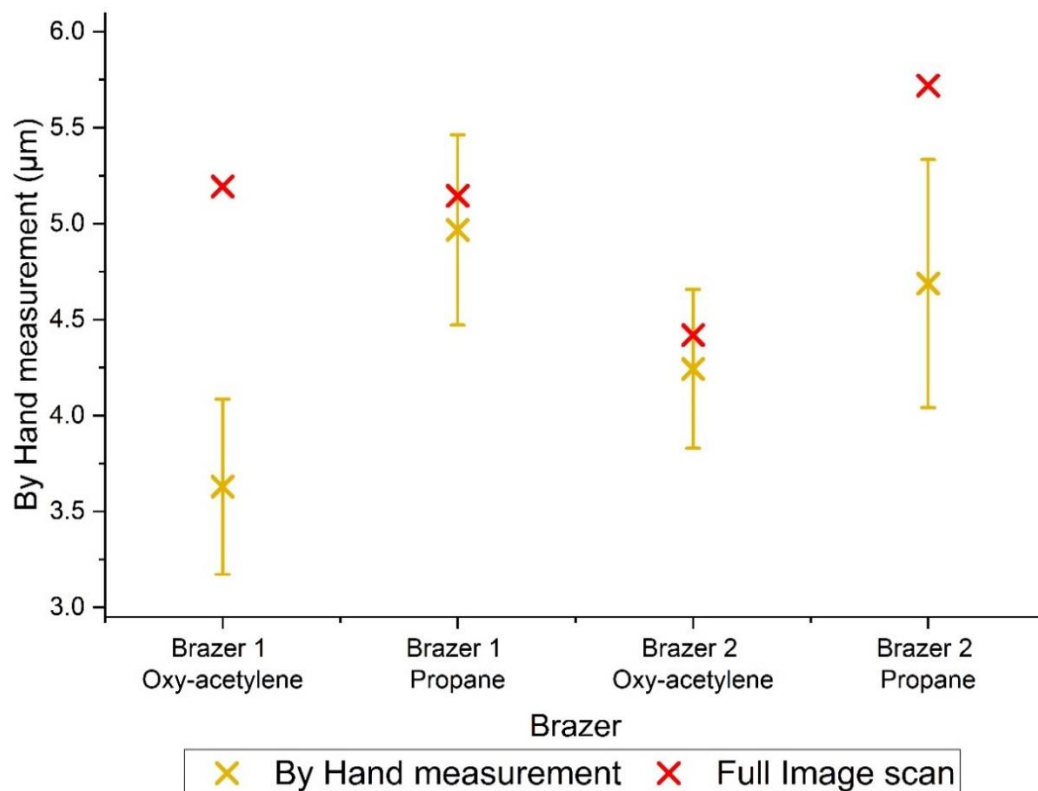


Figure 4.17: Bar chart displaying the measured average widths of diffusion zones using only methods 1 and 4. Error bars for the by hand measurement give the standard error of the mean ($S_{\bar{x}}$) for the by hand analysis method.

As can be seen from the above results, significant overlap can be seen between the error bars on all the by hand measurements making it difficult to conclude that either brazer or torch type had a significant impact on the size of the diffusion zone formed. This leads to the conclusion that the width of the diffusion zone is not significantly different for samples brazed by an experienced brazer and an inexperienced brazer and for those brazed using a propane torch or an oxyacetylene torch. Of all 16 measurements taken across 4 samples, 13 measurements place the diffusion zone width between 3.5 μm and 5.5 μm (Figure 4.16) and once the overestimating and underestimating methods are removed 7 of the 8 data points fall within the 3.5 μm to 5.5 μm range (Figure 4.17).

Finally, EDX maps of the interface between filler metal and base metal were taken to examine whether the diffusion zone was of a constant composition throughout or whether there was local variance in element diffusion due to grain boundary diffusion of specific elements or compound formation. A large variance in the spatial distribution of elements across the diffusion zone would require a more careful placement of EDX line scans across the interface in order to accurately evaluate the movement of different elements. Fortunately, this was not necessary as Figure 4.18 shows that the distribution of elements throughout the diffusion zone appears to be equal with no observable variations or anomalies along its length. The intensity of the signature for different elements within the maps does indicate that certain elements diffuse more prominently into the diffusion zone however, looking at each element individually there does not appear to be any lateral variance in their diffusion gradient.

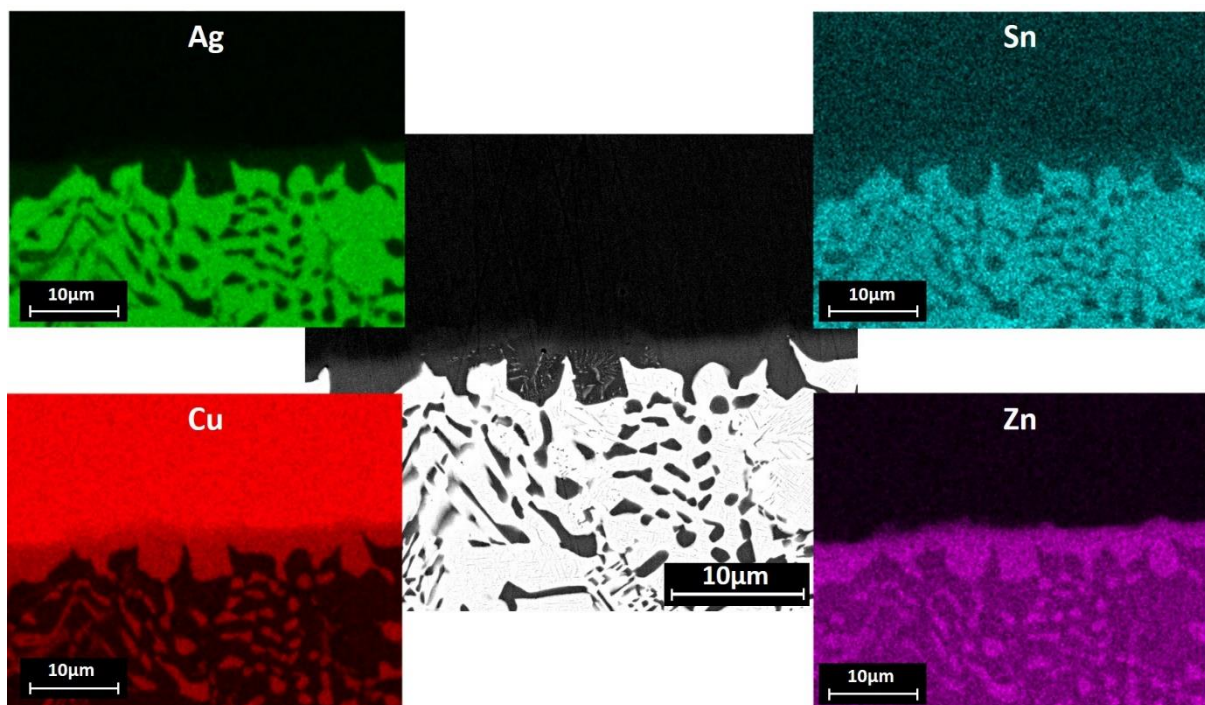


Figure 4.18: EDX map of the diffusion zone between copper plate and filler metal Ag-155 brazed by an inexperienced brazer using an oxyacetylene torch showing no obvious lateral variance in element concentration throughout the diffusion zone over the distance assessed.

As no obvious inhomogeneity could be observed within the EDX maps it was deemed that EDX line scans spaced equally in multiple locations across each sample would be sufficient to assess the diffusion lengths of different elements without specific placement of linescans being required.

A final point of note is that the EDX maps produced appear to show that the range of the tin diffusion is much higher than that of the silver and the zinc. A definite boundary for zinc and silver diffusion can be seen on the maps which corresponds with the size of the observed diffusion zone, however, the tin appears to diffuse much more evenly and to a much greater distance, extending well beyond the boundary of the diffusion zone which can be detected by the BSE image. A possible explanation for this unlikely phenomenon is that the images are coloured according to relative element concentration within each image and not within the sample as a whole. It is possible that the low amount of tin in the sample means that a bright colour is assigned to a relatively weak concentration of tin within the filler metal (and a weak signal in comparison to the background as a result) and as such even very low concentrations (or potentially misidentified elements) are assigned a brighter colour than they would be in one of the images with a higher concentration of elements present thus exaggerating the appearance of tin diffusion in the sample.

4.3.2. Diffusion Length of Silver in Different Base Metals

In addition to knowing the size of the diffusion zone, investigations were undertaken into finding what the constitution of the diffusion zone was. The primary aim of this investigation was to discern whether silver diffused further into nickel than other base materials as silver diffusion through an applied nickel diffusion barrier is a suspected issue in the joining of thermoelectric materials, targeted from the onset of this work by industrial partners Johnson Matthey.

Secondary benefits of this investigation were to ascertain if particular elements diffused further than others and thus could be added to future brazing filler metals developed in order to improve their adhesion. The reverse was also true; if limited diffusion was required then certain elements could be excluded to limit the diffusion of material into the substrates being joined by the filler metal.

To map the diffusion of elements from the brazing filler metal into the base metal (and vice versa: from base metal into filler), EDX linescans were taken across the interface region between filler and base metal which could be observed in the BSE SEM images discussed above. The interface between filler metal Ag-155 and 5 different base metals (O.F.H.C. copper; 99% pure annealed nickel; 99.4% pure 'common brass' – Cu₆₃Zn₃₇; half hard temper, low carbon steel; and annealed 304 grade stainless steel) were examined. Line scans were drawn to a length which encompassed the entire observable diffusion zone and any elements contained within the filler metal were tracked across the boundary with the base metal. An array of 10 line scans was used at 3 different locations on each sample, with each line scan spaced approximately 2.5 microns apart giving a total of 30 line scans for each sample and 150 linescans in total.

The diffusion length was evaluated by determining 2 points and measuring the distance between them. The 'onset point' (i.e. at the start of the diffusion zone) was the point at which the concentration of an element dropped below its initial value and the 'end point' where the level of that element reached a background or base level. In order to account for the normal variation in element concentration at any point an average was taken of the upper 'flat' portion of the elements EDX trace (i.e. the region before the diffusion zone).

The standard error of the mean ($S_{\bar{x}}$) was calculated for this average value (using Equation 4.4, where n is the number of points the average is taken across and S is the standard deviation of those points) and added and subtracted from the average to produce 3 lines which were overlaid on top of this upper 'flat' portion of the graph.

$$S_{\bar{x}} = \frac{S}{\sqrt{n}} \quad \text{Equation 4.4}$$

The onset of the diffusion zone was then defined as the point at which the EDX trace crossed below the line for the standard error of the mean subtracted from the average ($\bar{x} - S_{\bar{x}}$) and did not rise above it again. Figure 4.19 illustrates how the onset point is defined.

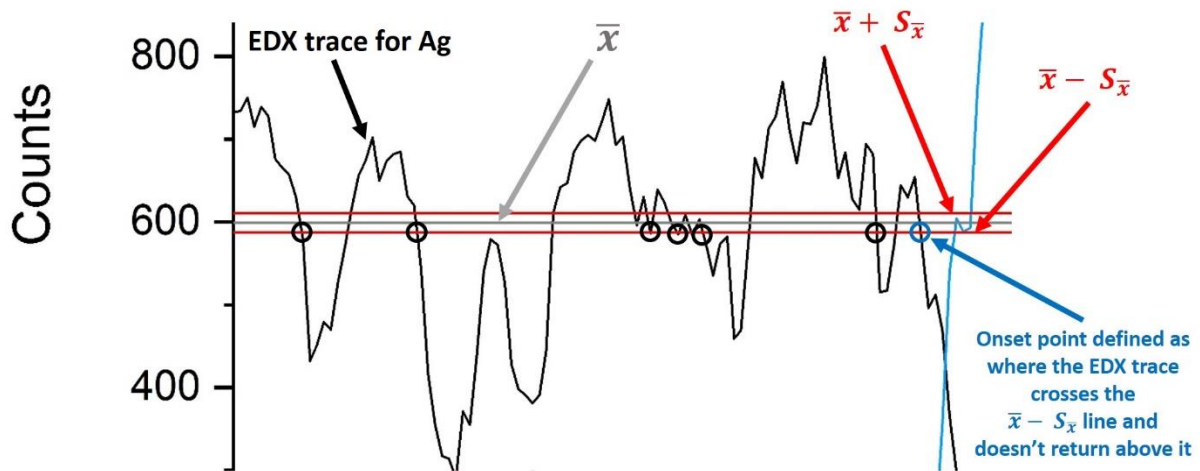


Figure 4.19: Diagram showing how the onset point of the diffusion zone was defined. The black circles indicate points where the EDX trace crosses below the ' $\bar{x} - S_{\bar{x}}$ ' line but subsequently rises above it again thus meaning they cannot be the onset point.

A similar process was used to define the ending of the diffusion zone. The lower flat portion of the trace was averaged and the standard error of the mean ($S_{\bar{x}}$) for this average calculated. Again, $S_{\bar{x}}$ was subtracted and added to the average and all 3 lines plotted on the graph. The ending point was defined as when the EDX trace first crossed the line which marked $\bar{x} + S_{\bar{x}}$. The diffusion length for the element whose trace was evaluated using this method was considered to be the distance between these two points.

An example linescan illustrating both the onset and end point can be seen in Figure 4.20. The point at which the data traces first drops below $\bar{x} - S_{\bar{x}}$ and doesn't return is highlighted in the enhanced region in the top right of the image and ringed with a blue circle. Similarly; for the baseline of the trace, the enhanced region to the left of the graph legend highlights where the trace first drops below the $\bar{x} + S_{\bar{x}}$ line for the baseline of the graph; again, the point is highlighted with a blue circle. The distance between these two points (8.06 μm and 9.61 μm) gives the diffusion length of the silver in this one linescan (1.55 μm).

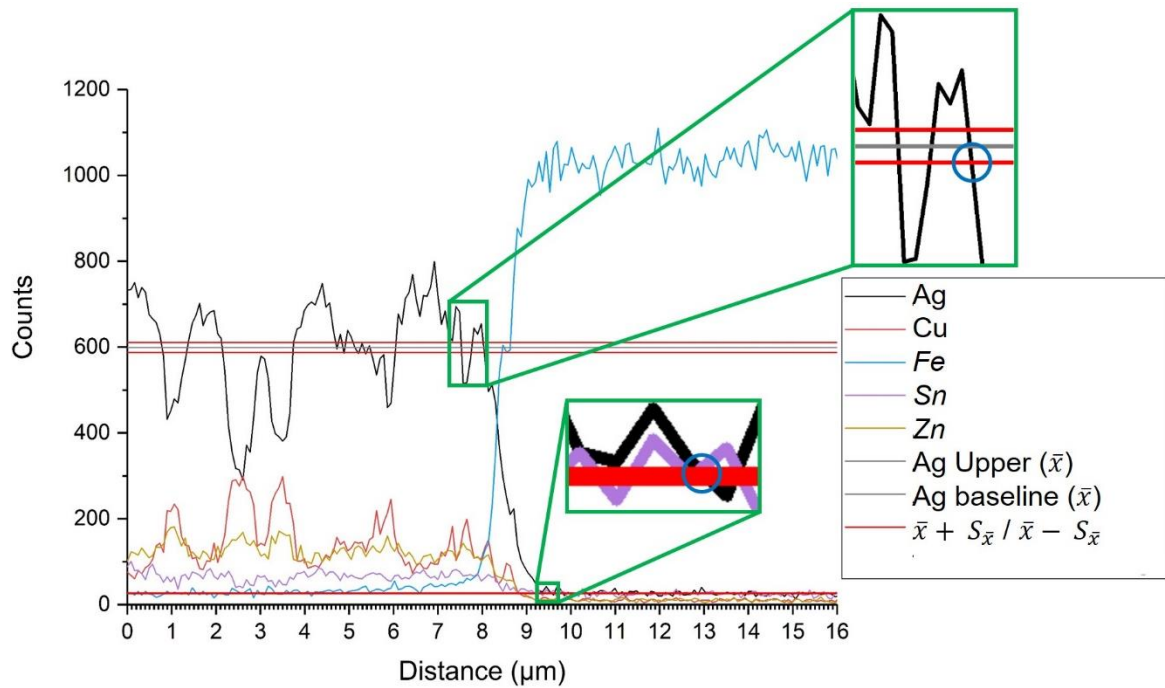


Figure 4.20: An example linescan highlighting how the diffusion length for each element was calculated using the standard error of the mean ($S_{\bar{x}}$) for each of the flat regions of the trace.

This diffusion length measurement is then repeated for the principle element in the base metal which show a large variance across the interface (in Figure 4.20 this would be Fe). Other elements present in the sample (e.g. Cu, Sn and Zn in Figure 4.20) are not evaluated as they are present in much smaller quantities and thus assessing their diffusion length is more prone to erroneous results due to local variations being a much more significant proportion of the maximum detected counts.

This process is then repeated for each of the 30 linescans taken on each sample. Once all 30 linescans were evaluated for each base metal, an average diffusion distance for each element was calculated and is shown in Table 4.4.

Table 4.4: Table of the diffusion distances of different base metal and filler metal constituents after a standard torch brazing cycle.

Base metal	Filler metal	Elements evaluated	Average diffusion distance in this system (μm)	Standard error of the mean ($S_{\bar{x}}$)
Steel	Ag-155	Ag	2.32	±0.12
		Fe	3.25	±0.11
Nickel	Ag-155	Ag	6.40	±0.27
		Ni	7.50	±0.28
Copper	Ag-155	Ag	4.88	±0.37
		Cu	4.83	±0.36
Brass (Cu63Zn37)	Ag-155	Ag	3.58	±0.34
		Cu	1.16	±0.13
Stainless Steel (grade 304)	Ag-155	Ag	3.36	±0.40
		Fe	3.69	±0.13

The data on silver diffusion was taken from the table and plotted on a graph to provide a simple visualisation of the diffusion length of silver in different base metals which can be seen in Figure 4.21.

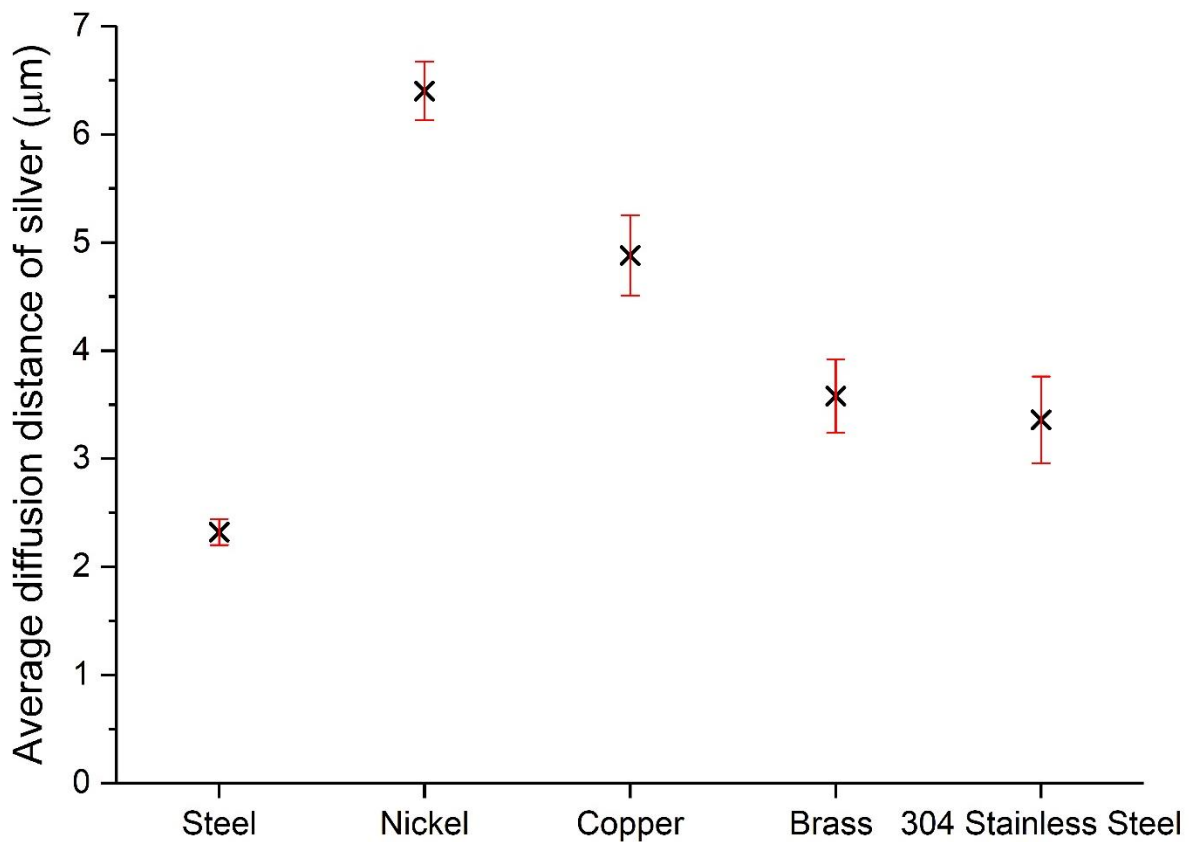


Figure 4.21: Graph depicting the average diffusion distance of silver from filler metal Ag-155 in various base metals.

Conclusions which can be drawn regarding the diffusion distances are as follows:

The primary conclusion of this section of the work is that silver does diffuse further in nickel than in any of the other base materials tested with an average diffusion distance of $6.40 \pm 0.27\mu\text{m}$ which is approximately a 25% increase above the next highest diffusion distance ($4.88 \pm 0.37\mu\text{m}$ for silver in copper). Some evidence exists to support this conclusion with some studies reporting that impurity diffusion of silver in nickel single crystals being 1-3 orders of magnitude quicker than impurity diffusion of other atoms in nickel including tin, copper, gold and iron [13]. Additionally, data books give the pre-exponential factor (D_0) for tracer impurity diffusion of silver in nickel to be substantially higher than other metals [14] (Table 4.5).

Table 4.5: Values for the maximal diffusion coefficient (D_0) for impurity diffusion of different metals in nickel. Data from [14].

Diffusing Species	Maximal Diffusion coefficient (D_0) (cm^2s^{-1})
Ag	8.25
Cu	0.57
Au	2.00
Fe	0.22

To be an effective diffusion barrier a material must bond effectively to the metals it protects and do so with a chemical reaction of a limited range; i.e. the bond formed must be within the confines of the thickness of the diffusion barrier and not further.

Nickel is an effective diffusion barrier to many metals and is employed in many applications. However as has been shown by the experiments above its ability to prevent the diffusion of silver is substantially weaker than its ability to prevent the diffusion of other atoms. Silver and nickel are known to be immiscible elements [15] which can be seen from their binary phase diagram (Figure 4.22) and in the positive value for mixing enthalpy of binary liquid alloys ΔH_i^{mix} calculated by Miedema's model [16].

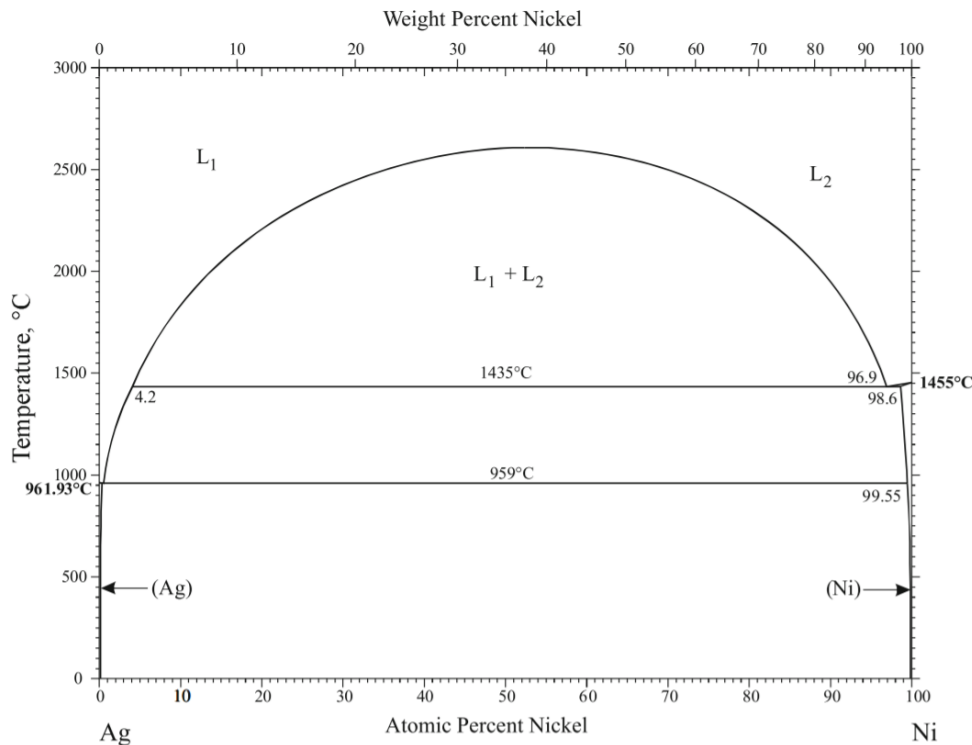


Figure 4.22: The Ag-Ni Phase diagram showing the immiscibility of silver and nickel.

Fick's first law (Equation 2.1 given in section 2.1.4) shows that the flux of atoms through an area is proportional to the concentration gradient across that area. In this particular case the concentration of atoms of silver in the brazing filler metal is high (Ag-155 is 55% Ag by weight) and in the thermoelectric material the concentration of silver is extremely low (in theory – 0). This makes the concentration gradient of silver across the diffusion barrier large and hence the driving force for diffusion is also large. As there is no driving force for the nickel and silver atoms to interact and form compounds (due to the enthalpy of mixing between silver and nickel being positive) there is no interaction between the silver and the nickel to form any compounds or a solid solution (as shown by the immiscibility of silver and nickel in the two phase region of the phase diagram in Figure 4.22). Due to this lack of interaction in the diffusion barrier, the silver diffuses straight through and onwards into the thermoelectric material beyond; leading to nickel being a poor diffusion barrier against silver diffusion.

This result goes some way to confirming why the formation of silver antimonide compounds are an issue in thermoelectric devices using antimony-containing skutterudites ($\text{Ce}_{0.5}\text{Yb}_{0.5}\text{Fe}_{3.25}\text{Co}_{0.75}\text{Sb}_{12}$ for p-type and $\text{CoSb}_{2.75}\text{Sn}_{0.05}\text{Te}_{0.2}$ for n-type) as

thermoelectric legs with joints formed from silver based filler metals. The nickel diffusion barrier which is meant to prevent the diffusion of elements from the filler metal into the sample is less effective as a barrier to silver diffusion than other materials are. As it appears to be effective at blocking the diffusion of other elements (as no other compound formation has been explicitly reported as an issue with this thermoelectric material use) it is recommended that the filler metal Ag-155 be replaced in the thermoelectric device with a filler metal which does not contain silver (or at least a very small amount of silver).

Secondary conclusions which can be drawn include that:

- Nickel diffuses well in Ag-155 as well as silver from the Ag-155 diffusing well in Ni. Nickel diffuses further into Ag-155 ($7.50\mu\text{m} \pm 0.28\mu\text{m}$) than silver in nickel ($6.40\mu\text{m} \pm 0.27\mu\text{m}$), probably due to nickel being a smaller atom than silver.
- The largest asymmetry between diffusion distances in the same system was in the brass. The silver diffused $3.58\mu\text{m} \pm 0.34\mu\text{m}$ in the brass whereas the copper diffused only $1.16\mu\text{m} \pm 0.13\mu\text{m}$ in the Ag-155. The concentration gradient for the copper is lower than for the silver (Brass is only 67wt% Cu and Ag-155 is 21wt% Cu whereas Ag-155 is 55wt% Ag and brass is 0wt% Ag giving a greater diffusion gradient for silver), reducing the driving force for diffusion.

4.4. Summary

In this chapter an array of experiments assessing the performance of an industrially available filler metal with a composition conforming to that of Ag-155 in the brazing filler metal standard BN ISO 17672-2016 were conducted. Experiments were conducted to assess the impact of surface roughness on the wetting capability of the filler metal, the influence of brazer skill and brazing torch type on the size of the diffusion zone formed and the size of the diffusion zone between Ag-155 and various base metals was measured. The findings of these experiments can be summarised as follows:

- Surface roughness has a definite and notable impact on the wetting angle formed between filler metal Ag-155 and copper substrates. In general, the smoother the surface the lower the wetting angle and hence the better contact will be formed. The data gathered in this thesis indicates the optimum roughness for giving a minimum wetting angle is $R_a = 0.09\mu\text{m} - 0.16\mu\text{m}$, significantly smoother than the industrially recommended value of $R_a = 0.6\mu\text{m} - 1.6\mu\text{m}$. Surfaces smoother than this produced a higher contact angle when tested although this could be due to the re-formation of an oxide layer which inhibits wetting. Regardless, roughness approximately in the range $R_a = 0.09 - 0.16\mu\text{m}$ will be used throughout experiments in the remainder of this thesis in order to optimise wetting between filler metals and substrates.
- No significant variance was found in the diffusion zone size of samples brazed by brazers with varying skill levels nor with different brazing torches. All 4 samples produced (novice brazer using propane, novice brazer using oxyacetylene, experienced brazer using propane and experienced brazer using oxyacetylene) had a diffusion zone size within the range of $3.5 - 5.5\mu\text{m}$. This leads to the conclusion that the performance of filler metals in future tests should not be significantly impacted by being brazed by a novice brazer and thus an experienced brazer is not required to form each joint.

- The diffusion distance of silver in nickel was further than in any other base metal tested with an average diffusion distance of $6.40 \pm 0.27 \mu\text{m}$ after being subject to a propane torch brazing cycle. As the nickel layer applied to thermoelectric materials examined in this thesis is designed to prevent diffusion and appears ineffective at preventing the diffusion of silver compared to other materials it is recommended that a replacement filler metal which does not contain silver is used as the filler metal in this application.

4.5. References

- [1] ISO/TC 44. Brazing — Filler metals (ISO 17672:2016) [Internet]. 3rd ed. British Standards Institution; 2016. Available from: <https://www.iso.org/obp/ui/#iso:std:iso:3677:ed-3:v1:en>.
- [2] Schwartz MM. Brazing [Internet]. 2nd Editio. ASM International; 2003. Available from: https://books.google.co.uk/books/about/Brazing_2nd_Edition.html?id=XSGaKuYQLjIC.
- [3] Zaharinie T, Huda Z, Izuan MF, et al. Development of optimum process parameters and a study of the effects of surface roughness on brazing of copper. *Appl. Surf. Sci.* [Internet]. 2015;331:127–131. Available from: <http://dx.doi.org/10.1016/j.apsusc.2015.01.078>.
- [4] Gremillard L, Rauch N, Saiz E. Drop_angle [Internet]. Berkeley: Lawrence Berkeley National Laboratory; 2002. Available from: http://lgremillard.free.fr/Lgremillard_Main_En.html.
- [5] Way M, Willingham J, Goodall R. Brazing filler metals. *Int. Mater. Rev.* [Internet]. 2019;0:1–29. Available from: <https://doi.org/10.1080/09506608.2019.1613311>.
- [6] Nowak WJ. Effect of Surface Roughness on Early Stage Oxidation Behavior of Ni-Base Superalloy IN 625. 2018;1–8.
- [7] Eubanks AG, Moore DG. Effect of Surface Roughness on the Oxidation Rate of Iron. 1962;382–389.
- [8] Evans JL. Effect of Surface Roughness on the Oxidation Behavior of the Ni-Base Superalloy ME3. 2010;19:1001–1004.
- [9] Roberts P. *Industrial Brazing Practice*. 2nd ed. Boca Raton, Florida: CRC press; 2013.
- [10] Porter M. *Gas Burners for Forges, Furnaces, & Kilns* [Internet]. SkipJack Press; 2004. Available from: <https://books.google.co.uk/books?id=nHkpb4cCKvQC>.
- [11] Shanmugam G. *Basic Mechanical Engineering* [Internet]. McGraw-Hill Education (India) Pvt Limited; 2000. Available from: <https://books.google.co.uk/books?id=NEfuei6gXogC>.
- [12] Justin R. Bickford. *Analyze Stripes* [Internet]. 2013. Available from: https://imagejdocu.tudor.lu/doku.php?id=macro:analyze_stripes#license_informati on.
- [13] Wazzan AR, Tung P, Robinson LB. Diffusion of silver into nickel single crystals. *J.*

Appl. Phys. 1971;42:5316–5320.

- [14] Brandes EA, Brook GB, editors. *Smithells Metals Reference Book*. 7th Editio. Butterworth-Heinemann; 1992.
- [15] Ma E. Alloys created between immiscible elements. *Prog. Mater. Sci.* 2005;50:413–509.
- [16] Takeuchi A, Inoue A. Classification of Bulk Metallic Glasses by Atomic Size Difference, Heat of Mixing and Period of Constituent Elements and Its Application to Characterization of the Main Alloying Element. *Mater. Trans.* 2005;46:2817–2829.

Chapter 5: Design of New Filler Metals for Thermoelectric Devices

5.1. Introduction

As noted in prior chapters, brazing is a metal joining technique which has evolved over thousands of years and which offers considerable advantages over other metal joining processes. It can not only join complex shapes and bond dissimilar materials but can do so with minimal microstructural evolution, producing joints which are often of relatively high strength and where necessary, electrically and thermally conductive. Whilst it is possible for a brazed joint to demonstrate this desirable array of properties, in order for the joint formed to accomplish this, the filler metal selected to form the joint must be chosen carefully. Compatibility with the materials it joins (*parent materials*) is required, as is a suitable melting temperature range, and appropriate joint design. Due to the unprecedented rate at which modern materials development occurs, in order for brazing to continue to be an effective joining technique the development of new filler metals (which can operate in particular temperature windows and the most hostile environments) is necessary.

This chapter focuses on the development of new brazing filler metals for joining thermoelectric devices as currently available filler metals are not well suited to this application and thus new filler metals must be developed. High entropy alloys have attracted considerable interest over the course of the last decade due to their unusual microstructures and array of remarkable properties which have the potential to exceed the performance of many currently used engineering materials. This chapter investigates the potential of using high entropy materials as brazing filler metals for joining thermoelectric devices within automotive exhaust systems. It outlines the design process followed to produce new high entropy alloy systems and the testing conducted in order to assess the viability of these newly developed alloy systems as filler metals for the chosen application.

Thermoelectric devices offer the potential to recover energy from waste heat lost in exhaust systems of automotive vehicles (Figure 5.1) and convert this heat into electricity which can be fed back into the vehicles' powertrain to perform useful work. With climate change being one of the principal issues engineers will face over the next century, the reduction of carbon dioxide emission is an immediate priority and the recycling of waste heat from inefficient automotive engines into electricity offers an opportunity to improve the efficiency of the modern automobile, thus indirectly reducing carbon dioxide emissions. Additionally, many governing bodies now impose financial penalties on vehicle manufacturers (such as the Corporate Average Fuel Economy imposed by the US congress [1]) to ensure vehicle efficiency. Thus the development of thermoelectric devices offers not only environmental benefits (by reducing vehicle emissions) but financial ones as well (by producing more efficient vehicles which will not be penalised for excessive emissions).

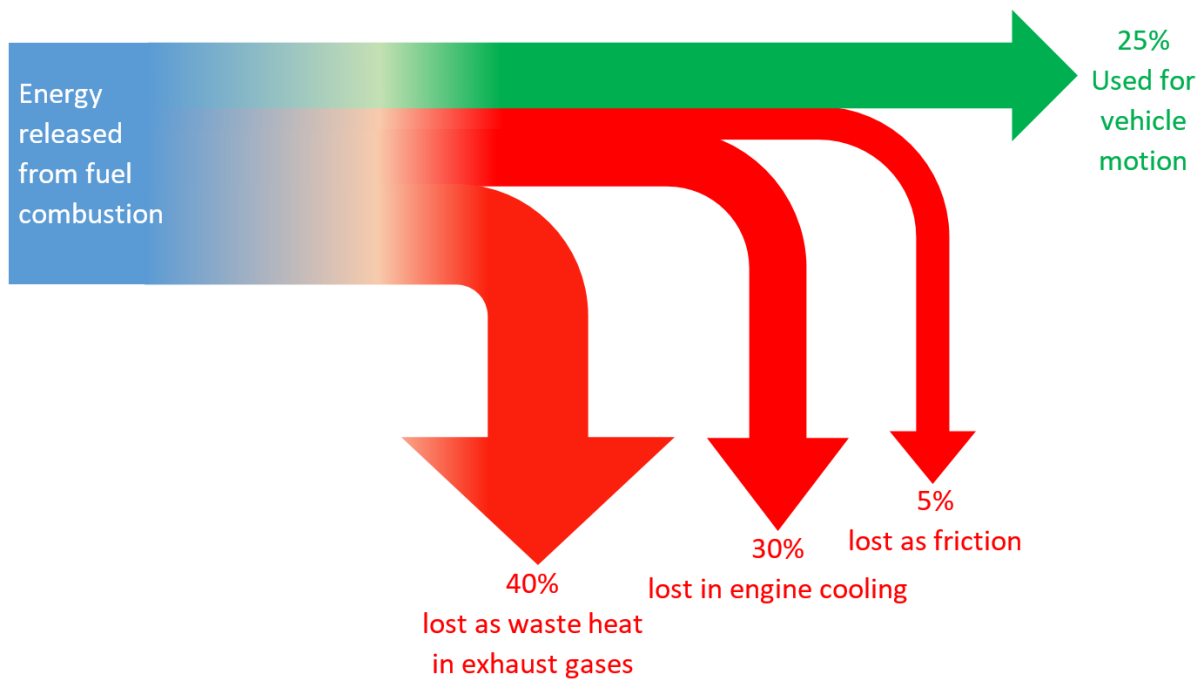


Figure 5.1: The breakdown of energy uses in an internal combustion engine, highlighting the inefficiency and showing that the heat lost in exhaust gases is a primary source of energy wastage.

Whilst the development of thermoelectric devices is a promising technological advancement, several issues must be solved before their successful implementation within automotive vehicles is viable.

Firstly, improvements in the efficiency of thermoelectric materials is necessary. Information on thermoelectric efficiency and current progress in this field can be found in Section 2.3.5.

Secondly, an appropriate joining process must be found. In the manufacture of thermoelectric modules, joining of thermoelectric materials is of critical importance. Brazing is one potential process by which this joining may be accomplished. In order for brazing to be an applicable joining technique a suitable filler metal is needed for bonding the thermoelectric material to the electrical contacts (often copper) which connect the thermoelectric device to the powertrain. The development and assessment of a filler metal suitable for this application is the primary objective of this thesis. The criteria by which the suitability of a filler metal for this application can be assessed are as follows.

1. The filler metal must be capable of wetting the bonding surfaces to be joined (in this application a copper electrical contact and a thermoelectric material coated with a nickel diffusion barrier). This means that the chosen filler metal must be able to form a metallurgical bond between copper and nickel. This metallurgical bond is often created by the interdiffusion between the filler metal and the constituent elements of both materials which it joins and the formation of compounds between them.
2. Secondly, the filler metal must possess an appropriate melting range for the application. Should the filler metal's melting range lie below the operating temperature then it will be unsuitable as it will melt in service

and hence the joint will fail. Should the filler metal possess a melting range which is too high then the temperature required to melt the filler metal during component assembly will be sufficient to damage the thermoelectric elements in the device and thus the joining method will not be viable. For this particular application a melting range within the temperature range 550°C-620°C is required. This optimal melting temperature range for developed alloys will be described as $T_{opt}=550-620^{\circ}$ for simplicity throughout the remainder of this work.

3. The filler metal chosen must not be capable of diffusing through the diffusion barrier (in this instance a 10 μ m nickel layer) applied to the thermoelectric material. As mentioned in Section 2.3.5, excessive diffusion during bonding can lead to a reduction in thermoelectric performance due to diffusive species altering the composition of thermoelectric compounds which can adversely impact electrical properties (e.g. the diffusion of Ni from a bonding layer forming a p-type region inside an n-type thermoelectric raising the contact resistance of the interface in a study by Liu [2],[3]) and give poor mechanical interfaces [4]. It is believed that a similar mechanism to that found by Liu may be occurring in the thermoelectrics in this study in which the silver contained in the Ag-155 filler metal used to join the skutterudite thermoelectric diffuses through the nickel barrier layer and reacts with antimony in the skutterudite thermoelectric, impacting its electrical performance.

The combination of these above requirements excludes current standard industrial filler metals from this application. A majority are unsuitable due to the melting temperature requirement alone; as can be seen from Figure 5.2, no solders (shown in black) and hardly any brazing filler metals fit the melting temperature range determined.

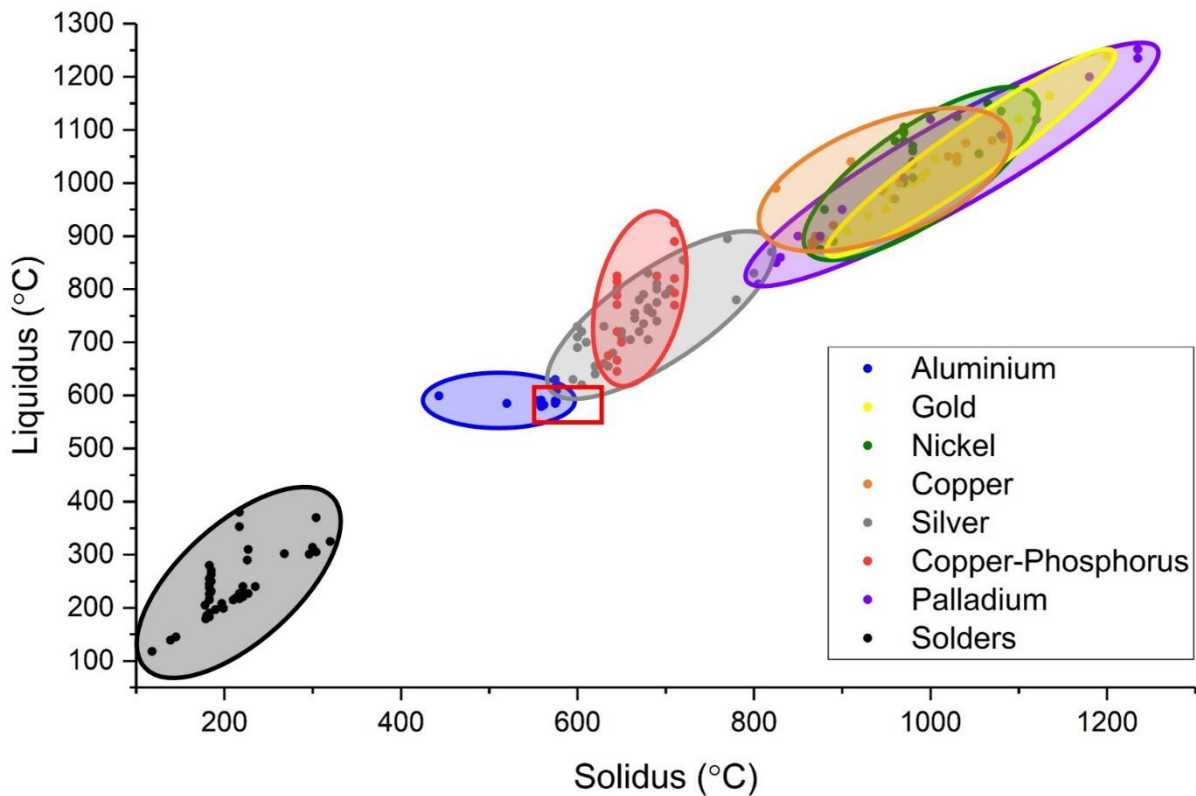


Figure 5.2: Graph showing the solidus and liquidus temperatures for all filler metals found in ISO 9453:2014 (solders) [5] and ISO 17672:2016 (brazes) [6]. The different families of filler metal are highlighted and the allowable melting temperature range for the thermoelectric joining application in this study is shown by a red box.

The few brazing filler metals which do melt in the correct temperature window (10 from the aluminium family and 2 from the silver family) are also unsuitable for various reasons; the silver family fillers both contain cadmium – an element banned from use in non-military applications ([7]) and the aluminium bearing filler metals all contain a high percentage aluminium. Aluminium and copper (the interconnect material of choice) readily form an array of high-hardness intermetallic compounds (Cu_2Al , Cu_3Al_2 , CuAl) especially when exposed to elevated temperatures (above 200°C) which substantially reduce the mechanical properties of the copper-aluminium interface [8]. Additionally, the growth of the intermetallic layer at this interface drastically increases the contact resistance of the joint adversely affecting its ability to act as an effective electrical contact. In a self-perpetuating issue the increased interface resistance leads to heating at the interface which further drives intermetallic formation. For these reasons aluminium based filler metals are unsuitable as the brazing filler metals for this application.

Thus the design of a new filler metal which can satisfy these 3 criteria sufficiently is required. It is the production of a filler metal capable of meeting these criteria that is the primary focus of this thesis.

5.2. Composition Modelling

5.2.1. Element Selection

As mentioned previously (Section 2.2) high entropy alloys (HEAs) have received significant attention since the principal papers observing their unique solid solution microstructures were published in 2004 [9] [10]. The unusually low number of phases often seen in alloys of this type often manifests in promising mechanical properties and numerous studies have been conducted on several systems of this type including CoCrFeMnNi [11] [12] [13] and alloys produced from refractory metals such as NbMoTaW, VNbMoTaW and MoNbTaTiV [14] [15] [16]; many of these studies focus on the mechanical properties of these alloys, particularly at elevated temperatures (perhaps unsurprisingly considering the refractory elements which constitute some of these systems). The systems referenced above are compliant with the original proposed definition of a high entropy alloy which specifies that alloys of this type should contain at least 5 principal elements in near-equiatomic ratios (each element within the range of 5-35at%) [10]. The large number of components within these systems gives rise to a substantially higher configurational entropy than would be seen in more standard engineering materials in which a single element makes up a large percentage of the alloy with only minor additions to improve properties. It is this elevated level of configurational entropy that is often cited as enabling the formation of single phase systems where multiple phases would be expected [10], however some researchers question how dominant the role of configurational entropy is in determining whether a HEA is single phase [17]. Early studies in the field championed the effect of entropic stabilisation ([18][19]) but more recent studies indicate that many compositions claimed to be single phase HEAs actually precipitate secondary phases when exposed to aging treatments including the original exemplar CrMnFeCoNi alloy (the ‘Cantor’ alloy) ([20]). Further evidence exists to counteract the view that high entropies are what stabilise solid solutions in alloys with multiple principal components. A study by Otto substituted elements in known HEAs with others that had the same crystal structure and similar atomic size in order to maximise solubility chances via the Hume-Rothery rules [21]. They found that in each substitution case that the substitution led to the formation of intermetallic phases in the structure even though the configurational entropy was the same. This led to the conclusion that entropy may stabilise solid solutions in rare cases but does not overcome the formation of an intermetallic when the enthalpic driving force is strong enough. Furthermore, rapid screening of alloy systems via computed phase diagrams generated with CALPHAD indicate that as the number of principal components increases (which increases configurational entropy) the fraction of potential alloys which are solid solutions decreases indicating that simply maximising entropy does not lead to an increased likelihood of finding solid solution alloy systems [22]. This balance of evidence leads the author to conclude that the impact of other parameters on the formation of a solid solution is likely greater (e.g. the atomic size difference and the enthalpy of mixing) and as such these parameters should be preferentially optimised ahead of the entropy of mixing.

The single phase structure allows some HEAs to demonstrate an array of impressive mechanical properties ranging from high yield strengths ($\sigma_{0.2} = 1246\text{MPa}$ for a $\text{V}_{20}\text{Nb}_{20}\text{Mo}_{20}\text{Ta}_{20}\text{W}_{20}$ alloy [14]), to good wear resistance (an $\text{Al}_{0.2}\text{Co}_{1.5}\text{CrFeNi}_{1.5}\text{Ti}_{0.5}$ high entropy alloy has been shown to demonstrate a wear resistance $3.6\times$ higher than conventional wear resistant steels (AISI 52100)) [23] and exceptional ductility (rolling

extensions of 4257% have been demonstrated with an Al-Cr-Fe-Mn-Ni alloy [18]). Additionally, HEAs have been shown to possess impressive corrosion resistance (Chen et al. found that the HEA Cu_{0.5}NiAlCoCrFeSi possessed superior corrosion resistance when compared to AISI 304 stainless steel when exposed to 0.1-1.0M H₂SO₄ and NaCl at 25°C (although it did suffer more from pitting) [24] [25]. This combination of impressive properties and potentially high corrosion resistance (backed up by the fact that many current industrial filler metals contain 4 or more components in relatively high atomic percentages [6]) make high entropy materials valid candidates for development as new brazing filler metals. Recently researchers have begun to investigate the potential of high entropy alloy compositions as filler metals with some promising evidence offered as to their suitability (see Section 2.1.7.4) [26][27][28][29].

Investigations into suitable high entropy materials for use as brazing filler metals required the narrowing of the elements to a pool of potentially suitable candidate elements. This was undertaken by eliminating elements which were gaseous or liquid at room temperature (marked in red in Figure 5.3 and those which were radioactive, too toxic or too reactive to be safely processed (marked in orange in Figure 5.3).

1																	2
H																	He
3	4											5	6	7	8	9	10
Li	Be											B	C	N	O	F	Ne
11	12											13	14	15	16	17	18
Na	Mg											Al	Si	P	S	Cl	Ar
19	20	21	22	23	24	25	26	27	28	29	30	31	32	33	34	35	36
K	Ca	Sc	Ti	V	Cr	Mn	Fe	Co	Ni	Cu	Zn	Ga	Ge	As	Se	Br	Kr
37	38	39	40	41	42	43	44	45	46	47	48	49	50	51	52	53	54
Rb	Sr	Y	Zr	Nb	Mo	Tc	Ru	Rh	Pd	Ag	Cd	In	Sn	Sb	Te	I	Xe
55	56	...	72	73	74	75	76	77	78	79	80	81	82	83	84	85	86
Cs	Ba	...	Hf	Ta	W	Re	Os	Ir	Pt	Au	Hg	Tl	Pb	Bi	Po	At	Rn
87	88	...	104	105	106	107	108	109	110	111	112	113	114	115	116	117	118
Fr	Ra	...	Rf	Db	Sg	Bh	Hs	Mt	Ds	Rg	Cn	Uut	Fl	Uup	Lv	Uus	Uuo
57	58	59	60	61	62	63	64	65	66	67	68	69	70	71			
La	Ce	Pr	Nd	Pm	Sm	Eu	Gd	Tb	Dy	Ho	Er	Tm	Yb	Lu			
89	90	91	92	93	94	95	96	97	98	99	100	101	102	103			
Ac	Th	Pa	U	Np	Pu	Am	Cm	Bk	Cf	Es	Fm	Md	No	Lr			

Figure 5.3: The periodic table of the elements highlighting elements eliminated from inclusion in the high entropy alloy design.

The remaining elements (those in white in Figure 5.3) were analysed in greater depth to assess which would be most suitable for inclusion in a python programme designed by Dr Robert Snell of the University of Sheffield. The remaining 19 elements were assessed using 3 criteria which correspond to the criteria a filler metal must meet for the thermoelectric application.

1. Wet, flow across and join copper and nickel - The filler metals developed must wet and flow across copper and nickel and be capable of forming a bond between copper and nickel otherwise they will not function as filler metals. A liquid is said to have a high wettability on a surface if it forms a contact angle <90°. As such, filler metals developed in this study will be deemed to suitably wet copper and nickel if they exhibit wetting angles <90°.
2. Melting temperature – Alloys derived from elements with high melting temperatures are more likely to possess high melting temperatures

(barring the presence of substantial eutectics) and as such there is a bias towards low melting temperature elements. As such, elements were ranked on their melting temperature on a 3-point scale. A green rating was given to elements whose melting temperature was <120% of the maximum of optimal temperature range ($T_{opt}= 550-620^{\circ}$) e.g. $T_m < 744^{\circ}\text{C}$; an amber rating was given to elements with a melting temperature in the range of $120\%T_{opt} < T_m < 200\%T_{opt}$ e.g. $744^{\circ}\text{C} < T_m < 1240^{\circ}\text{C}$, and a red rating assigned to elements whose melting temperature exceeded 200% of T_{opt} ($T_m > 200\%T_{opt}$) e.g. $T_m > 1240^{\circ}\text{C}$.

3. Diffusion coefficient in nickel – As the filler metal should not diffuse through the nickel diffusion barrier, ideally the constituent elements of a designed filler will diffuse slowly in nickel. Again a 3-point scale was used to rank elements diffusion coefficient in nickel with elements whose diffusion coefficient being the same order of magnitude (or a lower order of magnitude) as the self-diffusion coefficient of nickel at 773K being given a green rating, elements with a coefficient of diffusion one order of magnitude higher being given an amber rating and elements with a coefficient of diffusion in nickel being more than one magnitude higher than nickel self-diffusion at 773K being given a red rating.

As mentioned previously the formation of certain antimony compounds is highly detrimental to thermoelectric performance and as such, elements which are unlikely to form antimony compounds are preferential for inclusion within the filler metals developed. This is so that even if filler metal constituents diffuse through the diffusion barrier into the thermoelectric material they are less likely to have a serious impact on the performance of the thermoelectric. The assessment of the likelihood for elements to form compounds with antimony was made using the binary phase diagrams for each element with antimony. The example diagram shown in Figure 5.4 shows the large number of compounds that can form between silver and antimony.

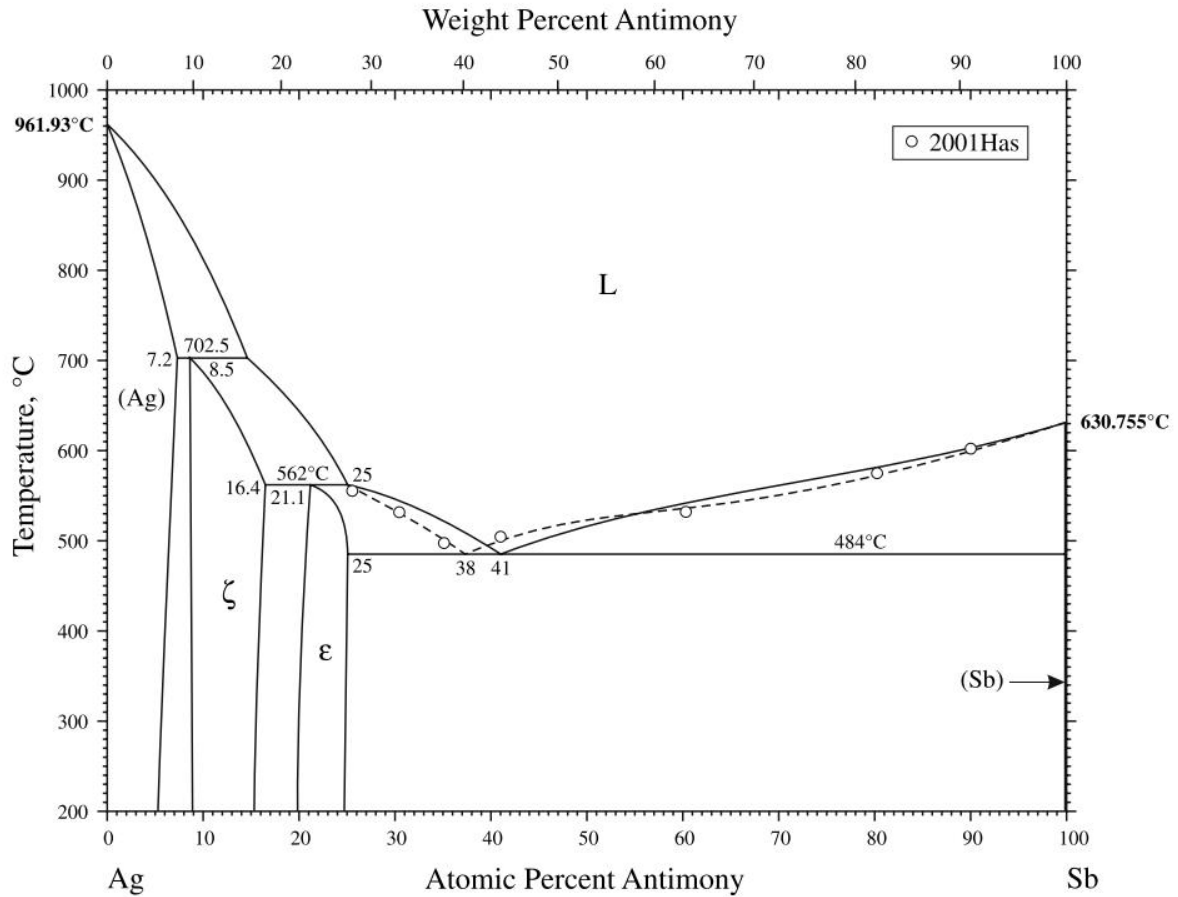


Figure 5.4: The silver antimony phase diagram illustrating the array of compounds which can be formed [30].

A summary of the data collected for these criteria is presented in Table 5.1. The ability of the filler metal to wet, flow over and join copper and nickel cannot accurately be assessed for at this design stage but information pertaining to criteria 2 and 3 (melting temperature and diffusion in nickel) can be researched. Additionally, awareness of which elements are likely to form compounds with antimony can be gleaned from examination of the phase diagrams of each respective element and antimony. A combination of this information alongside prior knowledge of elements likely to perform well in a brazing filler metal led to the selection of 10 elements to be entered into Dr Robert Snell's Python script [29].

Table 5.1: Table listing the properties of candidate elements for use in filler metal compositions.

Element	Diffusion coefficient in nickel at 773K (500°C) $\times 10^{-19} \text{ cm}^2\text{s}^{-1}$	Melting Temperature (°C)	Formation of antimony compounds? (Y/N)	Selection (Y/N)
Aluminium	15.01 [31]	660	Y	Y
Silicon	-	1414	N	N
Phosphorus	-	44	Y [32]	N
Vanadium	1.37 [33]	1910	-	N
Chromium	873675 [33]	1907	Y	N
Manganese	8.00 [31]	1246	Y	N
Iron	3.26 [33]	1538	Y	N
Cobalt	0.71 [31]	1495	Y	N
Nickel	2.46 [33]	1455	Y	Y
Copper	40.99 [33]	1085	Y	Y
Zinc	-	420	Y	Y
Gallium	-	30	Y	Y
Germanium	30.34 [34]	938	N	Y
Silver	11283 [33]	962	Y	N
Indium	110 [35]	157	Y	Y
Tin	90.72 [33]	232	Y	Y
Tellurium	-	450	Y	N
Gold	8.37 [33]	1064	Y	Y
Bismuth	-	271	Y	Y

The 10 elements taken forward as candidate elements for use in brazing filler metals are highlighted in column 5 of Table 5.1.

The ten elements chosen were input into a simple python model. The script models all potential compositions of any combination of 4 or 5 of the 10 inputted elements in 1at% intervals. An example for a 4 component alloy system using elements “A”, “B”, “C” and “D” is shown below in Table 5.2 as an example.

Table 5.2: An illustration of how the python program cycles through potential alloy compositions within a single system of 4 elements. Each different composition is calculated in steps of 1at%. For a 4 element system n= 156,849, for a 5 element system n= 211,876.

Composition number	Element 'A' (at%)	Element 'B' (at%)	Element 'C' (at%)	Element 'D' (at%)
1	97	1	1	1
2	96	1	1	2
3	96	1	2	1
Program proceeds through each possible combination of the 4 elements in 1at% increments				
n-1	2	1	1	96
n	1	1	1	97

For each composition within each alloy system the program calculates the value of the 6 parameters explained in Section 2.2.2 and stores them within an array. The formulae used to calculate each parameter are included below for clarity.

1) Atomic Size Difference

$$\delta = 100 \sqrt{\sum_{c_i}^n c_i \left(1 - \frac{r_i}{\bar{r}}\right)^2} \quad \text{Equation 5.1}$$

in which $\bar{r} = \sum_{i=1}^n c_i r_i$ where c_i is the atomic percentage of element i and r_i is the atomic radius of element i. 100 is a constant used as an amplification factor.

2) Enthalpy of Mixing

$$\Delta H_{mix} = \sum_{i=1, i \neq j}^n \Omega_{ij} c_i c_j \quad \text{Equation 5.2}$$

in which $\Omega_{ij} = 4^*(\text{mixing enthalpy of binary liquid alloys})$.

3) Entropy of Mixing

$$\Delta S_{mix} = -R \sum_{i=1}^n c_i \ln c_i \quad \text{Equation 5.3}$$

in which R is the gas constant ($8.314 \text{ Jmol}^{-1} \text{ K}^{-1}$)

4) Electronegativity Difference

$$\Delta X = \sqrt{\sum_{i=1}^n c_i (X_i - \bar{X})^2} \quad \text{Equation 5.4}$$

where X_i is the Pauling electronegativity for element i and $\bar{X} = \sum_{i=1}^n c_i X_i$

5) Valence Electron Concentration (VEC)

$$VEC = \sum_{i=1}^n c_i(VEC)_i \quad \text{Equation 5.5}$$

where T_m is the melting temperature of the alloy systems calculated via the rule of mixtures approach:

$$T_m = \sum_{i=1}^n c_i(T_m)_i \quad \text{Equation 5.6}$$

The data for each element required to calculate these formulae for each composition can be found in Table 5.3 [36] [37].

Table 5.3: Parameter values for each of the 10 elements chosen required to calculate the atomic size difference, Electronegativity difference, Valence Electron Concentration and the melting temperature of the alloy system using the rule of mixtures [36] [37].

	Al	Ni	Cu	Zn	Ga	Ge	In	Sn	Au	Bi
Atomic Radius r_i (Å)	1.432	1.246	1.278	1.395	1.392	1.240	1.659	1.620	1.442	1.640
Pauling Electronegativity X_i	1.61	1.91	1.90	1.65	1.81	2.01	1.78	1.96	2.54	2.02
Valence Electron Concentration VEC	3	10	11	12	3	4	3	4	11	5
Melting temperature T_m (°C)	660.3	1455.0	1084.6	419.5	29.8	938.3	156.6	231.9	1064.2	271.4

The array of mixing enthalpy of binary liquid alloys for each pair of elements can be found in Table 5.4.

Table 5.4: The mixing enthalpy of binary liquid alloys ΔH_{ij}^{mix} for each pair of elements in kJ/mol [38].

	Al	Ni	Cu	Zn	Ga	Ge	In	Sn	Au	Bi
Al		-22	-1	1	1	-14.5	7	4	-22	10
Ni			4	-9	-15	-23.5	2	-4	7	10
Cu				1	1	-11.5	10	7	-9	15
Zn					0	-15.5	3	1	-16	4
Ga						-15.5	3	1	-19	4
Ge							-13.5	-12.5	-21.5	-7.5
In								0	-11	-1
Sn									-10	1
Au										2
Bi										

Once the values for all 6 measured parameters are calculated they are stored in an array along with the exact composition they correspond to (in at%). The final stage is then to filter these results. Numerical values can be assigned to each parameter by which all compositions in the array are filtered. If the value of any one parameter from any composition falls outside the range input by the user, then that composition is omitted from the displayed results. The list of passed compositions and the value of each calculated parameter associated with each alloy composition is the output to the screen.

5.2.2. Modelling Results

Using the parameter values in Table 5.5 (taken from the solid solution formation boundaries in [39] – see Section 2.2.2), a series of alloy systems were identified as being potentially viable multicomponent filler metal systems. Additionally, a rule of mixtures calculation was used to provide an estimated melting temperature for each of the alloy systems evaluated which is similar to that used by *Yang and Zhang* [40]. This provides a rough estimate of melting temperature (which does not account for melting point suppression by eutectic compositions, or elevation by the formation of stable compounds) which should be sufficient to eliminate alloys whose melting temperature lies drastically outside the range required by this application.

Table 5.5: The filtering values used for each parameter in the python code based on the solid solution region defined by Zhang in [39].

Parameter	Accepted values
Atomic Size difference (δ)	$0 < \delta < 5$
Enthalpy of mixing (ΔH_{mix})	$-2.5455\delta - 2.4545 < \Delta H_{mix} < -\frac{15}{11}\delta + \frac{70}{11}$
Entropy of mixing (ΔS_{mix})	$11 < \Delta S_{mix} < \infty$
Electronegativity difference	No filter applied
Valence Electron Concentration (VEC)	No filter applied
Rule of mixtures melting temperature (T_m)	$550^\circ\text{C} < T_m < 620^\circ\text{C}$

Many systems which passed these filters had multiple compositions which were within the set parameters (e.g. the system AlCuZnGa had 3916 compositions pass the filters - Table 5.6); where multiple compositions within a single system passed the parameter values used, the composition with the lowest atomic size mismatch parameter (δ) was chosen as the composition to be manufactured. The chosen composition for each system evaluated can be found in Table 5.6.

Table 5.6: The weight percentages of the 5 alloy compositions manufactured as potential filler metal systems for joining thermoelectric devices.

Alloy Designation	System elements	No. passed composition	Weight %										Total
			Al	Ni	Cu	Zn	Ga	Ge	In	Sn	Au	Bi	
A	Al Cu Zn Ga	3916	17.40	-	20.50	40.93	21.17	-	-	-	-	-	100.00
B	Ni Cu Zn Ga	36	-	10.77	24.30	34.00	30.93	-	-	-	-	-	100.00
C	Ni Cu Zn Ga Ge	62	-	5.34	26.96	31.70	33.80	2.20	-	-	-	-	100.00
D	Cu Zn Ga Sn Au	4	-	-	25.45	31.42	24.20	-	-	3.17	15.77	-	100.00
E	Cu Zn Ga Au Bi	1	-	-	24.85	30.68	23.63	-	-	-	15.40	5.45	100.00

It was noted that the inclusion of gold within some of the compositions would considerably raise the cost of producing some of the potential filler metal compositions. Whilst the initial challenge of developing a new filler metal did not highlight any cost barriers it was advised by the technical staff from the industrial sponsor that the inclusion of gold may lead to filler metal compositions that might not be financially viable to implement. To combat this, any compositions containing gold were made as the python script suggested but were also formed into gold free alloys.

Two different methods for producing gold free compositions were considered.

1. Firstly, the system could be ‘re-optimised’ by re-running the initial program to examine the ‘Cu-Zn-Ga-Sn’ and ‘Cu-Zn-Ga-Bi’ systems (i.e. the original ‘Alloy D’ and ‘Alloy E’ systems but without gold included).
2. Secondly, the gold could simply be removed from the gold containing systems (‘alloy D’ and ‘alloy E’) and the remaining components scaled up to produce gold-free compositions with the 4 non-gold elements in the system maintaining the same ratios as they had before.

The advantage of the first method is that the system would be optimised identically to the first compositions and the advantage to the second method would be that the compositions are more directly comparable due to having the same ratios of elements as their gold-containing counterparts (‘alloy D’ and ‘alloy E’). Both methods were run and the 4 parameters that the python program filtered alloy compositions by were applied to each of the two methods for both compositions. The results of this analysis for ‘alloy D’ with gold removed can be seen in Table 5.7.

Table 5.7: Parameter comparison for 2 methods of producing gold-free analogues of ‘alloy D’ using the same parameters as alloy D was originally evaluated by the python code used to select alloy compositions.

	Atomic size difference (δ)	Enthalpy of mixing (ΔH_{mix}) kJ mol ⁻¹	Entropy of mixing (ΔS_{mix}) kJ K ⁻¹ mol ⁻¹	Melting Temperature (T_m) °C
Program optimised	7.75	2.35	11.0	551
Gold removed and components scaled	4.84	1.09	9.72	520

The removal of gold from the composition and the scaling up of the other constituents in order to attempt to keep the ratios of the other components of the alloy the same was deemed to be the most suitable method for producing gold-free alloy compositions. The 2 primary selection criteria for solid solution formation of minimising the atomic size difference (δ) and keeping enthalpy of mixing (ΔH_{mix}) close to 0 [41][42][36][43], both give the scaled composition as being superior to the program re-optimised composition. Although it should be noted that the scaled composition does possess a slightly lower entropy of mixing (ΔS_{mix}) and has a predicted melting temperature (T_m) slightly lower than the design criteria for brazing filler developed in this work. A similar result was found for the same analysis but with the constituents of alloy E (see Appendix 1).

As the scaled composition possessed values for δ and ΔH_{mix} closer to the optimum levels and as using the scaled composition gives a more similar basis for comparison between the gold containing and gold free versions of the alloy, this method of producing a gold-free alloy was chosen. The gold-free versions were thus made using the scaled composition method and tested alongside their gold-containing counterparts. The compositions of the gold free alloys used throughout the rest of this work can be found in Table 5.8.

Table 5.8: The nominal weight percentages of the 2 gold-free alloy compositions designed as potential filler metal systems for joining thermoelectric devices.

Alloy	System elements	Weight %					Total
		Cu	Zn	Ga	Sn	Bi	
DAuX	Cu Zn Ga Sn	30.21	37.30	28.73	3.76	-	100.00
E AuX	Cu Zn Ga Bi	29.37	36.26	27.93	-	6.44	100.00

5.3. Brazing Testing

5.3.1. Cu-Cu Joining

Once manufactured according to the experimental method in section 3.2.1 the brazing filler metals were sectioned and manufactured into a size suitable for brazing. Joining of copper coupons was used to assess whether the filler metal would wet and flow on a copper surface and form a sufficient joint. Observations of the wetting and flow behaviour of each alloy were recorded and are included in Table 5.9. An example of a joint formed (and a side-by-side comparison with a standard industrial filler metal) can be seen in Figure 5.5. This test was to assess whether joining to the copper interconnect within the thermoelectric device was feasible.

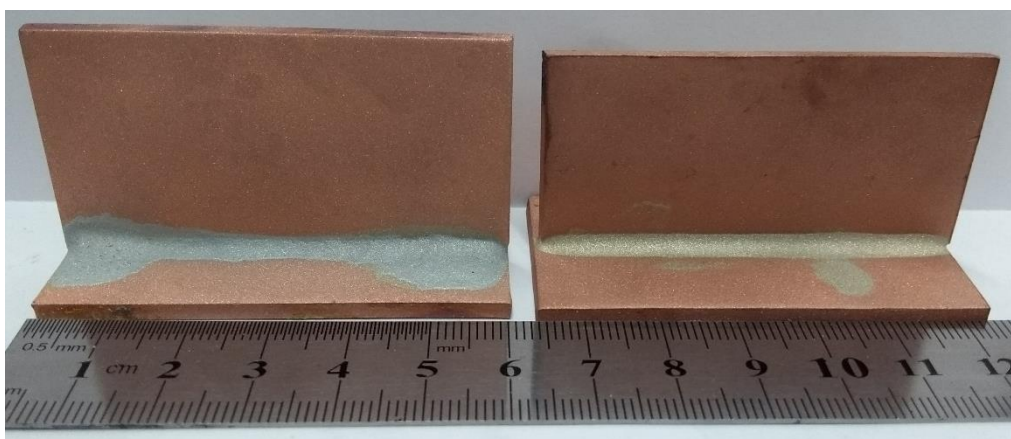


Figure 5.5: Photograph of joints between two copper coupons formed using alloy E and a comparison to a similar joint formed with industrially standard filler metal conforming to the specification of BS EN ISO 17672:2016 Ag-155.

5.3.2. Ni-Ni Joining

Once it had been established that suitable joins could be formed between copper coupons with some of the alloys systems developed, a similar test using nickel coupons was required to assess whether the developed filler metals would be able to adhere to the nickel barrier coating applied to the thermoelectric. Again, the filler metal would have to wet and flow well across a nickel surface and form an adequate joint. An example of a joint formed between nickel coupons using a developed filler metal can be seen in Figure 5.6 and observations on the wetting and flow of the alloy from the experiment are recorded in Table 5.9.

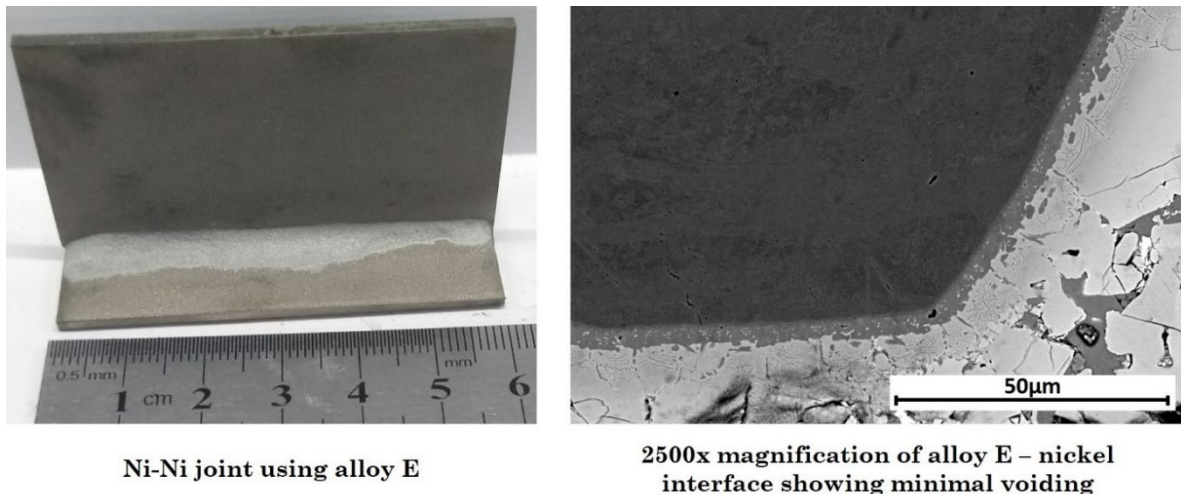


Figure 5.6: Photograph of a joint between two nickel coupons formed using alloy E (Left) and a 2500x BSE micrograph of the braze-nickel interface showing a lack of voids indicating a good joint (Right).

5.3.3. Cu-Ni Joining

A final assessment of the ability to join metals was made using one copper coupon and one nickel coupon in order to assess whether the joining of dissimilar metals using the developed filler metals was possible. Figure 5.7 shows a joint formed between copper and nickel, demonstrating that dissimilar metal joining using alloys developed in this work is possible.

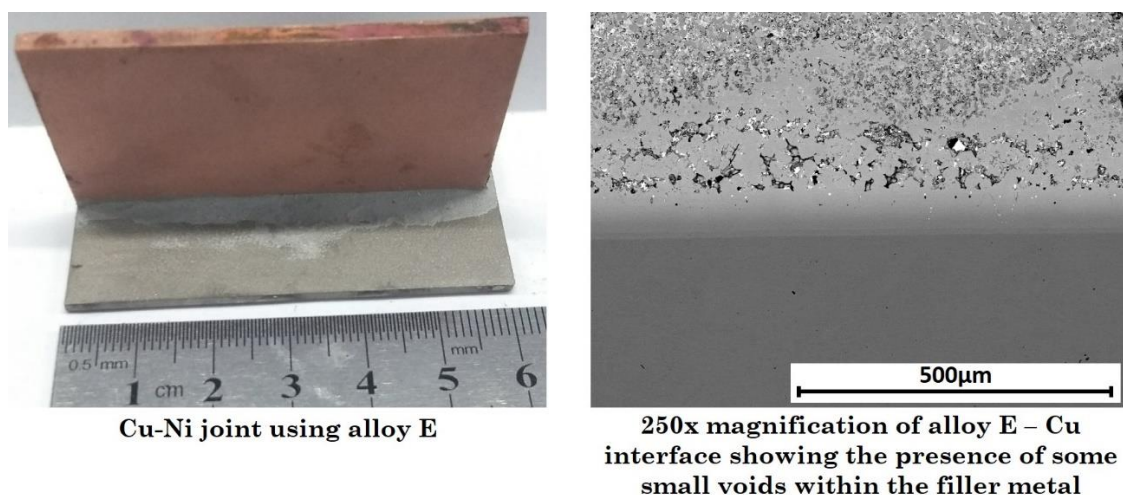


Figure 5.7: (Left) A joint between nickel and copper formed using alloy E and (Right), A 250x magnification SEM image of a Cu-braze interface. Some voids can be seen in the filler metal.

Table 5.9: Table of observations on flow, wetting and joining for each brazing filler metal tested.

Alloy	Observations			Nickel to nickel joint void % (%)
	Joining copper to copper	Joining nickel to nickel	Joining copper to nickel	
A	Did not melt or flow, even under direct heating.			N/a
B	Did not melt or flow even under direct heating. Alloy was brittle.			N/a
C	Did not flow (balled up in the corner). A joint formed but there was a crack in the filler metal			N/a
D	Melted easily, flowed well. Joint survived quenching. Cracking observed post quench.	Flowed well and melted easily. Penetrated both sides of the joint.	Flowed slowly but reasonably well, using plenty of torch encouragement it flowed through to the back of the joint	1.55
DAuX	Melted well. Did not flow well, with heavy prompting with the torch flame it flowed approximately 1cm along the joint but no further – poor wettability of Cu. Joint survived quenching	Flowed well, formed a join quickly, relatively little heating needed. Sample broke when sandblasted, the uneven fracture surface indicates a brittle fracture	Required direct heating to melt, metal ‘slid’ over Ni whilst partially solid. Didn’t penetrate the back of the joint (either due to insufficient filler, narrow joint gap or the filler having poor flow). Broke upon sandblasting.	11.33
E	Melted quite easily (less easily than D). Flowed very well along joint. Filler metal slightly penetrated to the back of the joint.	Melted slowly, flowed slowly but well, penetrated the back of the joint easily. Good wetting. Distributed well across the joint.	Flowed slowly but penetrated both sides of the joint well. High heating was required – copper was quite blackened.	2.02
E AuX	Melted after direct heating with the flame. Flow was slow and required a lot of dragging with the torch flame. Survived a quench.	Took a long time to melt (Ni was red hot), and to cool – joint was wobbly while cooling. Full length crack in the alloy after sandblasting (not known if this was due to the sandblasting or if sandblasting just revealed it)	Flowed well, penetrated both sides of the joint but required high heating. Small crack on the left hand side visible after sandblasting (not known if this was due to the sandblasting or if sandblasting just revealed it)	13.14

Alloys A, B and C all performed very poorly. Alloy A didn't melt or flow even under direct torch heating and whilst alloy B did melt, it did not flow across the copper surface at all. In both cases this indicates a poor ability of the filler metal to wet copper. Aluminium has a strong affinity for oxygen, readily forming an oxide layer, it is possible that in the case of alloy A, the aluminium constituent of the alloy reacted with oxygen present and formed a passivating layer on the surface of the filler metal which discouraged flow. Alloy B contained a substantial percentage of nickel (10.77at%) which was the highest melting point element used in any alloy developed in this study (1455°C). The fact that the alloy was very brittle indicates intermetallic formation within the alloy; if these intermetallic compounds were nickel containing intermetallics it is likely that their melting point would be quite high. It is possible that the presence of intermetallics in this system raised the melting temperature of alloy B to levels higher than could be attained by the propane torch and thus melting was not seen. Finally, alloy C melted well but did not flow across the copper surface at all. When fully molten the alloy balled up in the corner of the joint clearly demonstrating a poor ability to wet the copper surface. The poor performance of alloys A, B and C in these initial brazing tests (failing to melt easily or flow on copper surfaces) indicated that they were unlikely to perform as suitable brazing filler metals. Due to this conclusion these 3 alloy systems were removed from subsequent testing. An approximate joint void percentage for Ni-Ni joints determined by a particle analysis in ImageJ using 500x magnification SEM images of the braze region can be found in column 4 of Table 5.9 for the 4 alloys that successfully joined nickel to nickel. It indicates that void% is higher for the gold free alloy systems, however all 4 alloys examined have low void percentages (<15%).

5.4. Compositional Verification

The accuracy of the manufacturing technique was assessed using a number of analysis techniques to establish whether losses of any constituent elements had occurred during formation of the new alloy systems. The composition of each of the 4 filler metals which were carried forward to further testing (D, DAuX, E, EAuX) were verified by an external UKAS accredited laboratory working to ISO 17025 standard. The quantities of any metal elements within the samples were verified using Inductively Coupled Plasma – Optical Emission Spectroscopy (ICP-OES) on a Thermo ICAP instrument (6500). Impurity analysis was also undertaken to assess the effectiveness of the borax glass at preventing oxidation of the melt pool during processing. LECO elemental analysers were used to assess carbon, nitrogen and oxygen levels within the samples. Inert gas fusion using a helium carrier gas was used to detect nitrogen and oxygen levels within the samples. The samples nitrogen content was detected using thermal conductivity and the oxygen content was assessed with infrared. Carbon levels were detected using infra-red detectors to assess the sample when burnt under flux in an oxygen atmosphere.

The determined composition for each of the 4 alloys (D, DAuX, E, EAuX) can be found in Table 5.10 below, the impurity levels present in each assessed sample can be found in Table 5.11.

Table 5.10: Externally determined composition of each alloy system using ICP-OES performed to ISO 17025.

Alloy Designation	Determined Composition (Wt%)						Total identified Wt% (Wt%)
	Cu	Zn	Ga	Sn	Au	Bi	
D	26.19	31.19	24.25	3.07	15.65	-	100.35
DAuX	31.01	36.48	27.01	3.55	-	-	98.05
E	24.71	30.18	22.80	-	14.44	5.17	97.30
EAuX	29.33	35.84	21.28	-	-	5.85	92.30

Table 5.11: LECO elemental analysis of impurities within the 4 systems tested.

Alloy Designation	Impurities detected (wt%)		
	C	N	O
D	0.007	0.001	0.024
E	0.014	0.001	0.029
DAuX	0.005	<0.001	0.026
EAuX	0.010	0.001	0.041

A comparison of the differences between the nominal composition (Table 5.6 and Table 5.8) and the actual composition (Table 5.10) for can be seen in Figure 5.8.

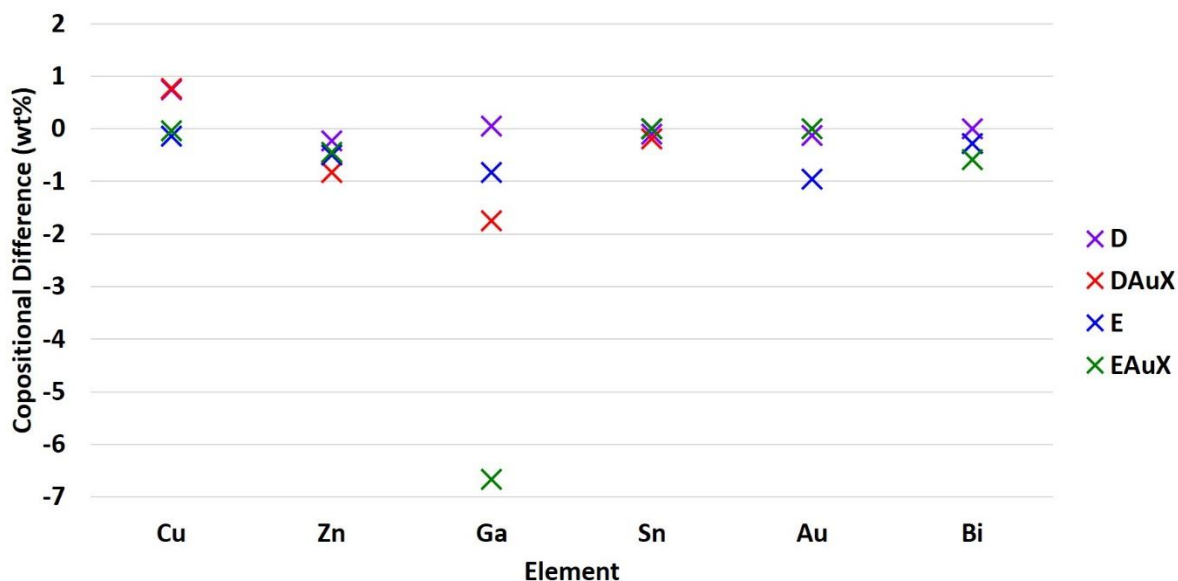


Figure 5.8: Differences between nominal composition and determined composition for each alloy composition split by element.

The compositional data provided by the ICP-OES shows that the compositions produced are largely as intended with the deviation of all elemental constituents in the range of +1/-2wt% aside from a single outlying result (gallium in alloy EAuX is recorded as 6.7wt% lower than intended). It should be noted that the sum wt% total of elements analysed for in alloy EAuX only reached 92.3% implying that 6.7% of the sample was an element not analysed for in the ICP-OES process (Table 5.10, column 8). No presence of any other element that is not expected to appear has been detected in any other sample to date. Of further note is the fact that in this sample the percentage of gallium ‘missing’ (i.e. the

amount of gallium below the nominal composition) was also 6.7%; exactly matching the 6.7% shortfall in the total alloy composition. To assess whether the missing gallium was a potentially erroneous result from the ICP-OES or if the sample was genuinely gallium deficient, alloy EAuX was assessed by XRF to provide a second measure of its composition. The results can be seen in Table 5.12 alongside the nominal composition and the ICP-OES determined composition.

Table 5.12: Comparison of the nominal and detected composition of alloy EAuX by various techniques.

Alloy	Weight %				Total
	Cu	Zn	Ga	Bi	
Nominal composition	29.37	36.26	27.93	6.44	100.00
ICP-OES	29.33	35.84	21.28	5.85	92.30
XRF	35.12	35.60	19.08	7.57	97.37

Whilst it is possible that some gallium has been misidentified as a different, un-measured, element, the XRF data collected for this sample (Table 5.12, row 4) also suggested that the gallium percentage of the sample was lower than the nominal composition with 19.08wt% gallium being detected by XRF compared to 27.93wt% gallium being the nominal percentage (Table 5.12, row 2). Again, the total sample wt% detected was lower than 100% (although not as low as the 92.3wt% detection recorded by the ICP-OES). With two analytical techniques both detecting a gallium deficiency in the sample and both failing to identify 100wt% of the sample this indicates that contamination of the gallium with an element not detected in either technique could be possible.

The maximum levels of specifically tested impurities detected (C = 0.014wt%, N = 0.001wt% and O = 0.041wt%) are all very low giving confidence to the statement that the alloys produced are largely as intended with only a single anomalous result in the wt% recorded for alloy EAuX, possibly due to contamination of the gallium used in its manufacture.

5.5. Phase Characterisation

5.5.1. Phase Modelling

Modelling of the 4 alloy systems taken forward was undertaken to gain an understanding of the potential phases present in the system to make phase identification easier. ThermoCalc was used to model the alloy phases present over the temperature range of 0-1000K. The SSOL4 database was used to model a system of each of the nominal compositions 1mol in size and graphs of the phases present in each sample across the temperature range were produced. An example graph can be seen for alloy E in Figure 5.9.

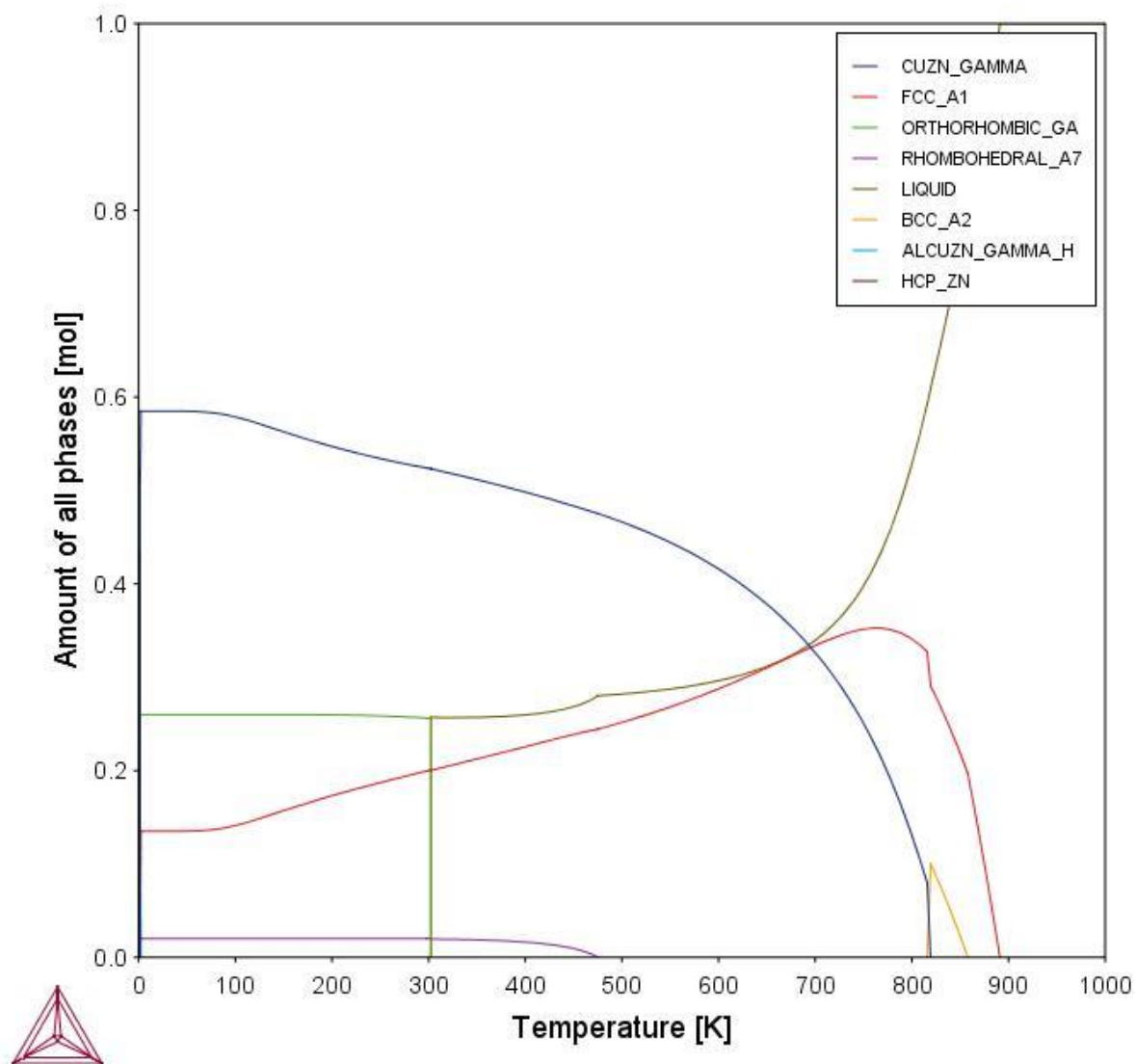


Figure 5.9: Thermo-Calc graph predicting the phases present in alloy E over the temperature range 0-1000K. The system size modelled was 1mol and thus the amount of phases present can be converted to a percentage of the sample as a whole.

A snapshot of the quantities of each stable phase present at STP (standard temperature and pressure) of 298K and 10^5 Pa was also taken and the composition and relative quantities of each phase predicted to exist was recorded in Table 5.13.

Table 5.13: The phases predicted by Thermo-Calc to exist at 298K and 10⁵Pa for each of the 4 systems examined in this study. The relative percentages of each phase in the sample and their composition are also listed.

Sample	Phase	Percentage of sample (%)	Composition of Phase (at%)					
			Cu	Zn	Ga	Sn	Au	Bi
D	FCC_A1	18.1	52.4	24.4	1.20	0.00	22.1	-
	AUSN	34.0	-	-	-	50.0	50.0	-
	CUZN_GAMMA	52.1	39.4	60.6	-	-	-	-
	ORTHORHOMMBIC_GA	25.8	-	-	100	-	-	-
DAuX	CU3SN	8.52	75.0	-	-	25.0	-	-
	CUZN_GAMMA	63.8	40.0	60.0	-	-	-	-
	ORTHORHOMBIC_GA	27.7	-	-	100	-	-	-
E	FCC_A1	20.0	48.1	19.9	1.90	-	30.0	0.00
	RHOMBOHEDRAL_A7	2.00	-	0.00	-	-	-	100
	CUZN_GAMMA	52.4	38.9	61.1	-	-	-	-
	ORTHORHOMMBIC_GA	25.6	-	-	100	-	-	-
E AuX	FCC_A1	12.8	60.8	38.8	0.36	-	-	0.00
	RHOMBOHEDRAL_A7	2.13	-	0.00	-	-	-	100
	CUZN_GAMMA	57.5	42.0	58.0	-	-	-	-
	ORTHORHOMMBIC_GA	27.6	-	-	100	-	-	-

The Thermo-Calc modelling software predicts similar phases for each of the 4 samples.

- In 3 of the 4 samples (D, E and EAuX) a solid solution FCC phase (labelled as FCC_A1) which constitutes 13-20at% of the sample at 298K is present. This phase is predicted to be a majority copper (49-61at%) with zinc (20-39at%), and a limited amount of gallium soluble within the phase (0.4-1.2at%). In the systems which contain gold that are predicted to exhibit this phase (D and E) the phase is predicted to contain 22-30at% gold.
- In both tin containing systems (D and DAuX) the tin is predicted to appear solely in one phase – a Au-Sn binary phase for the gold containing system (D) and a Cu-Sn binary for the gold free system (DAuX).
- In both bismuth containing systems (E and EAuX) the bismuth is predicted to be insoluble in any phase and incompatible with any of the other elements; remaining as essentially elemental bismuth in the rhombohedral crystal structure found in bismuth at STP.
- All 4 systems are predicted to be a majority copper-zinc binary phase (52-64%)
- The gallium in each system is predicted to exist almost exclusively as elemental gallium in its orthorhombic STP structure with only a small amount soluble within the FCC_A1 phase (if present).

It should be noted that these are the phases predicted by Thermo-Calc to exist at STP if the systems are allowed to reach equilibrium; as the samples are cast from the molten state into a copper mould which is at ambient temperature (and thus they experience rapid cooling) then it may be that some of the phases only predicted to occur at low temperatures (such as orthorhombic gallium or rhombohedral bismuth) may not appear as the alloy may not have reached equilibrium. Heat treatments of brazing filler metal samples could be used to promote the formation of equilibrium phases to provide a better comparison with Thermo-Calc phase predictions however this information is unlikely to be of much use in the design of alloys to be used as brazing filler metals. This is due to the fact that brazing filler metals are designed to melt when used to form joints and are often cooled quickly once the joint has been made. As such, any phases which arise in the filler from post-manufacture heat treatments (before they are used to form joints) would then be lost on reheating when they are used to form joints. As such whilst Thermo-Calc modelling of likely phases can provide guidelines for what phases should be expected in samples it should not be too heavily relied upon in analysis of filler metal samples.

The predictions provided by the Thermo-Calc must be inspected with caution for several reasons

- The rapid cooling the samples experience may lead to some of phases which are present at higher concentrations at higher temperatures (FCC_A1) and some which are only present at high temperatures (BCC_A2) appearing to feature in the alloys when examined at room temperature as the rapid cooling could potentially quench these phases and cause them to appear in the samples as samples are not annealed before being used as filler metals or for examination
- The software can only form predictions based on the information in the database. Higher order systems (e.g. 4-5 elements present) may contain phases that have never been investigated before and as such will not be known and thus not appear in the phase predictions. For example, in the systems modelled above, both gallium and bismuth are predicted to exist almost solely in their elemental form whereas

due to the high entropy of mixing found in solid solution alloys they may in fact be soluble in another phase. Assessments of the accuracy of CALPHAD modelling on higher order systems have been made by prominent researchers in the high entropy alloys field previously. Miracle et al. postulated that the credibility of CALPHAD modelling of high order alloys can be evaluated by examining the fraction of binary and ternary phase diagrams of the constituent elements of the high order alloy being modelled which are assessed within the database used for the modelling. Denoting the fraction of assessed binary diagrams as f_{AB} and the fraction of assessed ternary diagrams as f_{AT} , Miracle stated that good agreement between CALPHAD modelling and results are seen when $f_{AB}=1$ and nominal agreement is seen when f_{AB} is as low as 0.6 [44]. Taking the 5 components of alloy D (Cu-Zn-Ga-Au-Sn) the fraction of the 10 binary diagrams (Cu-Zn, Cu-Ga, Cu-Sn, Cu-Au, Zn-Ga, Zn-Sn, Zn-Au, Ga-Sn, Ga-Au and Sn-Au) which are assessed within the CALPHAD database (SSOL4) used to make the phase assessments above may give an indicator of the accuracy of the prediction. A list of which binary and ternary diagrams are assessed in SSOL4 is not available from Thermo-Calc software. An estimate of f_{AB} was obtained by using the SSOL4 database to draw each of the binary and ternary diagrams mentioned above and comparing them to known diagrams recorded in ASM Handbooks [45]. Where good agreement was seen the binary was said to be assessed within the database and where poor agreement was seen it was said not to be assessed. f_{AB} for alloy D developed in this study was approximated to be $f_{AB} = 0.3$; indicating that the predictions made for this system should be taken with caution.

Given that the f_{AB} for the 5 component alloy D was as low as 0.3, improvements to the predicted phases given by Thermo-Calc could be attained by improving the number of binary and ternary diagrams made of components of these systems which are assessed within the SSOL4 database. As only 3/10 constituent binary diagrams were assessed correctly in SSOL4, re-assessment of the other 7 binary diagrams (and indeed of all of the 10 ternary diagrams) would likely improve the predictions produced by Thermo-Calc. Regardless, such an effort even then may not yield predictions matching experimental data due to interactions between 4 or 5 elements (e.g. quaternary and quinary interactions) in phases are not considered by modelling binary and ternary diagrams alone. Additionally, Thermo-Calc models equilibrium phases and as alloys produced in this study are often cast (i.e. rapidly cooled) they may not display equilibrium phases in their microstructure, further reducing the chance that the phases modelled using Thermo-Calc are accurate reflections of experimentally produced alloys.

However, it can be noted that all 4 systems of interest developed thus far in this study (Alloy D, Alloy DAuX, Alloy E and Alloy EAuX) all contain high percentages of copper, zinc and gallium (79-96wt% of total being Cu, Zn and Ga combined depending on the alloy in question). As such it could be argued that the most important ternary diagram for assessing the alloys in this study is the Cu-Zn-Ga ternary. As such an attempt was made to draw a Cu-Zn-Ga ternary diagram to see if any better match to the experimentally observed phases could be produced. Firstly, the Cu-Ga and Ga-Zn binary diagrams needed to be recalculated as the SSOL4 database does not correctly assess these two binary diagrams. Thermodynamic data was taken from Li et al. (Cu-Ga) [46] and Terlicka et al. (Ga-Zn) [47] and used to produce accurate binary diagrams from these 2 systems which were added to a new Thermo-Calc database along with the thermodynamic parameters for Cu-Zn which were taken from a study by Miettinen (Cu-Zn) [48]. This enabled a ternary diagram to be drawn from this binary thermodynamic data (Figure 5.10) although

it must be noted that no ternary interaction parameters were used in the construction of this database which could significantly alter the diagram.

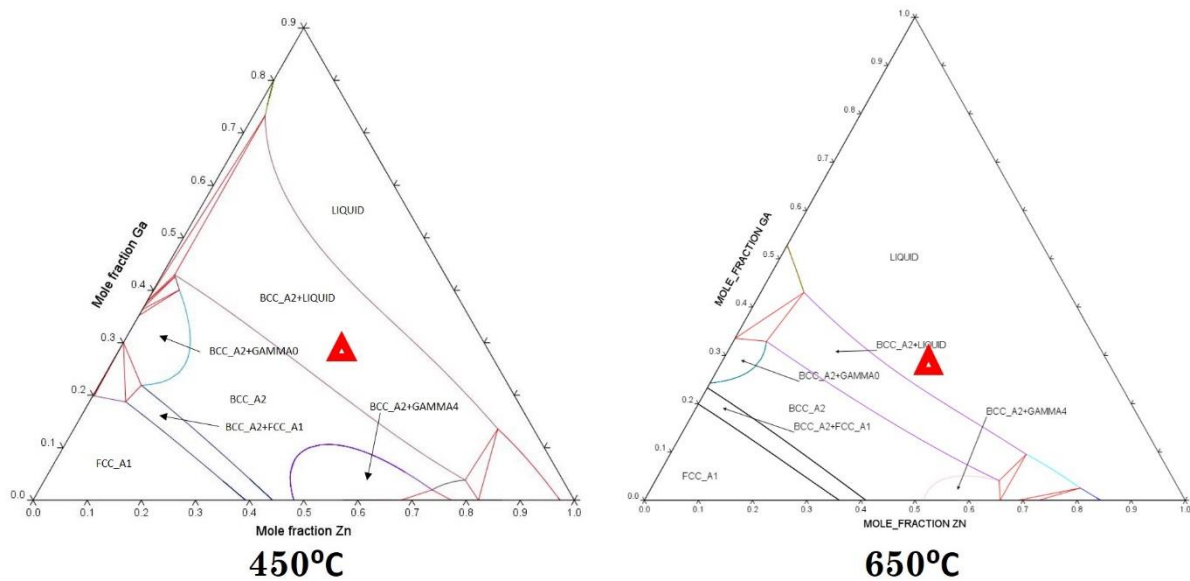


Figure 5.10: Simulated ternary phase diagrams drawn in Thermo-Calc using the Cu-Zn-Ga database developed in this work. The red triangles mark the approximate position of the composition DAuX (composition is approximate as DAuX also contains 3.76Wt% Sn).

Figure 5.10 shows isothermal ternary phase diagrams drawn at 450°C and 650°C. As liquid is present in both diagrams it shows that the alloy system in question has the potential to be molten over a wide range of temperatures. It indicates that with compositional modification the melting point of the alloy can be tuned which can be very desirable in filler metals as the melting temperature is of critical importance. Additionally, the transition from 650°C down to 450°C indicates that as solidification occurs a BCC phase will begin to form (as seen by the position of the red triangle in the 450°C diagram being in a dual phase BCC and liquid region). The indication of the transition to a solid solution BCC phase as cooling occurs is promising as the alloy compositions in this study were designed to form solid solution phases. Again, the results of this modelling should be used with caution and considered only as a guideline as ternary interaction parameters were not used in the generation of this diagram and alloy compositions in this study contain additional elements as well as copper, zinc and gallium.

5.5.2. Phase Identification

Phase characterisation of the 4 most successful alloys (D, DAuX, E, EAuX) was undertaken to better understand the composition of the filler metals produced. All 4 alloys systems were cut, ground, polished and imaged according to the standard schedule listed in section 3.3.1. Figure 5.11 below shows optical micrographs of each of the 4 alloy systems at 100× magnification. These images highlight that none of the alloy systems produced are single phase with all 4 appearing to exhibit at least 3 phases.

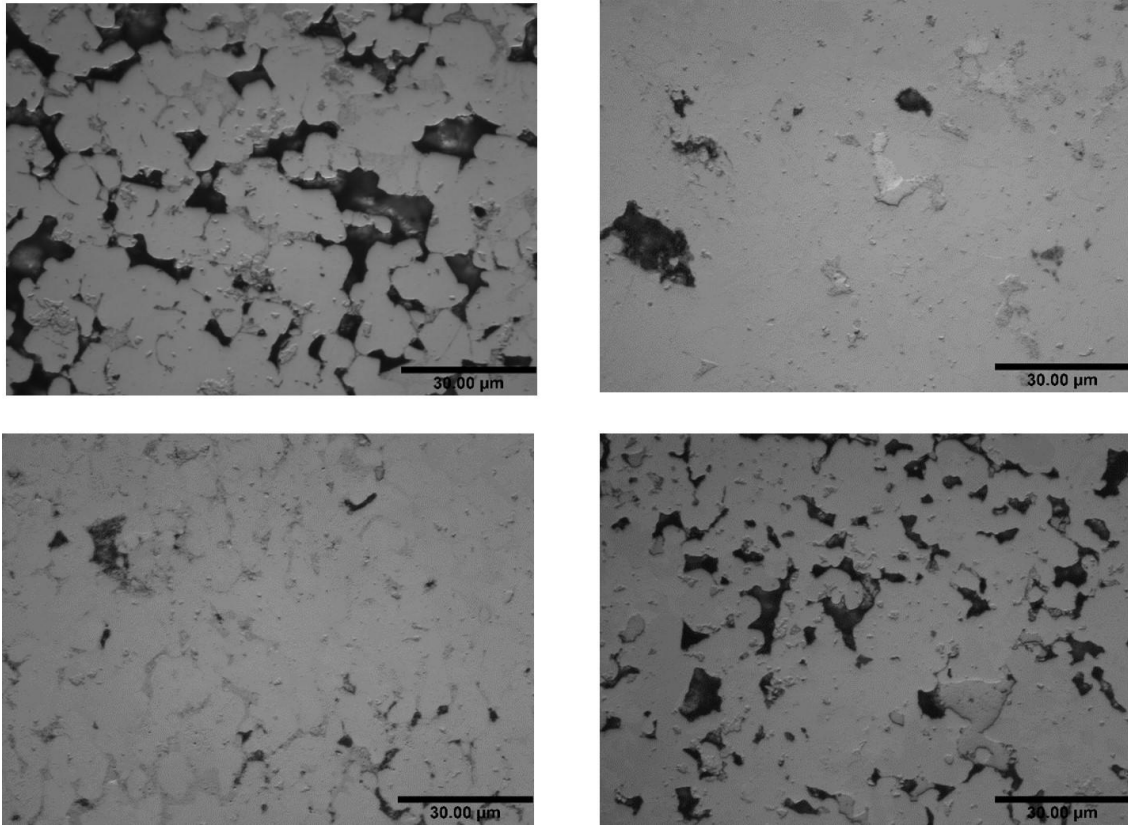


Figure 5.11: Optical micrographs of the microstructure of each of the 4 alloy systems at 100x magnification. D (top left), DAuX (top right), E (bottom left) and EAuX (bottom right). All 4 show the presence of multiple phases.

Further information on the number of phases present in each filler metal system was needed and so each alloy system was imaged using SEM. Any phases identified on the SEM images were also EDX spot mapped to obtain the compositional information for each phase. An example of the images taken (and the location of phase spot maps) can be seen in Figure 5.12.

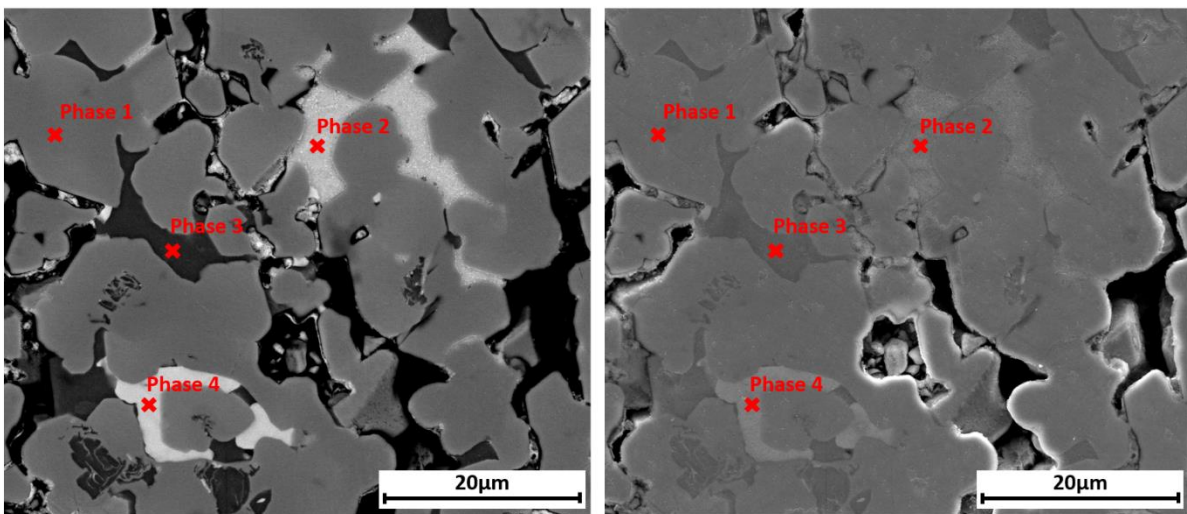


Figure 5.12: Left: back scattered electron image of alloy D showing 4 phases present. Right: secondary electron image of alloy D showing 4 phases present, micro-porosity that is obscured using BSE can be seen more easily using SE.

Each phase was EDX spot sampled in 3 different locations and the results averaged to provide an average composition for each phase in each sample. The averaged values over the 3 EDX scans can be found in Table 5.14 below. The standard error of the mean ($S_{\bar{x}}$) was calculated for each element of each phase and for clarity is recorded in Appendix 2. The maximum calculated error on any value was $\pm 2.6\text{wt}\%$. Each phase has been assigned an arbitrary phase number (and for clarity a brief description of the phase determined from analysis below has been added).

Table 5.14: Averaged composition of each phase within each of the 4 samples analysed. The Standard error of the Mean ($S_{\bar{x}}$) has been calculated for each value determined here but for clarity has been included in an extra table in Appendix 2.

Sample Name	Phase number (description)	Composition (Wt%)							
		Cu	Zn	Ga	Sn	Au	Bi	O	Si
D	1) primary solid solution	32.4	36.8	10.6	0.1	19.4	-	0.6	-
	2) predominantly tin phase	2.0	2.4	3.9	83.9	2.9	-	4.4	0.5
	3) CuGa ₂	30.3	2.5	65.5	0.1	0.9	-	0.6	0.1
	4) gold-gallium phase	5.0	6.4	36.4	0.5	49.3	-	1.4	0.2
DAuX	1) primary solid solution	34.4	58.0	7.5	-	-	-	-	-
	2) predominantly tin phase	2.7	1.9	5.7	89.7	-	-	-	-
	3) CuGa ₂	31.3	2.6	65.9	-	-	-	0.2	-
E	1) primary solid solution	31.0	37.5	11.1	-	19.5	0.4	0.3	-
	2) predominantly bismuth phase	2.6	3.5	2.3	-	0.4	91.0	0.3	-
	3) CuGa ₂	30.1	3.6	65.2	-	0.7	0.1	0.2	-
	4) gold-gallium phase	5.3	7.0	38.7	-	48.0	0.6	0.4	-
E AuX	1) primary solid solution	41.8	48.1	9.7	-	-	0.0	-	0.3
	2) predominantly bismuth phase	3.4	4.7	2.5	-	-	89.3	-	0.3
	3) CuGa ₂	31.2	6.2	62.1	-	-	-	-	0.1

Similarities between the phases present in each sample can be clearly seen. Each of the samples have a similar majority phase. In the gold containing samples this phase (phase 1 in Table 5.14 for samples D and E) is a zinc-copper-gold-gallium solid solution, in the gold free samples (DAuX and EAuX) the predominant phase (phase1) is similar but does not contain gold.

Each sample also has an intermetallic phase consisting of predominately tin (D and DAuX) or bismuth (E and EAuX), These elements appear to be unable to incorporate within the solid solution at such high percentages (3-6wt%) and as such they precipitate out as an intermetallic phase. As these elements make up a relatively small proportion of the alloy as a whole the amount of this phase present overall is low. An image point analysis using a 780-point, 2-micron spacing grid on the left image of Figure 5.12

estimated the percentage of the total sample comprised of this phase to be 6.28%. A rough estimate of the percentage of this phase present can also be made knowing the total tin percentage of the alloy. As the alloy is 3.17wt% Sn and the phase in question is 83.9% Sn assuming that no tin is present in other phases in the sample then the predominantly tin phase makes up $3.17 \div 83.9 \times 100 = 3.78\%$ of the alloy. Thus, both estimates for the total percentage of this phase contained in alloy D give it to be <6.5%.

A third phase found in all 4 of the alloys tested is a predominantly copper-gallium phase (with a roughly 30:60 ratio of the two constituents) with small amount of zinc also present. It is possible that this phase is a secondary solid solution possibly formed due to insufficient zinc being available to form the predominant Cu-Zn-Ga-(Au) phase. Finally, in the gold containing samples, a predominantly gallium-gold phase is also present, again with small quantities (6-7wt%) of zinc contained within the phase.

There are some similarities between the analysed phase composition and the predicted phase composition from Thermo-Calc modelling.

- The samples do indeed contain a solid solution phase based on copper, zinc and gold (if present) with a small amount of gallium soluble. The amount of gallium soluble is higher than predicted by Thermo-Calc and the gold content is lower than that predicted by Thermo-Calc.
- The tin containing samples do have the tin largely confined to a single phase, however it is a majority tin phase rather than a gold-tin or copper-tin binary phase.
- Bismuth is found almost solely in a majority bismuth phase in which only small amounts (<5wt%) of other elements are soluble; this is similar to the prediction of elemental bismuth existing within the sample as predicted by Thermo-Calc

There are also some major differences between the predicted phase structure and the actual phase composition.

- The gold-tin and gold-copper phases predicted by Thermo-Calc to appear in alloys D and DAuX do not feature in the actual phase composition, although a gold-gallium phase does in alloy D.
- The Cu-Zn phase predicted to appear in all 4 alloys doesn't appear but a Cu-Ga phase (with a small amount of Zn) does appear in all 4 systems.
- Elemental gallium on its own as a phase does not appear in any of the samples whereas the modelling predicted it to exist in all of them

With knowledge of the phases present in the sample from EDX analysis, XRD diffraction patterns for each of the 4 alloy systems were obtained, normalised and overlaid on top of each other in Figure 5.13 in an attempt to fully identify the structure of the phases present.

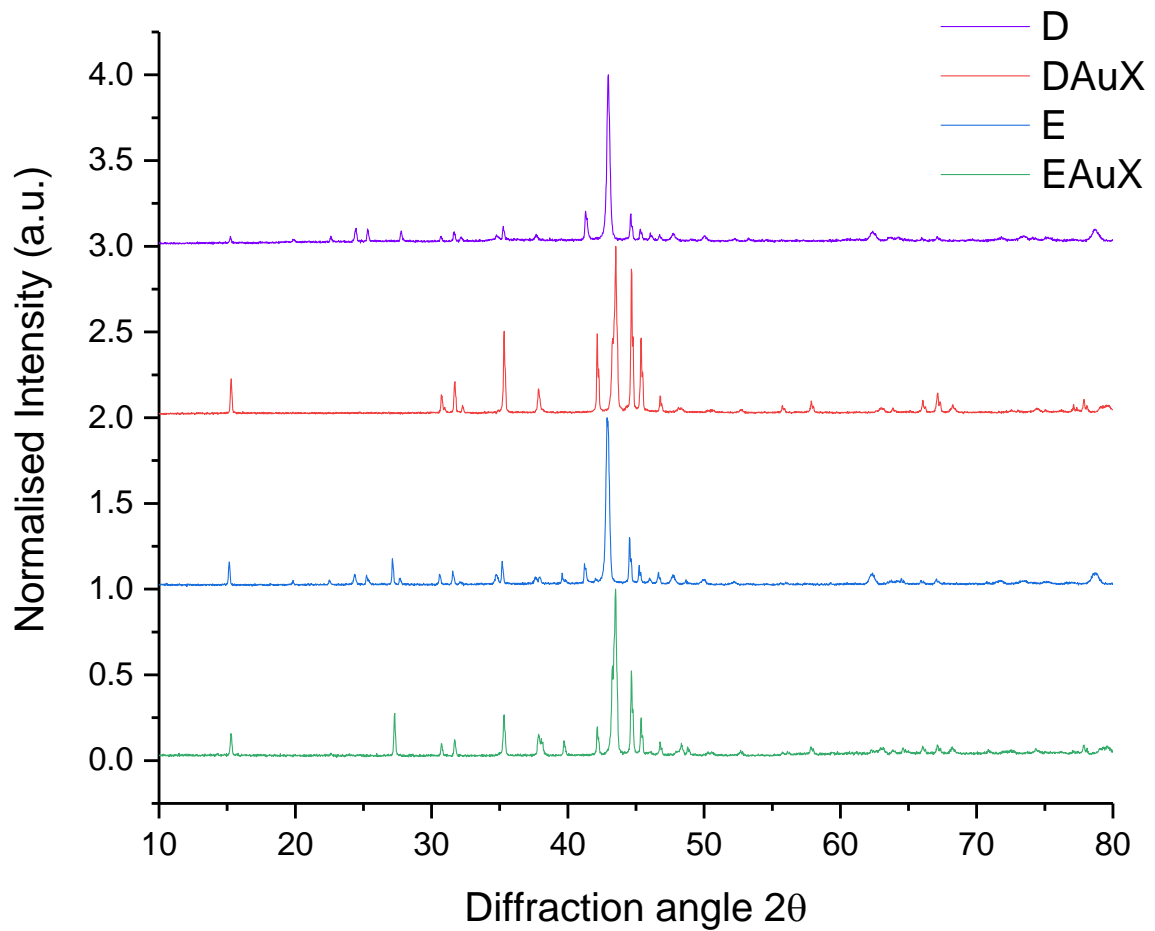


Figure 5.13: Normalised XRD diffraction patterns for each of the 4 alloys D, DAuX, E and EAuX.

The XRD diffraction pattern for each sample was then taken and compared to diffraction patterns in the PDF-4+ database using the Sieve+ software from the International Centre for Diffraction Data (ICDD).

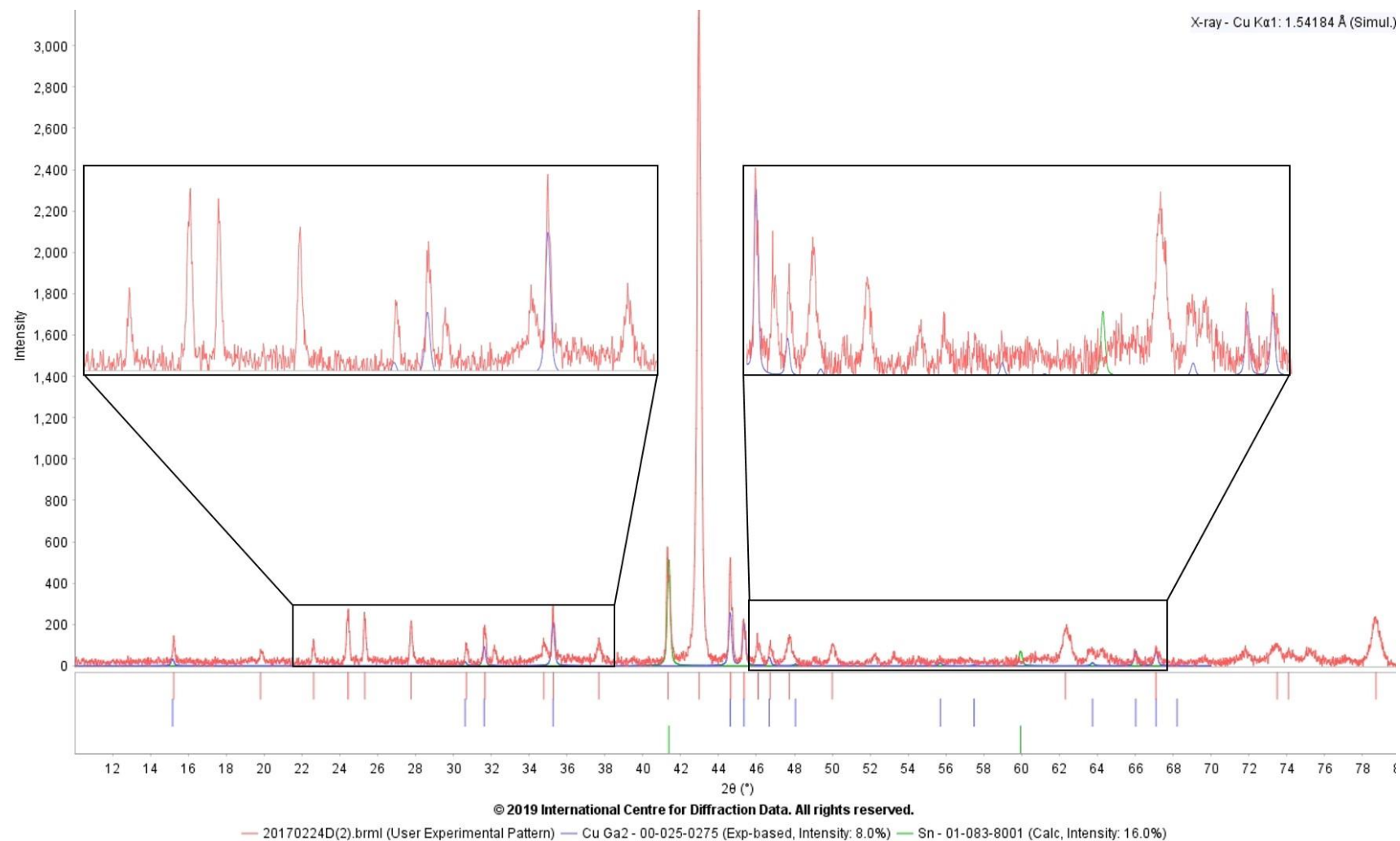


Figure 5.14: The Diffraction pattern for alloy D overlaid with diffraction patterns for CuGa₂ (PDF card number 00-025-0275) and tin (PDF card number 01-083-8001). The inserts in the top left and top right show close ups of smaller parts of the diffraction pattern to better highlight the quality of the match.

Figure 5.14 shows the diffraction pattern for alloy D overlaid with diffraction patterns for CuGa_2 (PDF card number 00-025-0275) and tin (PDF card number 01-083-8001). The good matches here indicate that the copper gallium compound found in the sample (phase 3 in Table 5.14) is likely to be CuGa_2 . In fact, all 4 samples matched well with this compound leading to the conclusion that phase 3 (which is common to all 4 samples) is CuGa_2 , a tetragonal phase with a $P4/mmm$ space group. The match with elemental tin indicates that the tin containing phase (phase 2 in Table 5.14) is likely elemental tin with small quantities of the other elements detected in the phase in solution. Examination of the binary phase diagrams for tin with the other constituents reveals some limited solubility of other constituent elements in $\beta\text{-Sn}$ (0.6% Zn, 6.4% Ga and 0.2%Au) lending weight to this theory. No matches were found in the database for the Cu-Zn-Ga-Au phase (phase 1 in Table 5.14) or the gallium gold phase (phase 4 in Table 5.14) and as such a number of peaks were left unidentified. A similar outcome was found for alloy E in which peaks matching the pattern for CuGa_2 and that for elemental bismuth (PDF card number 04-006-7762) could be found but no match for the solid solution Cu-Zn-Ga-Au phase or the gallium gold phase could be found. The diffraction pattern for alloy E can be found in Appendix 3.

Similarly, the gold free samples (DAuX and EAuX) were also analysed using the PDF-4+ database. Figure 5.15 shows the diffraction pattern for alloy DAuX with diffraction patterns for CuGa_2 and tin overlaid. Similarly to the gold containing samples the match here is good for these two phases however, a match for the primary solid solution phase (again labelled phase 1 in Table 5.14 under the DAuX row) is not found. Whilst the diffraction pattern did display similarities to copper-zinc compounds (e.g. $\text{Cu}_{0.8}\text{Zn}_{0.2}$) no diffraction pattern which adequately matched all remaining peaks could be found. This leads to the conclusion that the copper-zinc-gallium compound designated as phase 1 in the DAuX and EAuX rows of Table 5.14 is not adequately indexed in the PDF-4+ database. Again, as before, alloy EAuX matched diffraction patterns for the same CuGa_2 and elemental bismuth but no match for the copper-zinc-gallium phase could be found. The diffraction pattern for alloy EAuX can be found in Appendix 4.

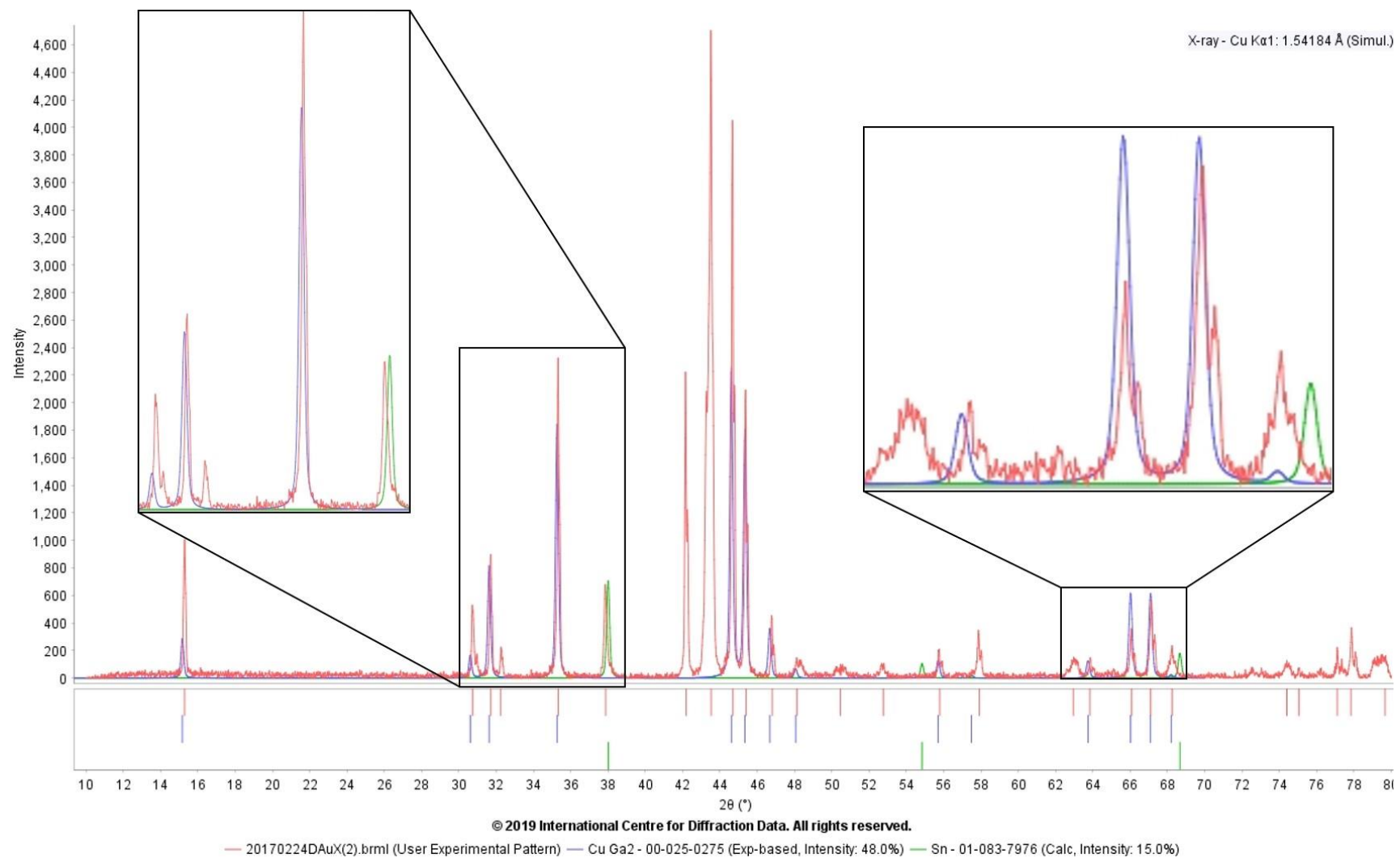


Figure 5.15: The Diffraction pattern for alloy DAuX overlaid with diffraction patterns for CuGa₂ (PDF card number 00-025-0275) and tin (PDF card number 01-083-8001). The inserts in the top left and top right show close ups of smaller parts of the diffraction pattern to highlight the match quality.

In order to try and identify the remaining peaks in the XRD diffraction, an attempt was made to experimentally produce a single phase composition using the average constitutions of the predominant solid solution phase in both the gold containing samples (phase number 1 in samples D and E see Table 5.14) and the gold free samples (phase number 1 in samples DAuX and EAuX, see Table 5.14) excluding any impurity constituents detected (i.e. any constituent with a wt% <0.5wt%). The intention was that XRD of these samples (should they prove to be single phase), would remove any ambiguity in the identification of the peaks associated with those phases. These single phase samples will be referred to as SS-Au-1 for the gold containing sample and SS-AuX-3 for the gold free sample throughout the remainder of this document. The weight percentages of the predominant solid solution phase from each contributing sample (i.e. phase 1 from samples D and E for the gold containing sample and phase 1 from samples DAuX and EAuX for the gold-free sample) are averaged and then scaled to make the compositions give 100% and then used as the nominal compositions for sample SS-Au-1 and SS-AuX-3 respectively. The samples were then analysed by XRF to determine the actual compositions produced.

The data for the gold containing alloys (which correspond with the single phase sample SS-Au-1) can be found in Table 5.15 and the data for the gold-free alloys (which correspond with the single phase sample SS-AuX-3) can be found in Table 5.16 (again with impurities with a wt% <0.5wt% removed).

Table 5.15: The determination of the composition used to attempt to produce a single phase gold containing alloy based off of the predominant solid solution phase in samples D and E.

Sample Name	Composition (Wt%)			
	Cu	Zn	Ga	Au
wt% single phase D	32.4	36.8	10.6	19.4
wt% single phase E	31.0	37.4	11.1	19.5
Average wt% of single phase	31.7	37.1	10.9	19.4
Scaled wt% of each single phase sample (i.e. solid solution sample nominal composition)	32.0	37.5	11.0	19.6
XRF wt% of produced solid solution sample SS-Au-1	36.1	33.2	9.0	20.9

Table 5.16: The determination of the composition used to attempt to produce a single phase gold free alloy based off of the predominant solid solution phase in samples DAuX and EAuX.

Sample Name	Composition (Wt%)		
	Cu	Zn	Ga
wt% single phase DAuX	34.4	58.0	7.5
wt% single phase EAuX	41.8	48.1	9.7
Average wt% of single phase	38.1	53.1	8.6
Scaled wt% of each single phase sample (i.e. solid solution sample nominal composition)	38.2	53.2	8.6
XRF wt% of produced solid solution sample SS-AuX-3	41.5	50.1	7.6

To analyse whether a single phase alloy had been produced the SS-Au-1 and SS-AuX-3 samples were analysed by X-ray diffraction and the results compared to the XRD diffraction patterns of samples D and DAuX. The results can be seen below.

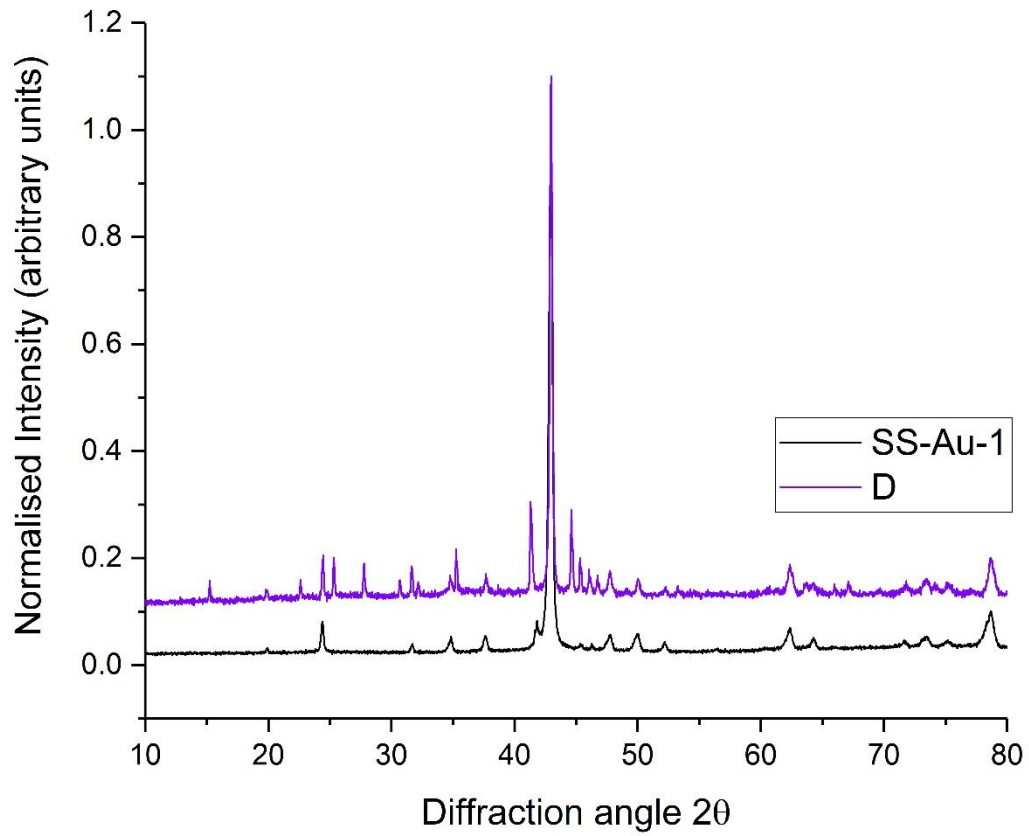


Figure 5.16: XRD diffraction patterns for alloy SS-Au-1 overlaid with the diffraction pattern for alloy D.

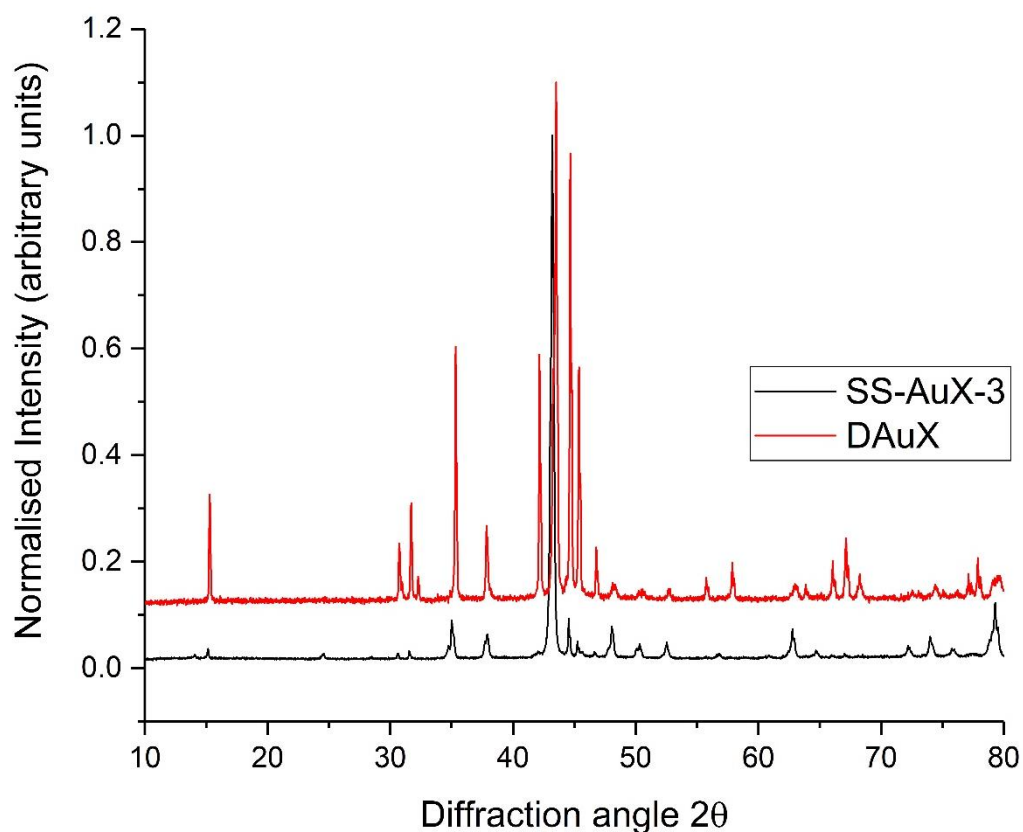


Figure 5.17: XRD diffraction patterns for alloy SS-AuX-3 overlaid with the diffraction pattern for alloy DAuX.

It can be clearly seen that several peaks within the sample alloy are not present within the SS alloy series alloys indicating that, as intended, a reduced number of phases are present. After using optical microscopy it appeared that a single phase sample had been produced (Figure 5.18, Figure 5.19), however high contrast BSE images in the SEM and EDX spot mapping confirm that the SS-Au-1 and SS-AuX-3 samples are not in fact fully homogenous (Figure 5.20) with some variation in composition being distinguishable (although only to the level of a few atomic percent.)

The diffraction patterns from these SS-Au-1 and SS-AuX-3 samples can be matched to Samples D, DAuX, E and EAuX to assign peaks to the primary solid solution phase in these alloys to assist with peak identification; however, as the SS-Au-1 and SS-AuX-3 alloys are not single phase they cannot be used to definitively identify which peaks in the diffraction patterns of D, DAuX, E and EAuX correspond to the primary solid solution phase as intended.

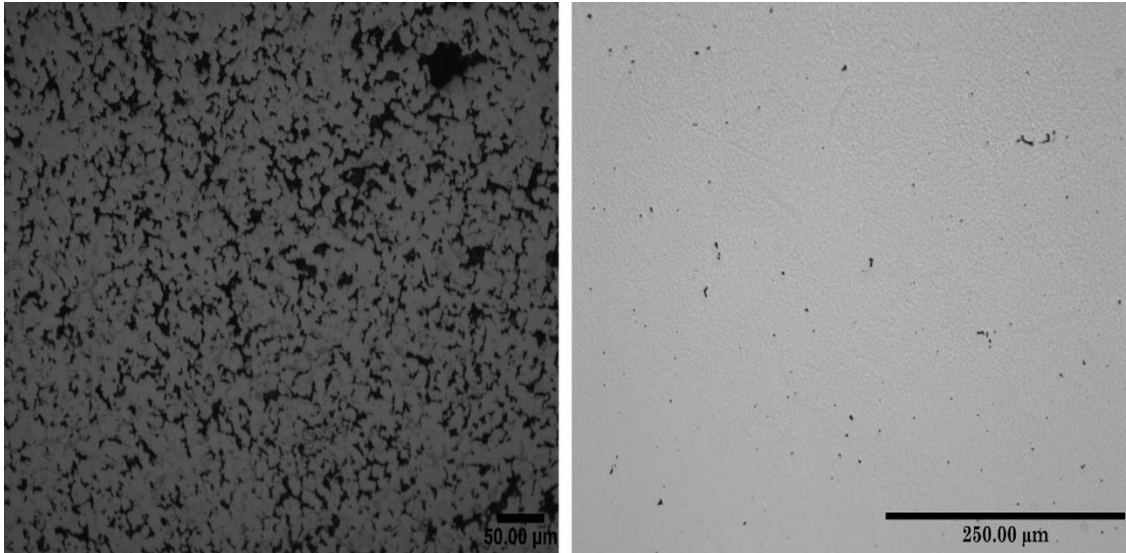


Figure 5.18: Comparison of optical micrographs of SampleD (left) and sample SS-Au-1 (right) at 20x magnification showing a substantially reduced quantity of secondary phases present in sample SS-Au-1.

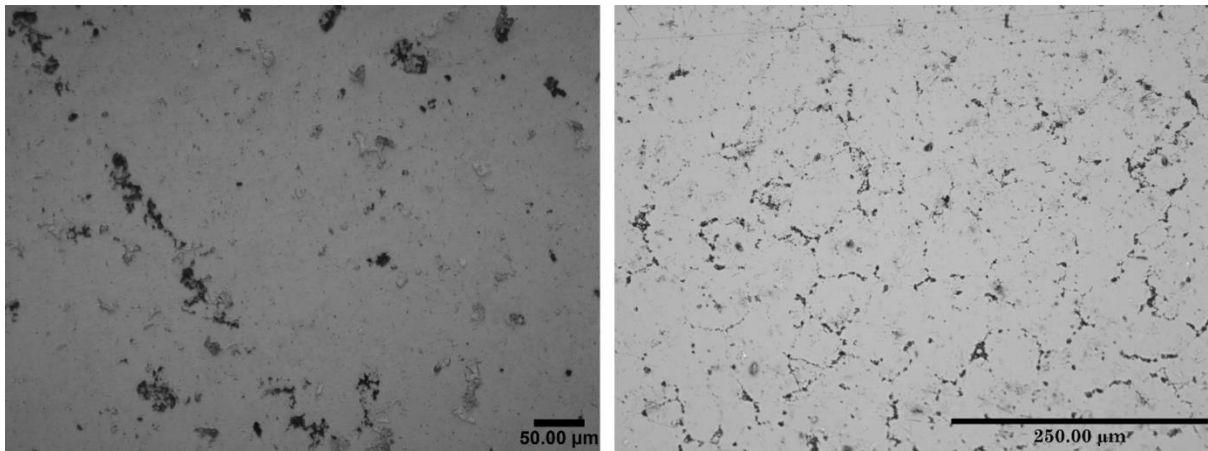


Figure 5.19: Comparison of micrographs of alloy DAuX (left) and sample SS-AuX-3 (right) at 20x magnification showing a lesser quantity of secondary phases present in sample SS-Au-3.

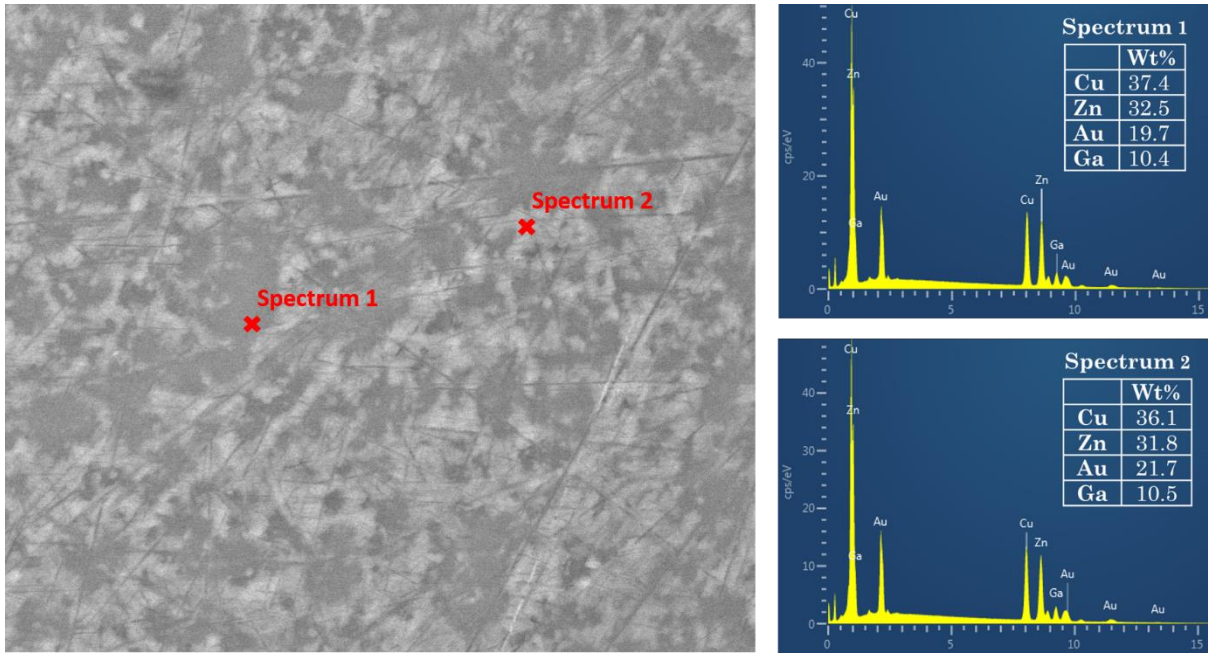


Figure 5.20: (Left) high contrast BSE SEM image of sample SS-Au-1 illustrating where EDX point scans were taken and showing compositional variation in the microstructure. (Right) EDX point scan spectra of the phase composition in these regions demonstrating similar (but not identical) compositions in the different regions.

Matching peaks from the solid solution samples to those not already assigned to CuGa_2 or tin/bismuth in the D, DAuX, E and EAuX leaves very few peaks remaining (which likely correspond to the gold-gallium phase which cannot be identified using the databases available). An example alloy peak matching can be seen in Figure 5.21 where the coloured symbols above the peaks in alloy D manufactured in this study are matched to the SS-Au-1 sample peaks and the peaks for CuGa_2 and tin given in the ICDD PDF-4+ database. It should be noted that as sample SS-Au-1 is not conclusively single phase that some of the peaks that match between alloy D and sample SS-Au-1 may be from multiple phases.

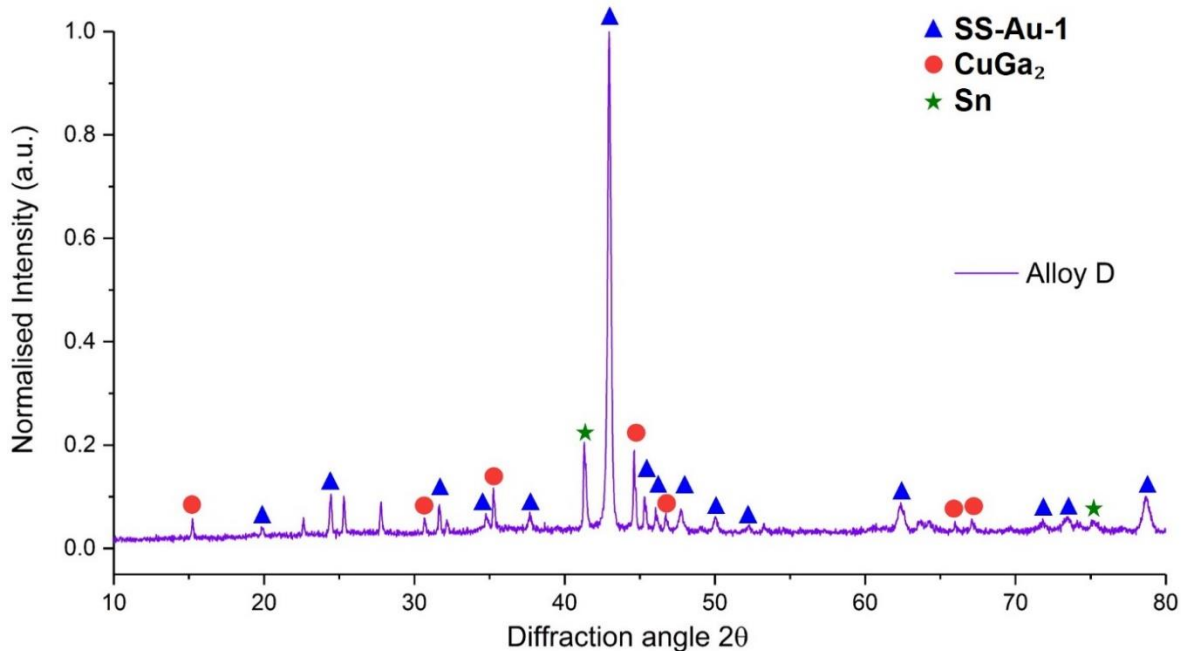


Figure 5.21: Alloy D's XRD diffraction pattern matched to the single phase solid solution sample produced in this work (SS-Au-1) and PDF-4+ database entries for CuGa₂ and tin.

To summarise the phase analysis of the 4 alloys produced in this study:

Gold containing alloy systems (D and E) contained 4 phases,

- The primary solid solution phase comprising of copper, zinc, gallium and gold which matched well to the attempt to produce single phase sample (SS-Au-1). Unfortunately, as sample SS-Au-1 could not be conclusively shown to be single phase, full identification of which peaks in the spectra of samples D and E belonged to the primary Cu-Zn-Ga-Au phase could not be completed.
- Either a predominately tin phase (alloy D) or a predominately bismuth phase (alloy E) with some solubility of other constituent elements.
- A CuGa₂ tetragonal phase with a P4/mmm space group.
- A gold-gallium phase of approximately 36-38wt% Ga and 48-49wt% gold (with the remainder being made of solute elements) which could not be identified in the PDF-4+ database and was considered too expensive to manufacture to complete the XRD analysis of these systems (which would provide little further industrial use). Conversion of the weight percentages of this phase determined from EDX analysis to atomic percentages gives an approximate formula of AuGa₂ (excluding minor solute percentages).

Gold-free alloys systems (DAuX and EAuX) contained 3 phases:

- The primary solid solution phase comprising of predominately copper and zinc with around 10wt% solubility of gallium which matched well to the attempt to produce a single phase sample (SS-AuX-3). Unfortunately, as sample SS-AuX-3 could not be conclusively shown to be single phase, full identification of which peaks in the spectra of samples DAuX and EAuX belonged to the primary Cu-Zn-Ga phase could not be completed.
- Either a predominately tin phase (alloy DAuX) or a predominately bismuth phase (alloy EAuX) with some solubility of other constituent elements.
- A CuGa₂ tetragonal phase with a P4/mmm space group.

5.6. Melting Point Determination

Before alloy melting points were experimentally analysed using thermal techniques, a prediction for the liquidus temperature of each alloy was found using Thermo-Calc 2018-b using data from the SSOL4 database. The two alloys predicted to have a liquidus in the optimal range ($T_{opt} = 550^{\circ}\text{C}-620^{\circ}\text{C}$) were also predicted by Thermo-Calc to fall into this range with D and E being predicted liquidus temperatures of 611.5°C and 617.9°C respectively.

The modified alloys (DAuX and EAuX) were both predicted to have liquidus temperatures slightly above the intended range with temperatures of 654.9°C and 649.9°C respectively (Table 5.17).

Table 5.17: The predicted liquidus temperatures of alloys D, DAuX, E and EAuX determined by Thermo-Calc.

Alloy designation	Predicted liquidus ($^{\circ}\text{C}$)
D	611.5
DAuX	654.9
E	617.9
EAuX	649.9

For an alloy to be successful as a brazing filler metal it must melt within an appropriate temperature range for the application it is designed for, in this instance, $T_{opt} = 550-620^{\circ}\text{C}$. The melting behaviour of each of the 4 alloy systems was assessed using DSC, an example of the DSC traces produced can be seen in Figure 5.22.

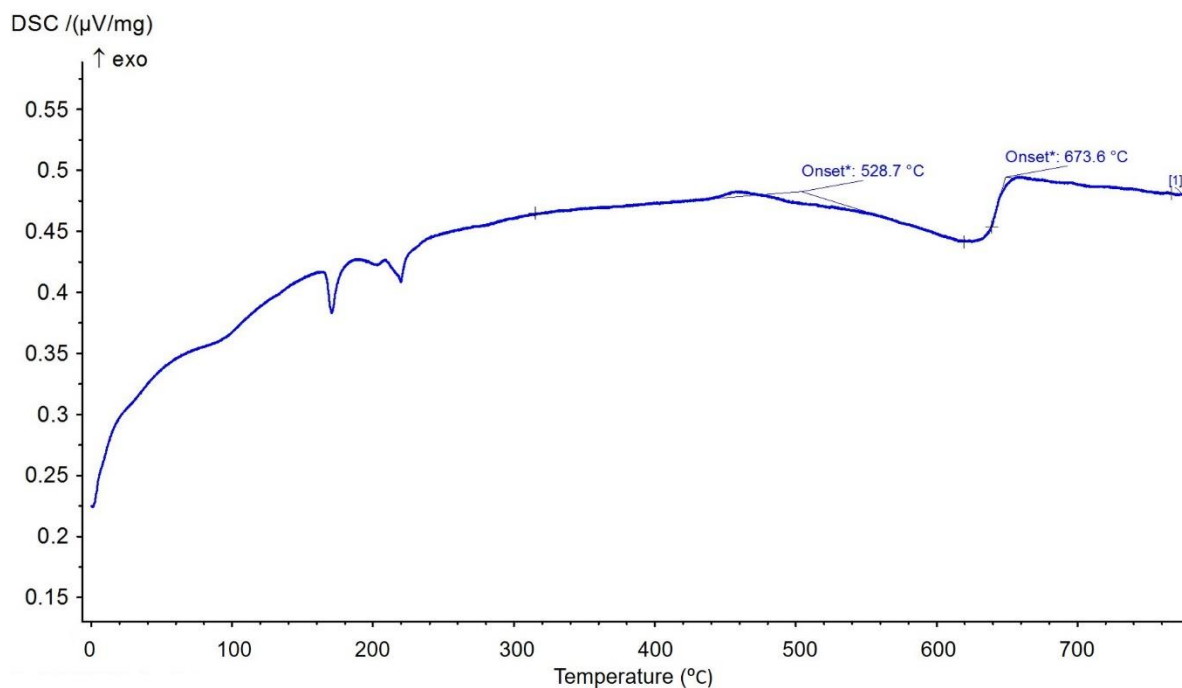


Figure 5.22: Graph showing the solidus and liquidus temperature determined for alloy D from the peak onset of a DSC trace.

Table 5.18: Comparison of DSC determined solidus and liquidus temperatures to CALPHAD predicted liquidus for samples D, DAuX, E and EAuX.

Alloy designation	Predicted liquidus (°C)	Determined solidus DSC (°C)	Determined liquidus DSC (°C)
D	611.5	528.7	673.6
DAuX	654.9	528.4	672.6
E	617.9	543.2	681.0
EAuX	649.9	557.9	671.3

It can be seen from Figure 5.23 that the melting ranges for the alloy systems exceed that of the design brief with 3 of the 4 alloys solidus temperatures (D- 528.7°C, DAuX - 528.4°C and E - 543.2°C) lower than the melting range minimum of 550°C. Additionally all 4 alloys demonstrate liquidus temperatures above the upper boundary of the ideal range set out in the criteria of 620°C.

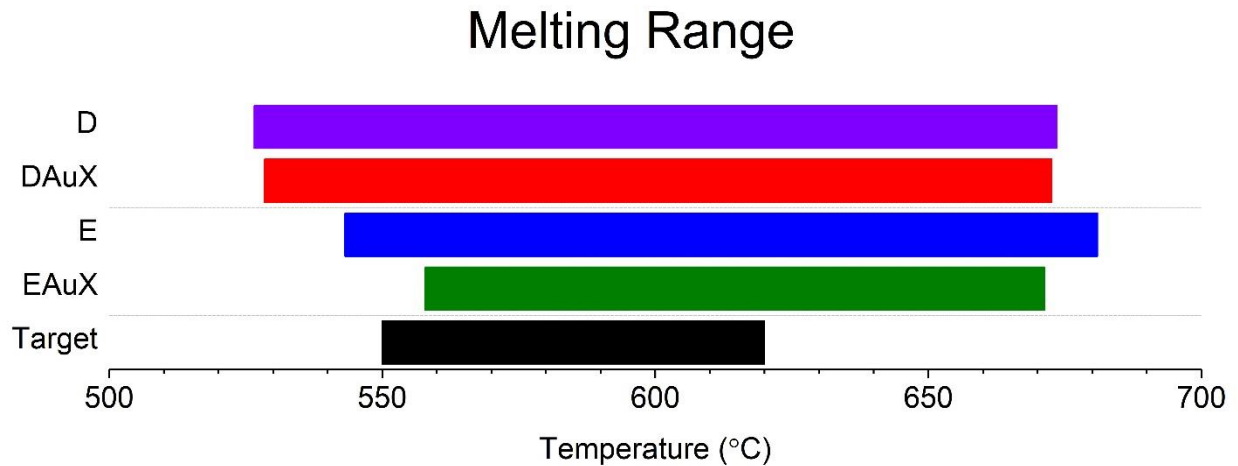


Figure 5.23: The melting ranges of the 4 alloys displayed over the target melting range. All four developed alloys exhibit a melting range wider than the target range.

Whilst the melting ranges of these alloy systems are outside the ideal range proposed by the brief they are within 25°C of the minimum solidus and within 61°C of the ideal liquidus. With compositional refinement there is the possibility that these alloy melting ranges could be fine-tuned sufficiently to fall within the designated range. The large temperature ranges over which various compositions are predicted to be liquid in the theoretical Cu-Ga-Zn ternary diagram drawn in this work (Figure 5.10) provides evidence to support this claim.

5.7. Diffusion distance in nickel

To assess the performance of these 4 alloy systems with regard to the 3rd selection criteria of the design brief the diffusion distance of the alloy systems within nickel was assessed. In order for the alloys to be deemed successful they must not diffuse through the 10µm nickel diffusion barrier and interact with the thermoelectric as this may alter the delicately doped thermoelectric composition. To assess the diffusion distance of these alloys during a standard torch brazing cycle the alloys were used to join nickel plate (>2000µm thick) together and the diffusion distance of the elements from the filler metal into the nickel plate was assessed using EDX line scans. If the filler metal was detected to have diffused less than 10µm into nickel when forming a joint it can be stated with

reasonable confidence that the filler metals are unlikely to diffuse through a 10 μm diffusion barrier applied to a thermoelectric device. EDX line scans were taken for all 4 samples (D, DAuX, E and EAuX) and for a reference joint between a commercially available filler metal (Filler metal ISO 17672: Ag-155) and nickel. An example EDX scan for the commercially available filler can be seen below in Figure 5.24.

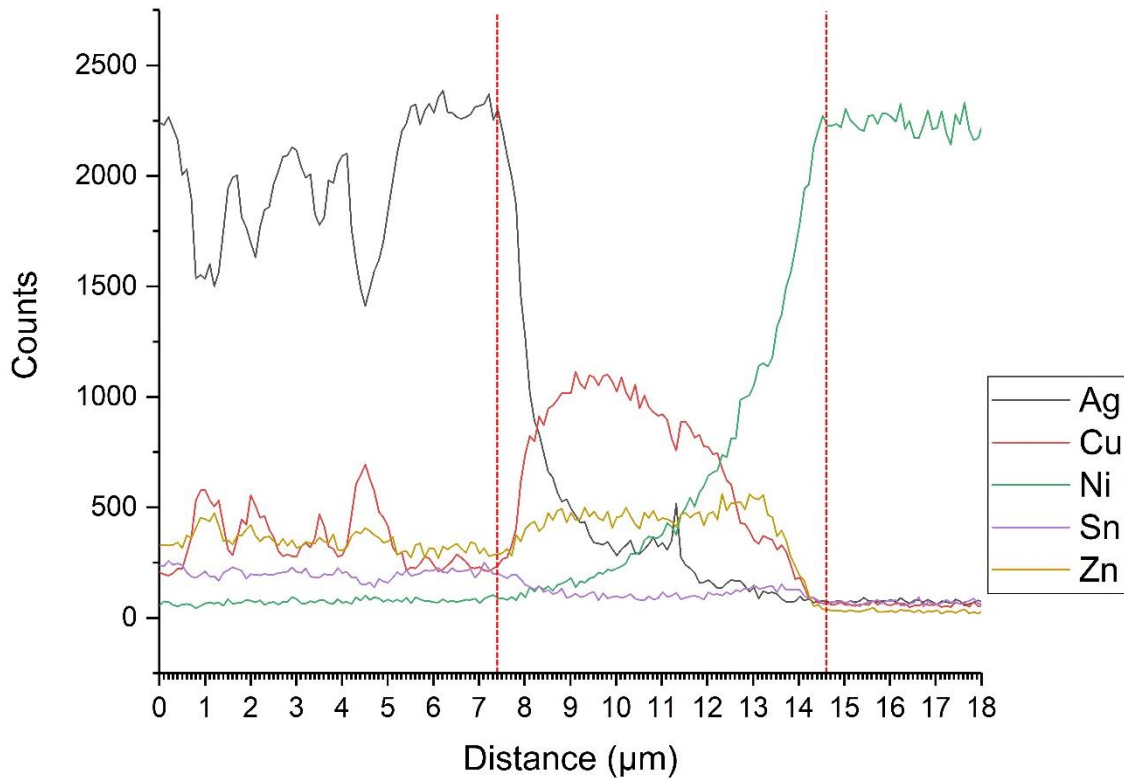


Figure 5.24: EDX line scans across the interface between a commercially available filler metal (Filler metal ISO 17672: Ag-155) and nickel plate. The diffusion zone is highlighted between the two red dotted lines.

Each of the samples (and the reference) was scanned 10 times in 3 different locations on the brazed joint interface giving a total of 30 scans for each sample. An example EDX line scan from one scan of alloy D can be seen in Figure 5.25.

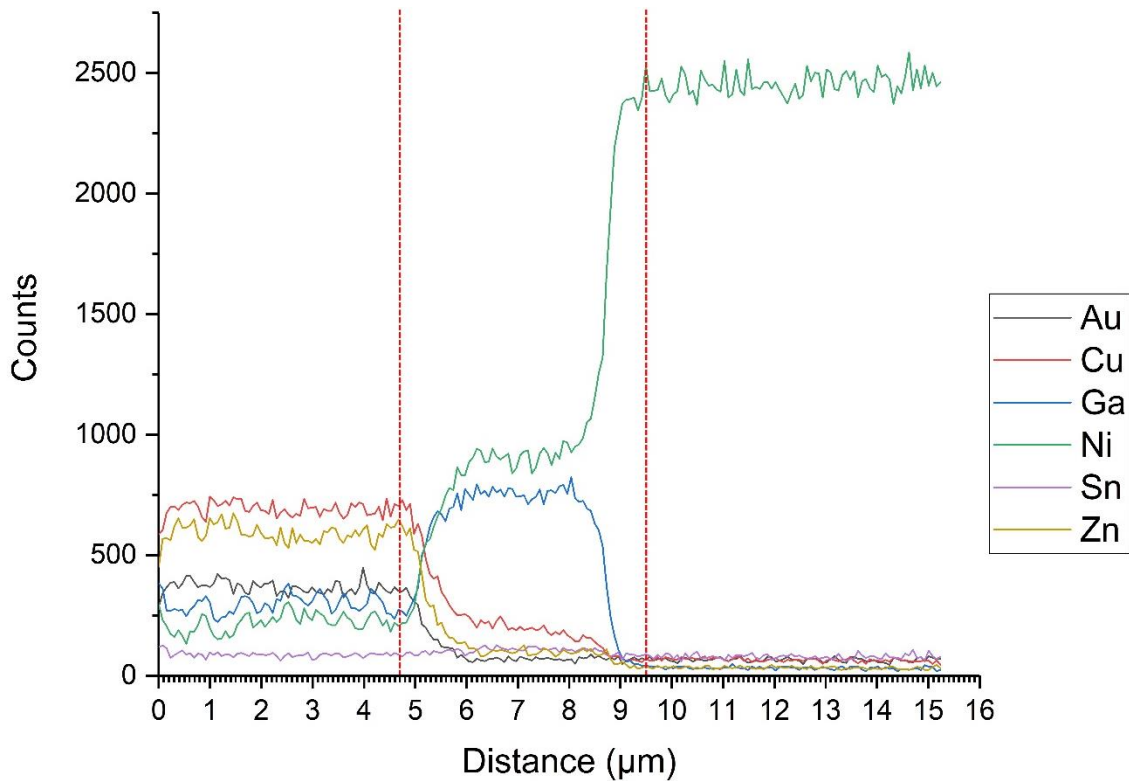


Figure 5.25: EDX line scans across the interface between alloy D and nickel plate. The diffusion zone is highlighted between the two red dotted lines.

The diffusion zone width was measured on each of the 30 scans for each of the 4 manufactured alloys and the reference and the diffusion zone sizes for all 150 scans are recorded in Table 5.19 with an average for each alloy calculated. Another promising artefact of note illustrated in Figure 5.25 is the apparent small diffusion distance of gallium (blue line). Gallium is well known for causing liquid metal embrittlement in other metals, particularly in aluminium in which it diffuses extensively along grain boundaries [49]. Whilst no reference can be found to the phenomenon occurring using the metals to be joined by the filler metals in this study (copper and nickel) and thus there is no specific cause for concern in using a liquid metal containing gallium in this application; it should be noted that automotive vehicles often contain significant amounts of aluminium and hence the use of a liquid gallium alloy in such an environment should be carefully controlled and managed. Additional care should also be taken when recycling such an alloy to ensure that it does not contaminate aluminium which may be recycled for re-use.

Table 5.19: Zone width sizes for each alloy system taken from the 30 EDX line scans taken for each sample. EDX1 Line2 for ISO 17672: Ag-155 is omitted as the diffusion zone was not clearly distinguishable.

	ISO 17672 Ag-155 (μm)			D (μm)			DAuX (μm)			E (μm)			EAuX (μm)		
	Start	Finish	Width	Start	Finish	Width	Start	Finish	Width	Start	Finish	Width	Start	Finish	Width
EDX1Line1	5.3	12.1	6.8	3.8	8.8	5.0	4.8	11.5	6.7	6.7	12.0	5.3	6.4	12.9	6.5
EDX1Line2	/	/	/	2.3	9.5	7.2	3.9	13.0	9.1	6.7	11.5	4.8	6.6	13.7	7.1
EDX1Line3	7.5	13.0	5.5	4.5	10.0	5.5	3.3	12.8	9.5	7.6	12.0	4.4	6.6	12.1	5.5
EDX1Line4	6.8	13.1	6.3	5.4	10.4	5.0	3.8	9.4	5.6	6.1	12.2	6.1	6.5	12.4	5.9
EDX1Line5	6.4	13.6	7.2	4.1	10.5	6.4	3.4	9.0	5.6	5.9	11.8	5.9	6.9	12.0	5.1
EDX1Line6	6.6	13.7	7.1	6.5	10.8	4.3	3.4	8.8	5.4	6.5	11.8	5.3	6.8	12.6	5.8
EDX1Line7	7.9	14.0	6.1	6.4	11.3	4.9	3.9	8.0	4.1	6.8	11.7	4.9	6.6	11.7	5.1
EDX1Line8	9.5	14.1	4.6	6.7	11.6	4.9	4.3	10.6	6.3	7.6	11.7	4.1	6.7	14.1	7.4
EDX1Line9	6.3	13.7	7.4	7.3	11.8	4.5	2.9	9.8	6.9	7.8	12.1	4.3	6.5	14.0	7.5
EDX1Line10	7.6	14.2	6.6	6.9	12.6	5.7	3.7	12.1	8.4	8.0	12.1	4.1	6.8	13.2	6.4
EDX2Line1	6.8	14.3	7.5	4.4	9.6	5.2	10.4	19.6	9.2	6.7	11.6	4.9	7.6	12.7	5.1
EDX2Line2	7.4	14.6	7.2	4.7	9.7	5.0	10.3	18.0	7.7	7.8	11.3	3.5	7.6	12.3	4.7
EDX2Line3	6.4	14.5	8.1	5.2	9.2	4.0	10.2	18.0	7.8	7.5	11.6	4.1	6.1	12.4	6.3
EDX2Line4	6.3	14.2	7.9	4.7	9.5	4.8	9.9	19.0	9.1	5.8	11.7	5.9	6.7	12.4	5.7
EDX2Line5	7.9	14.8	6.9	5.0	9.7	4.7	9.5	19.2	9.7	7.7	11.6	3.9	6.0	12.6	6.6
EDX2Line6	5.5	14.9	9.4	5.3	9.7	4.4	8.6	16.5	7.9	7.6	11.7	4.1	6.3	11.9	5.6
EDX2Line7	6.7	15.4	8.7	5.4	9.8	4.4	7.8	14.2	6.4	7.7	11.6	3.9	6.3	11.7	5.4
EDX2Line8	8.2	15.7	7.5	5.7	9.6	3.9	7.5	15.6	8.1	7.1	11.9	4.8	6.7	12.0	5.3
EDX2Line9	7.1	15.8	8.7	5.2	9.7	4.5	5.5	18.0	12.5	6.6	11.7	5.1	6.2	11.5	5.3
EDX2Line10	9.4	16.1	6.7	5.3	9.8	4.5	5.1	12.6	7.5	7.0	11.6	4.6	6.1	11.7	5.6
EDX3Line1	8.8	13.9	5.1	6.1	10.8	4.7	5.1	11.6	6.5	7.5	13.8	6.3	6.3	11.3	5.0
EDX3Line2	8.8	14.2	5.4	5.5	10.8	5.3	5.1	13.0	7.9	6.7	12.8	6.1	6.1	11.3	5.2
EDX3Line3	7.4	13.9	6.5	5.9	10.8	4.9	5.3	12.9	7.6	3.8	12.8	9.0	7.6	13.2	5.6
EDX3Line4	8.0	13.8	5.8	6.3	10.9	4.6	5.3	11.6	6.3	6.8	12.2	5.4	7.9	13.4	5.5
EDX3Line5	6.8	14.2	7.4	6.0	10.6	4.6	5.8	13.4	7.6	5.4	12.1	6.7	8.7	13.9	5.2
EDX3Line6	7.6	14.1	6.5	6.4	10.5	4.1	5.6	14.8	9.2	5.6	12.1	6.5	8.4	14.4	6.0
EDX3Line7	7.7	13.9	6.2	6.2	10.7	4.5	6.8	14.5	7.7	6.7	12.1	5.4	8.7	15.0	6.3
EDX3Line8	5.3	13.7	8.4	6.4	10.3	3.9	6.8	13.6	6.8	7.6	11.5	3.9	9.5	15.2	5.7
EDX3Line9	5.0	13.7	8.7	6.2	11.0	4.8	6.9	16.8	9.9	6.5	13.3	6.8	10.3	15.4	5.1
EDX3Line10	6.1	13.2	7.1	6.5	10.6	4.1	10.4	18.0	7.6	6.4	12.3	5.9	8.2	13.8	5.6
Average			7.0			4.8			7.7			5.2			5.8
Average distance as a percentage of ISO 17672: Ag-155 (%)			100.0			68.6			110.0			74.3			82.9

Plotting the average value for the 30 scans for each sample (Figure 5.26) and comparing them highlights that 3 of the developed alloys (D, E and EAuX) have an average diffusion distance in nickel less than that of the commercially available reference filler metal and all 4 have an average diffusion distance of less than 10 μ m in nickel during a standard torch brazing cycle.

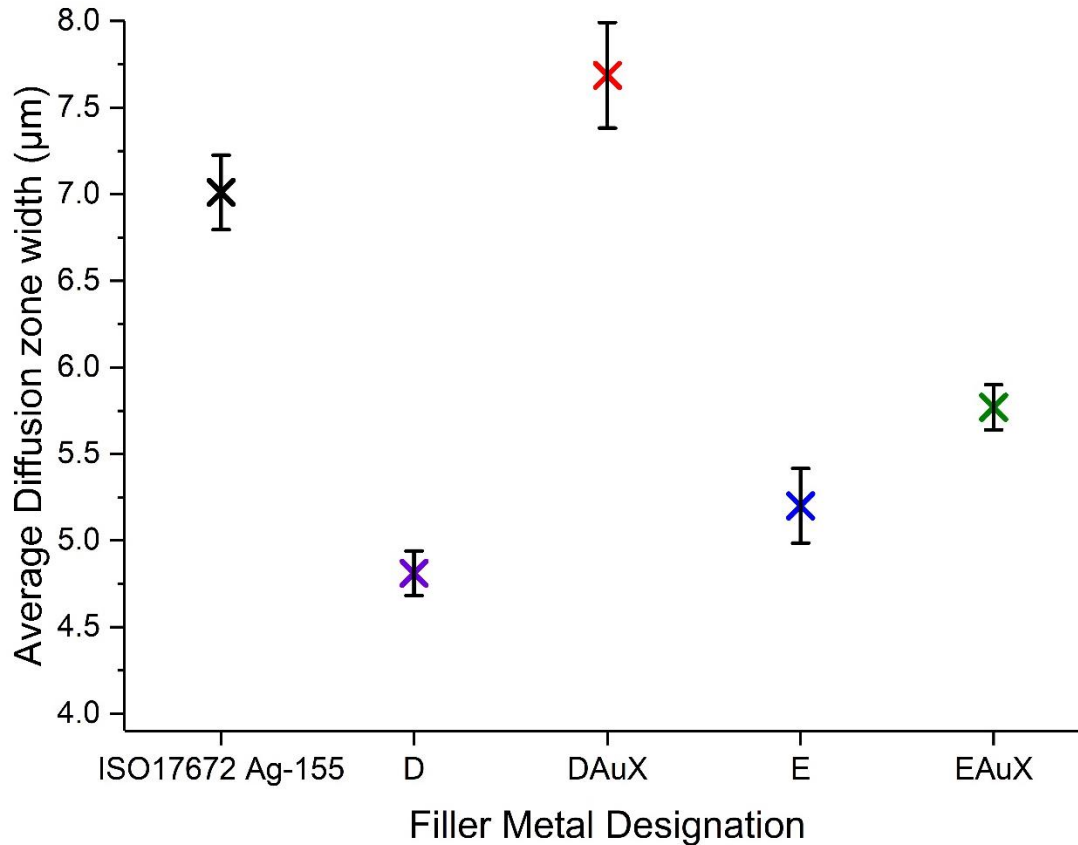


Figure 5.26: Graph showing the average diffusion distance through nickel for each developed alloy system compared to a commercially available reference filler metal (ISO17672 Ag-155). The averages for 3 samples (D, E, EAuX) are lower than the reference material. Error bars give the standard error of the mean ($S_{\bar{x}}$) for the average taken across 30 scans for each sample.

5.8. Summary

This chapter has covered the development of filler metals for brazing thermoelectric devices. HEA design criteria were used to design and manufacture 5 alloys. Three design criteria were used to assess the performance of these alloy systems:

1. They must be able to form a metallurgical bond between copper and nickel.
2. They should have a melting range within the optimum temperature range:
 $T_{opt} = 550^{\circ}\text{C}-620^{\circ}\text{C}$
3. The filler metal chosen should not diffuse through the diffusion barrier (in this instance a 10 μ m nickel layer)

Two of the alloy systems, (designated D and E) formed a metallurgical bond between copper and nickel which satisfied criteria one and were thus taken forward for further assessment.

Thermal analysis revealed that the alloy systems (and some of their gold-free counter parts – produced to reduce alloy cost) melted close to the melting range of interest with

solidus temperatures within 25°C of the desired value of 550°C and liquidus temperatures within 61°C of the desired value of 620°C. It is anticipated that compositional modification through alloying may be able to refine these melting temperatures and is a suggestion for future work in improving these alloy compositions for industrial use.

EDX linescans were used to assess the diffusion profiles of the newly designed filler metal constituents through nickel. Alloys D and E both demonstrated a reduced diffusion distance in nickel when compared with a commercially available filler metal conforming to ISO 17672: Ag-155 after being subject to a standard torch brazing cycle. Alloy D diffused only 4.8µm and alloy E diffused 5.2µm on average compared to the average diffusion distance of 7.0µm by ISO 17672: Ag-155 meaning both systems diffused less than 75% of the distance of the reference. In all cases the diffusion distance was less than the 10µm criteria boundary.

Sample phase identification was undertaken using XRD and EDX. The samples were shown to contain 4 phases. The primary phase is a solid solution phase of copper, zinc, gallium and gold. An intermetallic phase is present (based on either tin or bismuth depending on which alloy is observed, D or E) which has a very limited solubility (<4wt% each) of other elements such as copper, zinc, gallium and gold. A tetragonal CuGa₂ phase is also present which again contains <4wt% (each) of solute atoms of the other alloy constituents. Finally, a predominately gallium-gold phase with 5-7wt% (each) of zinc and copper is also found.

The alloy systems designed in this chapter largely met their design criteria and showed sufficient promise as potential filler metals (both for the application of joining thermoelectric devices within automotive exhaust systems and generally as filler metals) to be recognised as suitable for patenting by Johnson Matthey PLC (the sponsor of this work) and a patent application was filed before the UK Intellectual Property Office on these compositions under patent application number GB1819832.5 on the 5th December 2018.

5.9. References

- [1] United States department of Transport. National Highway Traffic Safety Administration [Internet]. [cited 2019 Feb 21]. Available from: <https://www.nhtsa.gov/>.
- [2] He R, Schierning G, Nielsch K. Thermoelectric Devices: A Review of Devices, Architectures, and Contact Optimization. *Adv. Mater. Technol.* 2018;3.
- [3] Liu W, Wang H, Wang L, et al. Understanding of the contact of nanostructured thermoelectric n-type Bi₂Te_{2.7}Se_{0.3} legs for power generation applications. *J. Mater. Chem. A.* 2013;1:13093–13100.
- [4] Xia H, Chen CL, Drymiotis F, et al. Interfacial reaction between Nb foil and n-type PbTe thermoelectric materials during thermoelectric contact fabrication. *J. Electron. Mater.* 2014;43:4064–4069.
- [5] BSI BSI. BS EN ISO 9453 : 2014 BSI Standards Publication Soft solder alloys — Chemical compositions and forms. 2014;
- [6] ISO/TC 44. Brazing — Filler metals (ISO 17672:2016) [Internet]. 3rd ed. British Standards Institution; 2016. Available from: <https://www.iso.org/obp/ui/#iso:std:iso:3677:ed-3:v1:en>.
- [7] European Commission. Commission regulation (EU) No 494/2011. *Off. J. Eur. Union*

- [Internet]. 2011;2–5. Available from: <http://www.tandfonline.com/doi/full/10.1179/1432891714Z.000000000992>.
- [8] Braunovid M, Aleksandrov N. Intermetallic compounds at aluminum-to-copper and copper-to-tin electrical interfaces. *Electr. Contacts, Proc. Annu. Holm Conf. Electr. Contacts*. 1992;1992-Octob:25–34.
- [9] Cantor B, Chang ITH, Knight P, et al. Microstructural development in equiatomic multicomponent alloys. *Mater. Sci. Eng. A* [Internet]. 2004;375–377:213–218. Available from: <http://dx.doi.org/10.1016/j.msea.2003.10.257>.
- [10] Yeh JW, Chen SK, Lin SJ, et al. Nanostructured high-entropy alloys with multiple principal elements: Novel alloy design concepts and outcomes. *Adv. Eng. Mater.* 2004;6:299-303+274.
- [11] Otto F, Dlouhý A, Somsen C, et al. The influences of temperature and microstructure on the tensile properties of a CoCrFeMnNi high-entropy alloy. *Acta Mater.* 2013;61:5743–5755.
- [12] Laplanche G, Gadaud P, Horst O, et al. Temperature dependencies of the elastic moduli and thermal expansion coefficient of an equiatomic, single-phase CoCrFeMnNi high-entropy alloy. *J. Alloys Compd.* [Internet]. 2015;623:348–353. Available from: <http://dx.doi.org/10.1016/j.jallcom.2014.11.061>.
- [13] Schuh B, Mendez-Martin F, Völker B, et al. Mechanical properties, microstructure and thermal stability of a nanocrystalline CoCrFeMnNi high-entropy alloy after severe plastic deformation. *Acta Mater.* [Internet]. 2015;96:258–268. Available from: <http://dx.doi.org/10.1016/j.actamat.2015.06.025>.
- [14] Senkov ON, Wilks GB, Scott JM, et al. Mechanical properties of Nb₂₅Mo₂₅Ta₂₅W₂₅ and V₂₀Nb₂₀Mo₂₀Ta₂₀W₂₀ refractory high entropy alloys. *Intermetallics* [Internet]. 2011;19:698–706. Available from: <http://dx.doi.org/10.1016/j.intermet.2011.01.004>.
- [15] Senkov ON, Wilks GB, Miracle DB, et al. Refractory high-entropy alloys. *Intermetallics* [Internet]. 2010;18:1758–1765. Available from: <http://dx.doi.org/10.1016/j.intermet.2010.05.014>.
- [16] Yao HW, Qiao JW, Hawk JA, et al. Mechanical properties of refractory high-entropy alloys: Experiments and modeling. *J. Alloys Compd.* 2017;696:1139–1150.
- [17] Pickering EJ, Jones NG. High-entropy alloys: a critical assessment of their founding principles and future prospects. *Int. Mater. Rev.* [Internet]. 2016;61:183–202. Available from: <http://www.tandfonline.com/doi/full/10.1080/09506608.2016.1180020>.
- [18] Yeh JW. Recent progress in high-entropy alloys. *Ann. Chim. Sci. des Mater.* 2006;31:633–648.
- [19] Yeh JW, Chen SK, Lin SJ, et al. Nanostructured high-entropy alloys with multiple principal elements: Novel alloy design concepts and outcomes. *Adv. Eng. Mater.* 2004;6:299-303+274.
- [20] Pickering EJ, Muñoz-Moreno R, Stone HJ, et al. Precipitation in the equiatomic high-entropy alloy CrMnFeCoNi. *Scr. Mater.* [Internet]. 2016;113:106–109. Available from: <http://dx.doi.org/10.1016/j.scriptamat.2015.10.025>.
- [21] Otto F, Yang Y, Bei H, et al. Relative effects of enthalpy and entropy on the phase stability of equiatomic high-entropy alloys. *Acta Mater.* [Internet]. 2013;61:2628–2638. Available from: <http://dx.doi.org/10.1016/j.actamat.2013.01.042>.
- [22] Senkov ON, Miller JD, Miracle DB, et al. Accelerated exploration of multi-principal element alloys with solid solution phases. *Nat. Commun.* 2015;6:1–10.
- [23] Chuang MH, Tsai MH, Wang WR, et al. Microstructure and wear behavior of

- Al_xCo_{1.5}CrFeNi_{1.5}Ti high-entropy alloys. *Acta Mater.* 2011;59:6308–6317.
- [24] Qiu Y, Thomas S, Gibson MA, et al. Corrosion of high entropy alloys. *npj Mater. Degrad.* [Internet]. 2017;1:15. Available from: <http://www.nature.com/articles/s41529-017-0009-y>.
- [25] Chen YY, Duval T, Hung UD, et al. Microstructure and electrochemical properties of high entropy alloys-a comparison with type-304 stainless steel. *Corros. Sci.* 2005;47:2257–2279.
- [26] Hardwick L, Rodgers P, Pickering EJ, et al. Development of novel nickel-based brazing alloys, utilising alternative melting point depressants and high entropy alloy concepts. *Brazing, High Temp. Brazing Diffus. Bond. LÖT* 2019. 2019. p. 7–17.
- [27] Tillmann W, Ullitzka T, Wojarski L, et al. Brazing of high temperature materials using melting range optimized filler metals based on the high-entropy alloy CoCrCuFeNi. 2019.
- [28] Bridges D, Zhang S, Lang S, et al. Laser brazing of a nickel-based superalloy using a Ni-Mn-Fe-Co-Cu high entropy alloy filler metal. *Mater. Lett.* [Internet]. 2018;215:11–14. Available from: <https://doi.org/10.1016/j.matlet.2017.12.003>.
- [29] Snell R. The Development of Novel Silver Brazing Alloys. PhD Thesis. 2017.
- [30] Okamoto H. Ag-Sb (Silver-Antimony). *J. Phase Equilibria Diffus.* [Internet]. 2007;28:403. Available from: <https://doi.org/10.1007/s11669-007-9113-y>.
- [31] Murarka SP, Anand MS, Agarwala RP. Diffusion of vanadium in aluminium and nickel. *Acta Metall.* 1968;16:69–72.
- [32] The phase diagram of the P-Sb system [Internet]. [cited 2017 Jun 21]. Available from: <http://www.himikatus.ru/art/phase-diagr1/P-Sb.php>.
- [33] Wazzan AR, Tung P, Robinson LB. Diffusion of silver into nickel single crystals. *J. Appl. Phys.* 1971;42:5316–5320.
- [34] Mantl S, Rothman SJ, Nowicki LJ, et al. The Tracer Diffusion of Ge in Ni Single-Crystals. *J. Phys. F-Metal Phys.* 1983;13:1441–1448.
- [35] Neuhaus P, Herzig C, Gust W. GRAIN BOUNDARY DIFFUSION OF INDIUM AND NICKEL-INDIUM. 1989;31.
- [36] Guo S, Liu CT. Phase stability in high entropy alloys: Formation of solid-solution phase or amorphous phase. *Prog. Nat. Sci. Mater. Int.* [Internet]. 2011;21:433–446. Available from: [http://dx.doi.org/10.1016/S1002-0071\(12\)60080-X](http://dx.doi.org/10.1016/S1002-0071(12)60080-X).
- [37] Lide DR. CRC Handbook of Chemistry and Physics. Internet v. Boca Raton, Florida: CRC press; 2005. Available from: <http://webdelprofesor.ula.ve/ciencias/isolda/libros/handbook.pdf>.
- [38] Takeuchi A, Inoue A. Classification of Bulk Metallic Glasses by Atomic Size Difference, Heat of Mixing and Period of Constituent Elements and Its Application to Characterization of the Main Alloying Element. *Mater. Trans.* 2005;46:2817–2829.
- [39] Zhang Y, Zhou YJ, Lin JP, et al. Solid-solution phase formation rules for multi-component alloys. *Adv. Eng. Mater.* 2008;10:534–538.
- [40] Yang X, Zhang Y. Prediction of high-entropy stabilized solid-solution in multi-component alloys. *Mater. Chem. Phys.* [Internet]. 2012;132:233–238. Available from: <http://dx.doi.org/10.1016/j.matchemphys.2011.11.021>.
- [41] Zhang Y, Zhou YJ. Solid Solution Formation Criteria for High Entropy Alloys. *Mater. Sci. Forum* [Internet]. 2007;561–565:1337–1339. Available from: <http://www.scientific.net/MSF.561-565.1337>.

- [42] Takeuchi A, Amiya K, Wada T, et al. Entropies in alloy design for high-entropy and bulk glassy alloys. *Entropy*. 2013;15:3810–3821.
- [43] Zhang Y, Zuo TT, Tang Z, et al. Microstructures and properties of high-entropy alloys. *Prog. Mater. Sci.* [Internet]. 2014;61:1–93. Available from: <http://dx.doi.org/10.1016/j.pmatsci.2013.10.001>.
- [44] Miracle DB, Senkov ON. A critical review of high entropy alloys and related concepts. *Acta Mater.* [Internet]. 2017;122:448–511. Available from: <http://dx.doi.org/10.1016/j.actamat.2016.08.081>.
- [45] Okamoto H. *Phase Diagrams for Binary Alloys*. Second edi. Materials Park, Ohio: ASM International; 2010.
- [46] Li JB, Ji LN, Liang JK, et al. A thermodynamic assessment of the copper-gallium system. *Calphad Comput. Coupling Phase Diagrams Thermochem.* 2008;32:447–453.
- [47] Terlicka S, Dębski A, Gašior W. Thermodynamic description of the Ga-Li-Zn system. *Thermochim. Acta.* 2018;659:66–73.
- [48] Miettinen J. Thermodynamic description of Cu-Mg-Ni and Cu-Mg-Zn systems. *Calphad Comput. Coupling Phase Diagrams Thermochem.* 2008;32:389–398.
- [49] Kolman DG. A review of recent advances in the understanding of liquid metal embrittlement. *Corrosion.* 2019;75:42–57.

Chapter 6: Suitability of Developed Filler metals for Joining Thermoelectric Components

6.1. Introduction

With the filler metals developed in the previous chapter showing sufficient promise to warrant further investigation, the final aim of this project (To investigate any promising filler metals developed in this project for their ability to perform as a filler metal in the intended application) becomes the focus of this chapter. Developed filler metals need to be assessed for an array of properties to determine their suitability for real world applications. For the sake of clarity these properties can be classified into three categories: the first covers the properties which have been demonstrated in prior chapters (even if only qualitatively); the second is the properties which will be tested in this section of this thesis. The third and final category is property tests which are suggested but are beyond the scope of this thesis. Recommendations for suitable tests to continue this work will be provided in the following chapter under the 'Future work' subheading.

As mentioned above, some of the required properties for these filler metals have already been shown in prior chapters during the development of the alloys. For instance, the filler metals developed are required to have a melting range suitable for application. The design brief indicated an optimal melting range of $T_{opt}=550^{\circ}\text{C}-620^{\circ}\text{C}$ and the melting ranges of developed fillers were measured and recorded in Chapter 5. Additionally, the ability of the developed filler metals to wet copper and nickel substrates has been demonstrated qualitatively as this was used as a means of assessing the suitability of the developed fillers for use in the previous chapter. Whilst this clearly demonstrates suitability for application, a quantitative value for the ability of these fillers to wet substrates is required in order to compare with current filler metals.

In this chapter assessment of 3 important properties for the application in question will be performed.

Firstly, the ability of the developed filler metals to wet copper surfaces will be assessed quantitatively via a variant of the sessile drop method as used to assess the influence of surface roughness on contact angle in Chapter 4.

Secondly the mechanical properties of the filler metals will be assessed. As mentioned in Chapter 2, the mechanical properties of the filler metal itself are often irrelevant as most brazed joints are designed so as to instigate failure in the parent materials and not the filler itself. However, the intended final use of the filler metals developed in this study is for joining components on such a small scale it may not be possible to implement the standard joint design rules. As such, the mechanical tests performed in this chapter will be applied to brazed joints specifically designed to encourage failure within the filler metal of the brazed joint and not the parent materials. The mechanical testing will evaluate the room temperature tensile strength of the developed filler metals in comparison to the currently used filler metal (Ag-155) in brazed lap joint tensile specimens with an overlap length of t (i.e. the thickness of the parent materials – see Figure 6.1).

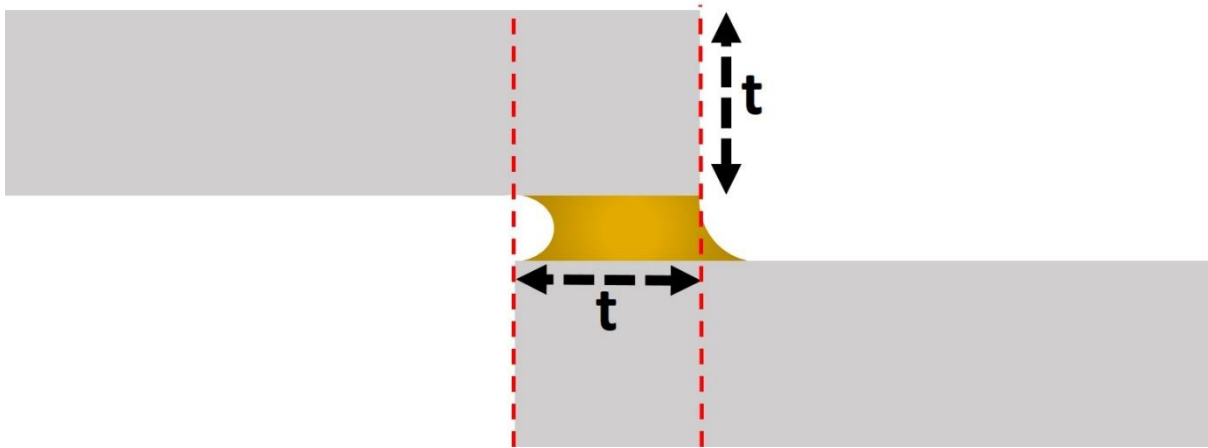


Figure 6.1: Diagram illustrating the dimensions of the brazed joints used to form tensile test specimens. The overlap length is equal to t . In the samples manufactured in this study $t=3\text{mm}$.

This overlap length is substantially lower than the recommended overlap length of 3.5 times the thinnest joint member ($3.5t$) which is recommended to ensure failure occurs in the parent materials instead of the filler, and as such a failure in the filler metal and not the parent material will be expected [1].

Further tensile testing on samples which have been subjected to thermal cycling will also be undertaken in order to assess the impact of stresses generated within the materials due to mismatch of thermal expansion coefficients between parent materials and filler metals. Again these data will be viewed comparatively with the intent of determining the performance of joints formed with the developed filler metals relative to those formed with the currently selected filler metal (Ag-155).

Finally, an attempt to characterise the electrical performance of the joints produced will be made. It is important that the final device has a good electrical contact through the filler metal chosen to ensure as little as possible of the energy recovered from waste heat is wasted. To assess this, samples of skutterudite thermoelectric were brazed together using the designed filler metals and the electrical contact resistances across the two interfaces at the brazed joint were measured and compared with a similar arrangement brazed with filler metal Ag-155.

6.2. Wetting Assessment of Designed Alloys

To assess the wetting performance of the alloys designed and selected in Chapter 5, a modified sessile drop experiment (as described in Section 3.6.2) was carried out on 4 developed filler metal samples (D, DAuX, E and EAuX) and a sample of Ag-155 for comparison. Copper substrates were again selected for this experiment as the electrical contacts to which the filler metals developed in this thesis must bond to when used in-situ are made of copper.

All copper substrates used in this experiment were used in the as-received condition; the sheet used to make all 5 samples was measured to have an average surface roughness of $R_a = 0.09 \pm 0.02 \mu\text{m}$ which is within the optimum roughness range as determined by the wetting experiments in Chapter 4 ($0.09\text{--}0.16 \mu\text{m}$). As the as-received roughness's were

within the optimum roughness range as determined previously, no extra grinding or preparation of the surfaces was undertaken.

Again, a cube of each filler metal measuring approximately $2\text{mm} \times 2\text{mm} \times 2\text{mm}$ was placed onto the copper substrate and heated through an identical heating schedule to that used in Chapter 4 (heated up to 800°C following the heating schedule in Figure 3.12). No flux was applied to the substrate or filler metal due to the experiment taking place in a controlled atmosphere furnace and any flux residues present could severely damage the vacuum pump used to remove air from the furnace before the reducing atmosphere was introduced. The filler metal was imaged at 1 minute intervals throughout the heating schedule and contact angles between filler and substrate were measured after the filler metal had become molten until the experiment ended. This allowed observation of how the contact angle varied with temperature; these readings were stopped once no further change in filler metal contact angle could be observed whilst the experiment was taking place or the experiment heating schedule concluded. Once photographs for all 5 substrates had been taken they were examined at 5 degree intervals (1 photograph per minute) using a piece of software called “Drop_angle” [2]. The plot in Figure 6.2 shows the variance in contact angle for each filler metal over the course of the recorded experiment until 800°C is reached. The final average wetting angle for each sample was calculated and is recorded in Figure 6.2.

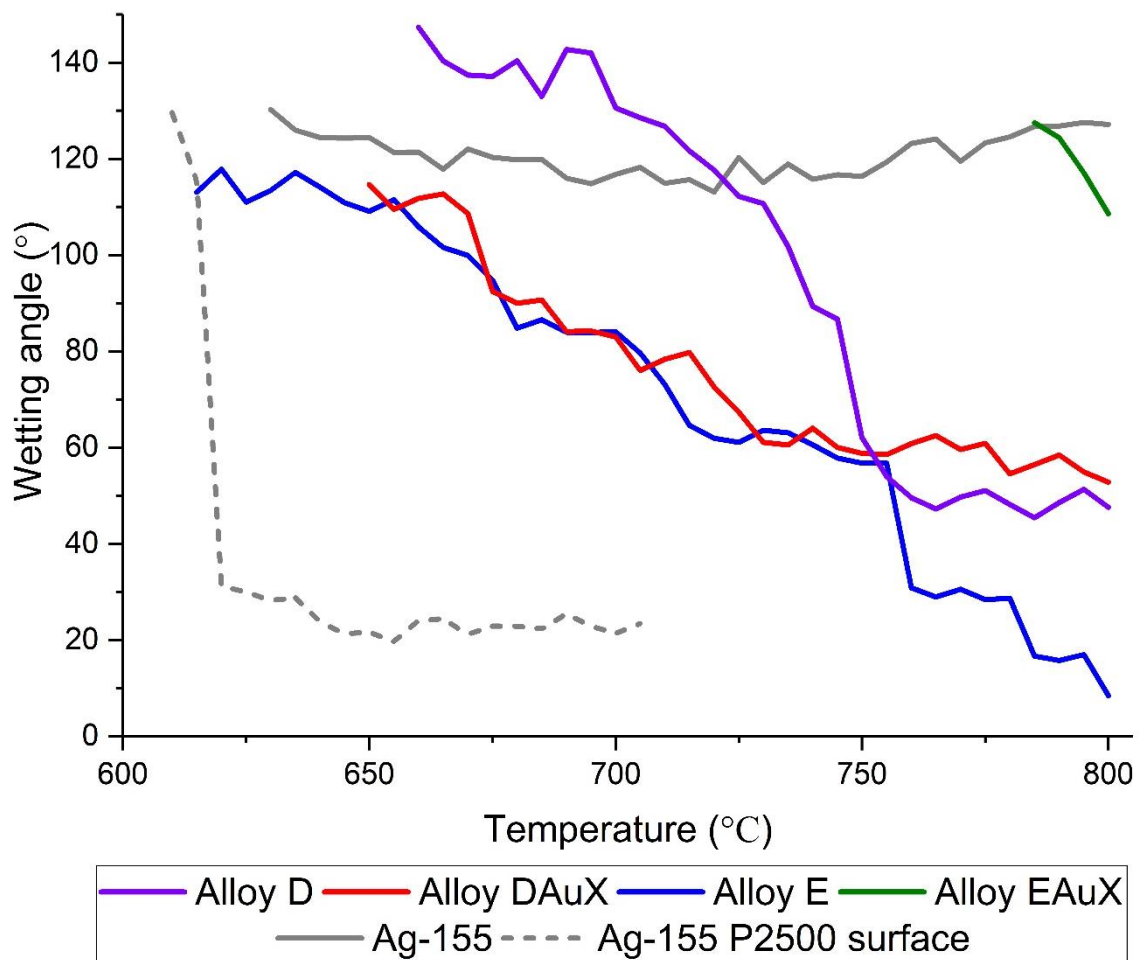


Figure 6.2: Graph of the temperature dependence of wetting angle of different alloys on unground copper substrates. Additional readings taken with the temperature held at 800°C for up to 3 minutes are not shown.

As can be seen in Figure 6.2 the alloys tested all melted at different temperatures and all had non-wetting initial contact angles (wetting angle $>90^\circ$ - Table 6.1). The contact angle of all samples reduced as the temperature was raised in the furnace with some samples wetting significantly better as the test proceeded.

Against expectation, the sample of Ag-155 (the intended benchmark for the assessment of the performance of the alloys developed in this work) showed little change in wetting angle from its initial contact angle (130.2°) to its final average wetting angle of $120.5 \pm 0.7^\circ$. This is a large contrast to the wetting profile seen in Chapter 4 using a sample of Ag-155 on a ground substrate with a $0.09\mu\text{m}$ surface roughness prepared by grinding. This result has been included in Figure 6.2 as a dotted grey line for comparison.

Alloy EAuX did not appear to melt or form a measurable contact angle until very high temperatures (785°C) relative to the other alloys developed in this study and as such analysis on such a small data set is difficult to draw meaningful conclusions from. It is therefore likely that the melting onset for the alloy (557.9°C) picked up by the DSC analysis in the previous chapter is for a phase making up a small portion of the overall alloy composition – enough to be detected by the sensitive DSC analysis but not a sufficient percentage to cause the cube of filler in this study to melt and visibly deform. Regardless, if sufficient filler metal flow is not seen until such high temperatures it is unlikely such an alloy system will be viable to braze components within a thermoelectric device.

The other 3 filler metals designed in this study (D, DAuX and E) illustrated behaviour more in line with expectations and more suitable for use in brazing thermoelectric devices. Alloy E was the best performing brazing filler metal designed in this study, exhibiting a final wetting angle as low as $9.0 \pm 0.2^\circ$; a result comparable to that of best result obtained from the experiment in Chapter 4 using Ag-155 filler on various substrates (P1200 ground substrate – final average wetting angle $8.8 \pm 0.5^\circ$). This result is of particular interest as the surfaces used in this study were not ground prior to the experiment and thus could have some sort of oxide layer present on the surface. The ability of alloy E to wet the unprepared surface as well as filler Ag-155 can wet a prepared surface is an indicator of potential resilience of alloy E to poor surface conditions. To confirm if this is the case, future investigations into the effectiveness of this filler could assess the impact of varying surface preparation or the presence of surface contaminants on the wetting angle formed between filler and substrate. It should however also be noted that the temperature required to attain this low contact angle was much higher than that required for the Ag-155 filler on the P1200 substrate. Alloy E attained its final average contact angle at temperatures as high as 800°C whereas Ag-155 on the P1200 surface reached that level at temperatures as low as 630°C . Exposure of thermoelectric components to temperatures high enough to attain such low wetting angles is likely to cause damage, potentially limiting the viable applications for this alloy.

Samples D and DAuX both melted sufficiently to obtain their initial contact angles at similar temperatures (660°C and 650°C respectively), with alloy DAuX having a significantly shallower initial wetting angle ($114.6 \pm 0.8^\circ$) than alloy D which had the highest of all the initial contact angles found in this study ($147.3 \pm 1.8^\circ$). Once molten, alloy DAuX exhibited very similar wetting angles to alloy E through the temperature range 650°C - 750°C before levelling off to give a final average contact angle of $58.9 \pm 0.8^\circ$. Alloy

D maintained a high contact angle ($>120^\circ$) until the temperature reached approximately 715° at which point its contact angle rapidly reduced to less than 50° at 750°C before levelling out to give a final average contact angle around 10° lower than its gold free counterpart ($47.0\pm 1.8^\circ$).

The final contact angles of the gold-containing version of both alloy systems (D and E) were lower than their gold-free counterparts; this is as expected as gold is well known to improve both wetting and flow properties in brazing filler metals [3]. The initial and final average contact angles for each alloy assessed in this study are summarised in Table 6.1.

Table 6.1: The average final wetting angle calculated for each filler metal evaluated.

Alloy designation	Initial contact angle ($^\circ$)	Average final contact angle ($^\circ$)	Standard error of the mean for averaged final contact angle ($S_{\bar{x}}$)
D	147.3	47.0	± 1.8
DAuX	114.6	58.9	± 0.8
E	113.0	9.0	± 0.2
E AuX	127.5	71.5	± 2.3
Ag-155	130.2	120.5	± 0.7

Against expectation, all 4 brazing filler metal samples designed in this study appear to perform better than the Ag-155 reference sample. This is unexpected as industrial manufacturers of fillers conforming to Ag-155 note that it is “*free flowing when molten, producing neat joints with small fillets*” [4]. Additional evidence to the disparity of this result can be seen in experiments earlier in this work in which an identical sample of Ag-155 obtained a wetting angle as low as $24.2\pm 0.8^\circ$ on a surface measured to have the same roughness as the samples used in this experiment ($R_a = 0.09\mu\text{m}$). It is therefore considered that at least one other factor must be influencing the ability of the Ag-155 filler metal to spread across the surface in this experiment. It is considered that the most likely source of discrepancy between the ground sample in the previous study and the ‘as-received’ sample used in this study is the presence of surface oxides/contaminants on the ‘as-received’ sample. The ‘as received’ samples were cleaned prior to use but no grinding of the surface had occurred so whilst the surface roughness profile of the samples used in this study may be the same as that of a P2500 ground sample it is possible that the grinding process removed surface oxides or contaminants from the P2500 sample which were not removed from the sample in this study. A recent review paper on the subject of brazing highlights the importance of cleanliness to ensure a high quality joint and highlights a lack of studies on the influence surface cleanliness has on joint quality [5]. One study of note for the influence of joint cleanliness specifically on wetting is a 2017 study by Bobzin et al. in which the impact of pre-cleaning and plasma cleaning of Inconel and stainless steel before brazing led to increased surface energy and better wetting by the filler metals used [6]. Normally when brazing, oxides are removed using a flux, due to restrictions in the use of flux due to the furnace setup used no flux was applied to samples in this study which may have influenced the performance of Ag-155.

If we assume that the presence of the oxide layer (the most likely difference between the samples used in this study and the study in chapter 4) causes the disparity between the performance of Ag-155 on a ground surface and Ag-155 on an ‘as-received’ surface it follows that the filler metals developed in this study are better at dealing with an oxide covered surface than Ag-155. One possible explanation as to why these fillers are better at bonding with oxide contaminated surfaces is that the filler metals developed in this study have similar characteristics to an active filler metal. As mentioned in Chapter 2, active filler metals contain a small percentage of an ‘active’ element which promotes wetting of ceramics (often carbides, oxides and nitrides) by reacting with the ceramic to form a layer on the surface which is more easily wet by the filler metal. A common example of this is the use of Ag-Cu filler metals containing a small percentage of Ti as an active element to join alumina ceramics. Titanium atoms have a stronger affinity for oxygen than aluminium does and as such the titanium will displace some of the aluminium from the alumina ceramic to form a titanium oxide reaction layer at the surface of the ceramic. The formation of this interfacial layer then allows better wetting of the surface by the remaining filler metal. Other elements often incorporated in filler metals as active elements include zirconium [7], niobium [8][9], hafnium [8], and chromium [10][11] which react with oxides, carbides or nitrides contained in the ceramic. Thus, the requirement for an active element within a filler metal is that it must be capable of displacing a metal atom from the ceramic compound it is joining.

The compounds of interest in this study are those which form the oxide layer on the surface of the copper substrate used in these wetting tests (Cu_2O and CuO). The two compounds form according to Equation 6.1 and Equation 6.2 [12].



To assess whether it is feasible that the performance difference between filler Ag-155 and fillers developed in this study on non-ground surfaces is due to the capability of fillers in this study to react with oxide layers requires knowledge on whether any of the elements contained within either filler has the ability to act as an active element when used to braze copper oxide at the temperatures used in this study.

Ellingham diagrams over the alloy melting ranges in this study (600°C-800°C) show that the oxidation of elements contained in filler Ag-155 is largely less preferable than the formation of copper oxide. The 4 components of filler metal Ag-155 (silver, copper, zinc and tin) are marked on the Ellingham diagram in Figure 6.3 and over the temperature range 600°C-800°C, only tin oxide and zinc oxide have a lower Gibbs free energy of formation than copper oxide.

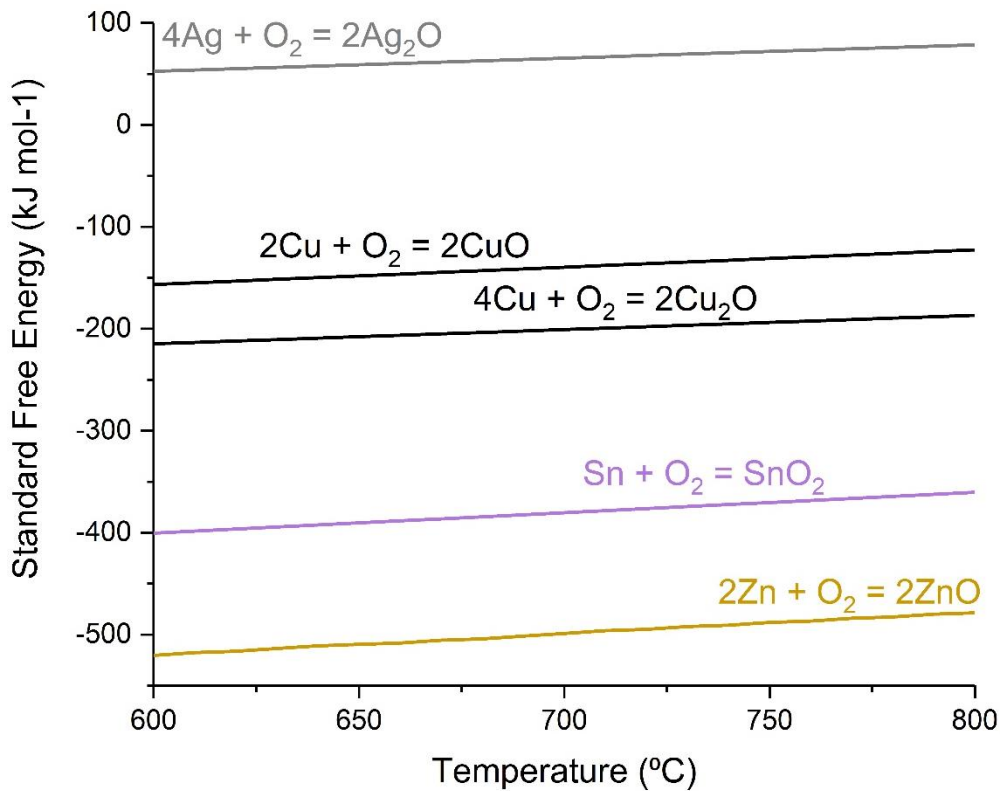


Figure 6.3: Ellingham diagram for the components of alloy Ag-155 compared to copper. Data replotted from DoITPoMS [13] where it is calculated from standard free energy data. Zinc data taken from [14].

The primary component of the alloy, silver (66.34at%), has a positive enthalpy of formation for its oxide across the 600°C-800°C temperature range and as such will not reduce copper oxide. Zinc and tin can both feasibly reduce copper oxide to copper at these temperatures however only make up a small fraction of the total alloy system (zinc: 16.08at%, tin: 2.65at%). It must be noted that the data in Figure 6.3 refers to elements in the standard state (i.e. as an element) and not in the alloy Ag-155. The activity of the elements in question will vary when not in standard state and it is likely that the Gibbs free energy for the formation of their oxide from their alloyed state is different than it is from their standard state.

A similar Ellingham diagram for the elements contained within filler metal 'alloy E' can be seen in Figure 6.4. Whilst the Gibbs free energy of formation for bismuth oxide is slightly higher than that of copper (I) oxide (CuO), the Gibbs free energy of formation for zinc oxide and gallium oxide are lower (data for gold forming gold oxide could not be found, but it is highly unlikely to have a favourable Gibbs free energy of formation given the known inertness of gold). Making up a total of 62.00at% of alloy E, both gallium and zinc have the potential to reduce copper oxide (of either form) to copper metal (although again, differences in Gibbs free energy of formation of oxides will vary as neither gallium nor zinc are in their standard state).

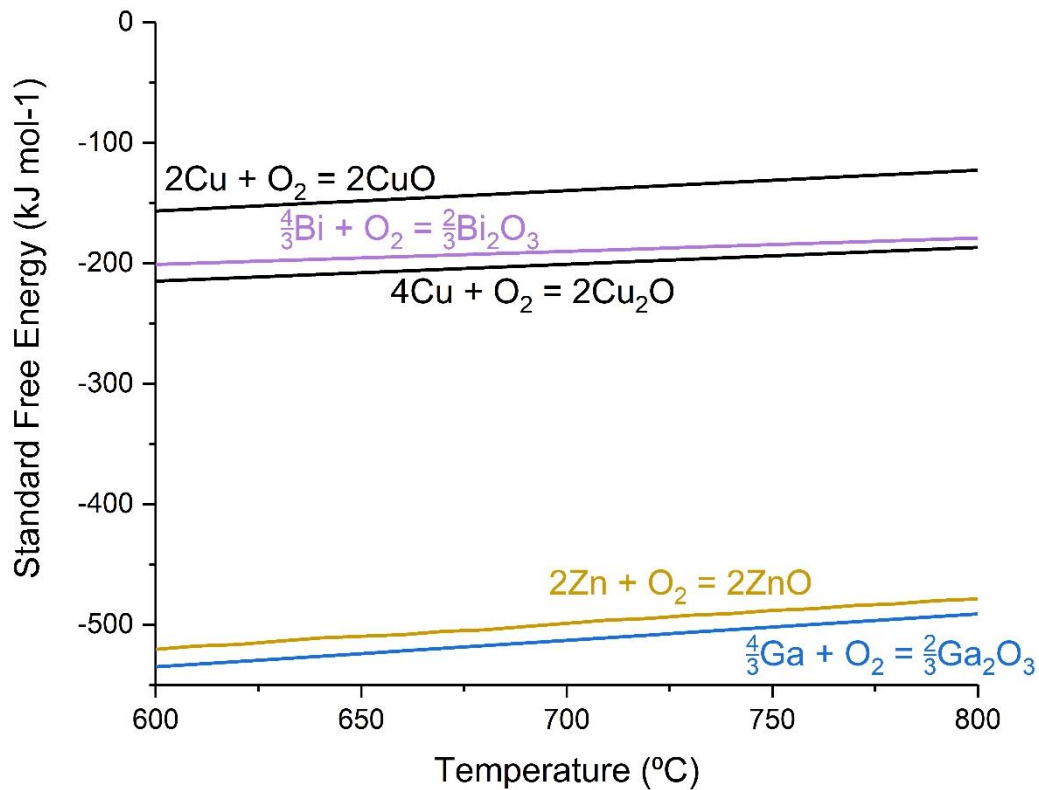


Figure 6.4: Ellingham diagram for the components of alloy E compared to copper. Data replotted from DoITPoMS [13], where it is calculated from standard free energy data. Zinc data taken from [14].

As zinc is present in both Ag-155 and alloy E it is unlikely that it is zinc is the sole element capable of removing the copper oxide as if it was, spreading of both fillers across the surface would be expected. It is likely that if any element contained in alloy E is capable of acting as an active element which can disrupt the copper oxide layer it is gallium. Further evidence of the potential of gallium to disrupt the oxide layer can be seen when the Ellingham diagram for gallium is compared to other elements used as the active element in various other filler metals (those designed to bond ceramics to metals), Figure 6.5.

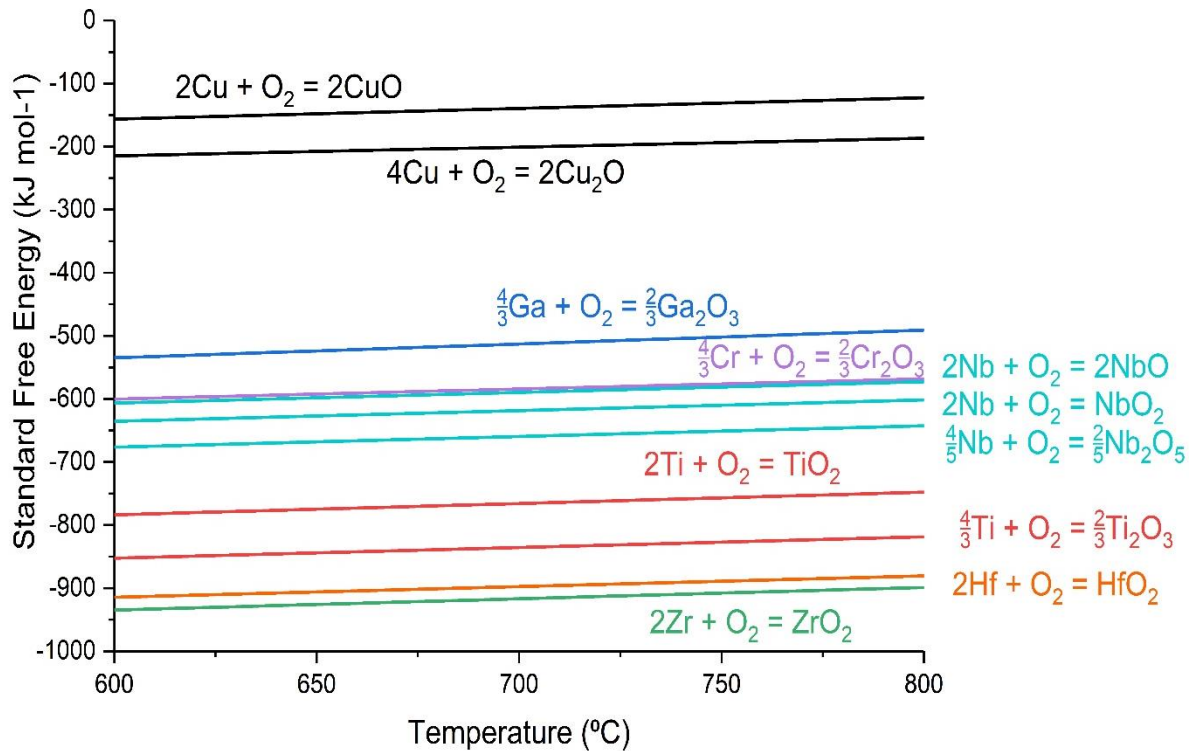


Figure 6.5: Ellingham diagram for several elements commonly found in active brazing filler metals compared to copper and gallium. Data replotted from DoITPoMS [13], where it is calculated from standard free energy data.

Whilst not having as high an oxygen affinity as titanium, hafnium or zirconium, gallium forming gallium oxide has a Gibbs free energy of formation similar to those of chromium forming chromium oxide and niobium forming niobium oxide across the temperature range of interest. Limited literature on the subject of gallium wetting copper oxide surfaces is available, although one source does mention that “*gallium actively wets clean copper with a thin (estimated at 100 Angstrom) CuO film.*” [15] and a 1964 report on low melting temperature brazing alloys for the Air Force Materials Laboratory in Ohio stated “*it is well known that gallium will react with most any metal or oxide composition*” [16] providing some evidence that the gallium in the alloys developed in this study is responsible for the wetting of the un-ground copper substrates.

In conclusion, according to the experimental results gathered in this section the alloy with the lowest wetting angle is alloy E, with a final average wetting angle of 9.0 ± 0.2 . All 4 developed alloys tested demonstrated final wetting angles lower than that of the reference alloy Ag-155 (Table 6.1). The apparently superior performance of the alloys developed in this study compared to Ag-155 is likely due to the presence of oxide layers on the copper substrates used in this experiment. The presence of oxide layers on substrate surfaces is known to disrupt the wetting performance of many standard filler metals [5]. The elements with high oxygen affinity (e.g. gallium) present in the alloys developed in this study may have acted as ‘active’ elements, forming compounds with the copper oxide layer present on the substrates. The formation of these compounds may have led to better wetting than would be expected from a standard filler metal on a substrate with an oxide layer. Further testing with copper substrates having oxide layers of varying thicknesses could be used to provide further evidence to this explanation.

6.3. Mechanical Properties of Designed Alloys

Mechanical properties of brazed joints are often of minor consideration when compared to other properties. This fact is even recognised in the British standard for destructive testing of brazed joints (BS EN 12797:2000) [17] which states in its scope:

“...there will usually be some level of strength required but this may not be explicitly stated and is frequently of minor importance compared to other criterion e.g. hermeticity. It follows that a test which measures strength may be totally irrelevant in assessing a joint for a particular application where strength is a minor consideration. This situation is made more complicated because brazed joints are almost invariably designed to be loaded in shear and the dimensions of the joint affect the shear strength to a much greater extent than they do the tensile strength.”

As acknowledged earlier (Section 6.1) the mechanical performance of the joints formed in the TEGs is indeed less important than in many other situations; however, some mechanical strength is still required as the components must resist the vibration they will be exposed to in use in an exhaust system. As these are complex and variable situations, no specific requirements or suitable values for strength were assigned in the development criteria. Regardless of this, qualitative comparisons with the industrial filler metal Ag-155 are considered to be of sufficient interest to warrant investigation.

Resistance to vibration is difficult to assess accurately. Few standards exist giving recommended test setups for assessment of mechanical resistance to vibration and those which do exist are often engineered to a fabricated component and not a single brazed joint [18]. As such it has been decided to evaluate the mechanical properties of brazed joints formed in this work by applying tensile forces to a brazed lap joint in order to assess its strength in shear. A single lap joint was selected to be the design of joint used in this test for the following reasons:

- Forming a brazed butt joint between two free pieces of metal without misalignment between the two pieces is difficult and often impractical, especially when brazing by hand; a lap joint does not suffer from misalignment and is much simpler to manufacture.
- The British standard for destructive testing of brazed joints (BS EN 12797:2000) [17] highlights that a substantial majority of brazed joints are designed to subject the joint to shear stresses whilst in service and that converting results of butt joint tests to shear strength is not possible. As such testing of brazed joints in shear is recommended.

The single lap joint was decided upon as the best design of specimen to assess the shear strength of these joints as it provides a measure of joint shear strength (the form of mechanical loading brazed joints are most often loaded in), is simple in design, simple and practical to manufacture (which should lead to better formed and more consistent joints) and economical as it uses the least amount of filler metal per sample produced (which as the filler designed in this study contain high percentages of expensive elements is an important consideration).

6.3.1. Room Temperature Tensile Strength

Firstly, the room temperature strength of brazed joints formed with these filler metals will be assessed. No exposure to heat or thermal cycling will have occurred to these joints other than what they will have experienced during the brazing process to form the joint itself. It should be noted that due to different melting temperatures of the brazing alloys

assessed, the thermal exposure received by samples brazed with different filler metals may be different, however this is unavoidable without compromising bonding.

The samples for this study were chosen to be manufactured from nickel joined to nickel rather than being made from the nickel-copper interface that will be used in situ and in the thermal cycling trials detailed below. The reason nickel – nickel joints were selected was to encourage failure of the brazed joint in the filler metal. Initial trials attempted to use copper to nickel joints formed with an overlap length of 9mm ($9\text{mm}=3t$; t being the thickness of the parent materials used – see Figure 6.1). Failure was found to occur in the copper parent material rather than in the brazed joint itself and thus the test did not reveal any information on the filler metal in isolation, but rather on the particular brazed joint as a whole. Similar results were seen with overlap lengths of 6mm ($2t$) and 3mm (t) with failures still occurring in the copper parent material (Figure 6.6).

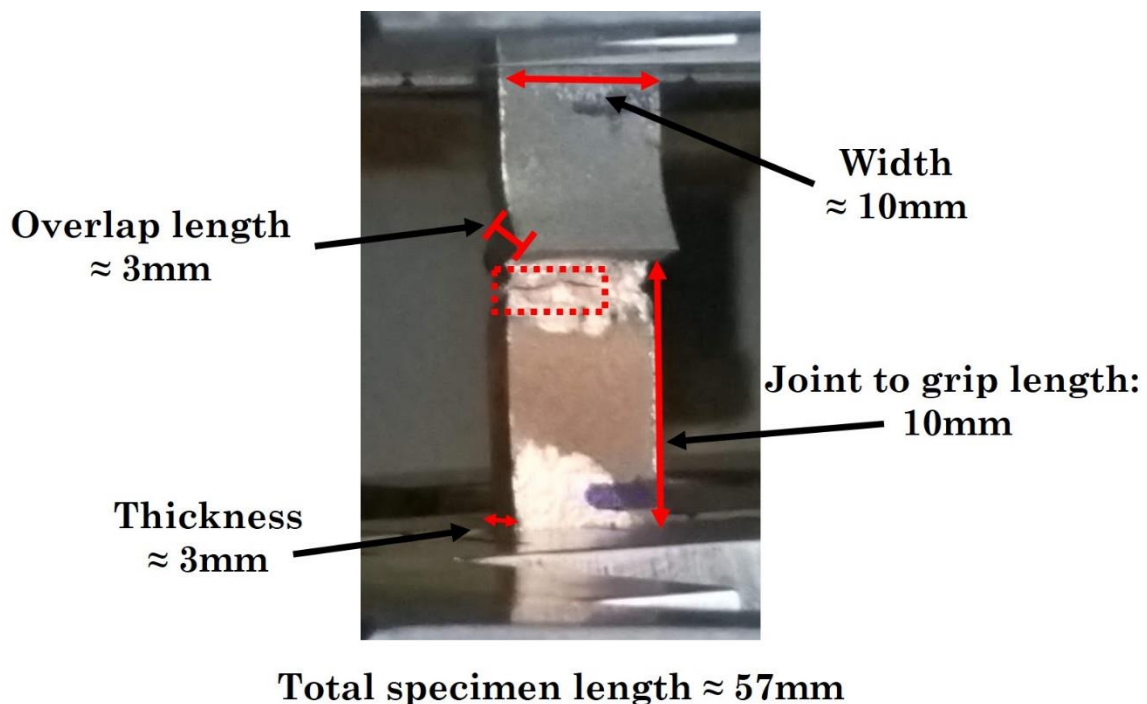


Figure 6.6: Photograph of a trial brazed joint between copper and nickel using filler Ag-155. The propagation of a failure in the copper parent material is highlighted in the red box. Dimensions of the specimen are indicated.

To alleviate this issue, it was decided that room temperature assessments of brazed joint strength would be conducted using nickel to nickel joints as nickel has a higher strength than copper and thus would be less likely to fail before the brazed joint did. In Ni-Ni joints with overlap lengths of 3mm (t) the samples failed in the brazed joint and not the parent materials. Whilst it is acknowledged that this form of test specimen is no longer directly comparable to the copper-nickel joints that will eventually be used in situ, it does allow direct comparison of joints formed with alloy D and Ag-155 thus providing a comparable measure of strength between the two brazing filler metals. 3 samples were manufactured for each of the two alloys assessed and compared. The “bond strength” – a term used here to describe the force required to break the brazed joint- (see below) withstood by each joint before failure under the test conditions described above can be found in Table 6.2.

Table 6.2: Room temperature bond strength of brazed joints between nickel parent materials using various filler metals.

Brazing filler metal	Bond Strength (MPa)				Standard error of the mean ($S_{\bar{x}}$)
	Sample 1	Sample 2	Sample 3	Average	
Alloy D	30.2	31.8	22.1	28.0	3.0
Ag-155	140.7	167.8	170.1	159.5	9.4

It should be noted that the absolute values for bond strength in Table 6.2 were obtained from samples which were not stressed parallel to the brazed joint; as such these samples were not tested purely in shear (Figure 6.7).

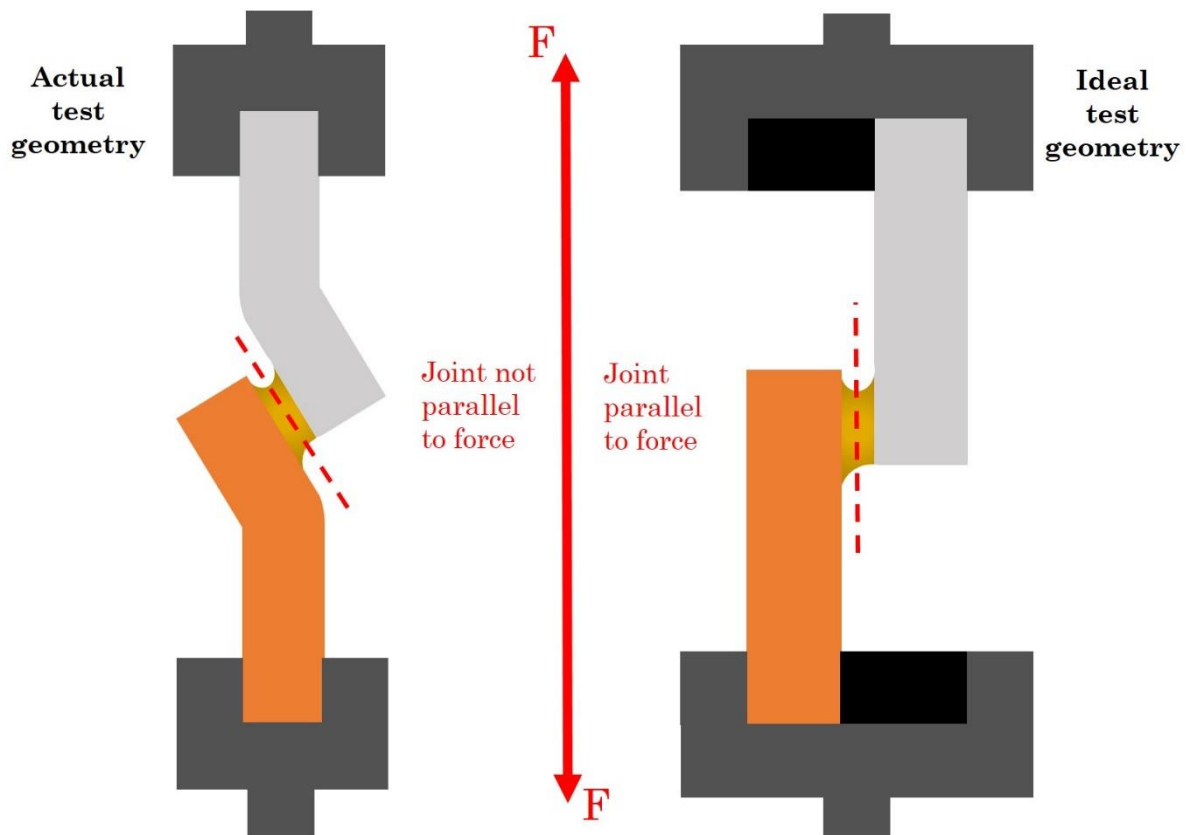


Figure 6.7: Diagram showing the test geometry used to assess brazed joint strength compared to the ideal test geometry.

The actual test geometry forces the samples to bend in the parent material and does not apply the force to the joint purely in shear. The actual test arrangement used does not contain the black spacer blocks used to align the brazed joint shown on the right of Figure 6.7 because in trial tests the brazed joint would slip against the spacer block and give inconsistent results. As such it was decided not to include the spacer blocks in order to make the testing more consistent, at the expense of producing true shear data. This means that the data gathered in this test is only comparative and should not be compared to externally collected standard shear test data. As such, the actual values obtained do not have rigorous meaning beyond the scope of these tests and as such the normalised data

presented below is only used to evaluate the performance of alloys developed in this study in comparison with Ag-155. No comparisons between these values and shear values found in literature can, or will, be made.

As can be seen from Table 6.2, the bond strength of a joint formed using the standard filler metal Ag-155 is considerably higher than one formed using the filler metal developed during this study. The graph in Figure 6.8 shows a normalised comparison between the two joints to indicate the relative performance of alloy D compared to the industrial filler Ag-155.

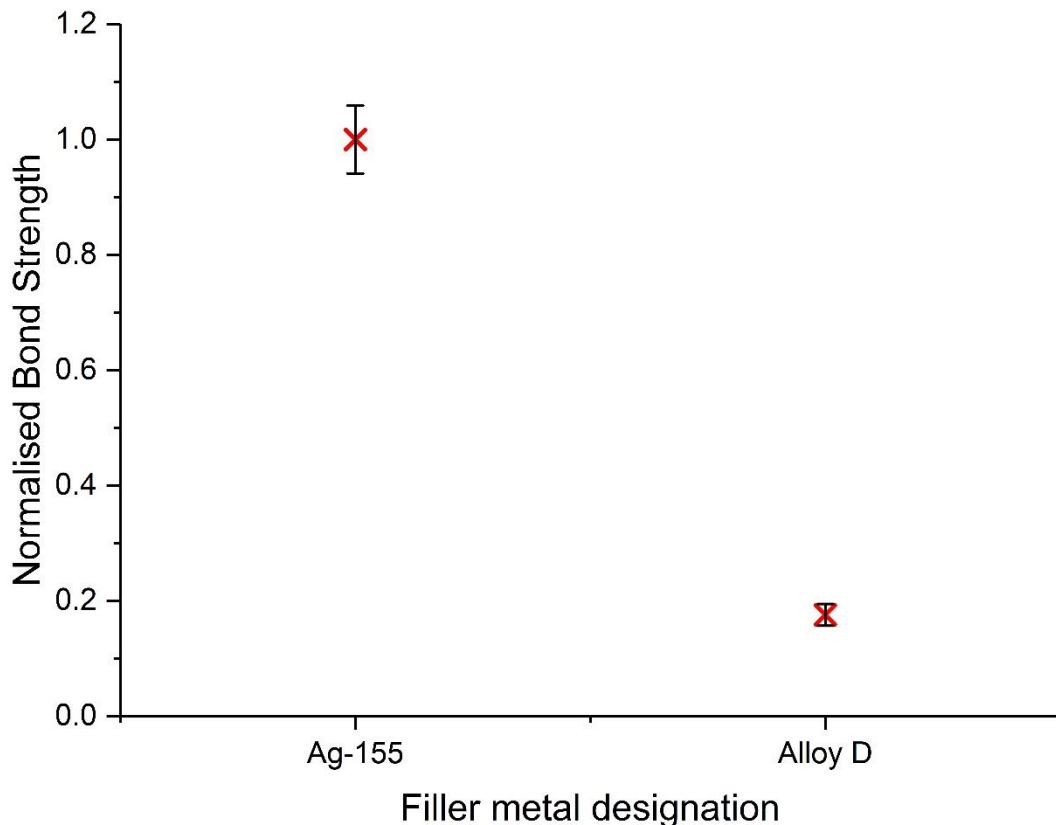


Figure 6.8: Graph depicting a normalised comparison of the bond strength between brazed joints formed with industrial filler metal Ag-155 and an alloy developed in this work (Alloy D).

Figure 6.8 clearly depicts that the bond strength of joints formed with the filler metal developed in this study is approximately 17.5% of that of the industrially used filler metal Ag-155. In the first instance this is clearly a reduction in performance on a mechanical level, however it must be noted that the end application for this filler metal does not have designated or stringent mechanical requirements. Instead, the ability of the filler to form an effective electrical interface without damaging the thermoelectric materials it joins is more important. Nevertheless, a minimum level of strength will be required, and an estimate of this for the brazed joints within the end application is conducted below to conclude whether this strength level is sufficient.

The minimum conceivable mechanical requirement for the brazed joints in the end application in a TEG is to support the weight of the TEG itself. Assuming the TEG in question is 40mm by 40mm and contains 31 thermocouples (typical dimensions of such components) there will be 62 thermoelectric legs within the TEG [19].

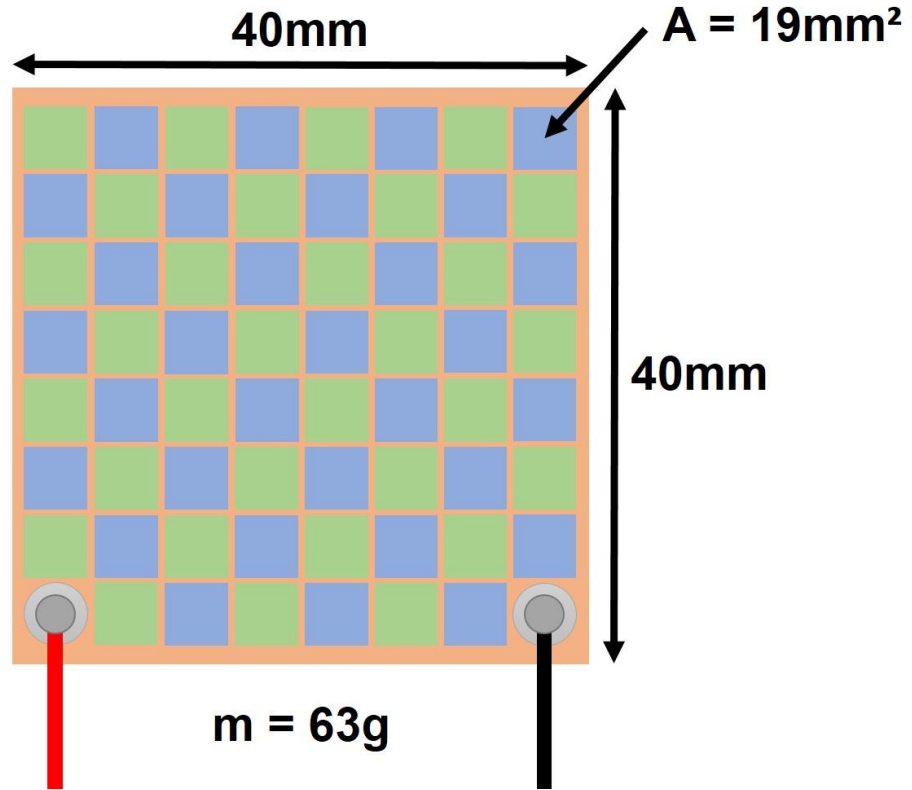


Figure 6.9: Dimensions and layout of an example 40mm thermoelectric module.

With each of these legs having an area of 19mm^2 [19] the total area on which the braze will be placed within the module is 1178mm^2 . With an estimated weight for the module of 0.063kg (63g) [19], the force acting on the brazed joints due to the weight of the TEG can then be calculated as:

$$w = mg = 0.063\text{kg} \times 9.81\text{ms}^{-2} = 0.618\text{N}$$

This allows calculation of the stress that the brazed joint area will be exposed to according to:

$$\sigma = \frac{F}{A} = \frac{0.618\text{N}}{0.001178\text{m}^2} = 524.6\text{Pa}$$

This rough estimate gives the minimum strength requirement for the braze to be 0.0005MPa ; substantially lower than the strength values produced by alloy D of $28.0 \pm 3.0\text{MPa}$ indicating that using alloy D as the braze within assembly of a similar thermoelectric module will provide sufficient strength to support the weight of the module. Additional evidence that average joint strength of alloy D will be sufficient for the application can be found in literature; Liu et al. described a bonding strength of $\sim 30\text{MPa}$ between nickel and a $\text{Bi}_{0.4}\text{Sb}_{1.6}\text{Te}_3$ N-type thermoelectric formed by hot pressing to be “very strong”, this value is very close to the $28.0 \pm 3.0\text{MPa}$ found for the joint strength of Alloy D joints to nickel in this study [20].

In conclusion, whilst the shear strength of the joints formed with the alloy developed in this work are approximately 17.5% of the strength of joints formed with a comparative industrial filler metal (Ag-155), they have sufficient strength to support the static weight of the device that they are used within and thus are suggested to be suitable for this application. Additionally, they possess similar bonding strengths to

those considered “very strong” for thermoelectric-nickel joints formed via hot pressing in a similar study [20]. However, it must be noted that the influence of vibration and the forces experienced due to sharp changes in momentum which the joints may be subject to, have not been assessed and may be substantially higher than the static loading forces assessed in these tests. As such it is recommended that further assessments of the resilience of these joints to vibration are made before they are recommended for use in components within a car exhaust.

6.3.2. Thermal Cycling

Thermal cycling of brazed joints was undertaken to assess the impact of repeated thermal exposure on the strength of joints formed with alloys created in this study. When placed in their end application inside an automotive exhaust, brazed joints between thermoelectric components will be exposed to (and expected to resist) many thousands of cycles of heating and cooling during the normal operation of the automobile they are installed on. These cycles will generate complex stresses, for example due to differences in thermal expansion coefficient between the different materials involved in the joint which could lead to damage or failure.

For several reasons it was decided to revert to using joints of copper joined to nickel in this experiment as opposed to the nickel to nickel joints used to assess the room temperature strength in the previous section:

- Thermal stresses are often invoked in brazed joints by differing thermal expansion coefficients between different parent materials. If Ni-Ni joints were used instead of Ni-Cu then there would be no difference between thermal expansion coefficients between the two parent materials and as such the joints will be subject to less stress during thermal cycling.
- When brazed joints are made, compounds are often formed between the filler metal and the parent materials during the brazing process. The compounds formed between filler and copper would not be present if Ni was used as both parent materials and as such the sample may not be an accurate representation of the system as a whole.

In order to design a suitable experiment to assess the impact of thermal cycling on the brazed joint, an idea of the temperatures that the brazed joint will be exposed to in service on an average journey will be required. Thermal data for the temperature profile within the exhaust system was obtained from the 2006 Diesel Engine-Efficiency and Emission Research (DEER) conference [21] in which the exhaust temperatures were recorded during an NEDC (New European Driving Cycle) assessment of a BMW 530i MY 2006 with an Inline 6-cylinder engine. This is of course just one example of a particular engine, but is here taken as a typical case. A graph depicting the recorded temperature over the test is shown in Figure 6.10. The test consists of 4 Urban Driving cycles (UDC or ECE-15), depicted between 0-780 seconds and one Extra Urban Driving Cycle (EUDC) depicted between 780 and 1180 seconds [22].

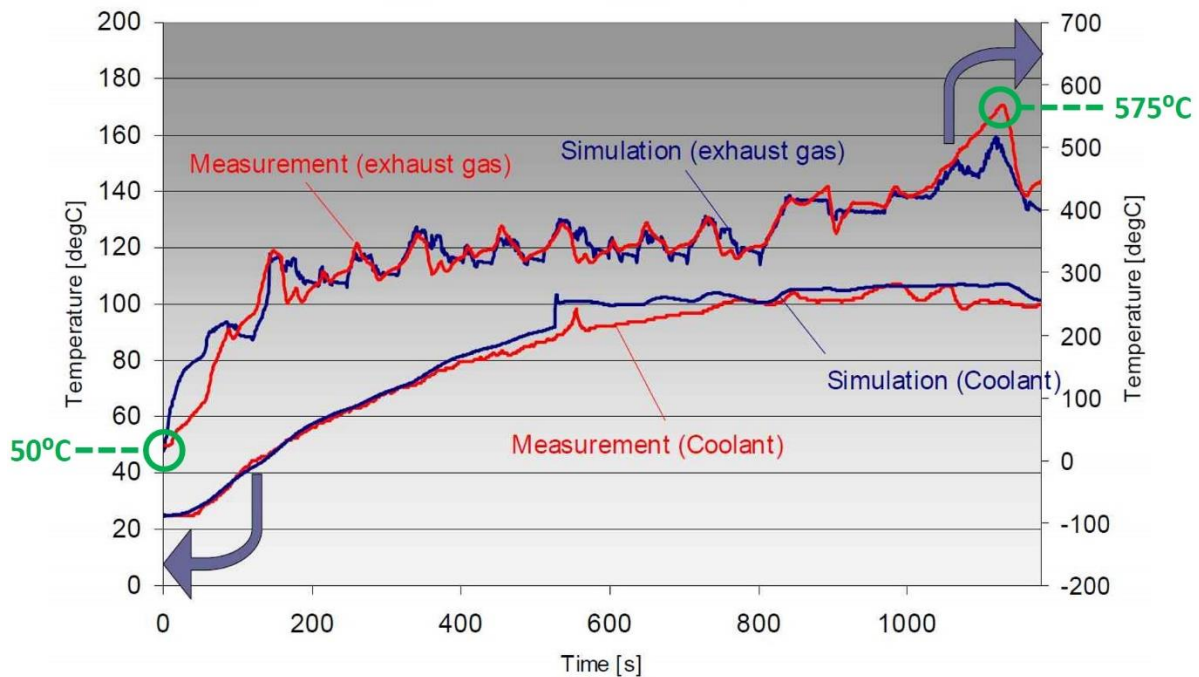


Figure 6.10: Exhaust gas temperature trace for a BMW 350i during the NEDC, presented at the Diesel Energy-Efficiency and Emission Research conference [21]. The peak temperature seen in the exhaust of 575°C is highlighted.

As can be seen from Figure 6.10, the maximum temperature reached is approximately 575°C. It is assumed that this is the maximum temperature that will be seen by any device placed within the exhaust of this vehicle and is further assumed to be a good representation of a vehicle in which a TEG system may be installed. Additionally, it should be noted that the 575°C maximum recorded temperature is believed to be a ‘worst case scenario’ for the temperatures the actual brazed joints will experience. The brazed joint will not be the most outward facing part of the TEG module and thus should be shielded to some degree from the most extreme temperatures felt in the exhaust system (Some experts also believe that use of a ceramic insulator for the TEG is likely in the final application which could limit the temperature the TEG is exposed to to around 450°C). As such, it is likely that thermal cycling up to 575°C will be a more severe test than the conditions a brazed joint employed in-situ on a TEG is likely to be subjected to. Tests proceeded with this temperature for two reasons, firstly as it is akin to allowing a margin of safety in testing and secondly, the higher temperature used may accelerate the failure of joints allowing comparison of developed filler metals and current filler metals with fewer cycles (and hence less experimental time) needed to differentiate the performance of the two different alloys.

The exhaust gas temperature fluctuations seen in the NEDC in Figure 6.10 are complex and difficult to replicate exactly without the use of an actual automobile engine to affix the TEG too. As such the decision was made to simulate the thermal exposure the brazed joint will face by inserting brazed joints into a furnace at a set temperature, until they reach the 575°C temperature peak and then removing them to cool in air until they reach 50°C (the lowest recorded temperature seen in the exhaust gas in the NEDC cycle in Figure 6.10); this raising and lowering of temperature was considered a single cycle. Samples would be subject to different numbers of cycles and then their bond strength assessed (as in Section 6.3.1) as a function of the number of cycles. A graph of the experimentally recorded temperature profile for a single cycle can be seen in Figure 6.11.

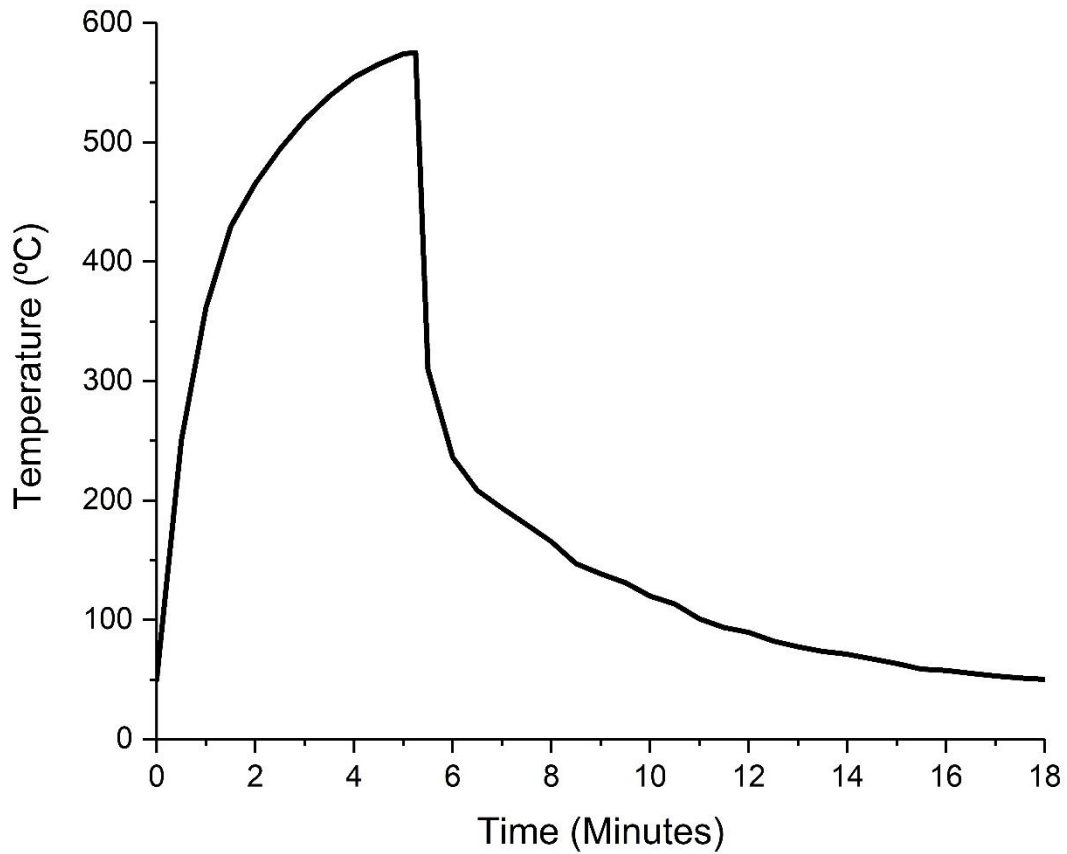


Figure 6.11: Temperature profile of a test sample during a single thermal cycle.

3 samples were produced for each cycle number tested for both of the two alloys assessed (an alloy developed in this study – Alloy D, and a standard filler conforming to Ag-155). The bond strength of the joint was recorded for each sample and averaged to give a value for the bond strength of joints formed with each alloy for various cycle numbers. The average bond strength withstood by each joint before failure is recorded in Table 6.3.

Table 6.3: Bond strengths of brazed joints between nickel and copper parent materials after various numbers of thermal cycles.

Number of cycles	Bond Strength (MPa)									
	Alloy D					Ag-155				
	Sample 1	Sample 2	Sample 3	Average	Standard error of the mean ($S_{\bar{x}}$)	Sample 1	Sample 2	Sample 3	Average	Standard error of the mean ($S_{\bar{x}}$)
0	20.5	6.0	19.6	15.4	4.7	138.8	118.1	139.0	132.0	6.9
10	28.1	8.6	25.4	20.7	6.1	131.9	151.0	137.0	140.0	5.7
20	/	5.8	/	5.8	/	157.7	133.4	16.8	102.6	43.5
30	6.6	/	14.7	10.7	4.1	150.0	112.1	107.2	123.1	13.5
50	/	/	/	/	/	120.7	121.9	148.7	130.4	9.1

Normalised data from Table 6.3 is plotted in Figure 6.12 as a function of the number of cycles the samples are subjected to. As the absolute values determined in this experiment are not true shear strengths, normalised data has again been used with all values normalised to the average value of the 3 repeats used for Ag-155 joints subjected to 0 cycles.

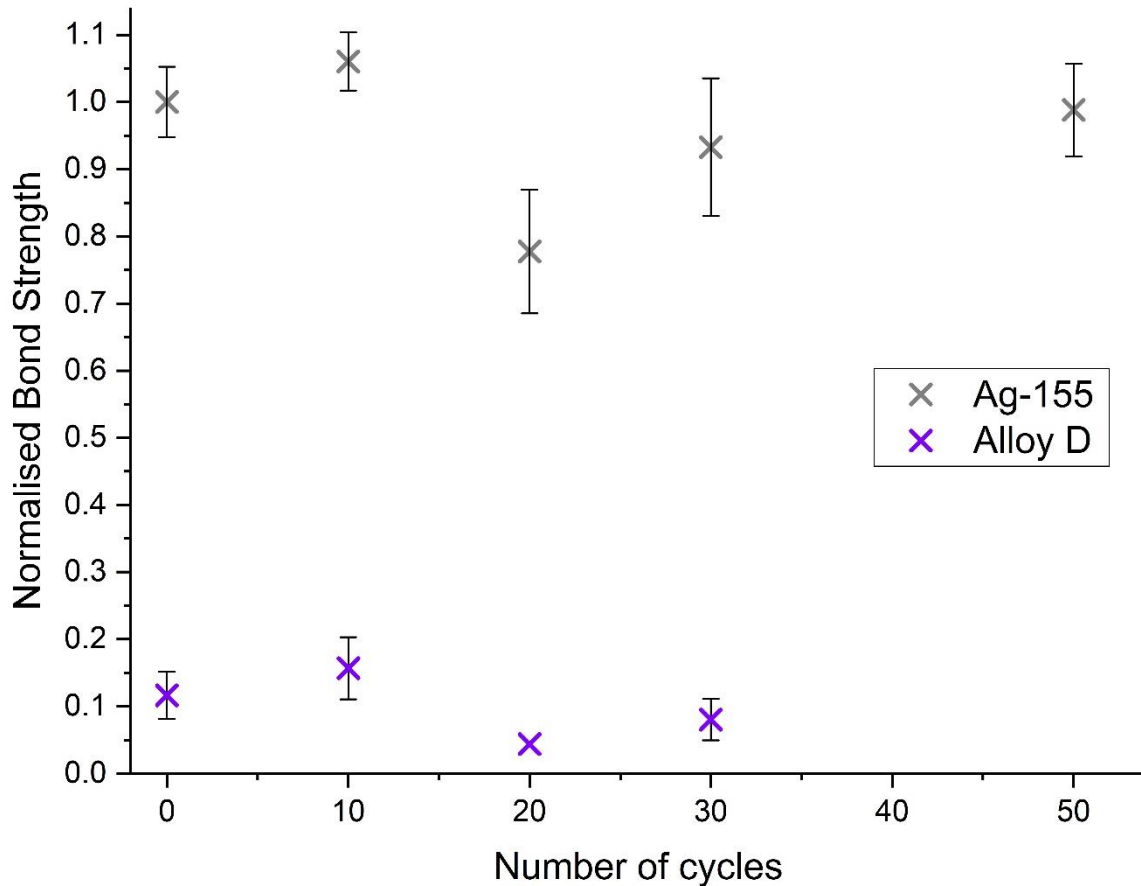


Figure 6.12: Normalised shear strength data for brazed joints formed using alloy D and Ag-155 assessed after differing numbers of thermal cycles.

As can be clearly seen in Figure 6.12, the normalised shear strength for joints formed with alloy D is lower at all cycle numbers tested than for joints formed with Ag-155, and across all cycle numbers tested is less than 20% of the strength of Ag-155 joints (consistent with the earlier results). It can be concluded that no increase or decrease in shear strength can be conclusively seen across 50 cycles for either Ag-155 or alloy D joints as the error bars for the values in each series for various cycle numbers overlap significantly.

Although collected data show no conclusive decrease in strength across cycle numbers, it must be noted that not all samples survived thermal cycling to then be tested for their strength and as such this apparent absence of a trend may be misleading. Every Ag-155 sample survived all the cycles it was subjected to, whereas 6 of the 15 samples joined with alloy D broke either during the heating and cooling cycles or during placement into the grips of the testing machine. Of the 12 alloy D samples subjected to thermal cycling, 6 broke. One broke after four cycles, one after 17 cycles, one broke as it was placed into the tensile testing machine (after surviving 20 cycles), one after 25 cycles, one after 28 cycles and one after 48 cycles. A % failure chart for alloy D can be seen in Figure 6.13.

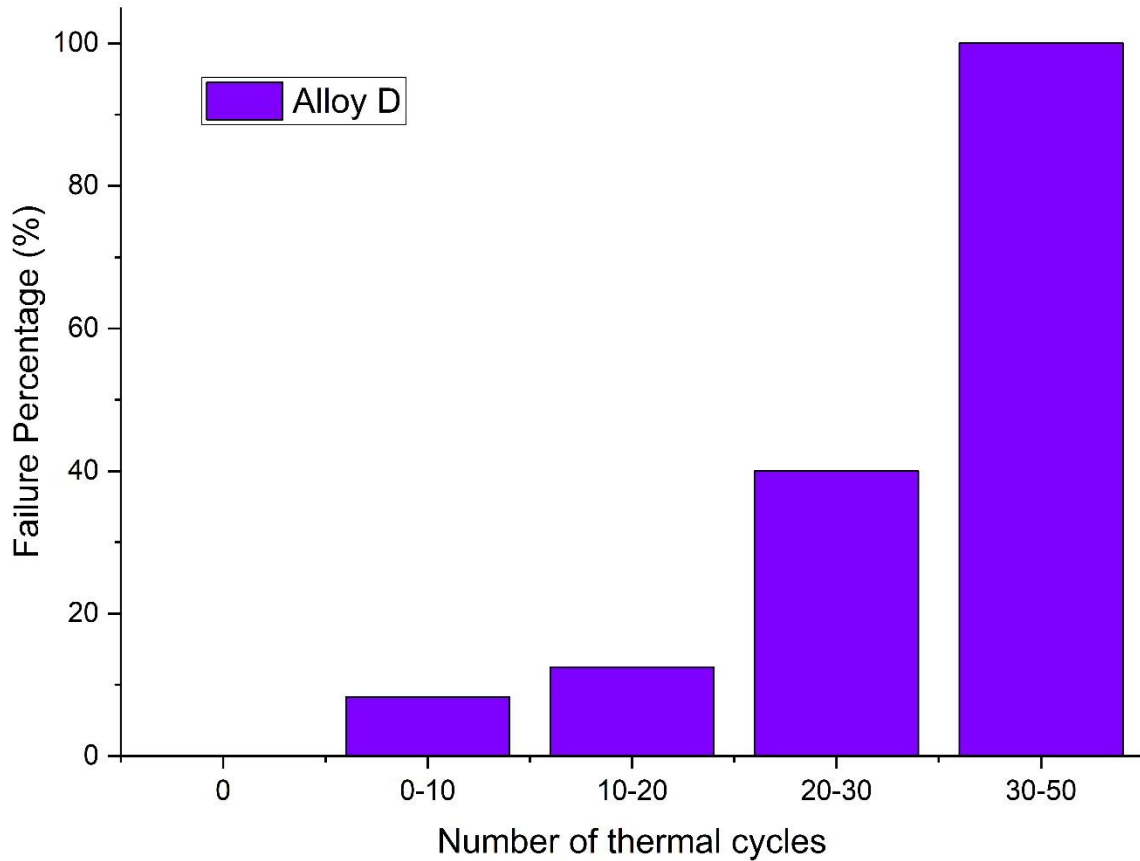


Figure 6.13: Failure percentage of brazed samples formed using alloy D for different numbers of thermal cycles.

As such it can be seen that although the apparent shear strength of alloy D samples which survived thermal cycling did not conclusively decrease across the cycle numbers assessed, the number of samples which survived to be tested reduced as the number of cycles increased. To reliably conclude on the actual failure percentages associated with different numbers of cycles, more data would need to be collected. However, what is important to draw from Figure 6.13 is the general trend of the failures, which increase with each band of cycles. This shows that the damage from thermal cycling builds up over a number of cycles as a cumulative effect which eventually manifests as a sample failure.

In conclusion, brazed joints formed with alloy D developed in this study exhibit about 17.5% of the bond strength of joints formed with Ag-155 without being subject to thermal cycling. Subjecting both types of joint to 50 cycles of being raised to 575°C and cooled to 50°C in air does not cause significant reduction in measured bond strength in samples which survive the thermal cycling process. However, an increasing number of samples formed with alloy D do not survive the thermal cycling process and break before their strength can be assessed over 50 cycles. All brazed joints tested formed with Ag-155 survived 50 thermal cycles indicating a superior resistance to thermal cycling above that of alloy D.

6.4. Electrical Contact Resistance

The final assessment of brazing alloy performance made here is the electrical contact resistance of the interface formed between the filler metal and the skutterudite thermoelectrics used in this study. As the principal function of the filler metal is to provide a good electrical interface between the thermoelectric material and the rest of the circuit without adversely affecting the composition of the thermoelectric this is probably the most critical assessment of performance for the newly developed filler metals.

For this investigation, brazed joints were formed between two pieces of n-type skutterudite thermoelectric material (composition: $\text{CoSb}_{2.75}\text{Sn}_{0.05}\text{Te}_{0.20}$). The resistance was measured across all interfaces in the samples by scanning a probe across the surface. A circuit diagram for the arrangement can be seen in Figure 6.14.

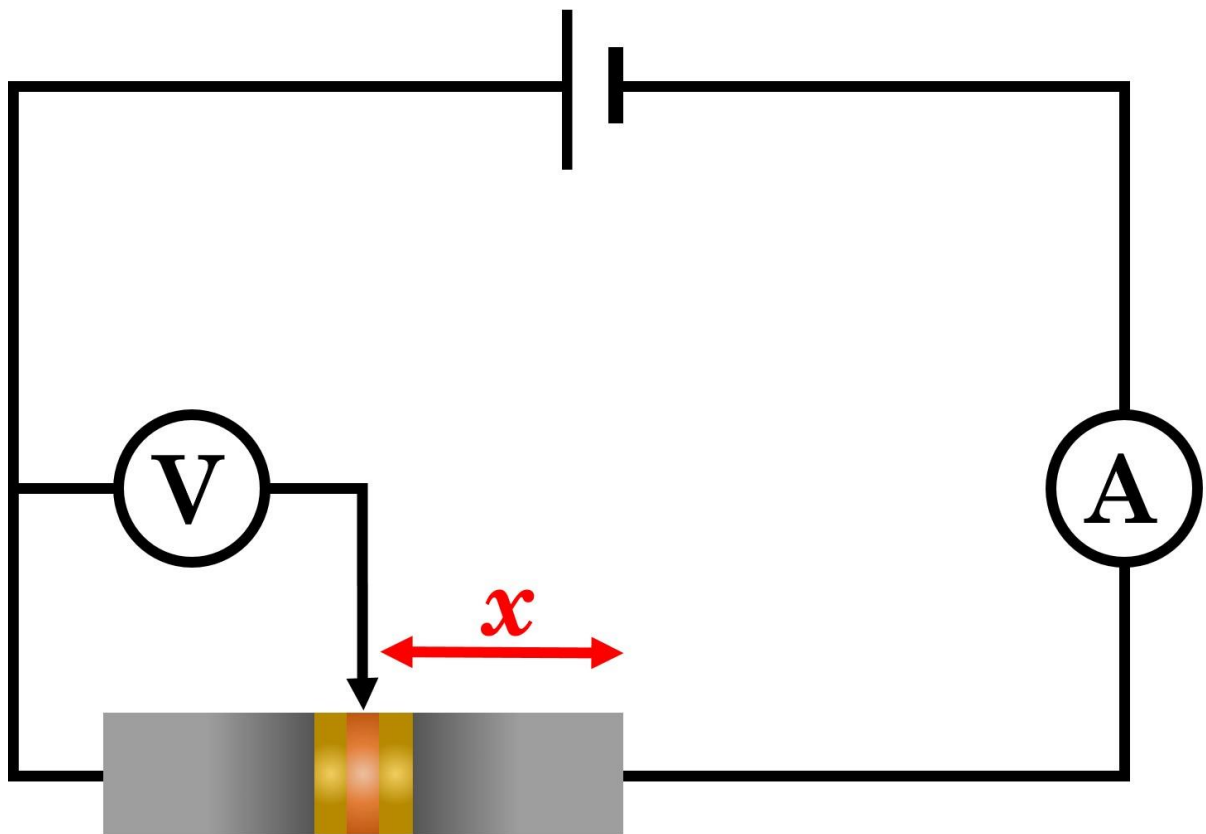


Figure 6.14: Circuit diagram for the circuit used to measure resistance as a function of position along the brazed thermoelectric sample.

In this setup 2 probes are attached to either end of the sample whilst a third probe (connected to a voltmeter) is positioned perpendicular to the interfaces being measured and moved across them, along the sample. Voltage is recorded at regular position intervals across the sample surface (in this instance, $40\mu\text{m}$). The voltage values are converted to a resistance measurement by using the ammeter in the circuit to calculate resistance. This allows the correlation of resistance to lateral position (x) along the length of the sample being analysed. The variation in resistance recorded as different interfaces within the sample are crossed then indicates which interfaces will impede electrical flow and to what extent.

The first sample analysed (Sample 1) had the geometry shown in Figure 6.15. This sample consists of a piece of n-type skutterudite approximating $2.5\text{mm} \times 2.5\text{mm} \times 3\text{mm}$ joined

using a thin layer of braze material to a thin copper interlayer ($0.3\mu\text{m}$ thick) which in turn is joined to another $2.5\text{mm} \times 2.5\text{mm} \times 3\text{mm}$ n-type skutterudite, again with the same thin layer of braze material to form a symmetrical sample.

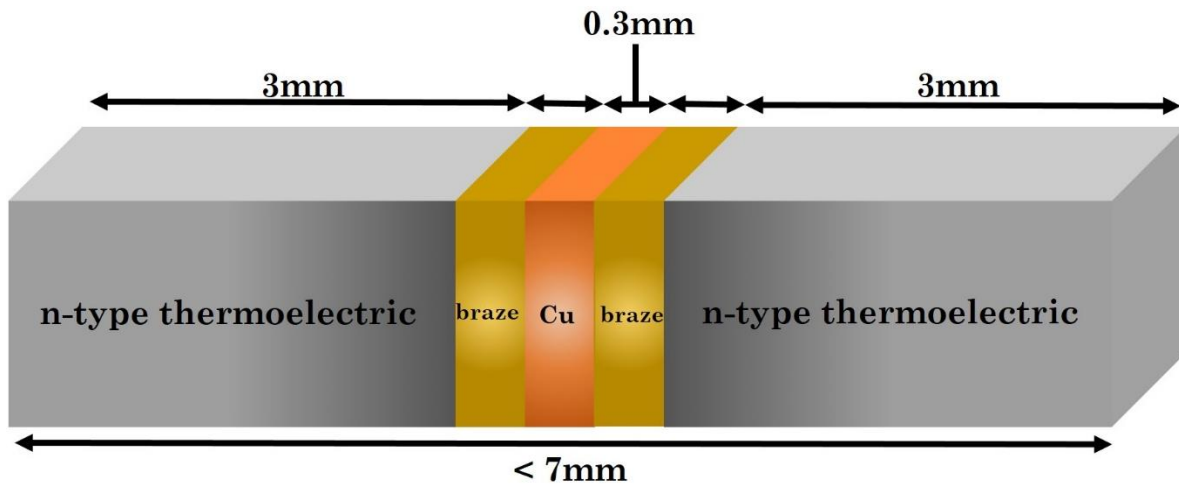


Figure 6.15: Diagram of the first thermoelectric sample used to assess the contact resistance across layers in the brazed joint.

The advantage of testing this 5-layer sample is that information on the contact resistance of the braze/copper interface can be obtained as well as information on the resistance increases at the braze/skutterudite interface. A plot of resistance against position along the sample can be seen in Figure 6.16. The large discontinuity in resistance seen either side of the braze and interlayer region correspond to the interface between the thermoelectric and the braze. By measuring the size of these resistance discontinuities, a value for the contact resistance of the interface in each case can be found. It should be noted that the actual values of resistance shown on the axis are of little importance and will vary with the circuit used; it is the magnitude of the change in resistance across the interface which is of interest.

In Figure 6.16 the two resistance discontinuities are defined as $0.92\text{m}\Omega$ and $1.07\text{m}\Omega$. The points these discontinuities are defined between are decided using lines of best fit for the regions of the graph corresponding to the first bulk thermoelectric region, the bulk braze/interlayer region and the second bulk thermoelectric region. For the first interface (corresponding to a gap of $0.92\text{m}\Omega$ on the lower left portion of the graph in Figure 6.16), A line of best fit was drawn encompassing the points of the lower bulk thermoelectric region (marked in purple in Figure 6.16) up until the single biggest gap between two points and the R^2 value for the linear fit recorded. One point was then excluded from the linear fit and the R^2 value for the new linear fit recorded. This process was repeated until the linear fit was not improved by removing a point (checked to 3 decimal places). At this point all points used to contribute to the line of best fit were acknowledged as being from the bulk thermoelectric and not the interface. A similar process was used to identify the braze and interlayer region. The points between these two separate series of points defining the central braze/interlayer region and the bulk thermoelectric region were defined as the interface region. The size of the resistance discontinuity ($0.92\text{m}\Omega$ in this instance) was found by subtracting the recorded resistance value for the last point in the bulk thermoelectric region (the final purple point in Figure 6.16 and the first point in the braze/interlayer region (the first red point in Figure 6.16). This process was repeated for the second interface (between the braze/interlayer region (red points) and the second bulk thermoelectric region (green points)). The two resistance discontinuity values were then

divided by the area of the sample (recorded in Table 6.4) to give the contact resistance of both interfaces. As both interfaces within each sample were assumed to be identical (due to the samples being symmetrical in all cases) the two values were averaged to give a final contact resistance for each sample tested.

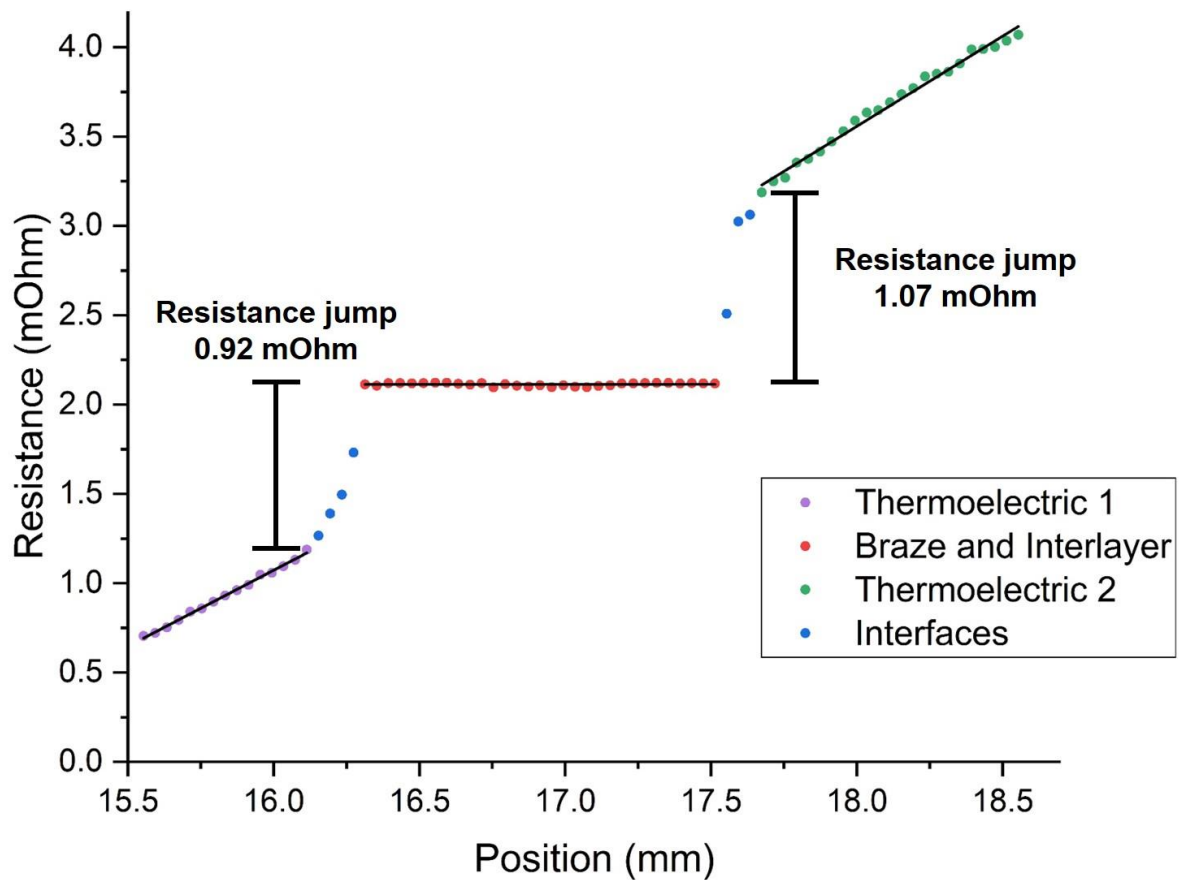


Figure 6.16: Graph of resistance against position for a thermoelectric sample with a copper interlayer brazed using alloy D developed in this study.

Several conclusions can be drawn from the above graph depicting the resistance change of sample 1 with position including:

- The central region of the graph (corresponding to the braze layer and the copper interlayer regions of the sample) is flat, with no measureable resistance discontinuities along its length. This demonstrates that the electrical conductivity of the braze material itself is good and that the electrical interface between braze and copper has a negligible resistance change.
- Resistance discontinuities can be seen at the interface between filler metal and the thermoelectric. This interface is often the limiting interface in TEGs and as such it is the magnitude of the resistance discontinuities at this interface which are of concern (not the fact that such discontinuities are present). The size of the two resistance discontinuities (one at each interface) are calculated as $1.04 \times 10^{-4} \Omega \text{ cm}^2$ and $1.20 \times 10^{-4} \Omega \text{ cm}^2$ respectively, giving an average resistance discontinuity of $1.12 \times 10^{-4} \Omega \text{ cm}^2$. The target contact resistance for this type of interface is of course as low as possible but acceptable contact resistances for similar interfaces (between copper and a CoSb_3 Half-Heusler material [23]) have

been quoted as around $5 \times 10^{-5} \Omega \text{ cm}^2$ meaning that the interface formed using the alloy developed in this study is around a factor of 2 greater than the target contact resistance.

It must be noted that the thermoelectric layers present in the above sample are not coated with nickel (as they are intended to be in the final application). In order to assess the influence that nickel coating may have on the conductivity of the interface, and to compare the performance of the alloy developed in this study to the currently used filler metal (Ag-155); 3 further samples were manufactured and tested using the same procedure as the first. The samples are as follows:

- Sample 2: A repeat of the first sample without the copper interlayer e.g. a $2.5\text{mm} \times 2.5\text{mm} \times 3\text{mm}$ piece of n-type skutterudite joined with a thin braze layer (approximately 0.3mm) made of the same alloy developed in this study (alloy D), joined to another $2.5\text{mm} \times 2.5\text{mm} \times 3\text{mm}$ piece of n-type skutterudite. The initial test (above) had shown that the copper-braze interface was electrically sound (no detectable resistance discontinuity between copper and braze) and as such subsequent samples do not require a copper interlayer. As manufacturing samples with an interlayer adds complexity to the manufacturing process it was decided that this interlayer was not necessary in these subsequent samples. The purpose of this sample was to provide a direct comparison to later samples which also would not contain an interlayer.
- Sample 3: A sample in the same configuration as in sample 2 but with the thermoelectric coated with a $0.7\mu\text{m}$ layer of Ni deposited by thermal deposition (see Section 3.9.1). The purpose of assessing this sample was to assess the impact the nickel layer had on the interface contact resistance.
- Sample 4: A sample in the same configuration as in sample 2 but with the filler metal used being Ag-155 instead of the alloy developed in this study for comparative purposes. The purpose of this sample was to compare the difference in electrical contact resistance between a sample formed with the filler metal in this study and one formed with Ag-155.

A diagram illustrating these 3 samples compared to the first sample tested can be seen in Figure 6.17.

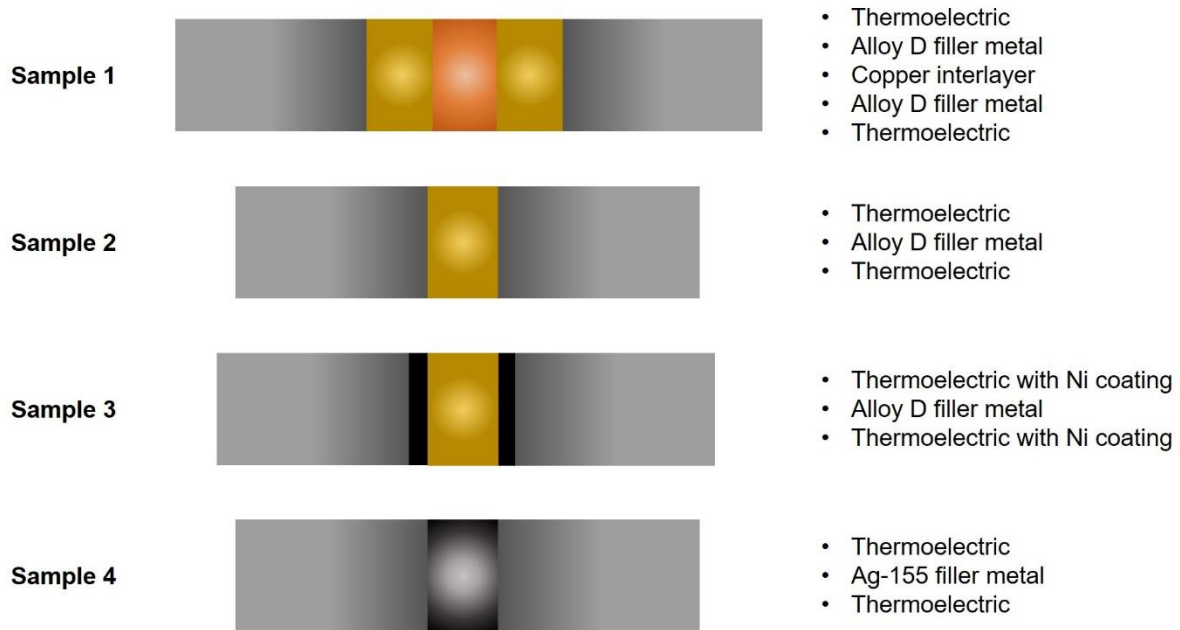


Figure 6.17: Diagrams of the 4 samples used to assess interface contact resistances.

The electrical contact resistance for both interfaces in each of the 4 samples tested were assessed identically to the first sample. The contact resistances are recorded in Table 6.4.

Table 6.4: Electrical contact resistances for interfaces between brazing filler metals and skutterudite thermoelectrics.

Sample	Surface area of interface (cm ²)	Resistance discontinuity (mΩ)		Electrical contact resistance (× 10 ⁻⁵ Ωcm ⁻²)		
		Interface 1	Interface 2	Interface 1	Interface 2	Average
1	0.112	0.92	1.07	10.4	12.0	11.2
2	0.084	0.26	0.22	2.16	1.88	2.02
3	0.081	0.45	0.47	3.64	3.81	3.72
4	0.087	0.56	0.43	4.88	3.73	4.31

Sample 1 (containing the copper interlayer) had substantially higher interface contact resistance than the subsequent 3 samples tested (by approximately a factor of 3-4). The sample manufactured to be similar to this sample but without the copper interlayer (sample 2) showed an average contact resistance of $2.02 \times 10^{-5} \Omega \text{cm}^{-2}$ compared to the $11.2 \times 10^{-5} \Omega \text{cm}^{-2}$ shown by sample 1. This result was unexpected as it was anticipated that the presence of the copper interlayer should not have an impact on the interfaces between braze and thermoelectric. It is possible that the increased difficulty in sample manufacture which arises from the inclusion of the copper interlayer (e.g. a 5-layer sample containing 2 brazed joints must be formed when a copper interlayer is included as opposed to a 3-layer sample with a single brazed joint when no copper interlayer is needed) led to

the formation of a poorer joint due to the difficulty in maintain a strong contact whilst simultaneously brazing 2 brazed joints.

Sample 3 was designed to assess the impact of Ni coating on the thermoelectric when compared with sample 2. In the manufactured thermoelectric devices, the Ni coating serves two functions. Its primary function is to act as a diffusion barrier; to prevent elements from the brazing filler metal from diffusing into the thermoelectric and impeding its thermoelectric performance, and its secondary function is to improve the ease at which the filler metal wets the surface of the thermoelectric. The Ni coated sample (sample 3) gives slightly higher contact resistances than the identical sample without the Ni coating (sample 2) with the Ni coated sample having an average contact resistance of $3.72 \times 10^{-5} \Omega \text{cm}^{-2}$ compared to the $2.02 \times 10^{-5} \Omega \text{cm}^{-2}$ on the non-coated sample. The increase in contact resistance in the Ni coated sample is likely due to the Ni coating preventing diffusion of the braze into the thermoelectric as intended. Evidence of this exists in the shape of the two graphs (Figure 6.18) with the Ni coated sample (Figure 6.18 - right) having a much sharper transition at the interface region than the graph for the uncoated sample (Figure 6.18 - Left) likely due to reduced inter-diffusion in the Ni coated sample making the interface sharper and thus the resistance discontinuity more prominent.

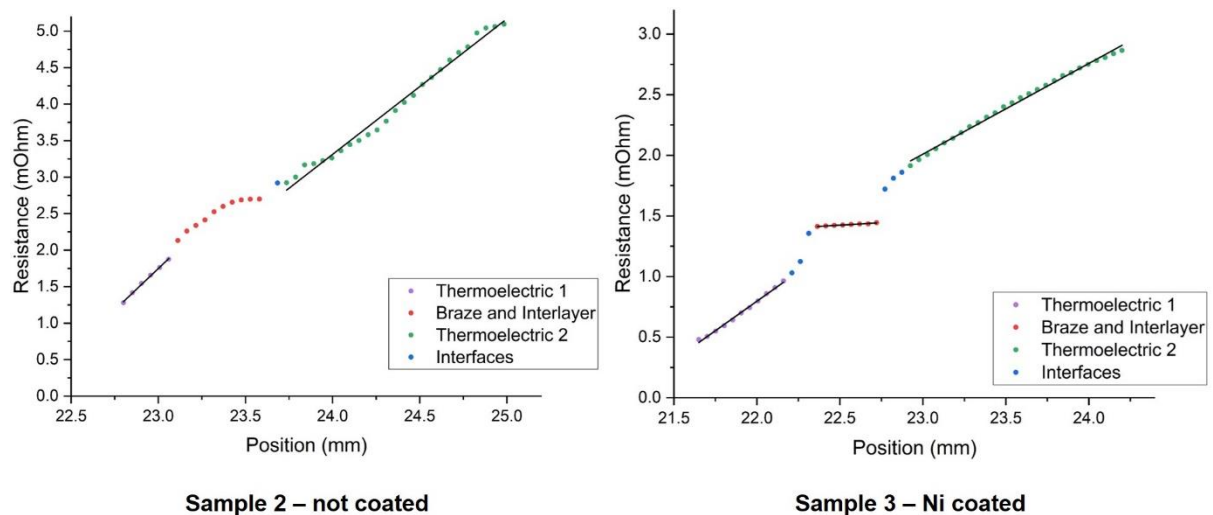


Figure 6.18: Comparison of the resistance profiles of samples 2 and 3 which show clear differences due to the presence of an Ni coating on the thermoelectric in sample 3.

To provide further evidence as to whether this is the cause of the disparity between the contact resistances in these two samples the interface could be examined with EDX and the diffusion distance of elements in the filler metal into the thermoelectric could be measured. If the diffusion distance of the elements into the non-coated sample is significantly higher than that in the coated sample, it would add further weight to this theory and provide more evidence that the Ni coating is performing its intended primary function.

Finally, sample 4 was used to compare the contact resistance of a thermoelectric sample brazed using the currently available filler metal Ag-155 to a thermoelectric sample brazed with an alloy developed in this study (alloy D – sample 2). With a final average contact resistance of $4.31 \times 10^{-5} \Omega \text{cm}^{-2}$, sample 4 (brazed with Ag-155), had an average contact resistance over double that of the identical sample brazed with alloy D ($2.02 \times 10^{-5} \Omega \text{cm}^{-2}$). This is good evidence for the potential benefit of using alloys developed in this work ahead of those currently available. To further substantiate this it is recommended that a

further sample is manufactured and tested using Ag-155 as the filler metal but with Ni coated thermoelectric components. This sample could then be directly compared with sample 3 to assess the impact of replacing the filler metal on Ni coated samples.

6.5. Summary

In conclusion, this chapter has assessed the suitability of filler metals developed in this work to perform as brazing filler metals in thermoelectric components, with a particular focus on comparative performance relative to the filler metal currently used in these thermoelectric devices which conforms to ISO17672:2016: Ag-155 [24].

Filler metals developed in this study all appear to be better able to wet ‘as-received’ copper substrates than Ag-155 according to data collected in this work. All 4 developed alloys tested exhibited a lower average final wetting angle on copper substrates (Alloy D: $47.0\pm 1.8^\circ$, Alloy DAuX: $58.9\pm 0.8^\circ$, Alloy E: $9.0\pm 0.2^\circ$ and Alloy EAuX: $71.5\pm 0.7^\circ$) than Ag-155 ($120.5\pm 2.3^\circ$), however this is likely due to the alloys in this study being better able to cope with the oxide layer which forms on copper substrates when they are left untreated in air. Filler metal Ag-155 is usually used with a flux to remove surface oxides; this was not possible to do in this study due to restrictions with the furnace used which may explain its higher than expected wetting angle.

Strength assessments of brazed joints formed between nickel plates were undertaken to comparatively assess the mechanical performance of an alloy developed in this study (Alloy D) with Ag-155. Brazed joints were deliberately formed with lower than recommended overlap distances (overlap less than 3 times the thinnest joint member) to ensure failure in the filler metal and were tested in shear. The shear strength values normalised for alloy D against Ag-155 indicate that alloy D possesses approximately 17.5% of the strength of the strength in shear than Ag-155 does. A calculated estimate using available data for the minimum strength required for joints within a TEG indicate minimum shear strength of 0.0005MPa would be required for the brazing filler metal. With the strength values measured in this study for alloy D of 28.0 ± 3.0 MPa, it is concluded that alloy D possesses sufficient strength for its intended function given the available data.

Assessment of the resistance of joints formed using alloy D to thermal cycling was also assessed; again in comparison to joints formed using Ag-155. Brazed joints formed with both alloys were raised to 575°C and cooled to 50°C in air up to 50 times; samples formed with either alloy showed no significant reduction in shear strength across this many cycles in samples which survived the thermal cycling process. All Ag-155 samples tested survived all 50 cycles however increasing numbers of joints formed using alloy D failed as the number of cycles increased indicating that brazed joints formed with Ag-155 have a superior resistance to thermal cycling than those formed with the alloy developed in this study.

Finally, the electrical performance of brazed joints formed with alloy D were compared to those formed with Ag-155 by examining the contact resistances of the braze-thermoelectric interfaces between each filler and an N-type skutterudite thermoelectric. The contact resistance of interfaces with either alloy were found to be lower than the target resistance of $5.0\times 10^{-5}\Omega\text{cm}^{-2}$ with joints formed with alloy D found to have a contact resistance approximately half that of joints formed with Ag-155.

6.6. References

- [1] American Welding Society. *Brazing Handbook*. 4th ed. Miami, Florida: American welding Society; 1991.
- [2] Gremillard L, Rauch N, Saiz E. Drop_angle [Internet]. Berkeley: Lawrence Berkeley National Laboratory; 2002. Available from: [http://lgremillard.free.fr/LgremillardMain En.html](http://lgremillard.free.fr/LgremillardMainEn.html).
- [3] Tasker AM. Gold-containing brazing filler metals. *Gold Bull*. 1983;16:111–113.
- [4] Johnson Matthey. Silver-flo™ Filler Metals [Internet]. [cited 2017 Nov 28]. Available from: <http://www.jm-metaljoining.com/products/silver-flo>.
- [5] Way M, Willingham J, Goodall R. Brazing filler metals. *Int. Mater. Rev.* [Internet]. 2019;0:1–29. Available from: <https://doi.org/10.1080/09506608.2019.1613311>.
- [6] Bobzin K, Öte M, Wiesner S. Investigation of the effect of contaminations and cleaning processes on the surface properties of brazing surfaces. *IOP Conf. Ser. Mater. Sci. Eng.* [Internet]. 2017;181:012027. Available from: <http://stacks.iop.org/1757-899X/181/i=1/a=012027?key=crossref.05d4535700ba1c8abb1c215e3e146ce9>.
- [7] Vianco PT, Walker CA, Smet D De, et al. Understanding the Run-out Behavior of a Ag-Cu-Zr Braze Alloy When Used to Join Alumina to an Fe-Ni-Co Alloy. *Weld. J*. 2016;95:36–42.
- [8] Lugscheider E, Tillmann W. Development of New Active Filler Metals in a Ag-Cu-Hf System. 1990;69:416–421.
- [9] Liu YZ, Zhang LX, Liu CB, et al. Brazing C/SiC composites and Nb with TiNiNb active filler metal. *Sci. Technol. Weld. Join.* [Internet]. 2011;16:193–198. Available from: <http://www.maneyonline.com/doi/abs/10.1179/1362171810Y.0000000021>.
- [10] Chen J, Mu D, Liao X, et al. Interfacial microstructure and mechanical properties of synthetic diamond brazed by Ni-Cr-P filler alloy. *Int. J. Refract. Met. Hard Mater.* [Internet]. 2018;74:52–60. Available from: <https://doi.org/10.1016/j.ijrmhm.2018.03.005>.
- [11] Zhang J, Wang T, Liu C, et al. Effect of brazing temperature on microstructure and mechanical properties of graphite/copper joints. *Mater. Sci. Eng. A* [Internet]. 2014;594:26–31. Available from: <http://dx.doi.org/10.1016/j.msea.2013.11.059>.
- [12] Garnaud G. The formation of a double oxide layer on pure copper. *Oxid. Met.* [Internet]. 1977;11:127–132. Available from: <http://link.springer.com/10.1007/BF00606399>.
- [13] DoITPoMS - The interactive Ellingham diagram [Internet]. Univ. Cambridge. 2019 [cited 2019 Nov 7]. Available from: https://www.doitpoms.ac.uk/tlplib/ellingham_diagrams/interactive.php.
- [14] Oar-Arteta L, Wezendonk T, Sun X, et al. Metal organic frameworks as precursors for the manufacture of advanced catalytic materials. *Mater. Chem. Front.* [Internet]. 2017;1:1709–1745. Available from: <http://dx.doi.org/10.1039/c7qm00007c>.
- [15] Burton RA, Burton G. Control of Surface Attack By Gallium Alloys in Electrical Contacts [Internet]. Raleigh N.C.; 1986. Available from:

- <https://apps.dtic.mil/dtic/tr/fulltext/u2/a168168.pdf>.
- [16] Glasser J, Few W. E. Study of Low Melt Brazing Alloys [Internet]. Ohio; 1964. Available from: <https://pdfs.semanticscholar.org/09c8/365c20c4a6fa2df9dd1a584a1ec3134002cf.pdf>.
 - [17] CEN/TC 121. Brazing - Destructive tests of brazed joints (BS EN 12797:2000). Brussels: British Standards Institution; 2000.
 - [18] United States of America - Department of Defense. DEPARTMENT OF DEFENSE TEST METHOD STANDARD (MIL-STD-810G) Method 514.7 - Vibration.
 - [19] Al-Habahbeh OM, Mohammad A, Al-khalidi A, et al. Design optimization of a large-scale thermoelectric generator. *J. King Saud Univ. - Eng. Sci.* [Internet]. 2018;30:177–182. Available from: <https://doi.org/10.1016/j.jksues.2016.01.007>.
 - [20] Liu W, Wang H, Wang L, et al. Understanding of the contact of nanostructured thermoelectric n-type Bi₂Te_{2.7}Se_{0.3} legs for power generation applications. *J. Mater. Chem. A.* 2013;1:13093–13100.
 - [21] LaGrandeur J, Crane D, Hung S, et al. Automotive waste heat conversion to electric power using skutterudite, TAGS, PbTe and BiTe. *Int. Conf. Thermoelectr. ICT, Proc.* 2006;343–348.
 - [22] UNECE Regulation No. 83 – Revision 5. Uniform provisions concerning the approval of vehicles with regard to the emission of pollutants according to engine fuel requirements [Internet]. Geneva; 2015. Available from: <http://www.unece.org/fileadmin/DAM/trans/main/wp29/wp29regs/R083r5e.pdf>.
 - [23] Ngan PH, Van Nong N, Hung LT, et al. On the Challenges of Reducing Contact Resistances in Thermoelectric Generators Based on Half-Heusler Alloys. *J. Electron. Mater.* 2016;45:594–601.
 - [24] ISO/TC 44. Brazing — Filler metals (ISO 17672:2016) [Internet]. 3rd ed. British Standards Institution; 2016. Available from: <https://www.iso.org/obp/ui/#iso:std:iso:3677:ed-3:v1:en>.

Chapter 7: Conclusion

7.1. Summary

This thesis has successfully developed innovative new brazing filler metals for joining nickel coated thermoelectric materials to copper conductive plates with the intended application of being used within heat recovery devices mounted in automotive exhaust systems. Theoretical filler metal compositions have been evaluated with a python modelling script to filter potential compositions using empirical parameters to select those most likely to form solid solutions. Compositions deemed most likely to form solid solutions have then been manufactured and trialled as brazing filler metals. The performance of these different compositions has been assessed and the most promising candidates assessed for their phase composition, melting ranges and diffusion properties in nickel. Further testing was conducted to provide comparative performance data between a common industrial filler metal (conforming to ISO 17672: Ag-155) and the filler metals developed in this study in an array of experiments designed to assess various properties of the filler metals which are required in the end application. The sessile drop technique was used to evaluate the ability of developed fillers to wet copper substrates; tensile testing of lap-joint samples was undertaken to assess joint strength and thermal cycling was performed on brazed samples to assess the resistance of joints formed with developed materials to repeated thermal loading. Finally, assessments of the electrical contact resistance of interfaces between thermoelectric materials and the filler metals developed in this study were carried out to assess their suitability to form joints where electrical conductivity is a concern.

The foundation work set out in Chapter 4 was designed to meet the first two aims of this work; to assess whether surface morphology influenced the ability of filler metals to wet a surface and to discern whether the problems associated with silver-antimonide compound formation in the skutterudite thermoelectrics used in this project were due to excessive diffusion of silver. Sessile drop experiments assessed the impact of substrate surface properties on the contact angle between filler metal and copper substrates using a common industrial filler metal on copper substrates of varying degrees of roughness (in the range $0.01\mu\text{m} < R_a < 1.02\mu\text{m}$). Samples were heated to 800°C over an 80-minute time frame and were regularly photographed throughout the experiment. Analysis of the images with the specialised Drop_angle software was used to measure the contact angle between filler metal and surface as the experiment progressed. The results of this study indicated a linear relationship between decreasing surface roughness and decreasing contact angle. The smoothest surface evaluated ($R_a = 0.01\mu\text{m}$) did not fit the trend displayed by the other assessed samples and instead led to a high contact angle ($108 \pm 0.8^\circ$) between filler and substrate. This may indicate that in fact an optimum roughness level exists and further smoothing of surfaces beyond the optimum level is not required. The surface prepared to a $0.09\mu\text{m}$ finish gave the lowest wetting angle of all surfaces assessed in this study and as such surface finishes of this magnitude were used in subsequent assessments using filler metals developed in later chapters in an attempt to maximise substrate wetting.

The remaining work in Chapter 4 was concerned with the investigation of diffusion zone sizes between filler metals and substrates. A principal reason for the need to develop new filler metals for the application in question was due to excessive diffusion of constituent elements of the filler metal Ag-155 (specifically silver) through nickel diffusion barriers and into the thermoelectric materials it was being used to join, drastically impeding their

performance. An investigation was conducted to assess whether changing the type of torch used (propane or oxy-acetylene) as the heat source for brazing or whether the skill of the brazer conducting the procedure influenced the diffusion distance of filler metal constituents into copper plate. T-shaped butt joints between copper substrates were manufactured by 2 brazers of varying experience levels (an experienced brazer with 6 years industrial brazing experience and a novice brazer with 2 years' laboratory brazing experience) using both propane and oxyacetylene torches. High contrast BSE SEM images of the diffusion zone were measured by hand and with image analysis software to estimate the size of the diffusion zone in each joint. Significant overlap between error bars associated with each diffusion zone measurement led to the conclusion that no significant variation in diffusion zone size could be detected when brazing torch or brazer skill were varied.

The final investigation into diffusion distances undertaken in Chapter 4 sought to investigate the diffusion of silver in various base materials to assess whether silver diffused further in nickel than in other engineering materials. This investigation was performed to assess whether it was specifically the silver component of filler metal Ag-155 which diffused excessively through the nickel diffusion barrier used on thermoelectric components and if it was, to prevent its use in replacement filler metals designed in later chapters to avoid this issue. EDX line scans were taken across the interface between various parent metals (nickel, steel, stainless steel, copper and brass) and Ag-155 and the diffusion distance of silver examined. Data concluded that silver did diffuse further in nickel than in any of the other 4 parent materials assessed with an average diffusion distance of $6.40 \pm 0.27\mu\text{m}$ which is approximately a 25% increase above the next highest diffusion distance ($4.88 \pm 0.37\mu\text{m}$ for silver in copper). This evidence provides an explanation as to why silver-antimony compounds are seen in the antimony based skutterudites which serve as the thermoelectrics in this project; the nickel layer applied is clearly not as effective a diffusion barrier to silver as other elements would be. As the nickel diffusion barrier appears to be effective aside from the poor protection against silver diffusion (as no other compound formation has been explicitly reported as an issue with this thermoelectric / diffusion barrier combination) it was concluded that the filler metals designed in this work to replace Ag-155 should not contain silver.

Chapter 5 comprised of the work targeted at meeting aims 3 and 4 of this project; the design development and characterisation of alternative filler metals to replace Ag-155 in the application of joining copper substrates to nickel-coated skutterudite thermoelectrics. Python modelling was used refine HEA compositions with empirical parameters and select a series of alloys which were manufactured and trialled as brazing filler metals. Two similar successful compositions were found which were capable of forming metallurgical bonds between copper and nickel with low void percentages (<15%) (designated alloy D and alloy E). Gold-free analogues of these two successful systems were also produced due to cost concerns from the industrial partners of this project and characterised and assessed alongside their gold-containing counterparts. Compositional verification of these systems was undertaken with Inductively Coupled Plasma – Optical Emission Spectroscopy to verify that the manufactured alloys were within $\pm 2\%$ of the nominal composition with low impurity levels (<0.015% C, <0.001% N and <0.0042% O). Phase modelling for the systems was trialled using the Thermo-Calc SSOL4 database and phase identification was undertaken with an array of analytical techniques including EDX and XRD to conclude that the alloys developed had a 4 phase structure including a majority solid solution phase, a predominately tin or bismuth phase, a CuGa_2 binary phase and a gold-gallium phase. Differential Scanning Calorimetry was used to assess the melting ranges for the 2 compositions and their gold free analogues and all were found

to have melting ranges between 528-681°C which is wider than the optimal target range of 550-620°C. EDX line scans were used to measure the diffusion zone size of brazed joints between filler metal and nickel plate for all 4 alloys mentioned above and Ag-155. The diffusion zone size of 3 of the developed alloys (D, E and EauX) were found to be lower than that of Ag-155 after an identical brazing process. Alloy D diffused 68.6% of the distance of Ag-155, alloy E 74.3% and alloy EAuX 82.9%. The final alloy (DAuX) diffused 110.0% of the distance of Ag-155. These developed alloys were judged to be sufficiently meeting their design criteria to warrant further investigation and thus were taken forward as the alloys to be investigated in the final aim of this project.

The final aim of this project was to investigate any promising filler metals developed in this study for their ability to perform in their intended application with a particular focus on comparative performance to the currently used filler metal Ag-155. All 4 developed alloys and samples of Ag-155 were subjected to modified sessile drop experiments on as-received copper substrates with a surface roughness of $R_a = 0.09 \pm 0.02 \mu\text{m}$ – the roughness determined to lead to optimal wetting in the foundation work in Chapter 4. Samples were heated to 800°C over a period of 80 minutes and their wetting angle assessed using the same Drop-angle software used in Chapter 4. Alloy E was found to have the lowest final wetting angle of the 4 designed alloys with a final wetting angle of $9.0 \pm 0.2^\circ$. All 4 of the developed alloys demonstrated final wetting angles lower than the control Ag-155 sample which achieved a wetting angle of $120.5 \pm 0.7^\circ$. The apparently superior performance of the alloys developed in this study compared to the Ag-155 control was predicted to be due to the presence of oxide layers on the copper substrates used in this experiment which were in the ‘as-received’ condition and not ground like those in the foundation work in Chapter 4. The presence of oxide layers on substrate surfaces is known to disrupt the wetting performance of many standard filler metals which led to the conclusion that the alloys developed in this study had an increased capability of interacting with surfaces possessing an oxide layer when compared to Ag-155 probably due to the elements with a high oxygen affinity (e.g. gallium) that they contain.

Bond strength of brazed joints was assessed using nickel plate lap joints in a tensile testing setup in order to assess the shear strength of brazed joints formed with alloy D developed in this study in comparison to those formed with Ag-155. The overlap length of the lap joints was approximately 3mm (approximately equal to the thickness of the nickel plate used) to ensure failure within the brazed joint as opposed to in the parent materials. The average bond strength was determined to be $159.5 \pm 9.4 \text{MPa}$ for the Ag-155 joints and $28.0 \pm 3.0 \text{MPa}$ for the joints made with alloy D. This gives the bond strength of joints with alloy D to be approximately 17.5% of the strength of joints formed with Ag-155 but of a similar strength to hot pressed nickel/thermoelectric joints produced in literature [1]. Thermal cycling was used on similarly brazed lap joints between copper and nickel plate to assess the impact of repeated thermal exposure on samples brazed with both Ag-155 and alloy D. Samples were raised to 575°C over approximately 5 minutes and then cooled to room temperature over approximately 13 minutes. This was considered a single ‘cycle’. Joints brazed with Ag-155 showed no appreciable decline in bond strength after 50 cycles with no brazed joints assessed failing over this number of cycles. Joints formed using alloy D also did not demonstrate a clear decline in bond strength for joints which survived the thermal cycling process, however the failure rate in these alloys was much higher with nearly 40% of samples failing when subject to between 20 and 30 cycles and all samples failing within 50 cycles demonstrating a significantly worse resistance to thermal cycling than joints formed with Ag-155.

Finally, the electrical interfaces between filler metal and samples of n-type skutterudite thermoelectric ($\text{CoSb}_{2.75}\text{Sn}_{0.05}\text{Te}_{0.20}$) were assessed for their electrical contact resistance.

A sample of the design thermoelectric/braze/copper interlayer/braze/thermoelectric (using alloy D as the braze) found that there was no measurable contact resistance between braze and copper interlayer; indicating a very good electrical joint. The average contact resistances between the alloy D braze and the thermoelectric was found to be $1.12 \times 10^{-4} \Omega \text{ cm}^2$ for this sample – approximately double that of the target resistance for similar joints ($5 \times 10^{-5} \Omega \text{ cm}^2$ [2]). The assessment was repeated using an identical sample but with the copper interlayer removed (e.g. thermoelectric/braze/thermoelectric) and again with another sample with the copper interlayer removed and an addition of a $0.7 \mu\text{m}$ nickel layer to the thermoelectric surface. Both samples were found to have lower contact resistances than the copper-interlayer containing sample with the nickel-coated sample having a contact resistance of $3.72 \times 10^{-5} \Omega \text{ cm}^2$ compared to the $2.02 \times 10^{-5} \Omega \text{ cm}^2$ on the non-coated sample. It is postulated that the increased contact resistance on the nickel containing sample is due to the nickel layer acting as a diffusion barrier preventing diffusion of filler metal constituents into the thermoelectric. Finally, a sample was manufactured using Ag-155 as the filler metal to compare the electrical performance of alloy D compared to Ag-155. The contact resistance of the Ag-155 sample was determined to be $4.31 \times 10^{-5} \Omega \text{ cm}^2$; a contact resistance twice that of the identical sample formed using alloy D ($2.02 \times 10^{-5} \Omega \text{ cm}^2$).

7.2. Future work

Whilst this project was successful in meeting the aims laid out in Chapter 1 there are many directions in which work leading on from this project could take. Detailed below are some ideas for expanding upon the conclusions already drawn in this study:

- Further assessment of the optimised surface morphology for brazing could be carried out via further sessile drop experiments with an increased number of samples at the smoother roughness ranges used in this study (e.g. $R_a = 0.01 \mu\text{m}$ – $0.16 \mu\text{m}$) and potentially on samples with an even lower roughness value ($R_a < 0.01 \mu\text{m}$) to confirm whether an optimum roughness for brazing does exist. Additionally, other aspects of surface morphology beside the roughness (e.g. the lay of the surface) could be systematically investigated to optimise filler to substrate contact and filler flow.
- Should further commercial interest in the alloy systems developed in this study be seen, improvements could be made to the Thermo-Calc databases used to model these systems by assessing a greater percentage of the binary and ternary diagrams comprising the constituent elements of these systems. In particular, the Cu-Zn-Ga ternary developed in this study could be refined and verified by the manufacture and characterisation of some alloys within the Cu-Zn-Ga system to improve its accuracy. An improvement to such a diagram may lead to refinement of the compositions produced in this study and enable tuning of properties (e.g. melting point and mechanical strength) of the systems investigated here to improve their performance in the application in question.
- Further in-situ testing (similar to that covered in Chapter 6) could be used to examine in greater detail the performance of these developed systems as filler metals in-situ. A full thermoelectric module could be constructed using the filler metals developed in this study and placed within an exhaust system in a laboratory environment whilst monitoring the electrical output of the thermoelectric module. This would have the dual purpose of assessing the resistance of the filler developed in this study to the corrosive environment inside an exhaust system and provide a more realistic measure of the thermal cycling a brazed joint is likely to experience

in its final application whilst giving insight into the comparative electrical performance of TEGs manufactured with the alloys developed in this study in comparison to those manufactured with Ag-155.

- In a broader sense the HEA design process developed in this study for the production of a new filler metal could be taken and applied more widely. A similar approach may work for developing alternative filler metals for different niche applications where current filler metals are not suitable for the task. An example area where such trials may be fruitful include the development of new reactive air brazes for use in the joining of Solid Oxide Fuel Cells [3].

7.3. References

- [1] Liu W, Wang H, Wang L, et al. Understanding of the contact of nanostructured thermoelectric n-type Bi₂Te_{2.7}Se_{0.3} legs for power generation applications. *J. Mater. Chem. A*. 2013;1:13093–13100.
- [2] Ngan PH, Van Nong N, Hung LT, et al. On the Challenges of Reducing Contact Resistances in Thermoelectric Generators Based on Half-Heusler Alloys. *J. Electron. Mater.* 2016;45:594–601.
- [3] Way M, Willingham J, Goodall R. Brazing filler metals. *Int. Mater. Rev.* [Internet]. 2019;0:1–29. Available from: <https://doi.org/10.1080/09506608.2019.1613311>.

Appendices

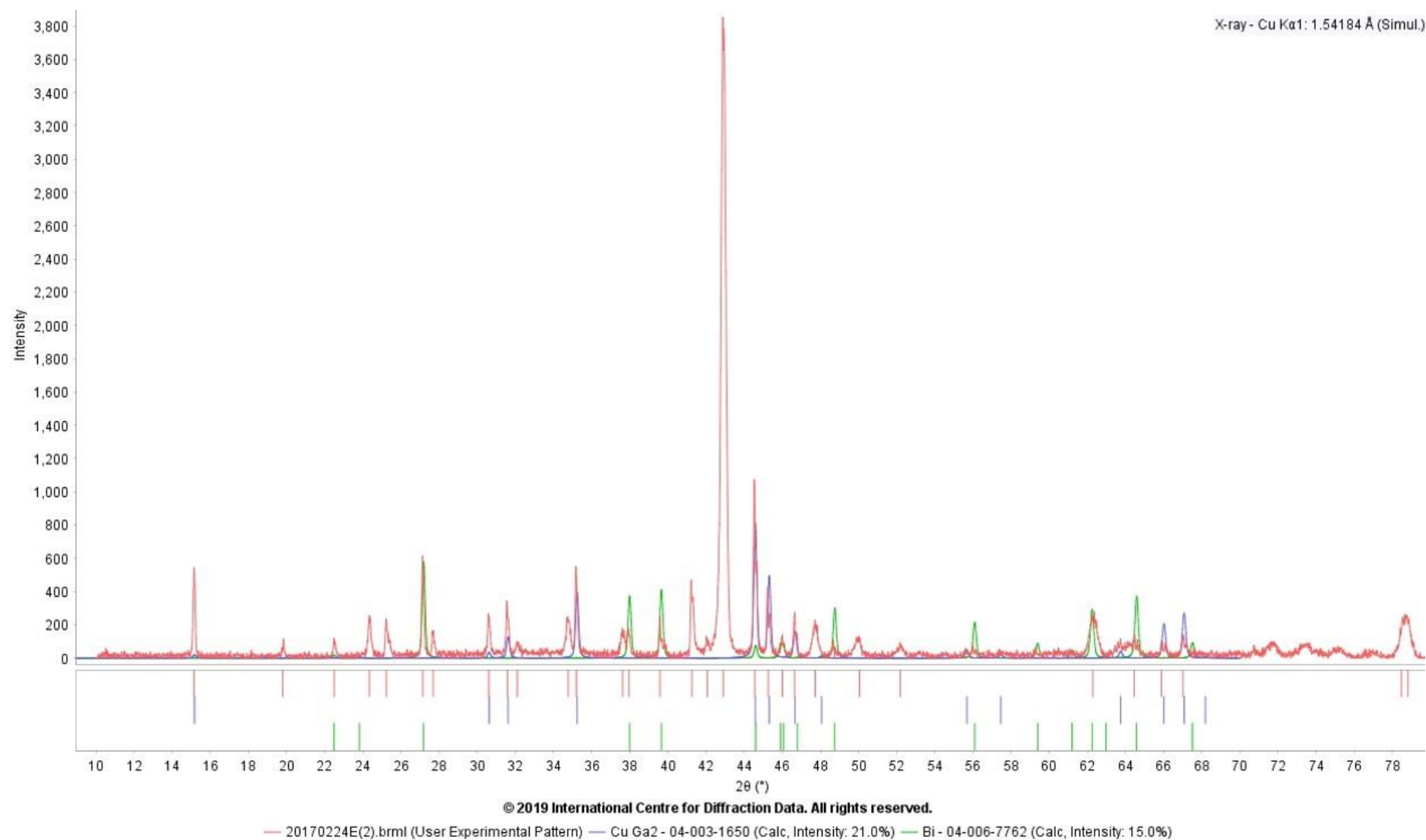
Appendix 1: Alloy E parameter optimisation

	Atomic size difference (δ)	Enthalpy of mixing (ΔH_{mix}) kJ mol ⁻¹	Entropy of mixing (ΔS_{mix}) kJ K ⁻¹ mol ⁻¹	Melting Temperature (T_m) °C
Program optimised	8.12	4.60	11.04	550.05
Gold removed and components scaled	4.96	1.47	9.72	520.80

Appendix 2: phases $S_{\bar{x}}$ table (Table 5.14)

Sample Name	Phase number (description)	$(S_{\bar{x}})$ for each average Composition (Wt%)							
		Cu	Zn	Ga	Sn	Au	Bi	O	Si
D	1) primary solid solution	0.5	0.2	0.2	0.0	0.5	-	0.1	-
	2) predominantly tin phase	0.3	0.2	0.5	1.8	0.4	-	0.9	0.1
	3) CuGa ₂	0.3	0.4	0.5	0.0	0.3	-	0.2	0.1
	4) gold-gallium phase	0.5	0.4	0.8	0.4	0.5	-	0.1	0.1
DAuX	1) primary solid solution	2.6	2.4	2.1	-	-	-	-	-
	2) predominantly tin phase	0.4	0.2	0.7	1.2	-	-	-	-
	3) CuGa ₂	0.2	0.2	0.2	-	-	-	0.2	-
E	1) primary solid solution	0.6	0.3	0.3	-	0.5	0.1	0.2	-
	2) predominantly bismuth phase	0.2	0.4	0.1	-	0.2	0.9	0.3	-
	3) CuGa ₂	0.1	0.2	0.3	-	0.2	0.0	0.2	-
	4) gold-gallium phase	0.6	0.8	2.0	-	1.2	0.1	0.3	-
E AuX	1) primary solid solution	0.9	1.8	0.9	-	-	0.0	-	0.2
	2) predominantly bismuth phase	0.1	0.1	0.2	-	-	0.2	-	0.3
	3) CuGa ₂	0.2	1.4	1.5	-	-	-	-	0.0

Appendix 3: Alloy E diffraction pattern (XRD)



Appendix 4: Alloy EAuX diffraction pattern (XRD)

